



**MEASURING AND MODELLING THE IMPACT OF THE IONOSPHERE ON
SPACE BASED SYNTHETIC APERTURE RADARS**

by

CHRISTOPHER ROBERT MANNIX, MSci

A thesis submitted to
The University of Birmingham

For the Degree
DOCTOR OF PHILOSOPHY

Space Environment and Radio Engineering Group
School of Engineering
College of Engineering and Physical Sciences
University of Birmingham
March 2016

UNIVERSITY OF
BIRMINGHAM

University of Birmingham Research Archive

e-theses repository

This unpublished thesis/dissertation is copyright of the author and/or third parties. The intellectual property rights of the author or third parties in respect of this work are as defined by The Copyright Designs and Patents Act 1988 or as modified by any successor legislation.

Any use made of information contained in this thesis/dissertation must be in accordance with that legislation and must be properly acknowledged. Further distribution or reproduction in any format is prohibited without the permission of the copyright holder.

ABSTRACT

Synthetic aperture radar (SAR) is a technique widely used in applications that require all-weather imaging. The ionosphere affects the operation of these radars, with those operating at L-band (1-2 GHz) and below at risk of being seriously compromised by the ionosphere. A method of using Global Positioning System (GPS) data to synthesize the impact of the ionosphere on SAR systems has been presented. The technique was used to assess the viability of using a signal phase correction derived from a reference location in a SAR image to correct ionospheric effects across the image. A dataset of SAR images and GPS measurements collected simultaneously on Ascension Island were used to test two techniques for deriving ionospheric strength of turbulence ($C_k L$) from SAR images – one using measurements of trihedral corner reflectors (CR) and the other measurements of natural clutter. The CR $C_k L$ values showed a correlation of 0.69 with GPS estimates of $C_k L$, whilst the clutter measurements showed a correlation of up to 0.91 with the CR values. Finally, a study of using the effects of intensity scintillation on SAR images to measure the S_4 index was performed. The study was not able to reproduce previous results, but produced significant practical conclusions.

Our doubts are traitors,
And make us lose the good we oft might win
By fearing to attempt.

William Shakespeare, "Measure for Measure", Act 1 scene 4

ACKNOWLEDGEMENTS

First and foremost, I would like to thank my supervisor, Paul Cannon OBE for all of the help, guidance and support he provided throughout my PhD. Your advice has been unfailingly excellent, both academically as well as more generally, and I will always appreciate the faith you placed in me. I am truly grateful.

I would also like to thank David Belcher. Your extensive knowledge of your field, patience, and the generosity with which you gave your time to assist me were invaluable in completing this work.

I must also place on record my gratitude to the rest of the Space Environment and Radio Engineering group at the University of Birmingham. Discussions within the group are always fun and enlightening, and I thoroughly enjoyed my time there. I must especially thank Matthew Angling, head of group for always being available to provide insightful comments and suggestions – or at the very least a terrible joke about tea!

A special thank-you goes to Sean Elvidge, who is always ready to have a coffee break and discuss the problem of the day, no matter how big or how small. I will always appreciate your friendship and advice.

Much of the experimental work described in this thesis was performed on Ascension Island, with the extremely able assistance of Stephen White. Your technical expertise and wide-ranging skills were absolutely invaluable and much appreciated. I must also thank Anders Gustavsson and the Swedish Defence Research Agency, for not only lending us the corner reflectors used in this work, but also coming out to the island to help with the assembly. Further, I would like to thank the Japan Aerospace Exploration Agency for providing the radar data used here.

I would like to place on record my gratitude to those who live and work on Ascension Island, who were nothing but kind, helpful and generous during our time on the island. I must especially mention those at the ESA Ariane tracking station, Two Boats School, Sure South Atlantic and the BBC relay station, all of whom kindly hosted our equipment for several years.

To all of my friends and family. Your support over the years means everything to me. Thank you.

Finally, I must thank my parents. Your tireless support and encouragement in all my endeavours has put me on the path to where I am today. The example you set has driven me to attain the highest level in everything I do, and given me the self-belief to achieve more than I ever thought possible.

TABLE OF CONTENTS

Abstract.....	i
Acknowledgements	iii
Table of Contents	v
List of Figures.....	ix
List of Tables.....	xviii
1 Introduction	1
2 The Ionosphere and Ionospheric Radio Propagation.....	5
2.1 The Ionosphere	5
2.1.1 Common Morphology	6
2.1.2 The Equatorial Ionosphere.....	7
2.1.3 Irregularities.....	9
2.2 Ionospheric Radio Propagation	12
2.2.1 Refraction of signals.....	13
2.2.2 Diffraction of signals.....	15
3 Synthetic Aperture Radar	21
3.1 Synthetic Aperture Radar Theory.....	23
3.2 The Point Spread Function	26
3.2.1 PSLR, ISLR.....	27
3.2.2 Window functions	28
3.3 SAR Applications.....	29

3.4 Impact of the ionosphere on SAR	30
4 Using GNSS Signals as a Proxy for SAR Signals: Correcting Ionospheric Defocussing ...	33
4.1 Theory	35
4.1.1 The Phase Spectrum.....	35
4.1.2 The Point Spread Function.....	36
4.1.3 Effect of the ionosphere on the SAR PSF.....	36
4.1.4 Synthesising the SAR PSF Using GPS Data	37
4.1.5 Practical Considerations.....	39
4.2 Experiment.....	48
4.3 Single Location Results	49
4.3.1 Point Spread Functions	49
4.4 Two location Results.....	56
4.4.1 Variation in RMS Phase Difference with Distance	56
4.4.2 Sharpening the PSF.....	59
4.5 Conclusions.....	64
5 Deriving ionospheric scintillation parameters from SAR signals – Corner Reflectors	67
5.1 Theory	68
5.1.1 The Phase Spectrum.....	68
5.1.2 The Point Spread Function.....	69
5.2 Experiment.....	72
5.3 Island Images	75

5.4 PSF Measurement Results	76
5.5 Comparison with GPS C_kL Results	84
5.6 Conclusions	96
6 Deriving ionospheric scintillation parameters from SAR signals – Images.....	99
6.1 Statistics of natural clutter	100
6.2 Effect of the ionosphere on clutter statistics.....	101
6.3 PALSAR-2 Data.....	104
6.4 Data Analysis.....	106
6.4.1 Clutter measurements	106
6.5 Comparison with corner reflector derived C_kL	115
6.5.1 Effect of correlation length.....	120
6.5.2 Effect of p value	125
6.5.3 Effect of distance	127
6.6 Discussion and conclusions	129
7 Deriving ionospheric scintillation parameters from SAR signals – Amplitude Scintillation	131
7.1 Effect of intensity scintillation on SAR images	131
7.2 PALSAR Data	133
7.3 Results	136
7.3.1 Estimating S_4	136
7.3.2 Effect of phase scintillation	140

7.4 Discussion	141
8 Conclusions and Future Work.....	143
8.1 Future Work	146
Appendix A. List of PALSAR-2 Images	149
Appendix B. Plots of PALSAR-2 Point Spread Functions Measured From Images	151
Appendix C. SAR/Ionosphere Theory	189
Formation and Structure of the SAR PSF	189
Effect of the ionosphere on the SAR image.....	190
Effect of the ionosphere on clutter statistics	191
Effect of ionospheric noise on the observed underlying RCS	192
Effect of ionospheric noise on speckle	193
Smoothing effect on the cross-section $\sigma_0(r)$	194
Effect on the mean of the distribution.....	195
Effect on the shape/order parameter of the distribution.....	195
Ionosphericly disturbed pdf.....	198
List of References	201

LIST OF FIGURES

Figure 2.1: Global regions of the Earth’s ionosphere [Cannon, Private Communication 2015].	6
Figure 2.2: Diurnal variation in the structure of the ionosphere [Angling et al., 2007].	7
Figure 2.3: Schematic of the formation of the latitude variation of ionization density in the equatorial F-region [de La Beaujardière, 2004].	8
Figure 2.4: Electron density contours ($\log_{10}n_e$) as a function of altitude and dip latitude for December solstice conditions [Anderson and Roble, 1981].	8
Figure 2.5: Regions of ionospheric irregularity formation. Adapted from Basu and Groves [2001].	9
Figure 2.6: 50 MHz radar interferometer results from Jicamarca Radio Observatory, September 27-28, 1994 [Basu et al., 1996].	11
Figure 2.7: Impact of ionospheric irregularities on power of received signals [van de Kamp et al., 2010].	11
Figure 2.8: Effect of small scale irregularities on incident plane wave.	16
Figure 2.9: Example of the effect of scintillation on GPS signal amplitude [Bhattacharyya and Beach, 2000].	16
Figure 2.10: Example of the effect of scintillation on relative total electron content, estimated using differential GPS phase. [Bhattacharyya and Beach, 2000].	17
Figure 2.11: Power spectra of ATS-6 signals received at Boulder, Colorado [Umeki et al., 1977] © American Geophysical Union	18
Figure 3.1: SAR strip-map operation	23
Figure 3.2: Range from the radar to a scatterer illuminated by the beam on the ground.	24
Figure 3.3: SAR spotlight-mode operation	26

Figure 3.4: Example point spread function illustrating different characteristics. Reproduced from Massonet and Souyris [2008].	27
Figure 3.5: Hamming window function.	29
Figure 3.6: Impact of the ionosphere on a PALSAR-2 image of Ascension Island. (left: undisturbed, right: disturbed)	31
Figure 4.1: Large phase variations produced by the single and dual frequency methods.	47
Figure 4.2: Phase variations present in single frequency data but not in dual frequency data.	47
Figure 4.3: Ascension Island (7.9°S, 14.8°W showing the ESA Tracking Station which was the location of the fixed receiver and the road (shown in black) along which the mobile measurements were made).	48
Figure 4.4: Examples of the residual phase modulation for quiet and disturbed ionospheric conditions as recorded by the GPS receivers on Ascension Island.	51
Figure 4.5: Point spread functions for different levels of ionospheric disturbance, generated from GPS signal data recorded on Ascension Island.	52
Figure 4.6: Relationship between RMS phase and PSLR of uncorrected SAR PSF.	55
Figure 4.7: Geometry of SAR signals and the ionospheric phase screen for two points in the image. Dashed lines illustrate the real beam width.	56
Figure 4.8: Differences in SAR signal paths in the along-track direction.	57
Figure 4.9: RMS phase difference (for pre-correction PSLR < 5 dB).	59
Figure 4.10: Uncorrected PSF, SVID 29, 26/01/2014.	61
Figure 4.11: Post-correction PSF (receiver separation ~250 m). SVID 29, 26/01/2014.	61
Figure 4.12: Uncorrected PSF, SVID 29, 24/01/2014.	62
Figure 4.13: Post-correction PSF (receiver separation ~2500 m). SVID 29, 24/01/2014.	62
Figure 4.14: PSLR change after phase correction for uncorrected PSF PSLR < 5dB.	63

Figure 4.15: PSLR change after phase correction for uncorrected PSF PSLR < 5dB, GPS amplitude data included in PSF calculation.	64
Figure 5.1: Left: eastward looking corner reflector at Devil’s Ashpit and right: westward looking corner reflector at Long Beach.	73
Figure 5.2: Map of Ascension Island showing corner reflector locations.	74
Figure 5.3: Whole island image (2014-08-18, no scintillation)	76
Figure 5.4: West corner reflector response, 2014-08-18 01:47.	80
Figure 5.5: West corner reflector response, 2014-08-22, 01:33.	80
Figure 5.6: West corner reflector response, 2014-11-14 01:33.	81
Figure 5.7: West corner reflector response 2014-10-02 01:12.	81
Figure 5.8: West corner reflector response, 2014-11-13 01:12.	82
Figure 5.9: West corner reflector response, 2015-01-31 01:06.	82
Figure 5.10: Histogram of phase spectral index (p) values from fit of theoretical sidelobe function to measured corner reflector response.	83
Figure 5.11: Histogram of C_kL values from fit of theoretical sidelobe function to measured corner reflector response (all p values).	83
Figure 5.12: Histogram of C_kL values from fit of theoretical sidelobe function to measured corner reflector response ($p \leq 5$).	84
Figure 5.13: GPS phase power spectral density - GPS SVID 5 - 2014/10/01.	87
Figure 5.14: GPS phase power spectral density - GPS SVID 25 - 2014/10/03.	87
Figure 5.15: GPS phase power spectral density - GPS SVID 5 - 2014/10/05.	88
Figure 5.16: GPS phase power spectral density - GPS SVID 11 - 2015/02/02.	88
Figure 5.17: Histogram of p values from fit to measured GPS phase power spectral density.	89

Figure 5.18: Histogram of C_{kL} values from fit to measured GPS phase power spectral density.	89
Figure 5.19: Comparison of CR and GPS values ($CR\ p \leq 5$).	90
Figure 5.20: Comparison of CR and GPS C_{kL} values ($CR\ p \leq 5$, incidence angles $> 30^\circ$). ...	91
Figure 5.21: Comparison of CR and GPS phase spectral index, p-values (600 s phase power spectrum).....	92
Figure 5.22: Comparison of CR and GPS C_{kL} values ($CR\ p < 3$ and $CR\ p > 1.5$, incidence angles $> 30^\circ$).....	93
Figure 5.23: Comparison of CR and GPS phase spectral index, p, values (30 s phase power spectrum).....	94
Figure 6.1: Effect of order parameter on K-distribution.....	101
Figure 6.2: Map of Ascension Island showing clutter locations (blue circles indicate selected areas of clutter and the red triangles indicate the location of the corner reflectors).	105
Figure 6.3: West clutter area (2014/08/18, no scintillation).	108
Figure 6.4: West clutter area (2014/10/27, moderate scintillation).	108
Figure 6.5: Central clutter area (2014/08/18, no scintillation).....	109
Figure 6.6: Central clutter area (2014/10/27, moderate scintillation).....	109
Figure 6.7: East clutter area (2014/08/18, no scintillation).....	110
Figure 6.8: East clutter area (2014/10/27, moderate scintillation).....	110
Figure 6.9: Histogram of west clutter intensity values (Figure 6.3, 2014/08/18, no scintillation)	111
Figure 6.10: Histogram of west clutter intensity values (Figure 6.4, 2014/10/27, moderate scintillation)	111
Figure 6.11: C_{kL} distribution from west clutter.....	114

Figure 6.12: C_kL distribution from central clutter.....	114
Figure 6.13: C_kL distribution from east clutter.	115
Figure 6.14: Corner reflector, clutter C_kL comparison - west clutter - $p_{CR} < 5$	117
Figure 6.15: Corner reflector, clutter C_kL comparison - central clutter - $p_{CR} < 5$	117
Figure 6.16: Corner reflector, clutter C_kL comparison - east clutter - $p_{CR} < 5$	118
Figure 6.17: Corner reflector, clutter C_kL comparison - west clutter - $p_{CR} < 5$, $\theta_{inc} > 30^\circ$	118
Figure 6.18: Corner reflector, clutter C_kL comparison - central clutter - $p_{CR} < 5$, $\theta_{inc} > 30^\circ$.	119
Figure 6.19: Corner reflector, clutter C_kL comparison - east clutter - $p_{CR} < 5$, $\theta_{inc} > 30^\circ$	119
Figure 6.20: Along-track intensity autocorrelation function - west clutter (Figure 6.3, 2014/08/18, no scintillation).....	122
Figure 6.21: Along-track intensity autocorrelation function - central clutter (Figure 6.5, 2014/08/18, no scintillation).....	122
Figure 6.22: Along-track intensity autocorrelation function - east clutter (Figure 4, 2014/08/18, no scintillation).....	123
Figure 6.23: Corner reflector, clutter C_kL comparison - west clutter - $p_{CR} < 5$, $\theta_{inc} > 30^\circ$, $I_r = ACF$ Fit.....	123
Figure 6.24: Corner reflector, clutter C_kL comparison - central clutter - $p_{CR} < 5$, $\theta_{inc} > 30^\circ$, $I_r = ACF$ Fit.....	124
Figure 6.25: Corner reflector, clutter C_kL comparison - east clutter - $p_{CR} < 5$, $\theta_{inc} > 30^\circ$, $I_r = ACF$ Fit.....	124
Figure 6.26: Corner reflector, clutter C_kL comparison - west clutter - $p_{CR} < 5$, $\theta_{inc} > 30^\circ$, $I_r = ACF$ Fit, $p_{clutter} = p_{CR}$	125
Figure 6.27: Corner reflector, clutter C_kL comparison - central clutter - $p_{CR} < 5$, $\theta_{inc} > 30^\circ$, $I_r = ACF$ Fit, $p_{clutter} = p_{CR}$	126

Figure 6.28: Corner reflector, clutter C_kL comparison - east clutter - $p_{CR} < 5$, $\theta_{inc} > 30^\circ$, $l_r = ACF$ Fit, $p_{clutter} = p_{CR}$	126
Figure 6.29: Corner reflector, clutter C_kL comparison - west clutter - $p_{CR} < 5$, $\theta_{inc} > 30^\circ$, $l_r = ACF$ Fit, $p_{clutter} = p_{CR}$, west corner reflector only.	127
Figure 6.30: Corner reflector, clutter C_kL comparison - central clutter - $p_{CR} < 5$, $\theta_{inc} > 30^\circ$, $l_r = ACF$ Fit, $p_{clutter} = p_{CR}$, west corner reflector only.	128
Figure 6.31: Corner reflector, clutter C_kL comparison - east clutter - $p_{CR} < 5$, $\theta_{inc} > 30^\circ$, $l_r = ACF$ Fit, $p_{clutter} = p_{CR}$, west corner reflector only.	128
Figure 7.1: Ascending node velocity ratio γ for a 2200 LT sun-synchronous satellite at an altitude of 698 km. Adapted from [Belcher and Cannon, 2014].....	132
Figure 7.2. a) Disturbed image (left) and b) Undisturbed image (right).....	135
Figure 7.3. a) Disturbed image (left) and b) Undisturbed image (right).....	135
Figure 7.4. a) Disturbed image (left) and b) Undisturbed image (right).....	136
Figure 7.5. Residual intensity image from images in Figure 7.2. Each resolution cell is $10 \times 25m$	139
Figure 7.6. Residual intensity image from Figure 7.3. Each resolution cell is $10 \times 25m$	139
Figure 7.7. Residual intensity image from Figure 7.4. Each resolution cell is $10 \times 25m$	140
Figure B.1: PALSAR-2 PSF – 2014-08-18	151
Figure B.2: PALSAR-2 PSF - 2014-08-19	151
Figure B.3: PALSAR-2 PSF - 2014-08-22	152
Figure B.4: PALSAR-2 PSF - 2014-10-01	152
Figure B.5: PALSAR-2 PSF - 2014-10-02	153
Figure B.6: PALSAR-2 PSF - 2014-10-03	153
Figure B.7: PALSAR-2 PSF - 2014-10-05	154

Figure B.8: PALSAR-2 PSF - 2014-10-11.....	154
Figure B.9: PALSAR-2 PSF - 2014-10-12.....	155
Figure B.10: PALSAR-2 PSF - 2014-10-21.....	155
Figure B.11: PALSAR-2 PSF - 2014-10-25.....	156
Figure B.12: PALSAR-2 PSF - 2014-10-26.....	156
Figure B.13: PALSAR-2 PSF - 2014-10-27.....	157
Figure B.14: PALSAR-2 PSF - 2014-10-28.....	157
Figure B.15: PALSAR-2 PSF - 2014-10-29.....	158
Figure B.16: PALSAR-2 PSF - 2014-10-30.....	158
Figure B.17: PALSAR-2 PSF - 2014-10-31.....	159
Figure B.18: PALSAR-2 PSF - 2014-11-01.....	159
Figure B.19: PALSAR-2 PSF - 2014-11-02.....	160
Figure B.20: PALSAR-2 PSF - 2014-11-04.....	160
Figure B.21: PALSAR-2 PSF - 2014-11-05.....	161
Figure B.22: PALSAR-2 PSF - 2014-11-06.....	161
Figure B.23: PALSAR-2 PSF - 2014-11-08.....	162
Figure B.24: PALSAR-2 PSF - 2014-11-09.....	162
Figure B.25: PALSAR-2 PSF - 2014-11-10.....	163
Figure B.26: PALSAR-2 PSF - 2014-11-11.....	163
Figure B.27: PALSAR-2 PSF - 2014-11-12.....	164
Figure B.28: PALSAR-2 PSF - 2014-11-13.....	164
Figure B.29: PALSAR-2 PSF - 2014-11-14.....	165
Figure B.30: PALSAR-2 PSF - 2014-11-15.....	165
Figure B.31: PALSAR-2 PSF - 2014-11-16.....	166

Figure B.32: PALSAR-2 PSF - 2014-11-18	166
Figure B.33: PALSAR-2 PSF - 2014-11-19	167
Figure B.34: PALSAR-2 PSF - 2014-11-20	167
Figure B.35: PALSAR-2 PSF - 2014-11-22	168
Figure B.36: PALSAR-2 PSF - 2014-11-23	168
Figure B.37: PALSAR-2 PSF - 2014-11-27	169
Figure B.38: PALSAR-2 PSF - 2014-11-28	169
Figure B.39: PALSAR-2 PSF - 2014-11-29	170
Figure B.40: PALSAR-2 PSF - 2014-11-30	170
Figure B.41: PALSAR-2 PSF - 2014-12-02	171
Figure B.42: PALSAR-2 PSF - 2014-12-03	171
Figure B.43: PALSAR-2 PSF - 2014-12-06	172
Figure B.44: PALSAR-2 PSF - 2014-12-07	172
Figure B.45: PALSAR-2 PSF - 2014-12-08	173
Figure B.46: PALSAR-2 PSF - 2014-12-11	173
Figure B.47: PALSAR-2 PSF - 2014-12-12	174
Figure B.48: PALSAR-2 PSF - 2014-12-16	174
Figure B.49: PALSAR-2 PSF - 2014-12-17	175
Figure B.50: PALSAR-2 PSF - 2014-12-20	175
Figure B.51: PALSAR-2 PSF - 2014-12-21	176
Figure B.52: PALSAR-2 PSF - 2014-12-22	176
Figure B.53: PALSAR-2 PSF - 2014-12-25	177
Figure B.54: PALSAR-2 PSF - 2014-12-26	177
Figure B.55: PALSAR-2 PSF - 2014-12-30	178

Figure B.56: PALSAR-2 PSF - 2014-12-31.....	178
Figure B.57: PALSAR-2 PSF - 2015-01-03.....	179
Figure B.58: PALSAR-2 PSF - 2015-01-04.....	179
Figure B.59: PALSAR-2 PSF - 2015-01-05.....	180
Figure B.60: PALSAR-2 PSF - 2015-01-08.....	180
Figure B.61: PALSAR-2 PSF - 2015-01-09.....	181
Figure B.62: PALSAR-2 PSF - 2015-01-13.....	181
Figure B.63: PALSAR-2 PSF - 2015-01-14.....	182
Figure B.64: PALSAR-2 PSF - 2015-01-17.....	182
Figure B.65: PALSAR-2 PSF - 2015-01-18.....	183
Figure B.66: PALSAR-2 PSF - 2015-01-19.....	183
Figure B.67: PALSAR-2 PSF - 2015-01-22.....	184
Figure B.68: PALSAR-2 PSF - 2015-01-23.....	184
Figure B.69: PALSAR-2 PSF - 2015-01-27.....	185
Figure B.70: PALSAR-2 PSF - 2015-01-28.....	185
Figure B.71: PALSAR-2 PSF - 2015-01-31.....	186
Figure B.72: PALSAR-2 PSF - 2015-02-01.....	186
Figure B.73: PALSAR-2 PSF - 2015-02-02.....	187
Figure B.74: PALSAR-2 PSF - 2015-02-05.....	187
Figure B.75: PALSAR-2 PSF - 2015-02-06.....	188
Figure B.76: PALSAR-2 PSF - 2015-02-10.....	188

LIST OF TABLES

Table 5.1: PALSAR-2 radar parameters.	72
Table 5.2: ALOS-2 orbit characteristics.	73
Table 5.3: Corner reflector location details.	75
Table 6.1: Locations of clutter areas on Ascension Island	106
Table 6.2: Incidence angle distribution for PALSAR-2 dataset.	113
Table 7.1. PALSAR images disturbed by scintillation (D) and undisturbed (U).	134
Table A.1: Details of the PALSAR-2 images used in this work.....	149

1 INTRODUCTION

Synthetic aperture radar (SAR) is a technique widely used in applications that require all weather imaging. SARs utilise the forward motion of the radar platform to produce high resolution imaging at long-ranges, without requiring impractically large antenna dimensions. As such, SARs have become increasingly popular for space-based (SB) remote sensing applications such as surveillance, measurement of the Earth's biosphere and disaster response.

A typical SB-SAR operates in low Earth orbit (LEO), and thus the SAR signals must pass through the ionosphere on their way to and from the satellite. The ionosphere affects the operation of these radars [*Quegan and Lamont, 1986*], with those operating at L-band (1-2 GHz) and below at risk of being seriously compromised by the ionosphere. Understanding and mitigating the effects of the ionosphere on SAR is therefore an important and relevant effort [*Pi, 2015*].

Ideally, SB-SAR imagery could be investigated under a range of known ionospheric conditions. Unfortunately, coincident SAR data and measurements of the ionosphere are relatively rare. In view of this, the first part of this work will present a new technique developed to estimate the ionospheric impact on a SAR system using Global Navigation Satellite Systems signals (Section 4). Such systems are widespread, and offer near-constant signal availability world-wide. They are also already in common use as ionospheric monitoring systems.

SB-SAR can be significantly affected by scintillation of the phase of the SAR signals, driven by the ionosphere. The random nature of the scintillation means that it is not easily predicted, and thus hard to correct. In Section 5 the GNSS technique described above is used to explore the possibility of using the measurement of a point target in an image to derive a phase correction that can be applied across the image to account for the effects of phase scintillation.

Whilst much work has focussed on mitigating the effects of ionosphere on SAR images, it is not unreasonable to suggest that the inverse may be useful – can the effects be measured, and used to infer information about the current state of the ionosphere?

Belcher and Rogers [2009], proposed a theory linking the shape of the ionospherically disturbed SAR point spread function (PSF) with conditions in the ionosphere, as measured by the height integrated strength of turbulence, $C_k L$. This work will test this theory using direct measurements of the PSF of the Phased Array type L-band SAR 2 (PALSAR-2), made using trihedral corner reflectors (CR) deployed on Ascension Island. (Section 5). The $C_k L$ values produced from the PSF measurements will be compared with independent measurements of ionospheric conditions made using GNSS.

In terms of measuring the ionosphere using SAR, the corner reflector technique is useful, but has a significant limitation – the requirement for a point target (such as a CR) to be present in the image. *Belcher and Cannon* [2013] recently suggested a new technique to indirectly measure the ionospheric impact on the SAR PSF using measurements of the statistical properties of images of natural clutter (such as forests). Natural clutter is extremely prevalent across the globe, and thus this technique could allow the derivation of ionospheric information from a wide range of images. The technique will be applied to a large dataset of PALSAR-2 images, and the results compared to those derived from the corner reflectors (Section 6).

The corner reflector and natural clutter measurement techniques described above relate to scintillation of the phase of the SAR signal by the ionosphere. However, SAR images may also be degraded by scintillation of the amplitude of the signal. This often manifests as striping in the along-track direction of SAR images recorded near the magnetic equator. It has been suggested that the intensity of this striping, relative to the intensity of the imaged scene, can be

related to the ionospheric amplitude scintillation parameter S_4 [*Belcher and Cannon, 2014*]. The final part of this work presents the results of attempting this with a small dataset of images affected by ionospheric striping (Section 7).

2 THE IONOSPHERE AND IONOSPHERIC RADIO PROPAGATION

The ionosphere is the ionized region of the atmosphere between ~80 km and ~1500 km altitude [Davies, 1990]. In the context of this research it is important because the free electrons produced by ionization affect the propagation of electromagnetic waves and consequently impact the operation of radio systems [Cannon, 2009].

At mid and low latitudes, the electrons are produced almost solely by photoionization of atmospheric neutrals to produce both ions and electrons but at high latitudes this is supplemented by particle precipitation from the magnetosphere above. At the bottom of the ionosphere the neutral density is high and thus the electrons and ions recombine quickly. Conversely, at higher altitudes the neutral density is low and the mean free path for electron collision is long resulting in higher electron densities.

The geomagnetic field is particularly important in determining the latitudinal variation of the ionosphere above 100 km. At high latitudes, the geomagnetic field lines tend to be vertical with respect to the surface of the Earth while at low latitudes the field is close to the horizontal. At extremely high latitudes, the close to vertical magnetic field lines provide coupling to the magnetosphere and ultimately to the solar wind enabling the entry of the high energy particles which ionize the high latitude ionosphere and also cause aurora.

2.1 The Ionosphere

The ionosphere is commonly divided into low, mid and high latitude regions, where the latter includes the trough, the auroral oval and the polar cap (Figure 2.1). The review below will consider those features common to all of these regions and also the low latitude region.

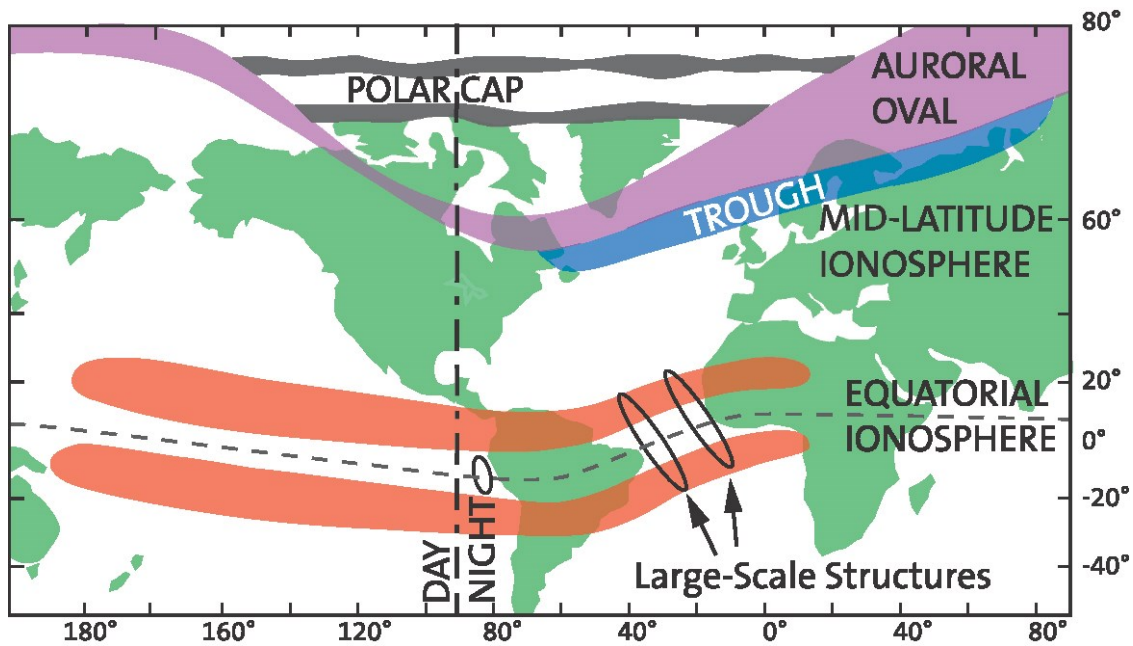


Figure 2.1: Global regions of the Earth's ionosphere [Cannon, Private Communication 2015].

2.1.1 Common Morphology

The vertical structure of the ionosphere is a consequence of the competing production of free electrons by photoionization from extreme ultra violet (EUV) radiation and their loss through recombination and transport. This produces a layered structure driven by both the diverse molecular makeup of the atmosphere and differences in how various parts of the solar radiation spectrum interact with the atmosphere [Kivelson and Russell, 1995]. The four main layers of the ionosphere are designated D, E, F1 and F2 (in order of altitude, lowest to highest). The F1/F2 regions contain the highest electron density and as such are often the most significant from the perspective of applications.

The ionosphere undergoes variations on several different time and length scales including diurnal variations in the vertical distribution of electron density (Figure 2.2). After sunset, the D, E and F1 layers almost disappear due to recombination, leaving only the F2 layer which is sustained by the low recombination rates at these altitudes.

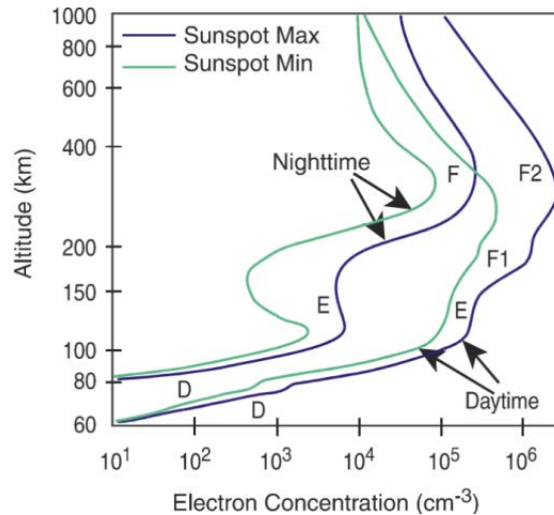


Figure 2.2: Diurnal variation in the structure of the ionosphere [Angling et al., 2007].

Seasonal variations also occur as a consequence of both changes in the solar zenith angle and chemistry. In the E-region the electron densities are highest in the summer, as the zenith angle of the Sun is then at a maximum. However, the F2 layer does not follow this pattern and peak electron densities occur in winter [Davies, 1990]. This is known as the winter, or seasonal, anomaly.

Longer term variations also occur. For example, the ionosphere is sensitive to the 11 year solar cycle with electron densities at all heights increasing as the sunspot number increases. The height of peak electron density also increases with sunspot number [Davies, 1990].

2.1.2 The Equatorial Ionosphere

The morphology of the equatorial ionosphere is quite different to other latitudes because here the geomagnetic field, \mathbf{B} , is nearly horizontal. In the equatorial region dynamo electric fields that have been generated in the equatorial E region by thermospheric winds are transmitted along the dipole magnetic field lines to the F region because of the high conductivity (Figure 2.3). During the daytime, the dynamo electric fields are eastward, which causes an upward $\mathbf{E} \times \mathbf{B}$ plasma drift, while the reverse occurs at night. The uplifted plasma then diffuses back down the field line due to gravity and pressure gradient forces. As a result, the equatorial (or

Appleton) anomaly is formed with a minimum F region ionization density at the magnetic equator and maxima in two crests at about 15 to 20 degrees magnetic latitude (Figure 2.4). This phenomenon is known as the fountain effect [Hanson and Moffett, 1966].

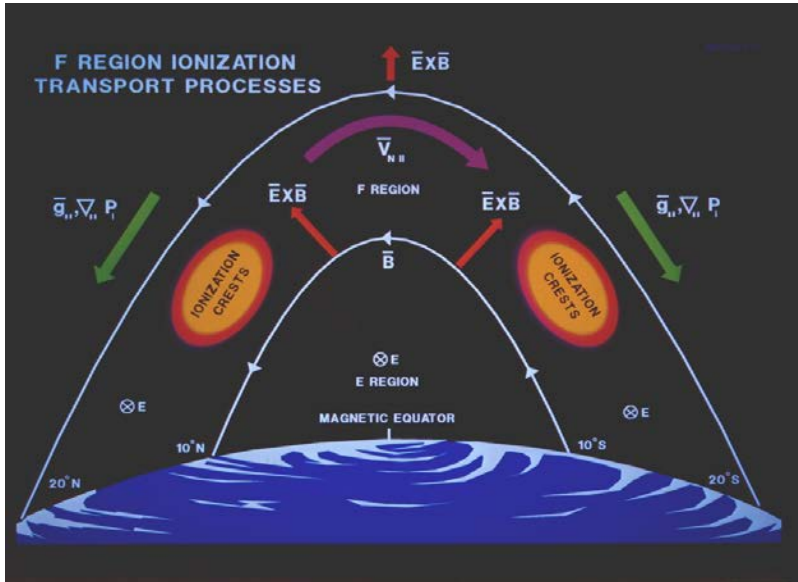


Figure 2.3: Schematic of the formation of the latitude variation of ionization density in the equatorial F-region [de La Beaujardière, 2004].

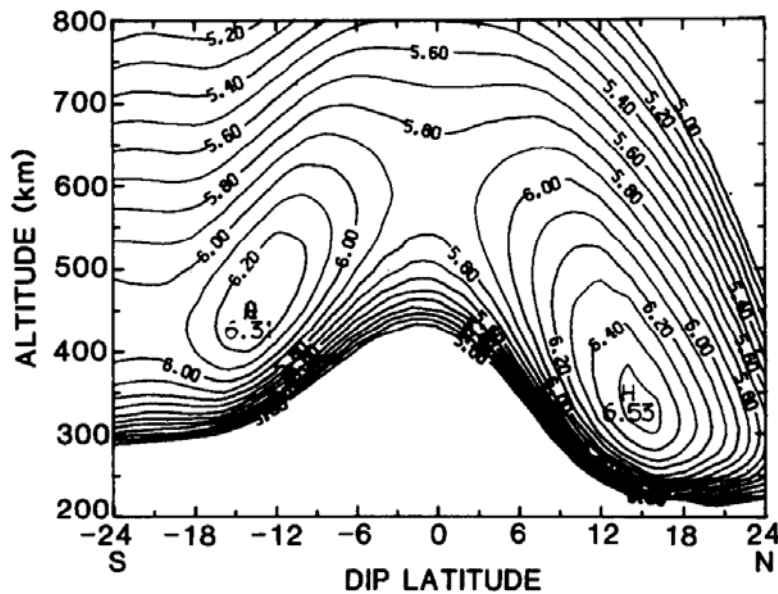


Figure 2.4: Electron density contours ($\log_{10} n_e$) as a function of altitude and dip latitude for December solstice conditions [Anderson and Roble, 1981].

Typically, the height of the F2 rises in the evening to a maximum at about 1900 local time (LT), before falling until at midnight it is approximately 100 km lower than at noon.

2.1.3 Irregularities

Ionospheric irregularities form at both low and high latitudes but only the former are relevant to this work. Figure 2.5 shows the regions where these irregularities occur and when.

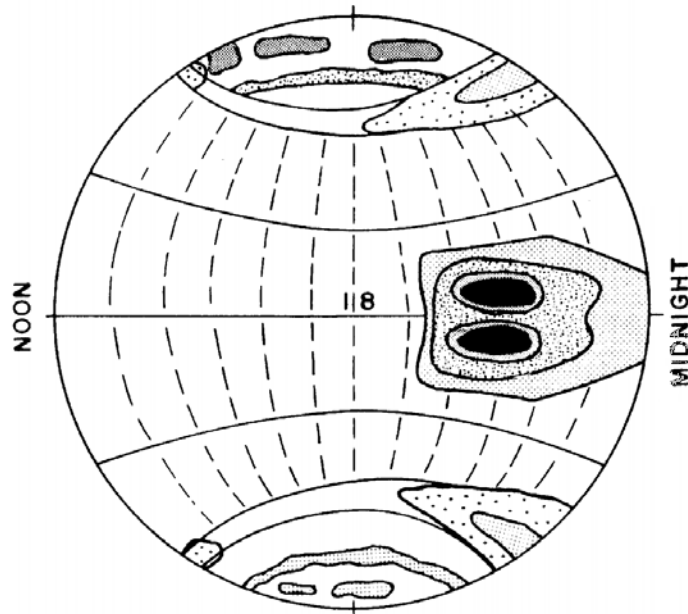


Figure 2.5: Regions of ionospheric irregularity formation. Adapted from Basu and Groves [2001].

The fountain effect previously described results in a rapid rise in the height of the F region, and a corresponding increase in the density gradient at the bottom-side of the F region during the day [Schunk and Nagy, 2009]. Near sunset the E region density and the E region dynamo electric field decrease and the Appleton anomaly starts to diminish. However, as the ionosphere co-rotates with the Earth towards dusk the eastward component of the neutral wind increases due to the wind blowing across the terminator from day to night. The increased eastward wind dynamo component, in combination with the sharp day-night conductivity gradient across the terminator leads to an enhancement in the eastward electric field (the pre-reversal enhancement). The F layer therefore continues to rise as the ionosphere co-rotates into darkness.

At the same time (in the absence of sunlight) the lower ionosphere rapidly decays and a steep vertical gradient consequently develops on the bottomside of the raised F layer. This produces the classical configuration for the Rayleigh-Taylor instability in which a heavy fluid is situated above a light fluid. Under such circumstances, small perturbations in the bottom-side of the F region can grow into huge ‘equatorial plasma bubbles’ of depleted plasma [Ott, 1978; Sultan, 1996]. These bubbles, and associated irregularities, can form plume-like structures as they rise through the denser regions above their initial location, extending to altitudes of more than 1000 km [Woodman and La Hoz, 1976]. An example of the distribution of these structures, as measured using a 50 MHz radar interferometer in a region near the equator is shown in Figure 2.6. Plume structures extending from 200-1000 km in altitude, and almost one hour (~2000 km) in longitude can be clearly seen.

Structure at the edges and within these bubbles, consisting of regions of varying electron density (irregularities) affect traversing signals. Figure 2.7 shows the impact on the received power of two signals that cross several such regions, each extending to ~500 km in longitudinal distance. The effects of the irregularities on signals is discussed further in Section 2.2.

At low-latitudes, the irregularities are elongated by a factor of up to 60 along the geomagnetic field lines due to plasma-diffusion processes in the F region [Hargreaves, 1992], and are thus often referred to as field-aligned irregularities.

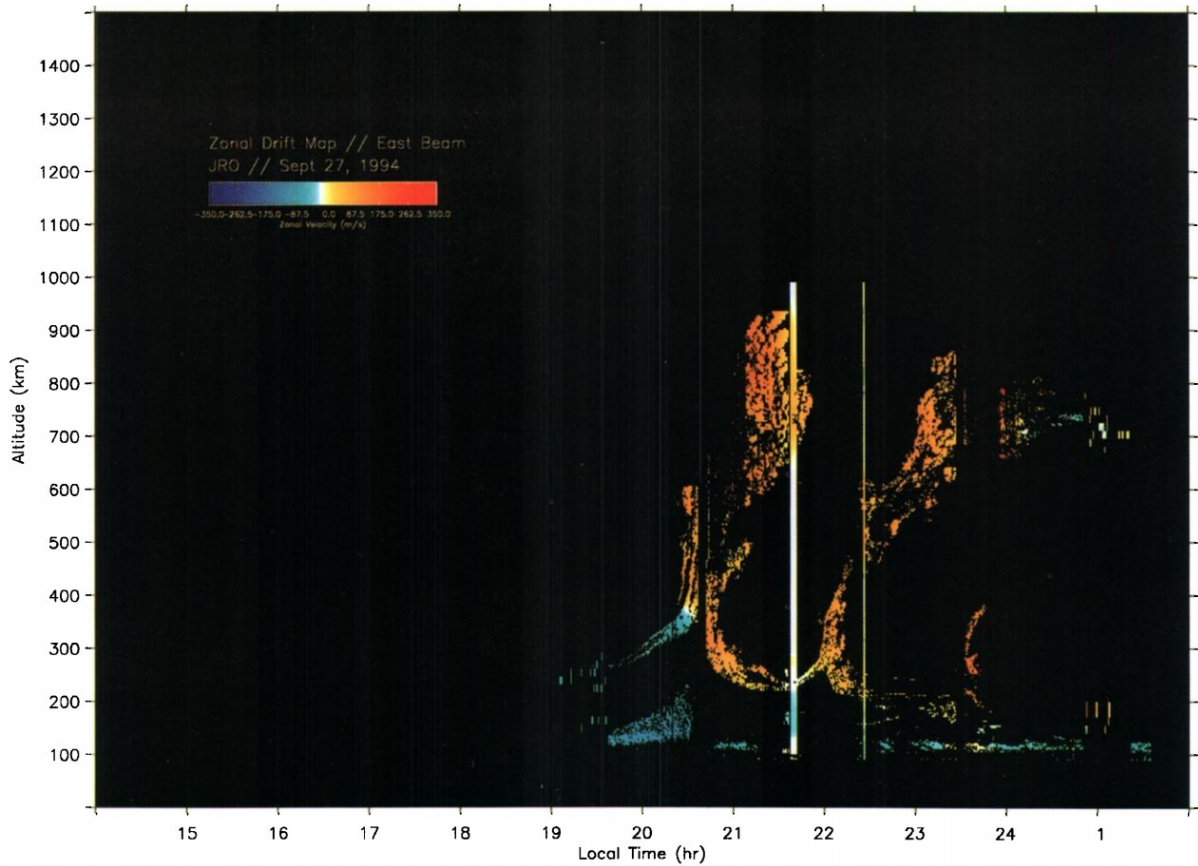


Figure 2.6: 50 MHz radar interferometer results from Jicamarca Radio Observatory, September 27-28, 1994 [Basu et al., 1996].

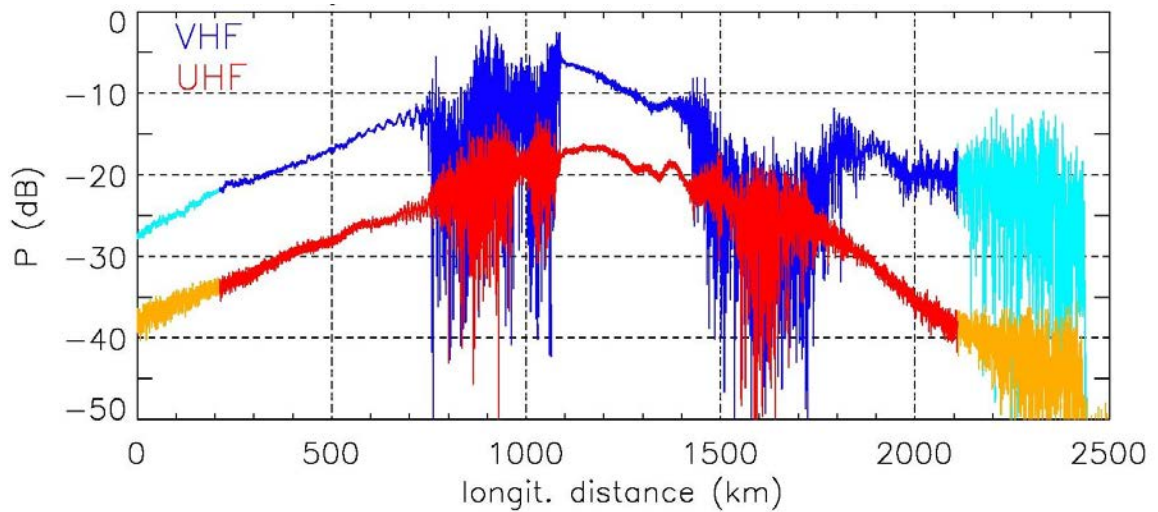


Figure 2.7: Impact of ionospheric irregularities on power of received signals [van de Kamp et al., 2010].

2.2 Ionospheric Radio Propagation

The ionosphere is a dispersive medium and consequently the propagation velocity depends on the frequency [Seeber, 1993]; the higher the electron density the greater the degree of dispersion. The refractive effects are described by the Appleton-Hartree Formula [Davies, 1990], which provides an expression for the refractive index in an ionized medium as follows:

$$n^2 = 1 - \frac{X}{1 - iZ - \frac{Y_T^2}{2(1 - X - iZ)} \pm \sqrt{\frac{Y_T^4}{4(1 - X - iZ)^2} + Y_L^2}} \quad (2.1)$$

where

$$X = \frac{N_e e^2}{\epsilon_0 m \omega^2}, \quad (2.2)$$

$$Y_L = \frac{e B_L}{m \omega}, \quad (2.3)$$

$$Y_T = \frac{e B_T}{m \omega}, \quad (2.4)$$

$$Z = \frac{\nu}{\omega}, \quad (2.5)$$

and N_e is the electron density, e is the charge of the electron (1.6×10^{-19} C), ϵ_0 is the permittivity of free space (8.85×10^{-12} Fm⁻¹), m is the mass of the electron (9.11×10^{-31} kg), ν is the electron collision frequency, ω is the angular frequency and B_T and B_L denote the transverse and longitudinal components of the magnetic field, respectively.

The ray optic Appleton-Hartree equation assumes that the ionosphere varies on length-scales that are large in comparison to the signal wavelength and the Fresnel zone. When the electron density irregularities are smaller than these dimensions, diffraction based approaches are required.

2.2.1 Refraction of signals

At very high frequencies (VHF) and above the Appleton-Hartree equation can be simplified.

At these frequencies collisions and magnetic field effects can be ignored [Davies, 1990] and it

can be shown [Elvidge, 2014] that the phase refractive index is given by:

$$n_{ph} = 1 + \frac{c_2}{f^2} + \frac{c_3}{f^3} + \frac{c_4}{f^4} + \dots, \quad (2.6)$$

where the coefficients c_2 , c_3 , c_4 , etc. depend on the electron density along the signal path.

Normally the quadratic term is sufficient, i.e.:

$$n_{ph} = 1 + \frac{c_2}{f^2}, \quad (2.7)$$

where c_2 is $-40.3N_e$ (where N_e is the number of electrons along the signal path). It can be

likewise shown that the group refractive index:

$$n_{gr} = 1 - \frac{c_2}{f^2}. \quad (2.8)$$

The measured range s is defined by the integral along the path of the signal:

$$s = \int n ds. \quad (2.9)$$

By setting $n = 1$, the geometric range s_0 between satellite and receiver may be obtained:

$$s_0 = \int ds_0. \quad (2.10)$$

The difference between measured and geometric range is the ionospheric delay:

$$\Delta S_{ION} = s - s_0 = \int n ds - \int ds_0. \quad (2.11)$$

For the phase refractive index:

$$\Delta S_{ION,ph} = \int \left(1 + \frac{40.3N_e}{f^2}\right) ds - \int ds_0, \quad (2.12)$$

and for the group refractive index:

$$\Delta S_{ION,gr} = \int \left(1 - \frac{40.3N_e}{f^2}\right) ds - \int ds_0. \quad (2.13)$$

These equations can be simplified by introducing the concept of slant total electron content (STEC), the electron density integrated along the signal path through the ionosphere:

$$STEC = \int_{s_0}^{s_1} N_e ds, \quad (2.14)$$

where s is the distance along the signal path, s_0 and s_1 are the start and finish points of the signal path and N_e is the number of electrons along the signal path. STEC is often quoted in TEC units, where one TEC unit = 10^{16} electrons m^{-2} .

Thus integrating the first terms of Equation (2.12) and Equation (2.13) along the signal path, and substituting in (2.14) gives:

$$\Delta S_{ION,ph} = -\frac{40.3}{f^2} STEC \quad (2.15)$$

$$\Delta S_{ION,gr} = \frac{40.3}{f^2} STEC. \quad (2.16)$$

These values characterise the group delay and phase advance due to the ionosphere. Converting these values to more appropriate dimensions gives:

a) **Carrier phase advance**

$$\Delta\Phi = \frac{8.44 \times 10^{-7}}{f} STEC \text{ (radians)}. \quad (2.17)$$

b) **Group path delay**

$$\Delta t = \frac{40.3}{cf^2} STEC (s). \quad (2.18)$$

These equations highlight the frequency dependence of ionospheric effects on radio wave propagation with lower frequency systems more affected. In practice this means that trans-ionospheric systems operating at frequencies below L-band are significantly affected by the ionosphere.

2.2.2 Diffraction of signals

Diffraction of signals by small scale irregularities leads to scintillation of signals which includes variations in signal phase, amplitude, polarization and angle of arrival [Davies, 1990]. It is the result of rapid variations in the refractive index, caused by changes in electron density. A schematic of the effect of the irregularities on signals is shown in Figure 2.8.

The impact of irregularities on the amplitude and phase (as measured using the total electron content (Equation (2.17))) of a Global Positioning System (GPS) signal is shown in Figure 2.9 and Figure 2.10 respectively. The onset of scintillation can clearly be seen as the large increase in the variation of the signal phase and amplitude. These large fluctuations are problematic for many trans-ionospheric systems operating at ~2 GHz and below. For example, the large phase variations often cause GNSS (such as GPS) receivers to lose signal phase lock, threatening positioning accuracy, or even the ability to resolve a position at all [Kintner *et al.*, 2001; Hernández-Pajares *et al.*, 2011; Ghafouri and Skone, 2015].

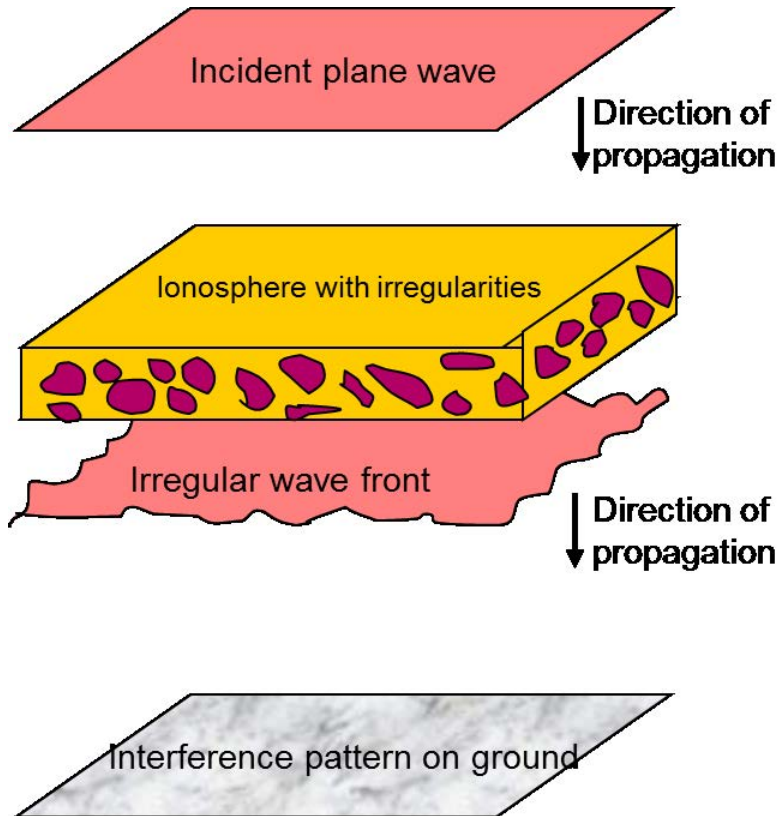


Figure 2.8: Effect of small scale irregularities on incident plane wave.

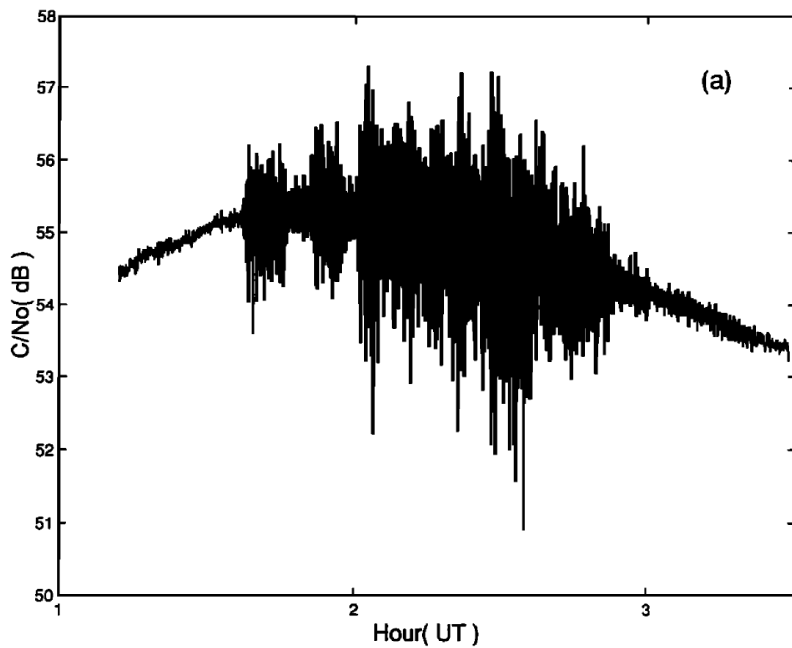


Figure 2.9: Example of the effect of scintillation on GPS signal amplitude [Bhattacharyya and Beach, 2000]

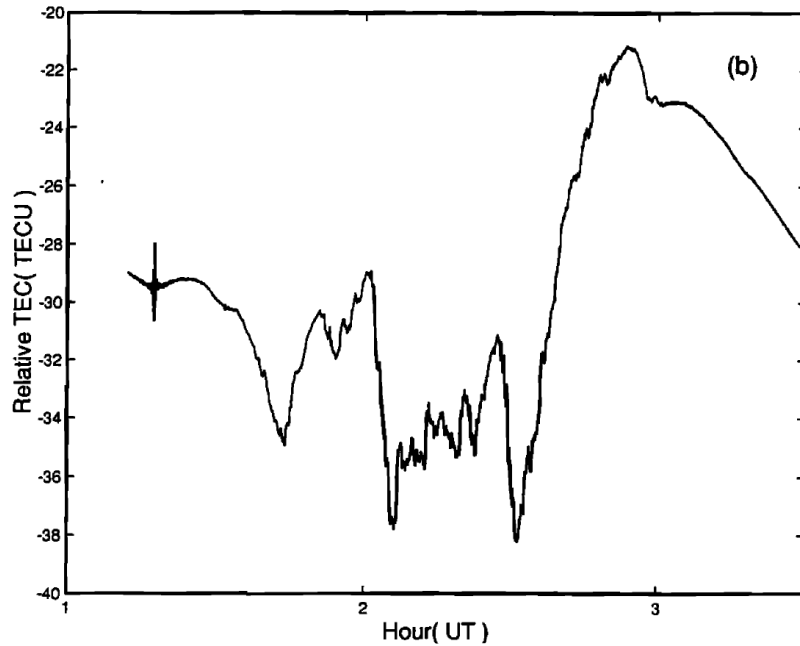


Figure 2.10: Example of the effect of scintillation on relative total electron content, estimated using differential GPS phase. [Bhattacharyya and Beach, 2000]

The effect of the irregularities on the phase of a signal propagating can be modelled by an equivalent thin diffracting phase screen. The irregularity-induced phase perturbation at this phase screen describes the phase scintillation, whilst the process of diffraction between the phase screen and the signal observation point produces variations in the amplitude of the signal.

The electron density irregularities that affect signals in the ionosphere range from a few metres to kilometres in size. Studies of the irregularity characteristics have determined that they can be described by a spatial power spectrum, which follows a power law between two characteristic scales sizes – the inner scale size (the electron gyro radius, ~ 2 cm), and the outer scale size (~ 10 -50 km) [Yeh *et al.*, 1975; Rino, 1982]. This power spectrum is quantified by two parameters – the spectral slope, p and a strength parameter T .

As the signal path moves across the phase screen it will induce fluctuations in the phase and amplitude of the signal measured on the ground. The temporal effect of the phase screen on the

signal can, therefore, be related to the spatial spectrum of the irregularities described above [Rufenach, 1972; Basu et al., 1980].

Some sample intensity power spectra are displayed in Figure 2.11. These spectra exhibit a ‘corner’ at the Fresnel frequency – below this frequency (which corresponds to irregularities of scales greater than the Fresnel zone size), amplitude fluctuations do not fully develop from the phase fluctuations induced at the phase screen [Hargreaves, 1992].

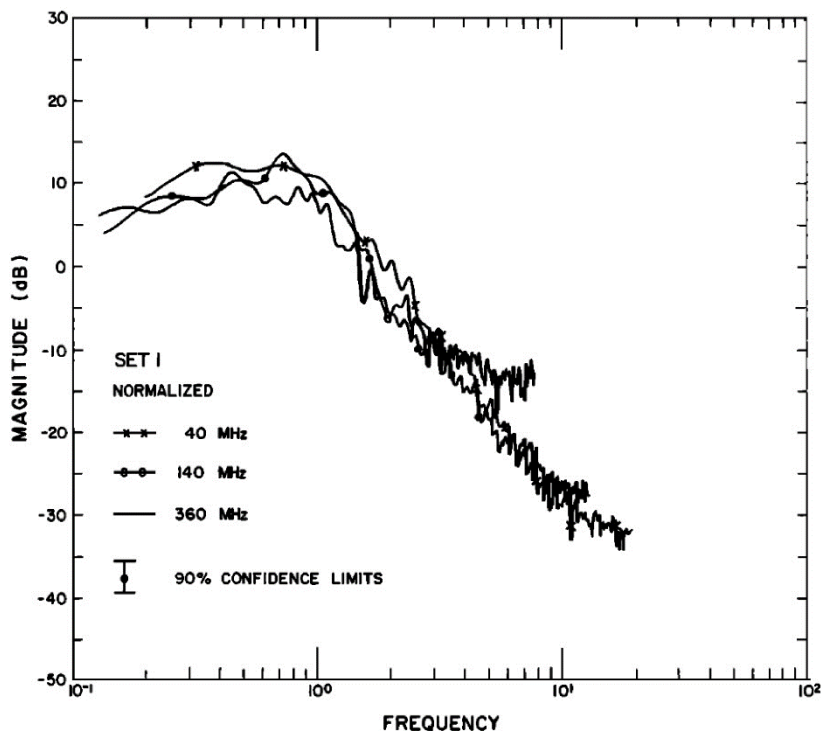


Figure 2.11: Power spectra of ATS-6 signals received at Boulder, Colorado [Umeki et al., 1977] © American Geophysical Union

The gross features of intensity and phase scintillation can be conveniently quantified using two parameters. The S_4 index describes intensity scintillation, and is defined as the square-root of the normalised variance of the signal intensity, I over a given interval [Briggs and Parkin, 1963]:

$$S_4 = \sqrt{(\langle I^2 \rangle - \langle I \rangle^2) / \langle I \rangle^2}. \quad (2.19)$$

Phase scintillation is quantified by the σ_ϕ index, the standard deviation of the signal phase over a given interval.

When a more detailed understanding is needed, one of two theoretical approaches are often employed. In both cases the characteristics of the thin phase screen need to be specified and this is achieved statistically via a ‘strength of turbulence’ parameter C_s or more usually $C_k L$ [Secan *et al.*, 1987, 1995], being the height-integrated strength of turbulence at a scale size of 1 km (i.e. it is a measure of the total power of the irregularities along the signal path). $C_k L$ will be discussed further in the relevant chapters.

Having specified the phase screen a modified version of the wave equation - the parabolic wave equation – can be conveniently used to calculate the characteristics of the signal. However, this technique is computationally expensive since it explicitly calculates the signal diffraction.

More usually a geometric optics technique proposed by *Rino* [1979a, 1979b], for respectively weak and strong scattering regimes is used. It assumes straight line propagation with the phase perturbation directly proportional to the phase screen irregularity electron content. The weak scattering approximation has been very successful in describing the effects of scintillation, and will be used throughout this work with the theoretical background developed when required.

3 SYNTHETIC APERTURE RADAR

Radar systems are used in a diverse range of fields and typically transmit a pulsed signal which is reflected or scattered from objects in the signal path. A receiver, typically collocated with the transmitter, then receives and processes the scattered waves (echoes). The delay between transmission of the pulse and reception of the echoes is used to determine the distance of the objects in the signal path.

The resolution of a radar system, i.e. its ability to distinguish two separate objects, has two components, range and azimuth. The range component describes the ability to identify two separate targets that exist in the same direction from the radar, but at different distances, whilst the azimuth resolution describes the ability to resolve targets at different angles from the antenna.

The range resolution is determined by the duration of the emitted radar pulse. The minimum possible range separation that two distinct targets can still be identified is half the pulse width. If the targets are closer, the returns from each target will be indistinguishable from each other. Thus a shorter pulse width is desirable for better range resolution. However, shorter pulse widths (at the same operating frequency) contain less power – making it more difficult to detect the returned echoes.

This limitation can be overcome by using a pulse compression technique. Typically, this is done by applying a linear ‘chirp’ modulation to the frequency of the emitted pulse. Thus the frequency of the pulse is increased at a constant rate throughout its length, and the returns from different points can be identified. When the radar receives the returns from the pulse, they are filtered in such a way that a frequency dependent time-lag is introduced to the signals. This compresses the returned echo, and allows signals from closely spaced targets to be separated

[*Stimson, 1998*]. Thus, long pulse durations can be used whilst retaining the resolution benefits of shorter pulses. In digital systems, this is often achieved by removing the carrier frequency of the returned pulse and then cross-correlating it with a replica of the transmitted pulse (a process known as ‘matched filtering’) [*Oliver and Quegan, 2004b*].

The azimuth resolution is determined by the beamwidth of the transmitted signal, which is in turn driven by (in the diffraction-limited case) the size of the radar antenna in the azimuth direction and the wavelength of the transmitted signal:

$$\theta_{az} = \frac{\lambda}{d_{az}}, \quad (3.1)$$

where θ_{az} is the azimuth beamwidth, λ is the wavelength of the signal and d_{az} is the length of the radar antenna in the azimuth direction. The beamwidth is a constant angular value, and so the azimuth resolution, L_{az} , at a given range R is given by:

$$L_{az} = R \sin(\theta_{az}) \approx \frac{R\lambda}{d_{az}}, \quad (3.2)$$

where the small angle approximation has been applied.

As an illustration of the quantities involved, consider a side-looking radar (mounted on an aircraft) operating at X-band ($\lambda \sim 3$ cm), at a range (R) of 25 km, with an aperture length in the azimuth direction (d_{az}) of 5 m. Equation (3.2) provides an azimuth resolution (L_{az}) of 150 m. An airborne radar with these characteristics is able to resolve small ships and geographical features. However, to image smaller or features, or to operate at longer ranges would require increasing the antenna to impractical sizes, or reducing the wavelength so much that the signal would experience severe attenuation in the atmosphere [*Stimson, 1998*].

Synthetic aperture radar techniques combat the restriction on physical aperture size by utilising the forward motion of the radar platform and signal processing techniques to synthesize an aperture of nominal size. Each time the radar transmits a pulse, it has moved slightly further forwards. By summing the returns from successive pulses over a time period T , the equivalent of a side-looking array of length vT can be produced (where v is the velocity of the radar platform). The quantity vT is the synthetic aperture length L_{SA} . By increasing T , the synthesized aperture length is increased and so the higher the resolution that can be achieved. A prerequisite for the successful synthesis of an aperture is coherent processing of the signals.

3.1 Synthetic Aperture Radar Theory

In the simplest case, a SAR system consists of a side-looking radar attached to an airborne or spaceborne platform. The image is formed by coherently combing the results from successive pulses as the platform moves along the flight path (Figure 3.1). As the platform moves, the range from the radar to the scatterers on the ground changes.

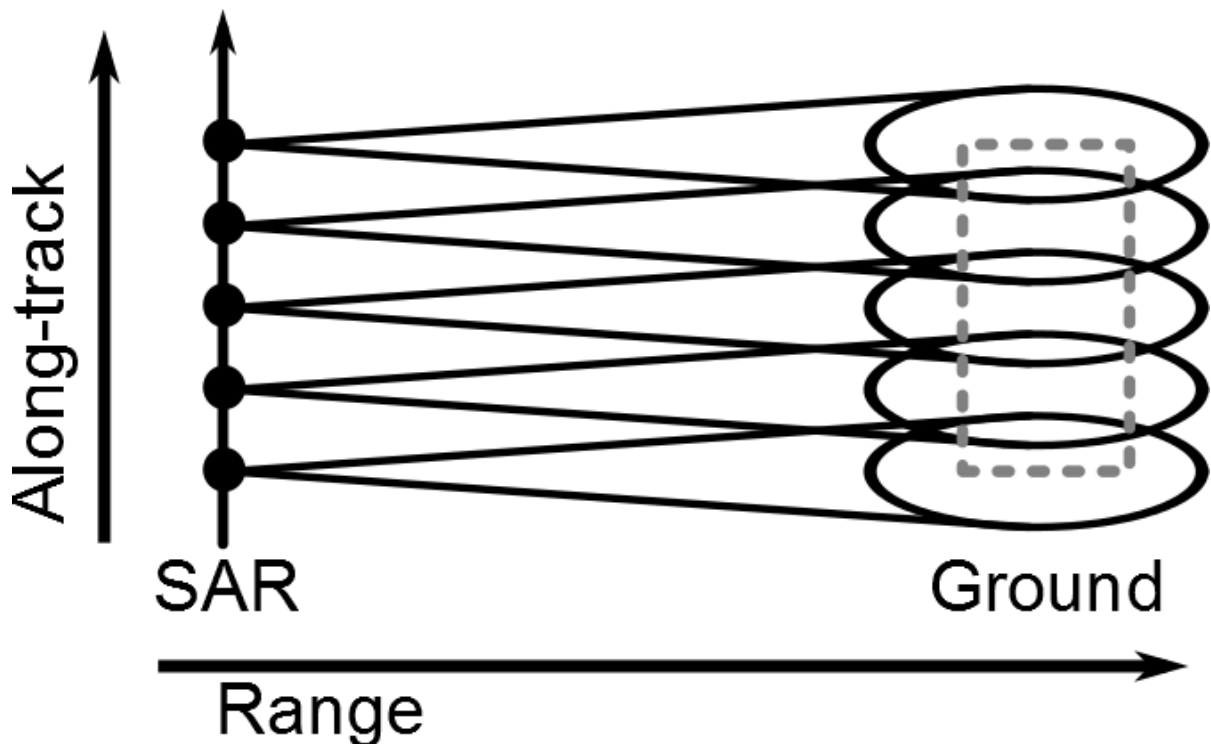


Figure 3.1: SAR strip-map operation

The following description of SAR operation is drawn largely from the work of *Oliver and Quegan* [2004b]. Consider a point scatterer illuminated by the radar beam on the ground. As the beam traverses the point, the range from the radar changes. If the point is located at the origin of an axis x (i.e. at $x = 0$), then the range to the point as the radar moves along the aperture is given by:

$$R^2 = R_0^2 + x^2 \quad (3.3)$$

where R_0 is the range when the platform is broadside to the point, and x is the point on the axis that the radar is currently broadside to (Figure 3.2).

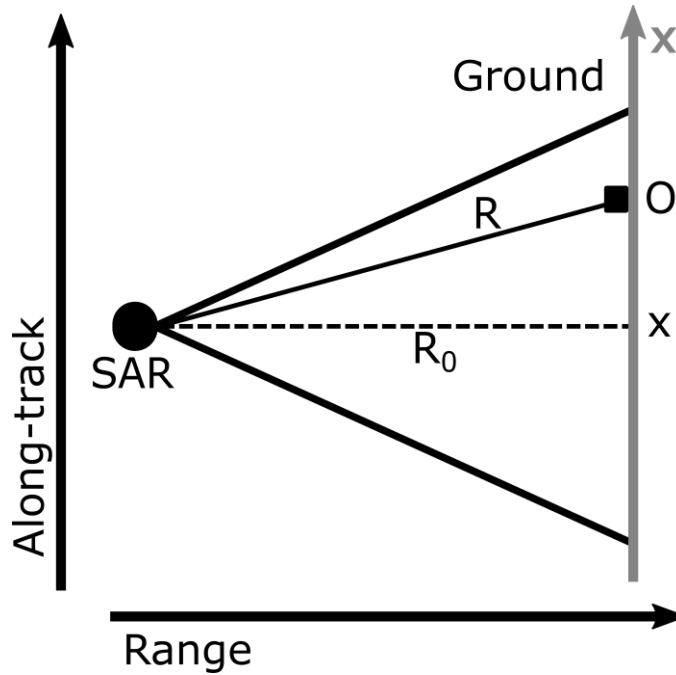


Figure 3.2: Range from the radar to a scatterer illuminated by the beam on the ground.

For cases where the along-track width of the beam on the ground is much smaller than the range to the target (i.e. $x \ll R_0$), typical for an air-borne or space-borne SAR, a Taylor expansion shows that the range to the scatterer varies quadratically as the radar moves along the flight path.

$$R = R_0 + \frac{x^2}{2R_0} \quad (3.4)$$

This change in range results in an equivalent quadratic change in the two-way phase of the returned signal:

$$\Psi(x) = -\frac{4\pi R_0}{\lambda} - \frac{2\pi x^2}{\lambda R_0} \quad (3.5)$$

The rate of change of phase with distance is linearly dependent on the platform position x , and is functionally equivalent to the linear frequency modulation often used to increase the range resolution of a radar system. A similar process of matched filtering can thus be applied to account for the phase change and improve the azimuth resolution.

The maximum possible synthetic aperture length is determined by how long an individual target remains with the radar beam footprint on the ground, i.e. by the azimuth beam-width of the radar. It can be shown that the maximum achievable azimuth resolution is equal to half the azimuth dimension of the physical antenna [Oliver and Quegan, 2004b]. This leads to the counter-intuitive consequence that in order to maximise the achievable resolution, the physical azimuth dimension of the antenna should be made as small as possible. This contrasts with the real-aperture case, in which the antenna dimensions must be maximised to provide the best resolution.

However, in order to avoid undersampling of the processed image, the spacing along the path between pulses must be less than or equal to the resolution. As such, smaller antenna sizes mean proportionally higher frequency of pulse emission for a given platform velocity, which limits the degree to which the dimensions of the antenna may be reduced. Smaller antennas also result in a lower signal-to-noise ratio.

If the area to be imaged fits inside the radar beam footprint on the ground, these issues can be avoided by electronically steering the antenna, such that the beam footprint remains centred

over a fixed position as the radar platform moves (Figure 3.3). This means that a scatterer will remain within the beam for longer, allowing improvement in the azimuth resolution. This is known as spotlight mode SAR. In this mode, larger antennas (with correspondingly smaller beamwidths) may be used, as long as the beam footprint covers the area to be imaged.

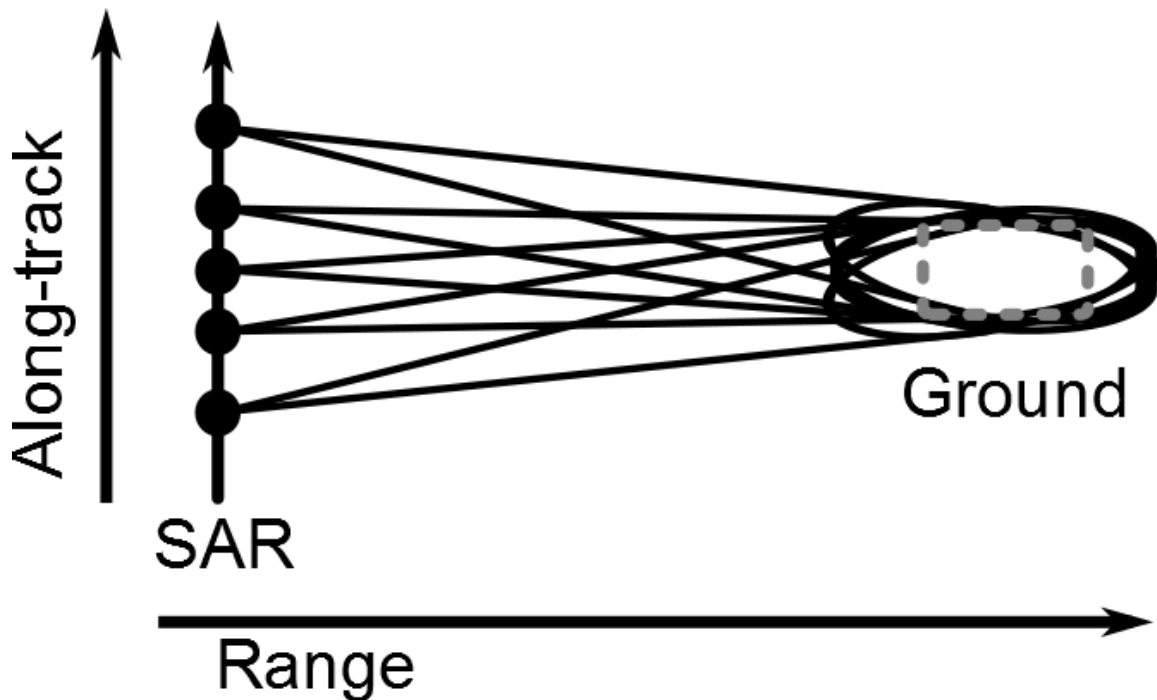


Figure 3.3: SAR spotlight-mode operation

SAR systems, like all imaging systems that require coherent phase, are susceptible to the effects of speckle noise. This arises because the signal from any one resolution cell in the image is an aggregation of the complex signals from many scatterers distributed throughout that resolution cell. The returns from the scatterers interfere constructively or destructively, producing a pattern of increased and decreased intensity across the image.

3.2 The Point Spread Function

The point spread function (PSF) describes the response of an imaging system to a point input. The shape of the PSF offers insight into the quality and characteristics of images produced by

an imaging system, and as such the structure of the point spread function is an important measure of SAR image quality. The PSF can be quantified using several parameters, including:

- Peak to sidelobe ratio (PSLR)
- Integrated sidelobe ratio (ISLR)

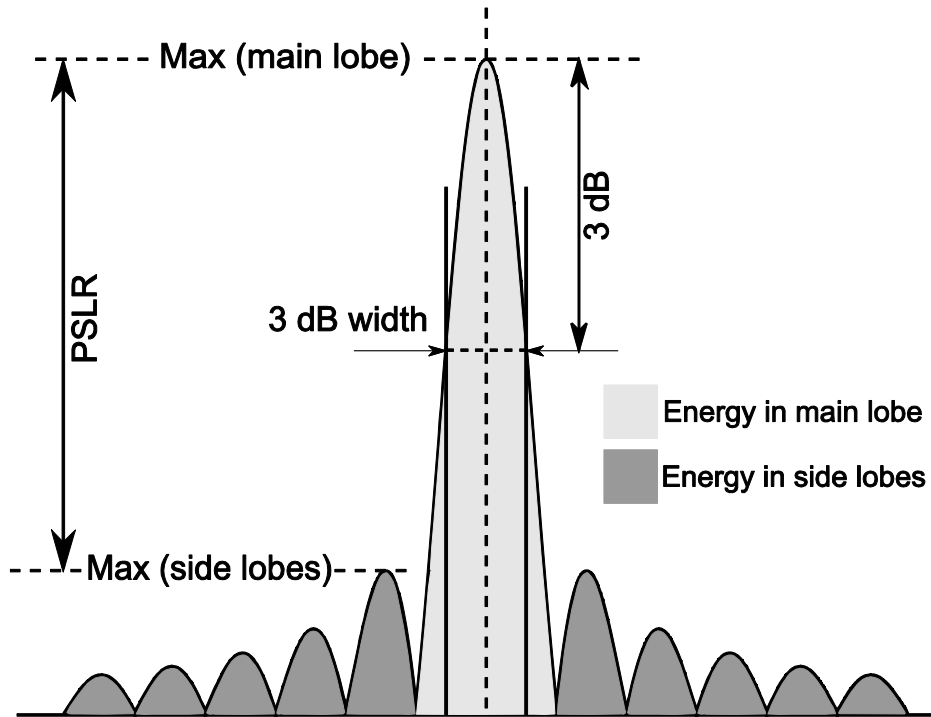


Figure 3.4: Example point spread function illustrating different characteristics. Reproduced from Massonnet and Souyris [2008].

3.2.1 PSLR, ISLR

The peak to sidelobe ratio of the PSF is defined as the ratio of the mainlobe intensity to the peak intensity of the sidelobes [Massonnet and Souyris, 2008]:

$$PSLR (dB) = 10 \log_{10} \frac{I_{ML}}{I_{PSL}}. \quad (3.6)$$

The integrated sidelobe ratio is the ratio between the energy contained in a width of 10 resolution cells, excluding a central band of two resolution cells, (the sidelobes), to the energy contained in the central band (the mainlobe) [Massonnet and Souyris, 2008]:

$$ISLR (dB) = 10 \log_{10} \frac{\int_{-5}^5 |PSF(s)|^2 ds - \int_{-1}^1 |PSF(s)|^2 ds}{\int_{-1}^1 |PSF(s)|^2 ds} \quad (3.7)$$

Both the PSLR and the ISLR measure the impact of any one point in the image on the area around that point, with the PSLR being more relevant for the area close in to the point in question.

3.2.2 Window functions

The nature of the signal received by a SAR from a point target (a top-hat function - Section 4.1.2), means that there are discontinuities at the edges of the signal. These discontinuities will cause undesirable effects when performing the Fourier Transform to produce the final SAR image. To mitigate the effects of the discontinuities, the signal can be tapered by the application of a window function such as a Hamming window (Figure 3.5, Section 4.1.4) that mitigates the discontinuities at the edges of the signal.

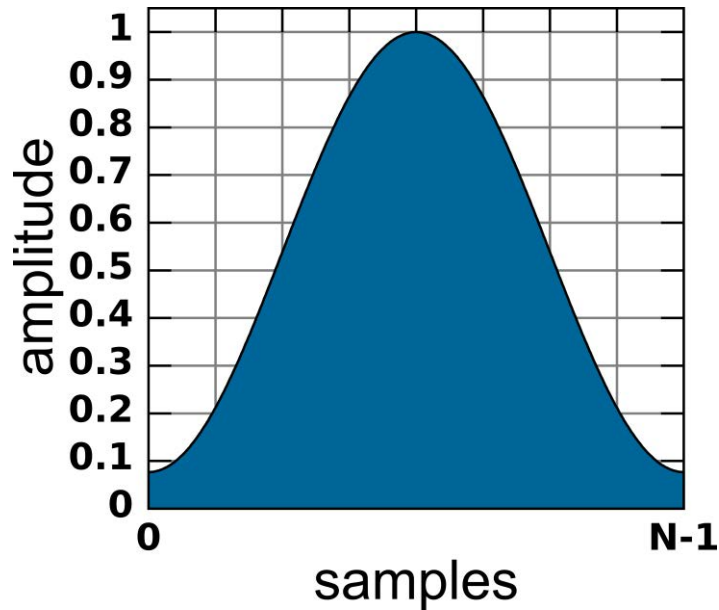


Figure 3.5: Hamming window function.

3.3 SAR Applications

The ability of SAR systems to produce high resolution images at long range, independent of weather conditions, means that they are used in a wide variety of remote sensing applications including surveillance, global measurement of biomass (and other characteristics of the biosphere) [Rignot *et al.*, 1995; Kerr, 2007; Entekhabi *et al.*, 2010] and disaster response [Tralli *et al.*, 2005].

Each of these applications has corresponding design requirements in terms of operating location (airborne or spaceborne) and operating frequency. Many of the SAR systems developed in recent years for these applications have been spaceborne radars operating at L band or P band. These include the Phased Array type L-Band SAR (PALSAR) 1 and 2 on board the Advance Land Observing Satellite (ALOS) 1 and 2 [Rosenqvist *et al.*, 2007; Kankaku *et al.*, 2013] and the ESA Biomass mission [Hélière *et al.*, 2013]. Typically these radars operate in polar low-earth-orbit, providing nearly complete coverage of the Earth's surface over a period of several days. However, the relatively long revisit time (14 days for ALOS-2), limit the effectiveness of

some types of monitoring. To overcome this, SAR missions operating in a geostationary orbit, with revisit times of 1 day have been proposed [Hobbs *et al.*, 2014].

SAR signals are affected by the medium they propagate through. For air-borne systems this is mainly the troposphere, whilst for space-based systems (operating at L-band and below), the effects of the ionosphere become the most significant propagation effect [Quegan and Lamont, 1986]. The vulnerability of the space-based SAR systems discussed above to the effects of the ionosphere (Section 2) has driven much research in recent years [Ishimaru *et al.*, 1999; Belcher, 2008b; Meyer and Nicoll, 2008a; Shimada *et al.*, 2008; van de Kamp *et al.*, 2009; Carrano *et al.*, 2012c; Pi *et al.*, 2012a; Belcher and Cannon, 2014; Rogers *et al.*, 2014a], and is the main motivation of this work.

3.4 Impact of the ionosphere on SAR

Figure 3.6 shows a comparison of two SAR images of the same area. The left image is unaffected by the ionosphere, whilst the right image shows blurring caused by the ionosphere. The operation of SAR systems may be severely compromised by the effects of the ionosphere.

The ionospheric impacts can be split into two main categories – those caused by the bulk electron content of the ionosphere, and those caused by small or medium scale electron density irregularities within the ionosphere (Section 2.1.3). In addition, the ionospheric impact manifests differently in the range and along-track directions [Belcher, 2008b]. This thesis will focus on the effects in the along-track direction.

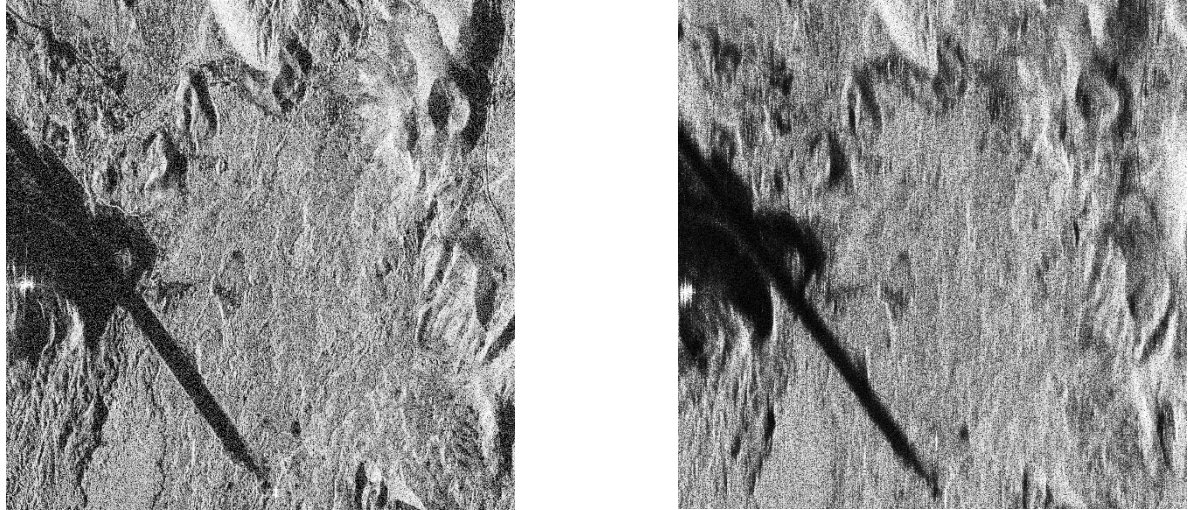


***Figure 3.6: Impact of the ionosphere on a PALSAR-2 image of Ascension Island.
(left: undisturbed, right: disturbed)***

As described in Section 2, the impact of the bulk electron content in the ionosphere (as measured by the total electron content (TEC)), is to cause a phase shift in the received signal proportional to the TEC. Even if the ionosphere is homogenous, consisting of a constant TEC, as the radar platform moves along the flight path, the path length through the ionosphere will change, and thus the phase delay will not remain constant in the along-track direction, and in fact will vary in a nearly quadratic fashion, similar to the range variation discussed in Section 3.1 [Belcher, 2008b]. However, if an estimate can be made of the bulk TEC, this variation is relatively easily removed [Belcher, 2008b]. In addition, the bulk TEC will cause Faraday rotation of the polarization vector of the signal, although again, with an estimate of the bulk TEC, or by using polarimetric techniques this effect can be mitigated too [Meyer and Nicoll, 2008a].

The SAR processing relies on coherent summing of the returns from multiple pulses, and this requires that the phase variation due to the ionosphere be constant across the aperture. Any deviation from this ideal will affect the image. For example, a linear ramp in the TEC in the along-track dimension will cause a shift in the image position as a result of the linear phase term introduced to the returned phase. More troublingly, the effects of TEC irregularities at

scales equivalent to or less than the synthetic aperture length will cause distortion of the image as they will introduce unaccounted for phase shifts in the returned signals. These phase shifts can result in blurring and defocussing of the image, as seen in Figure 3.6. Measurements of the ionosphere have suggested that in the equatorial regions, the probability of image defocussing can be as much as 50% [*van de Kamp et al.*, 2009].

The effects of amplitude scintillation on SAR images are not as prevalent as those of phase scintillation, but are sometimes much more striking in the images, typically manifesting as striping in the along-track direction of the SAR image [*Shimada et al.*, 2008].

Clearly, the impact of the ionosphere on SAR systems can be severe, and much work has focussed on the study and mitigation of these effects (recently reviewed by *Pi* [2015]). However, given that the ionosphere so clearly impacts the images, it is reasonable to suppose that if the effect on the image could be measured, that information about conditions within the ionosphere itself could be inferred, providing new possibilities for studying and monitoring the ionosphere. Several avenues of research have already been explored, [*Meyer and Bamler*, 2006; *Pi et al.*, 2011], and this work will explore three techniques for exploiting SAR data to measure ionospheric conditions.

4 USING GNSS SIGNALS AS A PROXY FOR SAR SIGNALS: CORRECTING IONOSPHERIC DEFOCUSING

The work presented in this chapter is an extended version of a paper previously published in *Radio Science* [Mannix *et al.*, 2016].

Space-based (SB) synthetic aperture radar (SAR) can provide high-resolution, all-weather ground imaging. The possible degrading effects of the ionosphere on these radar systems was discussed in Section 3. Two categories of ionospheric effect are commonly identified – those associated with Faraday rotation of the polarization vector [Meyer and Nicoll, 2008b] and those associated with small and medium-scale electron density irregularities which impose variations on the signal amplitude [Belcher and Cannon, 2014] and on the signal phase [Xu *et al.*, 2004; Cannon, 2009] (called ionospheric scintillation – Section 2).

The ionospheric irregularities can be described by a spatial power spectrum, which follows a power law between two characteristic scales sizes – the inner scale size (the electron gyro radius, ~ 2 cm) and the outer scale size ($\sim 10 - 50$ km) [Yeh *et al.*, 1975; Rino, 1982]. Given that the size of the irregularities are both smaller and comparable to the synthetic aperture of L-band SB-SARs (typically 10-20 km) both systematic and random phase changes can be introduced across the synthetic aperture. These ionospheric phase changes reduce the signal coherency and once the size of the phase variations reaches $\sim \pi/4$ radians image reconstruction is severely affected [van de Kamp *et al.*, 2009] unless autofocus techniques can be successfully employed [Knepp and Groves, 2011]. Amongst other effects, phase scintillation reduces the image contrast and, if sufficiently strong can defocus SB-SAR images. Rino and Gonzalez [1983] provide evidence for these effects in the high latitudes and similar effects have recently been shown at low latitudes [Belcher *et al.*, 2015].

It is clearly desirable to quantify these effects, yet there are few L-band radars and even fewer coordinated SB-SAR and ionospheric measurements. This work seeks to circumvent this problem by developing a technique to quantify ionospheric scintillation effects on L-band SB-SAR based on widely available L-band Global Navigation Satellite System (GNSS) signals [Aarons *et al.*, 1996; Pi *et al.*, 1997]. Although the work described here is applicable to all GNSS constellations, the results presented use Global Positioning System (GPS) data only, and henceforth the term GPS rather than the more general GNSS will be used.

In Section 4.1, an approach to synthesise L-band SB-SAR signals from GPS signals is developed and the limitations of using this proxy data are explained. Then in Sections 4.3 and 4.4, using data from an experiment described in Section 4.1.5.4, a number of analyses are described which build upon each other. First, in Section 4.3, proxy point spread functions (PSFs) are calculated and shown to possess the expected characteristics. Then, in Section 4.4, GPS data simultaneously collected on two receivers are used to determine over what distance a measurement of the PSF at one location can be used to sharpen the PSF (and consequently the image) at another location.

In this chapter reference will be made to the PALSAR-2 radar [Kankaku *et al.*, 2013] which was launched in 2014. It operates at L-band and provides 5 m resolution in strip-map mode and up to 1 m resolution in spotlight mode.

4.1 Theory

4.1.1 The Phase Spectrum

As radio frequency (RF) signals propagate through the ionosphere they experience a phase shift due to the electron content along the signal path. This is determined by the three dimensional distribution of electrons which, for weak scattering, is well modelled as one or more horizontal two-dimensional thin phase screens by integrating the electron distribution in the vertical direction [Rino, 1979a; Knepp, 1983]. The phase shift is assumed to occur at the ionospheric pierce point (IPP), where the ray intersects the screen.

For non-geosynchronous satellites, the ray path scans the phase screen and the resultant temporal variation can be represented as a (phase) power spectral density (PSD) [Rino, 1979a]:

$$PSD_{\phi}(f) = T(f_o^2 + f^2)^{-\frac{p}{2}}, \quad (4.1)$$

where f is the spectral frequency, f_o is the outer scale frequency, T is a constant and p is the phase spectral index. The latter lies between 1 and 4 and is typically ~ 2.5 [Basu *et al.*, 1987].

This temporal spectrum can be transformed to the spatial domain [Belcher and Rogers, 2009] to give:

$$PSD_{\phi}(\kappa) = T'(\kappa_o^2 + \kappa^2)^{-\frac{p}{2}}, \quad (4.2)$$

where $\kappa = \frac{2\pi}{x}$ is the spatial wave number, x is the distance along the phase screen, κ_o is the spatial wave number associated with the outer scale size, and T' is given by:

$$T' = \frac{r_e^2 \lambda^2 G C_s L \sec \theta \sqrt{\pi} \Gamma\left(\frac{p}{2}\right)}{4\pi^2 \Gamma\left(\frac{p+1}{2}\right)}. \quad (4.3)$$

Here r_e is the classical electron radius, λ is the wavelength of the signal, G is a factor that depends on the propagation geometry, C_s is the three-dimensional strength of the ionospheric

turbulence, L is the effective thickness of the ionosphere, θ is the zenith angle and Γ represents the Gamma function.

The root mean square (RMS) phase variation over a distance L_C along the phase screen (with κ_C as the associated spatial wavenumber), is obtained by integrating equation (4.2) over all spatial wavenumbers above κ_C . To simplify the integral the assumption $\kappa_0 \ll \kappa$ has been made, being appropriate to many of the spatial scales relevant to this work:

$$\phi_{RMS}^2 \simeq \frac{2T'}{p-1} \kappa_C^{1-p}. \quad (4.4)$$

4.1.2 The Point Spread Function

This work will make much use of the point spread function (PSF) which describes the response of an imaging system to a point target and provides insight into the eventual quality of the images. It can be quantified by the peak-to-sidelobe ratio (PSLR).

For PALSAR the PSLR is defined as the ratio of the peak sidelobe intensity to the intensity of the mainlobe, considering only the sidelobes within plus/minus ten resolution cells of the mainlobe [*Vexcel Corporation*, 2003].

$$PSLR (dB) = 10 \log_{10} \frac{I_{PSL}}{I_{ML}}. \quad (4.5)$$

4.1.3 Effect of the ionosphere on the SAR PSF

The along track point spread function of a SAR system – assuming no degradation by the propagation medium - can be measured by imaging a point target, such as a trihedral corner reflector (CR) [*Freeman*, 1992]. However, as the radar moves in the along-track direction the ray path traverses the time varying ionosphere resulting in modulation of the phase and amplitude of the signal.

The signal received by a SAR from a point target, after compensating for the satellite motion, and performing the usual SAR processing [Oliver and Quegan, 2004b] can be written as:

$$S(x) = A(x) \exp\{i\Psi(x)\}. \quad (4.6)$$

Here $\Psi(x)$ is the residual phase modulation over the synthetic aperture due to the ionosphere (zero for a perfectly focussed image), and $A(x)$ is the amplitude modulation over the aperture due to the ionosphere. The PSF can then be represented as the Fourier transform of this function:

$$PSF = \mathcal{F}\{A(x) \exp\{i\Psi(x)\} W(x)\}, \quad (4.7)$$

where $W(x)$ is a window function to reduce sidelobes (and with the consequential trade-off of widening the mainlobe). If there are no ionospheric effects and no window function, the processed signal from a point target will be a top-hat function, and hence its PSF will be described by a sinc function.

Equation (4.7) describes Fraunhofer diffraction of the signal from a one-dimensional aperture, where the small-angle approximation has been applied to leave the PSF in the spatial, rather than the angular domain. The relatively large synthetic aperture means that there will be a large variation in range between the radar and a given point on the ground as the radar moves along the aperture. Whilst this would seem to preclude the use of the small-angle approximation, in fact the SAR processing removes these range variations via the application of a matched filter (Section 3.1).

4.1.4 Synthesising the SAR PSF Using GPS Data

This chapter proposes an alternative to measuring the PSF from a radar signal – that is to synthesize the PSF using GPS carrier phase and amplitude data. Firstly, in order to derive an equivalent SB-SAR PSF from GPS data it is necessary to double the measured phase and square the amplitude in order to compensate for the fact that the GPS signal only passes once through

the ionosphere. In so doing it is assumed that the down and up legs of the propagation path are perfectly correlated [Rogers *et al.*, 2009].

Secondly, the GPS phase must be detrended. This is an important practical problem because the movement of the satellite introduces phase changes of many thousands of radians which mask the effects of the irregularities. Fortunately, because SAR processing removes (through a matched filter) the quadratic component of phase introduced by the satellite motion (Section 3), the second-order terms in the GPS carrier phase can be removed (using a polynomial fit in our processing). Constant and linear terms can also be removed as these terms are caused by the bulk ionosphere, rather than the smaller scale irregularities.

Defining the detrended and doubled GPS phase data as Ψ_{DT} and the two-way amplitude modulation derived from the one-way GPS amplitude (i.e. the square) as $A_{2GPS}(t)$ the synthesised signal derived from the GPS data can be written as:

$$S(t) = A_{2GPS}(t) \exp[i\Psi_{DT}(t)]. \quad (4.8)$$

$S(t)$ is equivalent to the SAR signal from a point target. The SAR along-track PSF is then given by applying equation (4.9):

$$PSF = \mathcal{F}\{A_{2GPS}(t) \exp[i\Psi_{DT}(t)W(t)]\}, \quad (4.9)$$

where $W(t)$ has been chosen to be a Hamming window function [Harris, 1978]:

$$W(n) = \alpha - \beta \cos\left(\frac{2\pi n}{N-1}\right), \quad (4.10)$$

where $\alpha = 0.53836$, $\beta = 1 - \alpha$, N is the width (in samples) of the window function, and $0 \leq n \leq N - 1$. The Hamming window was chosen to reduce the sidelobes of the point spread function, and because of its ease of computation. The Hamming window is often used in SAR applications [Belcher and Baker, 1996; Carretero-Moya *et al.*, 2010].

The process of deriving the quantities Ψ_{DT} and A_{2GPS} from the GPS carrier phase and amplitude is described in section 4.1.5.

4.1.5 Practical Considerations

4.1.5.1. Ionospheric drift velocity

When considering a phase screen at a fixed height, it is important to note the differences in the orbital characteristics between GPS and SAR systems. Careful consideration is required to ensure that the IPPs of the respective systems cover the same distance along the phase screen.

The effective velocity of the IPP as it scans across the screen depends on both the velocity of the IPP, and the drift velocity of the ionosphere:

$$v_{eff} = \sqrt{v^2 + v_d^2 - 2vv_d \cos(\beta - \alpha_d)} \quad (4.11)$$

where v is the IPP velocity, v_d is the drift velocity, β is the bearing of the IPP and α_d is the direction of the drift velocity.

At nighttime in the equatorial region, v_d takes typical values of 100 – 200 ms⁻¹ in an eastward direction [Aarons, 1982]. As such, $v_d \ll v$ for a SAR in low Earth orbit (LEO, ~700 km altitude), and so the effect of the drift velocity for a SAR will be minimal. For GPS however, the irregularity drift velocity and the IPP velocity are of the same order. The drift velocity should therefore be taken into account when choosing the GPS analysis period.

4.1.5.2. GPS analysis period

The analysis period of the GPS signal data was chosen to ensure that the distance travelled by the GPS IPP properly corresponds to the length of a typical PALSAR-2 synthetic aperture (L_{SA}) projected to ionospheric height (L_C). This is the distance moved by the SAR IPP along the phase screen as the radar traverses the synthetic aperture L_{SA} and is the distance over which signal coherency is required. These two quantities can be written as:

$$L_{SA} = \gamma L_C \quad (4.12)$$

where γ is the ratio between the SAR velocity and the effective velocity in the ionosphere. It accommodates the height difference between SAR and ionosphere and anisotropy of the ionospheric irregularities [Belcher and Cannon, 2014]. A SB-SAR such as PALSAR-2 in LEO at an altitude of ~ 700 km is at approximately twice the height of the ionosphere F-region peak (the assumed height of the phase screen). Consequently, for an isotropic ionosphere $\gamma = 2$. However, if due allowance is made both for the anisotropy of the irregularities and the PALSAR-2 orbit $\gamma = 3$ is a better approximation while imaging Ascension Island. Near the magnetic equator, the irregularities tend to extend along the geomagnetic field lines, and since PALSAR-2 operates in a near-polar orbit the effect of this is to reduce the effective velocity of the PALSAR-2 IPP, thus increasing γ . Consequently, the required ionospheric coherence length for this study is one third that of the synthetic aperture length.

For a SAR operating in strip-map mode:

$$L_{SA} = \frac{R_0 \lambda}{2\rho_{az}}, \quad (4.13)$$

where ρ_{az} is the along track resolution, R_0 is the broadside slant range to the target and λ is the carrier wavelength. For PALSAR-2, at a typical broadside slant range of 847 km, a maximum along-track resolution of 2 m and a wavelength at the centre frequency of 1270 MHz, the maximum synthetic aperture (L_{SA}) is ~ 50 km and it follows that $L_C = 17$ km.

The velocity of the GPS IPP combined with the distance L_C gives the duration of the corresponding GPS data block which will be analysed. GNSS satellites, in medium Earth orbit have IPP velocities that depend heavily on the elevation and azimuth angles of the satellite to the receiver. For GPS at an elevation angle of 40° , IPP velocities in an east-west/west-east direction of $26\text{-}37 \text{ ms}^{-1}$ are typical [Forte and Radicella, 2002]. However, the pertinent velocity

in this analysis is the effective velocity, being the vector addition of the IPP velocity, due to the satellite motion, and the ionospheric drift speed. As the latter is typically 100 ms^{-1} (west to east) in the pre-midnight sector it is the dominant velocity component.

For the purposes of this analysis the effective IPP velocity has been fixed at 100 ms^{-1} west-east representing a reasonable average between lower and higher values. Clearly, this will introduce some errors, as the actual drift velocity will not always match this, but without recourse to well validated measurement data it is considered a reasonable approximation. It follows that 170 s (180 s was used in practice) of GPS data is required to synthesise a 2m resolution image by PALSAR-2 of Ascension Island ($L_c = 17 \text{ km}$).

Of course correspondingly shorter and longer data sets can be used to synthesise smaller and larger synthetic apertures. It is important to note that SB-SAR in LEO have an IPP velocity of $\sim 3700 \text{ ms}^{-1}$ and take less than 3 s to scan 10 km along the ionospheric phase screen. The time evolving ionospheric structure can thus be considered frozen-in. In contrast, GPS data blocks of hundreds of seconds will mix temporal and spatial effects.

4.1.5.3. GPS orbit altitude

The irregularities which cause scintillation are produced at altitudes ranging from 200 – 1000 km. The signals from a SAR in LEO ($\sim 700 \text{ km}$ altitude) will only experience the effects of irregularities at altitudes $< 700 \text{ km}$. Signal from GPS satellites in MEO ($\sim 20000 \text{ km}$) will travel through all altitudes at which irregularities can be found. However, the principle region of irregularity production is between altitudes of 250 and 400 km, and so this discrepancy should not influence the data analysis significantly [Aarons, 1982].

4.1.5.4. GPS Phase

This work seeks to establish a GPS proxy for the ionospheric impact on a SAR signal. The signal between a GPS receiver and a GPS satellite scans across the ionospheric phase screen in the same manner as the signal between a point target and a radar. Thus, with appropriate processing to adjust for differences in system geometry, and to isolate the small-scale effects of the ionosphere (i.e. those driven by electron density irregularities), GPS signals can be used as a proxy for the complex signal received by a SAR from a point target across the synthetic aperture.

The GPS carrier phase may be expressed as:

$$\begin{aligned} \Phi = \frac{2\pi}{\lambda} (\rho - \lambda N - c(dt_{sv} + dt_{rx}) + c(d_{ion} - d_{trop}) + \xi) \\ + \Phi_0 + M + \epsilon(\Phi), \end{aligned} \quad (4.14)$$

where λ is the GPS carrier wavelength (m), ρ is the geometric range (m), N is the integer phase ambiguity, dt_{sv} is the satellite clock bias (s), dt_{rx} is the receiver clock bias (s), ξ is the instrumental delay (m), M is the effects of multipath (radians), Φ_0 is the initial phase value (radians), d_{ion} is the ionospheric phase delay (s), d_{trop} is the tropospheric phase delay (s), and $\epsilon(\Phi)$ is phase measurement noise (radians).

Equation (4.14) demonstrates that there are many contributions to the phase recorded at the receiver and as such it is difficult to isolate the impact of the ionosphere using single frequency measurements. Much of the previous work in this area focuses on estimating (using models or pseudorange measurements), and removing the absolute phase delay introduced by the ionosphere, in the interests of improving GPS positioning accuracy [Øvstedal, 2002; Chen and Gao, 2005].

In the context of synthesizing SAR data, the absolute values of the phase delay due to the bulk ionosphere are less important than the relative variations caused by the electron density irregularities. The relaxation of the requirement for absolute values allows the use of detrending methods to remove frequency components of the phase signal below a certain cut-off frequency (typically 0.1 Hz), leaving just the higher frequency variations that characterise scintillation, allowing characteristic scintillation parameters such as the S4 (a measure of amplitude scintillation) and σ_{Φ} (a measure of phase scintillation) to be estimated [Van Dierendonck *et al.*, 1993].

The choice of this cut-off frequency is influenced by the geometry of the satellite-ionosphere-receiver system, and the use of 0.1 Hz is not always appropriate for GPS signals [Forte and Radicella, 2002]. To minimise the possibility of removing wanted signal with an overly aggressive frequency cut-off, an approach based on removing unwanted components of the GPS phase observable on a single frequency was investigated.

Phase: Single-frequency Approach

Knowledge of the path geometry between receiver and satellite was used to remove the range contribution to the raw carrier phase observable. This was achieved through the use of IGS final orbit products (3 – 5 cm accuracy [Kouba, 2009]). Similarly, the satellite clock biases were removed from the phase data using IGS products.

Providing that the receiver does not lose lock during the data analysis period, the initial phase value and the phase ambiguity remain constant. Assuming that the instrument delay also remains constant, differencing all samples with the first recorded sample removes these terms. Multipath was minimised through careful site selection and the imposition of an elevation mask to ignore signals from satellites below 40° elevation, so this was also neglected.

This reduces Equation (4.14) to:

$$\Phi_1 = -\frac{2\pi}{\lambda}cdt_{rx} + cd_{ion} + \epsilon(\Phi), \quad (4.15)$$

describing the received phase in terms of the receiver clock bias, a noise term and the ionospheric phase term.

So far no filtering has taken place even though a trend of typically 10^6 radians (over 180 seconds) has been reduced to 10^3 radians, the data integrity has been fully maintained. This allows any subsequent filtering to be relatively light.

The receiver clock bias, dt_{rx} , refers to any offset the receiver clock may have from its nominal frequency. If the clock is running at a fixed offset, a linear ramp will be introduced to the data. Similarly, if the offset itself is drifting, a quadratic term will be introduced to the recorded phase. Since we have no independent way of measuring the receiver clock bias, it is modelled as a polynomial up to quadratic order, and removed with a least-square polynomial fit to each data block.

In terms of isolating the effect of the ionosphere on the signal phase, this approach is not perfect, as it will remove low-frequency, quadratic-like ionospheric effects. However, it can be assumed that a SAR autofocus procedure will remove these terms. After these terms have been removed, it is typically found that the phase variation is 1 to 10 radians over 3 minutes.

Phase: Dual Frequency Approach

Rather than determine the one-way carrier phase directly from the signal it was indirectly calculated by differencing the L1 and L2 phases (the geometry free combination) to give the slant TEC (STEC). This approach removes many of the unwanted errors common to both frequencies.

Dual frequency GPS receivers use the frequency dependence of the phase shift imposed by the ionosphere to allow measurement of the slant total electron content (STEC) along the signal path.

$$STEC_{\phi} = \frac{f_1^2 f_2^2 (\Phi_{L1} - \Phi_{L2})}{40.3(f_1^2 - f_2^2)} + B, \quad (4.16)$$

where Φ_{L1} is the phase on L1, f_1 is the L1 frequency (1575.42 MHz) Φ_{L2} is the phase on L2, f_2 is the L2 frequency (1227.60 MHz) and B is a bias term from ambiguity in phase difference.

This differencing has the effect of removing sources of error that are common to both the L1 and L2 phase signals – the range, the satellite and receiver clock biases - and the approach is often described as the geometry free solution. We find that

$$\Phi_{L1} - \Phi_{L2} = \Delta\lambda N + \Delta\Phi_0 + c(\Delta d_{ion} - \Delta d_{trop}) + \Delta M + \epsilon(\Phi). \quad (4.17)$$

$\Delta\lambda N$ and $\Delta\Phi_0$ are constant bias terms (assuming phase lock is maintained), $\Delta c d_{trop}$ is insignificant for satellites at high elevations, and assuming the location is chosen such that the effect of multipath is minimised, this may be neglected also:

$$STEC_{\phi} = \frac{f_1^2 f_2^2 (c\Delta d_{ion} + \epsilon(\Phi))}{40.3(f_1^2 - f_2^2)} + B. \quad (4.18)$$

The corresponding ionospheric component of the carrier phase is then given by [Hofmann-Wellenhof et al., 1997]:

$$\psi = \frac{8.44 \times 10^{-7}}{f} STEC_{\phi} \text{ (radians)}. \quad (4.19)$$

The advantage of using the TEC is that none of the interpolation or fitting methods described in the previous section are required to determine the ionospheric component. However, this comes at a cost, since the signals on each frequency take slightly different paths through the ionosphere and the TEC is an approximation.

The horizontal spatial separation for two signals of different frequencies f_1 and f_2 is given by [Belcher, 2008b] as:

$$\delta x = \frac{8|f_1 - f_2|}{(f_1 + f_2)^3} \cdot \frac{r_e c^2 VTEC}{\pi} \tan \theta \sec^2 \theta, \quad (4.20)$$

where f_1 and f_2 are the GPS carrier frequencies as before, r_e is the classical electron radius, $VTEC$ is the TEC measured in the vertical direction and θ is the incidence angle to the ionosphere.

Using a large VTEC value of 100 TEC, and a satellite elevation angle of 40° , the largest horizontal spatial separation encountered will be approximately 30 m. The separation of the L1 and L2 signals is a limitation of the dual frequency approach.

Comparison of Methods

A comparison of the results produced shows that the phase variations produced by the two methods generally matched well when the variations were relatively large (a representative example is shown in Figure 4.1). However, those produced using the single frequency method are noticeably noisier. In addition, the single frequency data often showed relatively small, slow variations when the variations derived from the STEC were negligible in comparison (Figure 4.2). Given that the variation is not present in the dual frequency STEC data, it is apparent that the variations in the single frequency data are therefore of identical size in the phase data recorded on L1 and L2 (and hence eliminated when differencing to produce the STEC). This suggests that these variations do not have an ionospheric origin, as they are not frequency dependent (Equation (4.19)).

The residual variations found in the single frequency data present an obstacle to this analysis, which seeks to extract only the impact of electron density irregularities from the GPS signals. Thus, the STEC derived phase variations will be used for the following analysis.

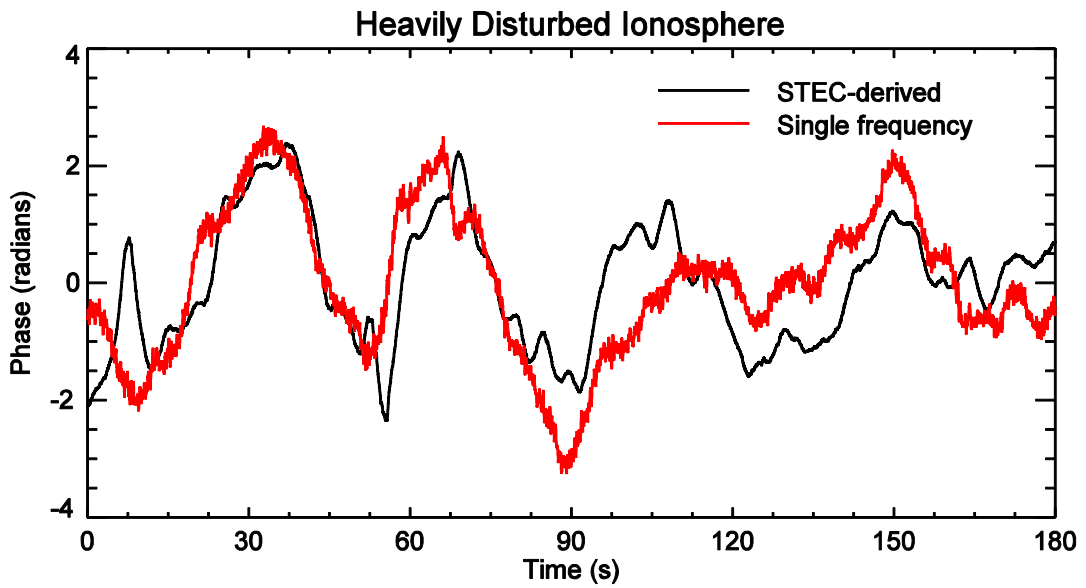


Figure 4.1: Large phase variations produced by the single and dual frequency methods.

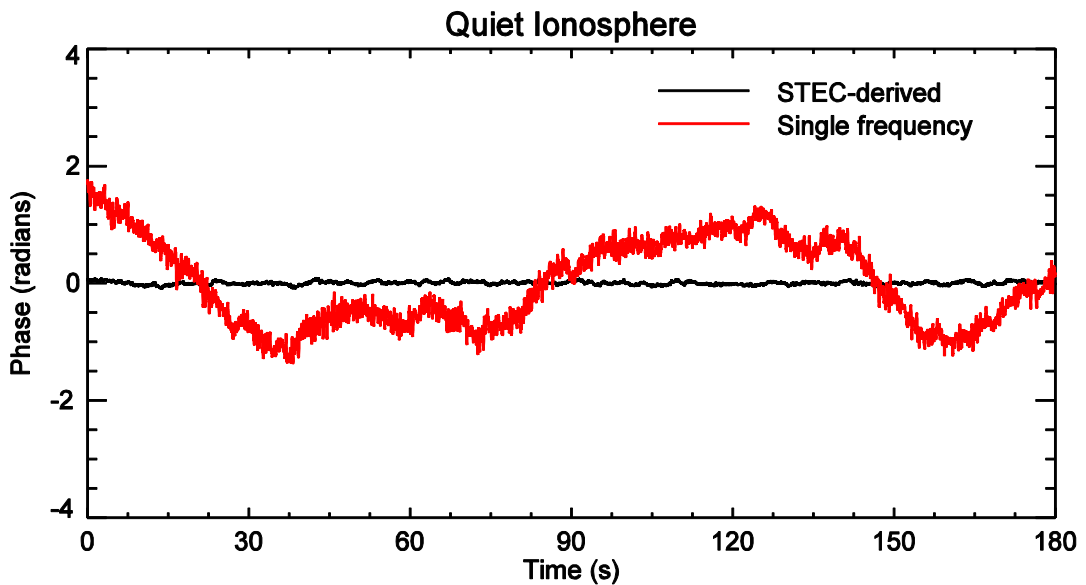


Figure 4.2: Phase variations present in single frequency data but not in dual frequency data.

4.1.5.5. GPS Amplitude

The GPS signal amplitude was derived from the receiver correlator inphase and quadrature (IQ) output components, and were combined as:

$$A = \sqrt{I^2 + Q^2} \quad (4.21)$$

The amplitude was then normalized and detrended by removing a smoothed version of itself (using a 60 s boxcar filter) to isolate the effects of the irregularities on the signal [Carrano *et al.*, 2012a]. (Note, the IQ data only provides instantaneous phase, and so the unwrapped phase data was derived from RINEX files and processed to obtain the TEC-derived phase as described in section 4.1.5).

4.2 Experiment

GPS data was recorded on Ascension Island in the south Atlantic, (7.9°S , 14.8°W , magnetic latitude -16°) (Figure 4.3). Ascension Island lies in the ionospheric equatorial region where small and medium scale electron density irregularities are likely to occur between 21 local time (LT) and 00 LT [Aarons, 1982]. Data was collected during the period 25 January 2013 to 31 January 2013, and 20 January 2014 to 30 January 2014.

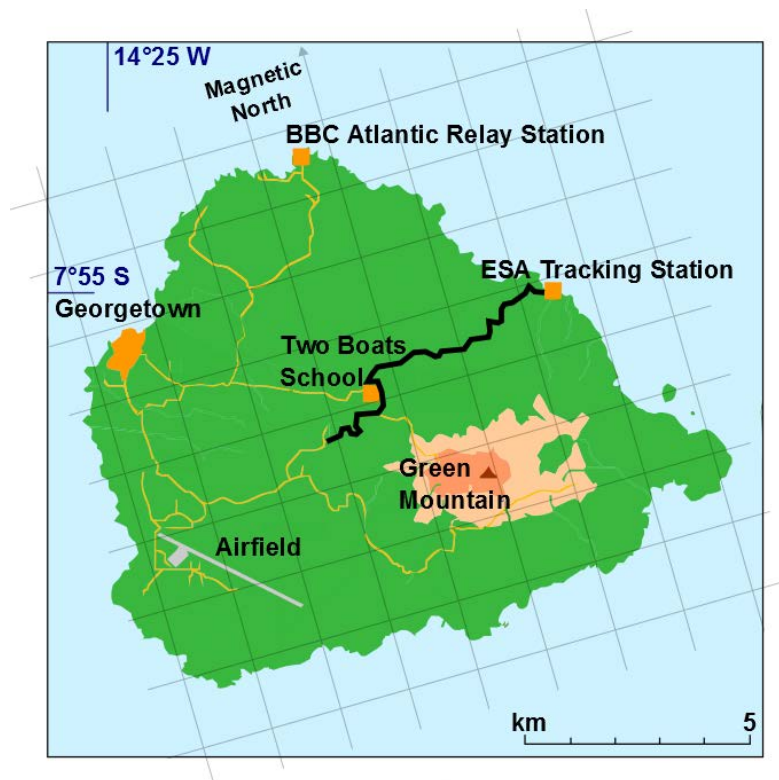


Figure 4.3: Ascension Island (7.9°S , 14.8°W showing the ESA Tracking Station which was the location of the fixed receiver and the road (shown in black) along which the mobile measurements were made).

Two Septentrio PolaRx4 PRO GNSS receivers were used to collect the data, with each locked to a rubidium oscillator to ensure stability. One was located at the European Space Agency (ESA) Tracking Station on the north-eastern coast of the island (marked on the map in Figure 4.3), whilst the other was moved to various locations at distances ranging from ~100 - 9000 m along an approximate (dictated by road access and marked with a black line in Figure 4.3) magnetic east-west axis with the ESA station. This axis was chosen as it lies in the direction of minimum irregularity correlation (the irregularities are assumed to be aligned with, and elongated along, the magnetic field lines), and parallel to the F-region drift direction [Aarons, 1982]. The signal phase and amplitude were recorded at 50 Hz. To minimise multipath effects and minimise the horizontal spatial separation of the GPS L1 and L2 signals, only data from satellites above an elevation angle of 40° were considered. Only data without cycle slips were analysed.

4.3 Single Location Results

4.3.1 Point Spread Functions

The proxy (detrended) signal phase from four 180 s (9000 samples at 50 Hz sampling rate) blocks of GPS data with contrasting levels of ionospheric effect is shown in Figure 4.4, and the effect of the phase modulation on the shape of the PSF is illustrated in Figure 4.5. The top-left panel in each figure shows artificially generated test data that corresponds to no ionospheric effects, and so the shape of (Figure 4.5, top-left) is dictated by the windowing function. The Hamming window provided a PSLR of 42 dB.

Figure 4.5 (top-right) shows the PSF corresponding to very small phase variations of 0.05 radians RMS in Figure 4.4 (top-right). These phase variations are considered likely due to receiver noise, not ionospheric scintillation, as the signals were completely uncorrelated

between two receivers. The sidelobes close-in to the mainlobe are raised slightly and drop-off more gradually than the ideal (top-left).

The phase variations produced by the disturbed ionosphere (Figure 4.4, bottom-left (0.50 radians RMS), bottom-right, (1.65 radians RMS)) have a more severe effect on the PSF (Figure 4.5, bottom-left and right), and are due to ionospheric scintillation. The terms ‘slightly’ and ‘heavily’ are indicative and based on the RMS phase. Figure 4.5, bottom-left still retains an obvious mainlobe, but the sidelobes closest to the mainlobe have been raised significantly leading to a PSLR of only 18 dB (although the sidelobes more than 10 resolution cells away from the centre of the PSF are only slightly raised compared to those of Figure 4.5, top-right). The low PSLR indicates that the contrast of a SAR image of this point would be reduced. The phase variations shown in Figure 4.4, bottom-right correspond to the heavily distorted PSF shown in Figure 4.5, bottom-right. There is no mainlobe in the PSF and, therefore, the point target would be obscured in the image. The lack of mainlobe means that the PSLR ceases to be a sensible metric for the PSF and, in cases like this, it was set to zero for subsequent analysis. Nearly 2400 point spread functions were produced from the GPS data, collected from multiple satellites on both receivers, during a wide variety of ionospheric conditions. The variation of the PSLR with RMS phase variation over the 180 s apertures is shown in Figure 4.6. The PSLR decreases with increasing RMS phase values, and above ~0.5 radians the PSLR is sufficiently low that few details would be visible in an image.

In certain cases, the effect of the ionosphere was so severe that the GPS receivers would undergo ‘loss of lock’, i.e. stop tracking the signals from the GPS satellites. When this happened (on either receiver), it was identified during post-processing, and any data within 5 minutes after the receiver regained lock was discarded. Using this procedure approximately 10% of the recorded data was deemed invalid, and was not analysed.

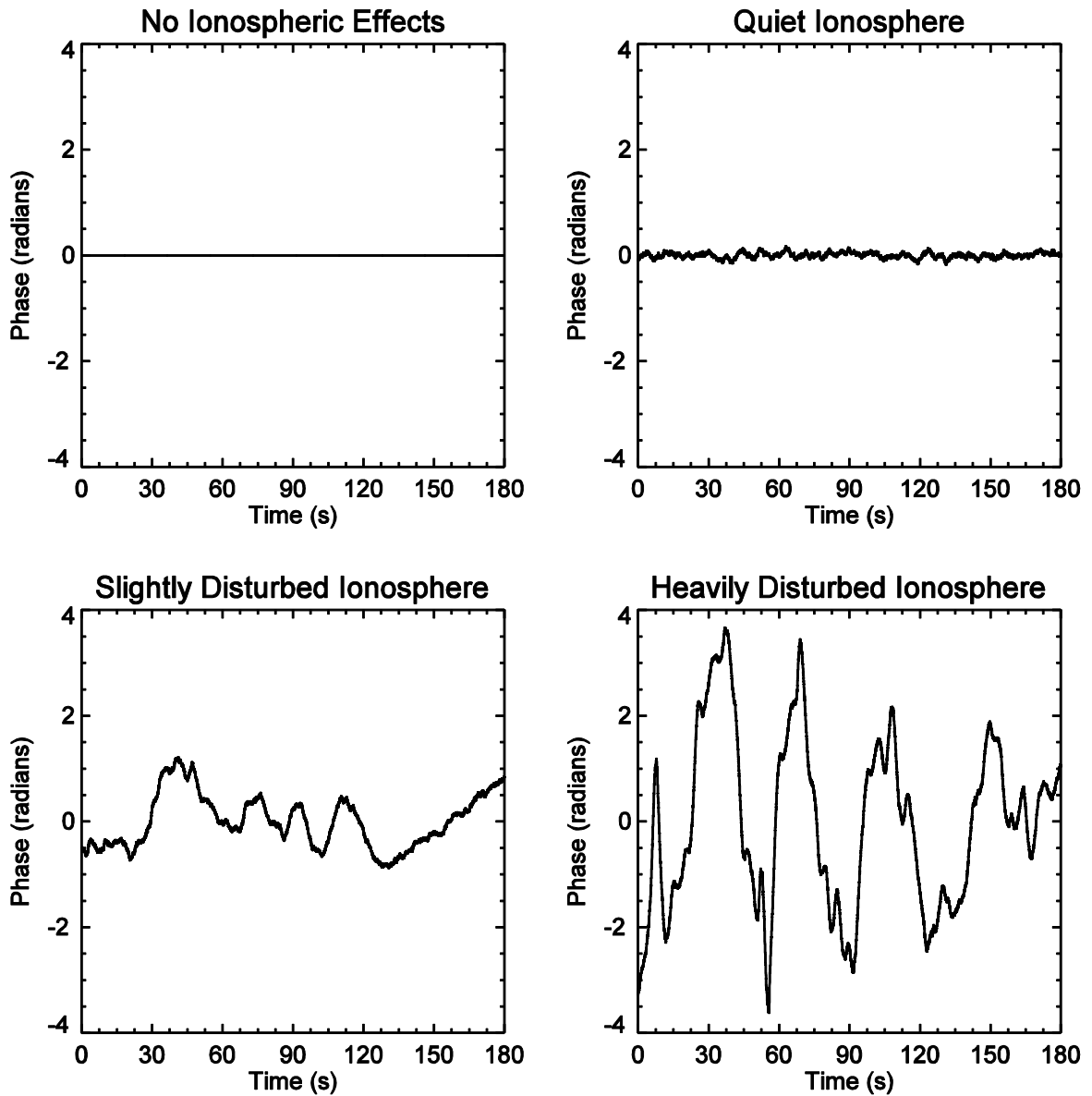


Figure 4.4: Examples of the residual phase modulation for quiet and disturbed ionospheric conditions as recorded by the GPS receivers on Ascension Island.

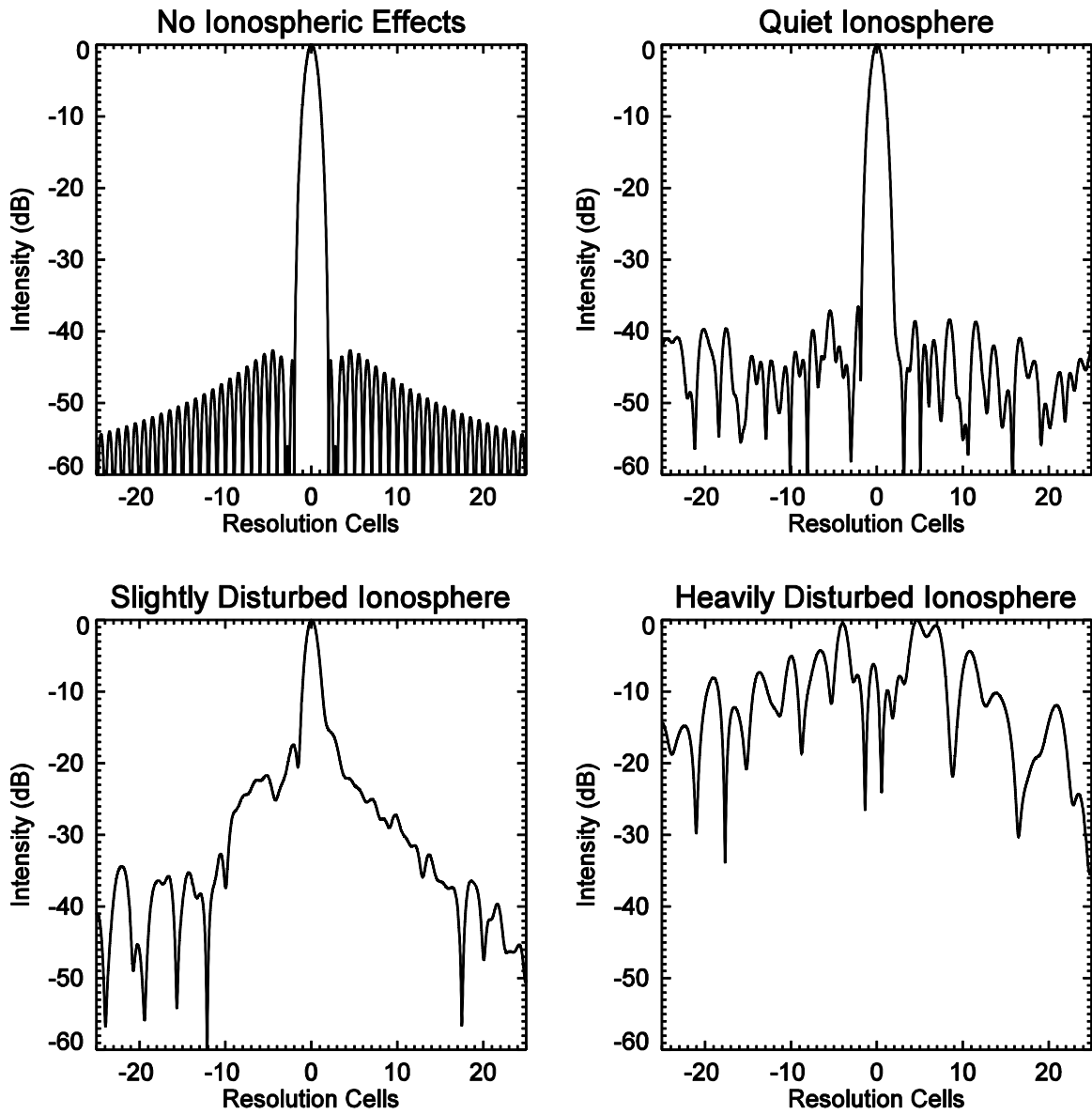


Figure 4.5: Point spread functions for different levels of ionospheric disturbance, generated from GPS signal data recorded on Ascension Island.

Belcher and Rogers [2009] described an analytical form for the ensemble-average SAR PSF which has been degraded by ionospheric irregularities lying in a single phase screen. They provided expressions for the effect of phase scintillation on the sidelobes (the sidelobe function or SLF) and the peak of the mainlobe, as a function of the RMS phase ϕ_{RMS} at the phase screen. This theory has been adapted to fit the data in Figure 4.6.

For a given ϕ_{RMS} , the sidelobe intensity, as a function of distance from the mainlobe in resolution cells r (where the mainlobe is located at $r = 1$) is given by:

$$\langle |SLF(r)|^2 \rangle = 2\gamma r^{-p} (p - 1) \phi_{RMS}^2, \quad (4.22)$$

and the main lobe peak intensity is:

$$MLP = (1 - 2\phi_{RMS}^2)^2. \quad (4.23)$$

The first measurable sidelobe is located at $r = 2$, as the sidelobe at $r = 1$ is obscured by the mainlobe. Assuming that this is the largest, the the peak-to-sidelobe ratio is:

$$PSLR = \frac{MLP}{\langle |SLF(2)|^2 \rangle}. \quad (4.24)$$

However, in this study the relevant RMS phase is that at the synthetic aperture, rather than in the phase screen. To address this we recall that the RMS phase in the phase screen is determined by integrating over the phase power spectrum:

$$\phi_{RMS}^2 = 2 \int_{\kappa_c}^{\infty} PSD_{\phi}(\kappa) d\kappa, \quad (4.25)$$

where κ is the associated spatial wavenumber and $\kappa_c = 2\pi/L_C$, where L_C is the phase screen coherence length required to form a coherent synthetic aperture.

Belcher and Rogers [2009] show that the SLF can be calculated as:

$$\langle |SLF(r)|^2 \rangle = 4\gamma\kappa_c PSD_\phi(\kappa)|_{\kappa=r\kappa_c}, \quad (4.26)$$

and by integration and using (4.25):

$$2 \int_1^\infty \langle |SLF(r)|^2 \rangle dr = 4\gamma\phi_{RMS}^2. \quad (4.27)$$

Alternatively, the SLF can be considered a function of the phase at the synthetic aperture. The latter is determined by the Fourier transform of the phase variations received at the SAR synthetic aperture with power conserved. Thus, the integral over the square of the sidelobe function is also equal to the square of the RMS phase values received at the aperture, ψ_{RMS}^2 .

$$2 \int_1^\infty \langle |SLF(r)|^2 \rangle dr = \psi_{RMS}^2. \quad (4.28)$$

It follows from equations (4.27) and (4.28) that:

$$\psi_{RMS}^2 = 4\gamma\phi_{RMS}^2. \quad (4.29)$$

Here the factor of four is a consequence of the two-way path of the signal at the aperture and γ has been previously defined.

(It is worth noting that experimentally the integrations in equations (4.27) and (4.28) can only be performed from the first measurable sidelobe. The derivation of (4.29) is, however, not constrained by practical limitations.)

It follows from (4.29) that in terms of the phase variations at the synthetic aperture:

$$MLP = \left(1 - \frac{\psi_{RMS}^2}{2\gamma}\right)^2, \quad (4.30)$$

and:

$$\langle |SLF(2)|^2 \rangle = 2^{-p-1}(p-1)\psi_{RMS}^2. \quad (4.31)$$

Consequently, the PSLR is:

$$PSLR (dB) = 10 \log_{10} \left[\frac{2 \left(1 - \frac{\Psi_{DT}^2}{2\gamma} \right)^2}{2^{-p}(p-1)\Psi_{DT}^2} \right], \quad (4.32)$$

where ψ_{RMS}^2 has been replaced by the detrended GPS RMS phase, Ψ_{DT}^2 being a good estimate of ψ_{RMS}^2 .

Setting $\gamma = 3$, being appropriate to PALSAR-2 imaging Ascension Island, and p to a typical value of 2.5 [Basu *et al.*, 1987; Carrano and Groves, 2010], provides a good fit to the data in Figure 4.6. This provides confidence in the GPS proxy approach.

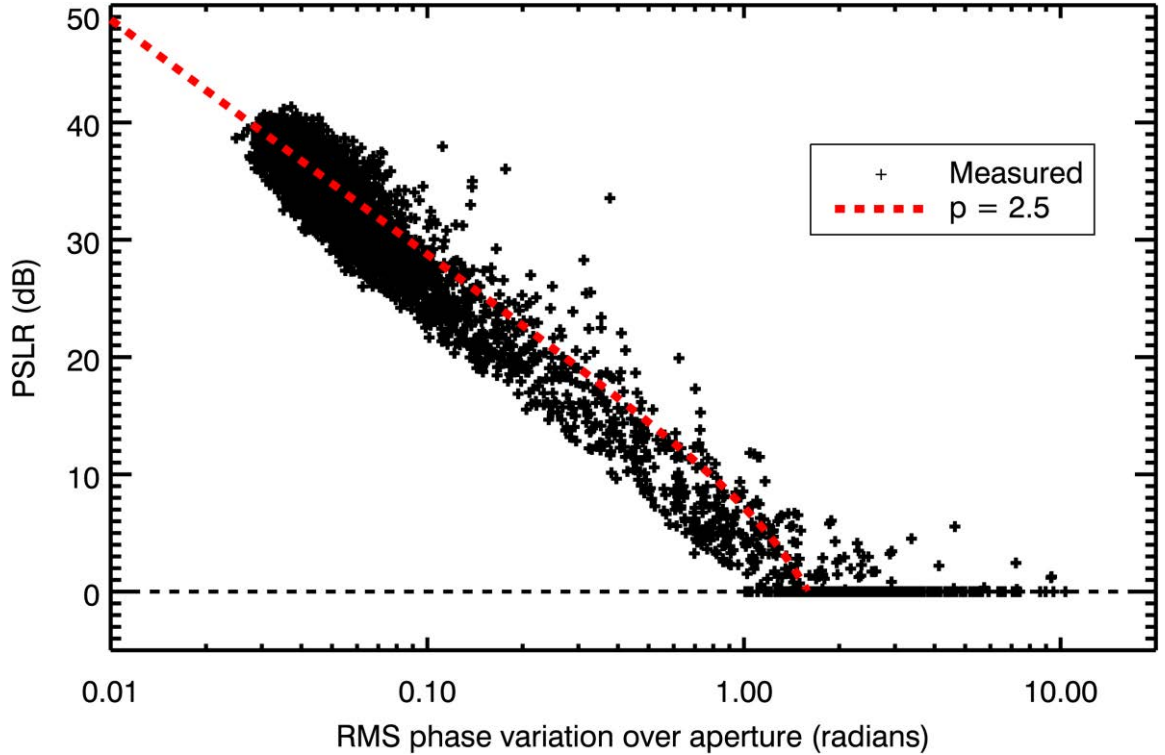


Figure 4.6: Relationship between RMS phase and PSLR of uncorrected SAR PSF.

4.4 Two location Results

4.4.1 Variation in RMS Phase Difference with Distance

Techniques to correct ionospheric distortion from small scale irregularities which affect SB-SAR might be achieved by measuring the signal from a point target, for example a corner reflector (CR). Assuming that the response from the CR dominates the return from its resolution cell, then, after performing the SAR processing, the phase history of the signal across the synthetic aperture is a measure of the ionospheric impact. This estimate might then be applied to mitigate the ionospheric degradation at other locations in the image.

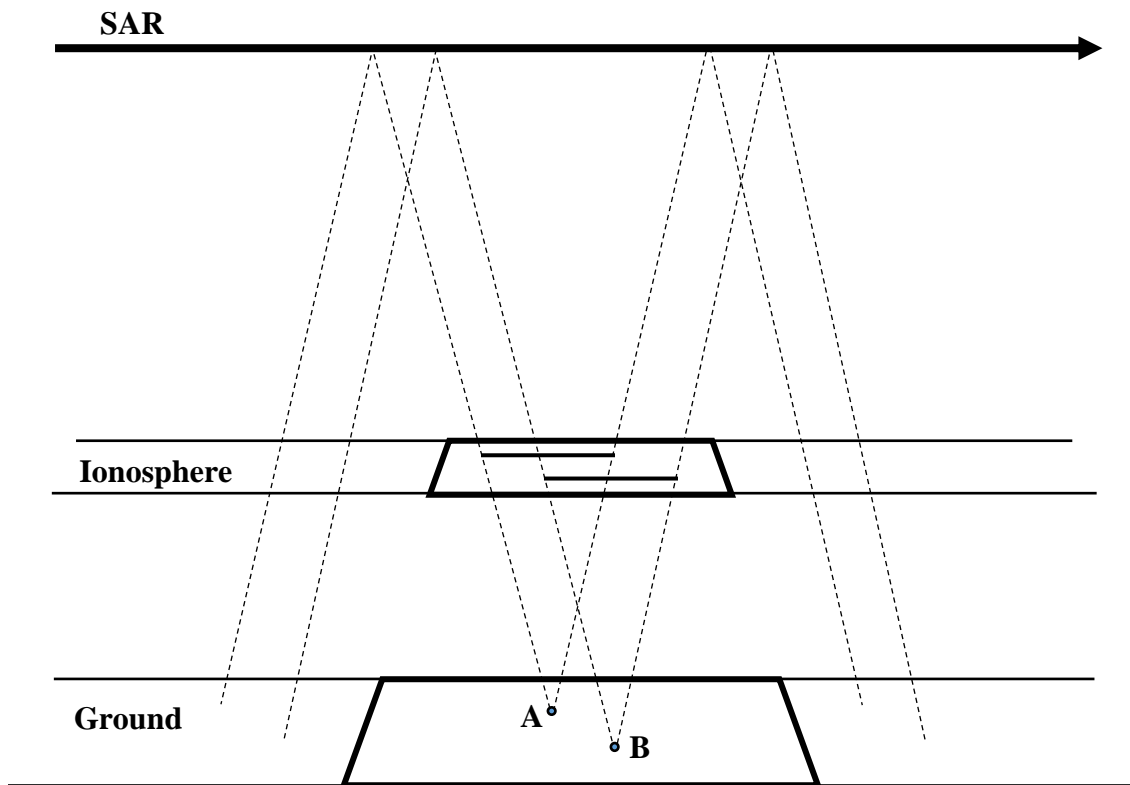


Figure 4.7: Geometry of SAR signals and the ionospheric phase screen for two points in the image. Dashed lines illustrate the real beam width.

Applying a phase correction derived from one location to the phase received from another location separated in the range and the along-track directions requires careful consideration of the geometry (see Figure 4.7 for a SAR in strip-map mode). For points sufficiently close (in the

along-track direction) the IPP tracks overlap and the signals are received simultaneously. It follows that a correction can be achieved by aligning the CR calibration signal with the signal from the remote location. Figure 4.8 describes a simplified, one-dimensional example where the solid diagonal lines describe the signal paths from two points within the real antenna beam (denoted by the dashed lines). In this example the signal from location A received by the SAR at time t_1 intersects the ionosphere at the same IPP as that from location B at time t_0 . Thus, to properly correct the signal from location A received at t_1 , the phase correction from point B at t_0 must be used. The use of this time offset effectively aligns the two signals spatially, allowing the correction to be performed.

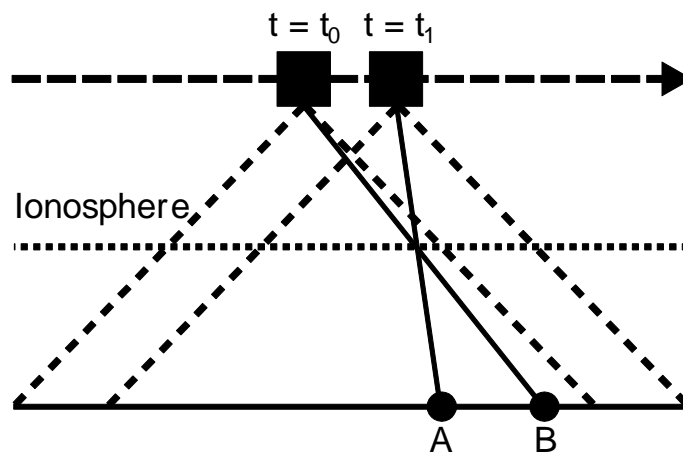


Figure 4.8: Differences in SAR signal paths in the along-track direction.

In Figure 4.7 the IPP tracks do not fully overlap in the along-track direction (the general case) and only a portion of the signal can be corrected. However, a series of corner-reflectors separated by a fraction (determined by the ratio of the phase screen height to the radar height) of the real radar beam width in the along-track direction would provide a continuous series of phase corrections in the along-track direction.

The same geometry issues also apply to the GPS data, where the points ‘A’ and ‘B’ from Figure 4.7 are analogous to the GPS receivers. The two GPS receiver data sets were aligned by cross-

correlation, with the peak correlation giving the along-track time offset between the two. Writing the sample-by-sample phase difference between the two data sets as:

$$\text{Phase Difference} = \Psi_{DT}^{\alpha}(t) - \Psi_{DT}^{\beta}(t + \Delta t), \quad (4.33)$$

the RMS phase difference (over 180 s) at a range of IPP separations was determined (Figure 4.9). As expected there is a general upward trend in the residual RMS phase post correction as the IPP separation increases - although at each separation there are a wide spread of values. This may be a result of differences in the GPS IPP scan length due to errors in the assumed scan velocity, or due to the data being collected at different times with correspondingly different strengths of turbulence (see equation (4.4)) or due to different phase power law indices. Noting that the two GPS receivers were deployed along an approximate magnetic east-west axis, the experiment provides a worst-case estimate of the distance dependence of the phase correction. The average RMS value at each distance follows the form given in equation (4.4), i.e. a linear relationship with a (log-log) slope of $\frac{1}{2}(p - 1)$. The least-squares slope (the solid line in Figure 4.9) is 0.64 ± 0.09 at the 95% confidence level, corresponding to a phase spectral index value of $p = 2.28 \pm 0.18$, very close to the expected value of $p = 2.5$.

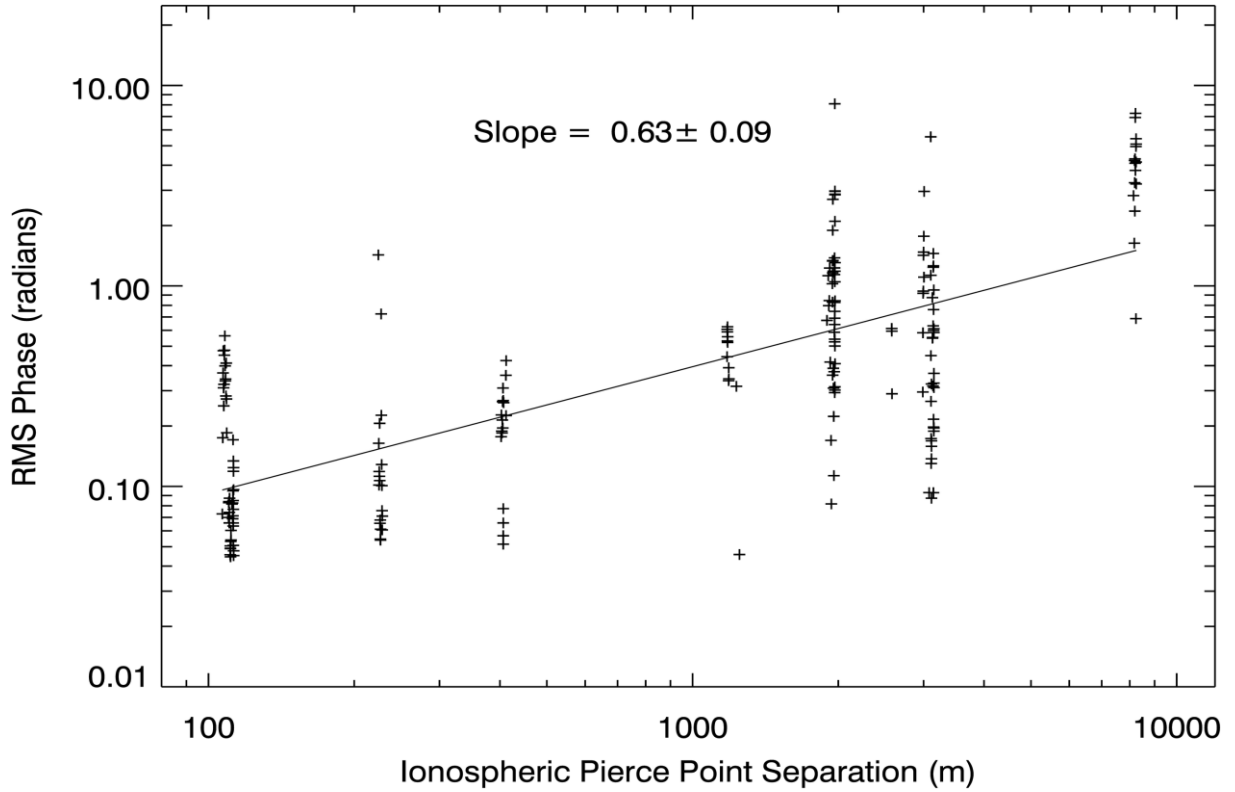


Figure 4.9: RMS phase difference (for pre-correction PSLR < 5 dB).

4.4.2 Sharpening the PSF

The proxy data can now be used to determine the benefits of using measurements at one location (β) to correct the phase at another location (α).

The corrected PSF can be written as:

$$PSF(s) = \mathcal{F}\{A_{2GPS}^{\alpha}(t) \exp[i(\Psi_{DT}^{\alpha}(t) - \Psi_{DT}^{\beta}(t + \Delta t))]\} \quad (4.34)$$

where $\Psi_{DT}^{\alpha}(t)$ is the phase block recorded at the primary receiver, and $\Psi_{DT}^{\beta}(t + \Delta t)$ is the phase recorded at the secondary receiver, offset by the peak correlation lag.

Two examples of the effect of applying this phase correction on the PSF are shown in Figure 4.10 - Figure 4.13. The first pair of plots (Figure 4.10 and Figure 4.11) show the pre and post-correction PSF respectively, with the correction performed using data collected with the secondary receiver only ~250 m away from the primary receiver. Figure 4.10 shows a heavily

distorted PSF, with no mainlobe at all, in a similar manner to the bottom-right plot in Figure 4.5. Despite this, the phase correction is very effective, restoring a narrow mainlobe and drastically reducing the level of the sidelobes to ~38 dB down from the mainlobe.

The latter pair (Figure 4.12 and Figure 4.13, show the impact of performing the correction using more widely spaced receivers. In this case, the correction is performed using data collected at a separation of ~2500 m. It can be seen that, for a similarly disturbed pre-correction PSF (compared to the previous example), the correction is less effective. The mainlobe is much wider, and the peak sidelobes either side of the mainlobe are only ~20 dB down.

The degree of benefit is dependent on many factors, but Figure 4.14 shows the impact of applying the correction on apertures that have been heavily affected by the ionosphere (defined as having a PSLR of less than 5 dB), as a function of signal separation in the ionosphere.

The greatest benefits (30 dB) are seen at the smallest IPP separations with decreasing benefit (10 dB) out to IPP distances of ~3 km. Again there is large variability which is likely driven by different ionospheric conditions. Notwithstanding the variability in benefit, the correction consistently improves the PSLR and rarely does the application of the reference phase correction degrade the PSF and, therefore, the associated image. A least-squares fit shows that, at the 95% confidence level, the benefit decreases at 13.0 ± 1.6 dB per decade (in distance).

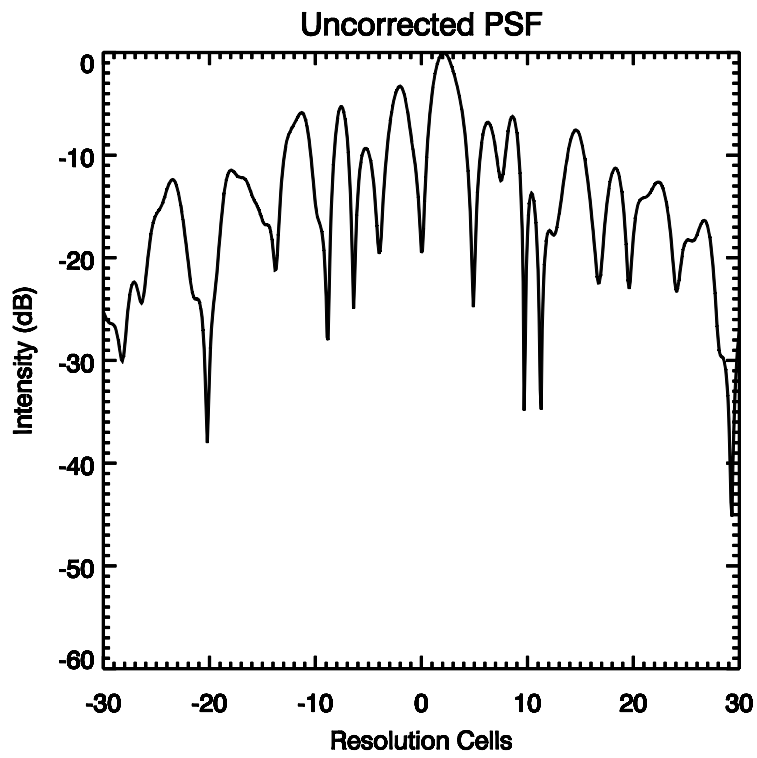


Figure 4.10: Uncorrected PSF, SVID 29, 26/01/2014.

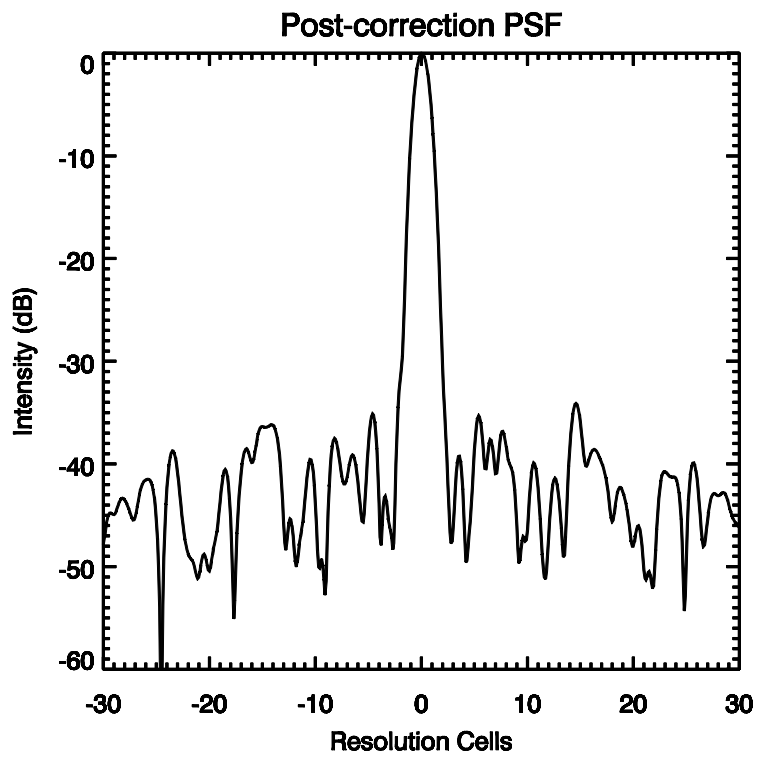


Figure 4.11: Post-correction PSF (receiver separation ~250 m). SVID 29, 26/01/2014.

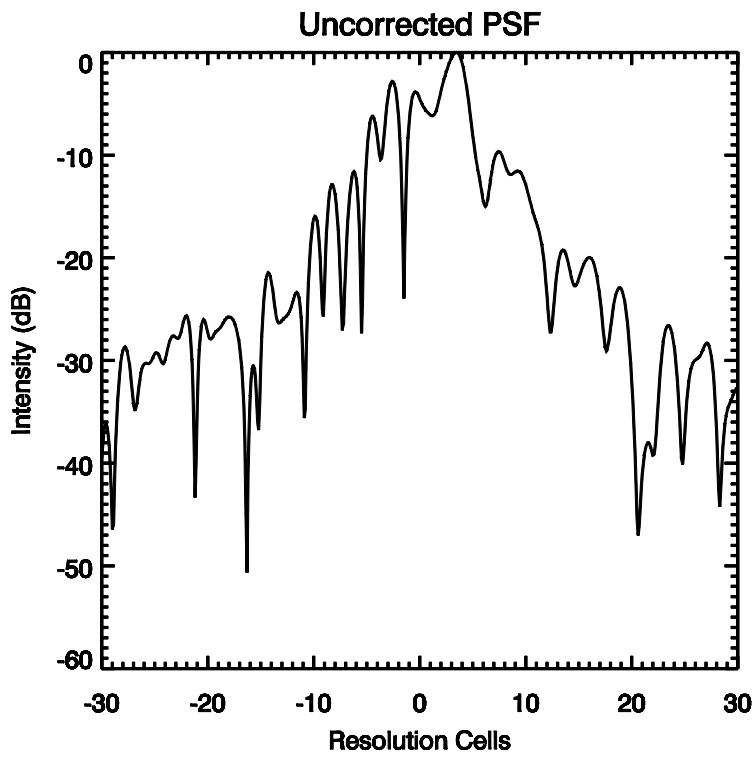


Figure 4.12: Uncorrected PSF, SVID 29, 24/01/2014.

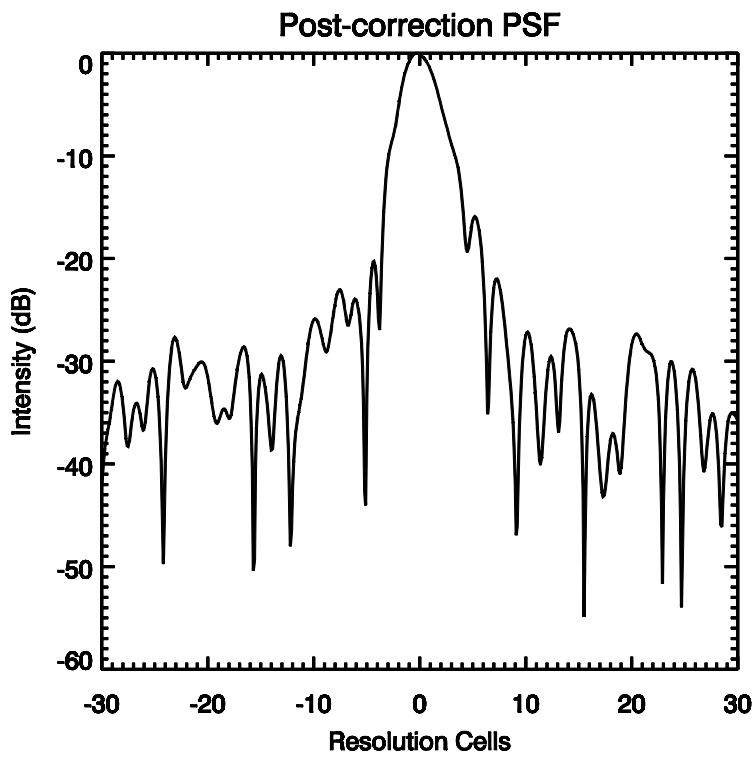


Figure 4.13: Post-correction PSF (receiver separation ~ 2500 m). SVID 29, 24/01/2014.

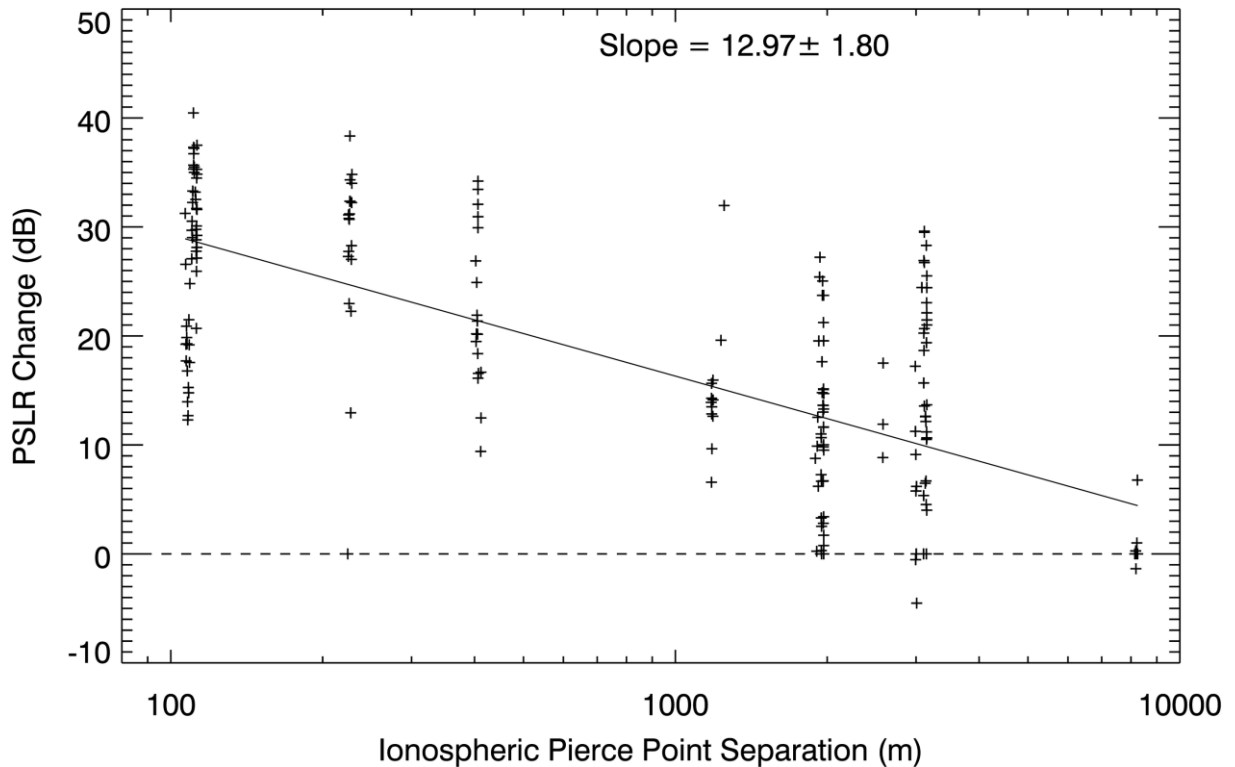


Figure 4.14: PSLR change after phase correction for uncorrected PSF PSLR < 5dB.

Up to this point, the analysis has focussed on studying the viability of the proposed phase correction method, and as such the amplitude variation has been set to unity to allow the effects of phase to be studied in isolation. However, in practice SAR systems are affected by amplitude scintillation and so it is instructive to calculate the PSF using the recorded GPS amplitude as well as phase. The results of applying the phase correction technique to PSF data calculated with both amplitude and phase data are shown in Figure 4.15.

The slope of the linear fit has decreased to 10.8 ± 1.7 dB per decade, driven by a reduction in the PSLR change at IPP separations of less than 1000 m.

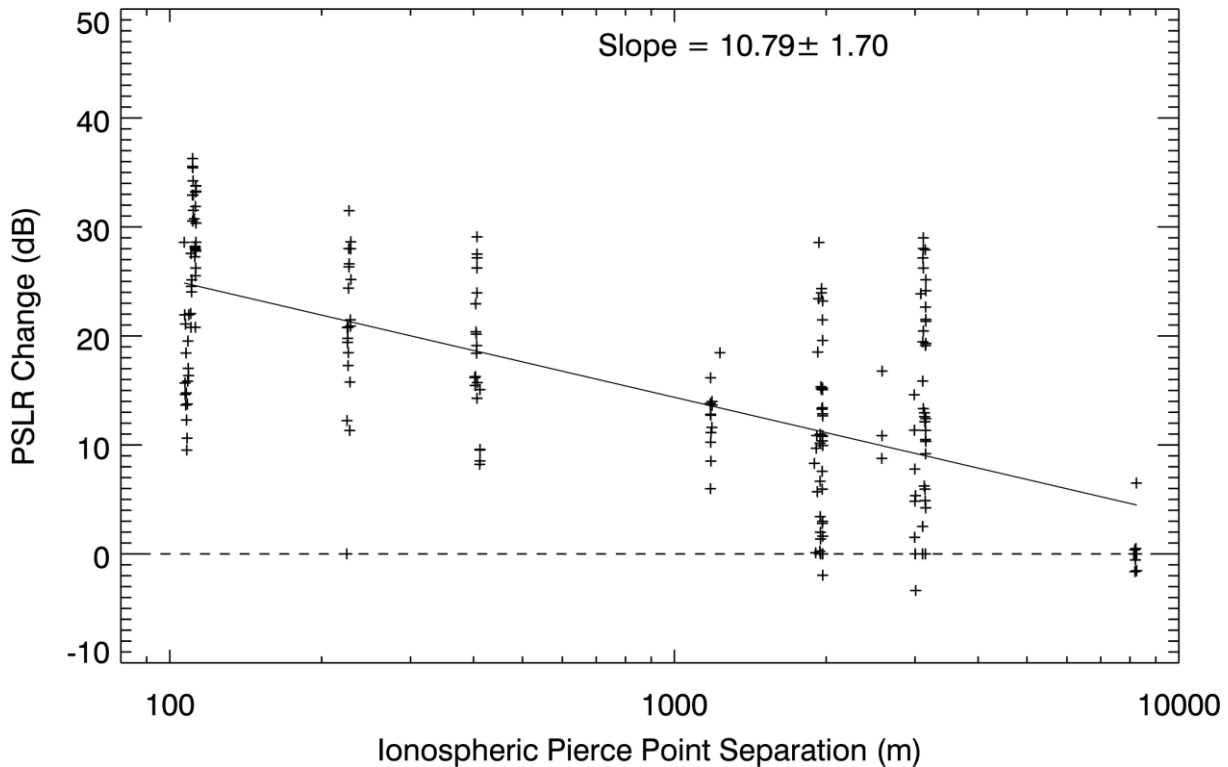


Figure 4.15: *PSLR change after phase correction for uncorrected PSF PSLR < 5dB, GPS amplitude data included in PSF calculation.*

4.5 Conclusions

A method has been described which utilises L-band GPS amplitude and phase data as a proxy for L-band space-based synthetic aperture radar (SB-SAR) signals. This is further developed to synthesize the equivalent SAR point spread function (PSF).

The technique has been tested using measurements at a single location and the synthesised peak-to-side-lobe ratio (PSLR) has been shown to approximately follow the expected weak scattering theory variation with RMS phase. Then, using two position measurements the synthesised SB-SAR RMS phase has been shown to exhibit spatial characteristics which are consistent with a phase screen, again described by the weak scattering theory. These tests provided confidence in the SB-SAR synthesis technique.

Using the synthesized L-band SAR PSF, the viability of correcting the phase recorded at one location using the phase recorded at another was investigated. This was achieved by exploring

whether the ionospheric GPS phase (after the geometric terms had been subtracted) at one location could be used to improve the PSF at another location. This was quantified in terms of the difference between the PSLR of the pre-correction PSF, and the PSLR of the post-correction PSF. At short distances (i.e. 100 m between IPP points) the benefit was ~30 dB, but this fell to around 10 dB at an IPP separation of 3000 m. An IPP separation of 3000 m corresponds to a ground range of ~6000 m for a LEO L-band SB-SAR. Consequently, these results suggest that ionospheric mitigation techniques based upon a reference corner reflector would be effective in improving a L-band SAR image at ground separations up to 6000 m.

The impact of amplitude variation on the effectiveness of the phase correction was also studied. It was found that for IPP separations of less than 1000 m, the maximum effectiveness of the correction was reduced by up to 8 dB. It is worth noting that, even with this reduction, at the IPP separations studied here the phase correction was still able to improve the PSLR by up to 38 dB. This suggests that the shape of the PSF is largely driven by the phase variations, and is relatively insensitive to the amplitude variations.

5 DERIVING IONOSPHERIC SCINTILLATION PARAMETERS FROM SAR SIGNALS – CORNER REFLECTORS

As has been discussed in Section 3.4, the ionosphere imposes a number of effects on the signals and images collected by space-based L- and P-band synthetic aperture radars (SARs), including Faraday rotation, image shift, defocusing and amplitude modulation.

Previous studies of the impact of the ionosphere on SAR systems have primarily addressed Faraday rotation e.g. *Rogers and Quegan* [2014]. However, the impact of small scale ionospheric irregularities on radars has also been recognized [*Ishimaru et al.*, 1999; *Belcher*, 2008b; *Belcher and Rogers*, 2009; *Belcher and Cannon*, 2013].

A few authors have also explored the inverse problem of how a space-based SAR might be used to image large-scale features in the ionosphere. For example, *Meyer et al.* [2006] discussed how the phase advance and group delay might be measured by interferometric techniques and *Pi et al.* [2011] developed a technique using PALSAR-1 polarimetric data to generate 2-D ionospheric images. Through measurements of the Faraday rotation, the latter were able to see enhancement arcs associated with aurora, the mid-latitude trough, medium-scale travelling ionospheric disturbances, and plasma bubbles.

Measuring and imaging the bulk ionosphere is important, but tells only part of the complex ionospheric story. In addition, the effects of small-scale irregularities which cause amplitude and phase scintillation on signals must be considered. The effect of these irregularities can be quantified through the intensity index S_4 and the integrated strength of irregularity turbulence, $C_k L$. This chapter uses the theoretical framework proposed by *Belcher and Rogers* [2009], which describes how ionospheric turbulence affects SAR signals, to solve the inverse problem, that is, given a SAR measurement of the point spread function (PSF) can the ionospheric

strength of turbulence parameter $C_\kappa L$ be inferred? This chapter is an extension of preliminary analysis by *Belcher et al.* [2015].

The experimental principle involves imaging a point target, such as a trihedral corner reflector (CR), to produce a point spread function (PSF) - such targets are typically used for radiometric calibration and image quality analysis of SAR systems [*Shimada et al.*, 2009]. To facilitate this, two corner reflectors were deployed on Ascension Island in the South Atlantic. The PALSAR-2 satellite was then used to image the island and specifically the corner reflectors on multiple occasions.

5.1 Theory

5.1.1 The Phase Spectrum

For satellites in a non-geosynchronous orbit, the orbital motion of the satellite results in a spatially changing ray path through the ionosphere between the radar and a fixed point on the ground. Electron density irregularities consequently introduce a variable advance in the signal phase. These phase shifts are usually modelled as occurring in a thin phase screen at the altitude of peak ionisation (350 km). The spatial variation of the phase modulation induced by this ionospheric phase screen ($\phi(x_p)$, where x_p is the distance across the phase screen) can be described by a phase power spectral density (PSD) [*Rino*, 1979a; *Belcher and Rogers*, 2009]:

$$PSD_\phi(\kappa) = T'(\kappa_0^2 + \kappa^2)^{-\frac{p}{2}}, \quad (5.1)$$

where $\kappa = \frac{2\pi}{x_p}$ is the spatial wave number, $\kappa_0 = \frac{2\pi}{l_0}$ is the outer scale wavenumber, l_0 is the

outer scale size of the irregularities, p is the phase spectral index and T' is given by:

$$T' = \frac{r_e^2 \lambda^2 G C_s L \sec \theta \sqrt{\pi} \Gamma\left(\frac{p}{2}\right)}{4\pi^2 \Gamma\left(\frac{p+1}{2}\right)}. \quad (5.2)$$

Here r_e is the classical electron radius, λ is the wavelength of the signal, G is a factor that depends on the propagation geometry, C_S is the three-dimensional strength of the ionospheric turbulence, L is the effective thickness of the ionosphere, θ is the zenith angle and Γ represents the Gamma function.

This formulation allows the strength of turbulence C_S to be determined from the phase spectrum. The more commonly used height-integrated strength of turbulence, $C_k L$ (a parameter of the Wideband Model (WBMOD)), is in turn related to $C_S L$ by [Nickisch, 2004]:

$$C_S L = \left(\frac{2\pi}{1000} \right)^{p+1} C_k L. \quad (5.3)$$

5.1.2 The Point Spread Function

The point spread function (PSF) of an imaging system describes the response of that system to a point input. The shape of the PSF is principally determined by the system design, but external factors can also affect the characteristics of the PSF. For example, the effects of the ionosphere on the phase of a SAR signal can have a significant impact (Section 2).

A space-based SAR has a two-dimensional PSF, with components in both the range and along-track directions. However, given that the range PSF is mainly affected by the bulk electron content in the ionosphere rather than scintillation [Belcher and Rogers, 2009] only the along-track PSF is considered.

Belcher and Rogers [2009] developed an analytical description of the shape of the PSF, under the weak scattering assumption, using the phase spectrum model described above.

The description splits the PSF into the sum of a mainlobe plus sidelobes, with the sidelobe shape, or sidelobe function (SLF), given by the Fourier transform of the ionospheric phase variation across the synthetic aperture:

$$SLF(s) = F\{\psi(x)\}, \quad (5.4)$$

where s is the position in the image, and $\psi(x)$ is the ionospheric modulation on the signal received by a SAR. $|F\{\psi(x)\}|^2$ is equivalent to the phase power spectrum of the ionospheric variations received by the SAR. We can instead express this in terms of the phase power spectrum in the phase screen by making the substitution:

$$\psi(x) = 2\phi(x/\gamma) \quad (5.5)$$

where $\phi(x/\gamma)$ is the phase variations at the phase screen, with a phase spectrum given by:

$$PSD_\phi(s\gamma) = |F\{\phi(x_p)\}|^2 \quad (5.6)$$

where $x_p = x/\gamma$ and s is the spatial position in the image. The phase variations recorded by the SAR are twice that of the phase screen, as the signal traverses the phase screen twice. γ is a factor that accounts for the difference between the velocity of the satellite and the effective velocity of the SAR signal across the phase screen. For an isotropic ionosphere and a satellite in a circular orbit, $\gamma = H_{SAR}/H_{ion}$, where H_{SAR} is the altitude of the satellite, and H_{ion} is the height of the ionospheric phase screen [Belcher and Cannon, 2014].

Combining equations (5.4), (5.5) and (5.6) gives:

$$|SLF(s)|^2 = \left| F\{2\phi(x_p)\} \frac{dx}{dx_p} \right|^2 = 4\gamma^2 PSD_\phi(s\gamma) \quad (5.7)$$

The spatial position in the image s can be related to the spatial wavenumber κ by:

$$\kappa = \frac{4\pi\gamma s}{R\lambda} \quad (5.8)$$

where R is the radar range [Belcher, 2008a].

This substitution, along with the Jacobian $\frac{d\kappa}{d(s\gamma)}$ to account for the change in variables gives:

$$|SLF(s)|^2 = \frac{4\gamma^2 4\pi}{R\lambda} PSD_\phi(\kappa) \quad (5.9)$$

If we express the sidelobe function in units of resolution cells r rather than metres, ($r = s/\rho_{az}$), the relationship between spatial wavenumber and position in the image is given by:

$$\kappa = r\kappa_C, \quad (5.10)$$

where $\kappa_C = 2\pi/L_C$ is the spatial wavenumber of the projection of the synthetic aperture length onto the phase screen, L_C . L_C is related to the length of the synthetic aperture L_{SA} as $\frac{L_{SA}}{L_C} = \gamma$.

The sidelobe function is then given by:

$$|SLF(r)|^2 = 4\gamma\kappa_C PSD_\phi(r\kappa_C). \quad (5.11)$$

Combining equations (5.1) and (5.11) gives:

$$\begin{aligned} |SLF(r)|^2 &= 4\gamma\kappa_C T' \left(\sqrt{\left(\frac{2\pi}{l_0}\right)^2 + \left(\frac{2\pi r}{L_C}\right)^2} \right)^{-p} \\ &= 4\gamma\kappa_C T' \left(\frac{2\pi}{L_C}\right)^{-p} \left(\sqrt{\left(\frac{L_C}{l_0}\right)^2 + r^2} \right)^{-p} \end{aligned} \quad (5.12)$$

Rearranging further gives:

$$|SLF(r)|^2 = T_{SLF} \left(\sqrt{r_0^2 + r^2} \right)^{-p}, \quad (5.13)$$

where $r_0 = \frac{L_C}{l_0}$ and r is the number of resolution cells away from the mainlobe. T_{SLF} is given by:

$$T_{SLF} = 4\gamma \left[\kappa_C^{1-p} G \sec(\theta) (r_e \lambda)^2 \frac{\sqrt{\pi} \Gamma\left(\frac{p}{2}\right)}{(2\pi)^2 \Gamma\left(\frac{p+1}{2}\right)} \left(\frac{2\pi}{1000}\right)^{p+1} \right] C_k L. \quad (5.14)$$

A fit of Equation (5.13) to the SLF data renders T_{SLF} and p which in turn, with knowledge of the propagation geometry, gives $C_k L$ via Equation (5.14).

5.2 Experiment

PSF data was collected using PALSAR-2, an L-band space-based SAR carried by the Advanced Land Observing Satellite 2 (ALOS-2) in combination with two trihedral corner reflectors. Initial results from the corner reflector measurements were presented in *Belcher et al.* [2015].

The main technical characteristics of the radar are described in Table 5.1, whilst the orbital details of ALOS-2 are described in Table 5.2. All of the PALSAR-2 data used in this work correspond to the radar in spotlight mode, which gives the highest resolution data. The orbit of ALOS-2 is sun-synchronous, with a 14-day repeat cycle; in each cycle there are 207 different ground tracks.

Table 5.1: PALSAR-2 radar parameters.

Centre frequency	1257.5 MHz		
PRF	1-6 kHz		
Antenna length	10.0 x 3.0 m (azimuth x elevation)		
Look direction	6.1 kW		
Maximum range	1160 km		
Radar modes	Spotlight	Strip-map (Ultra-fine)	Strip-map (High)
Resolution (along-track)	1 m	3 m	6 m
Resolution (slant range)	3 m	3 m	6 m
Incidence angles	8-70°	8-70°	8-70°
Swath size	25 x 25 km	50 km	50 km

Table 5.2: ALOS-2 orbit characteristics.

Altitude (above mean equatorial radius)	628 km
Inclination angle	97.92°
Orbital time period	97.39 minutes
Local time of equator crossing	00:00 (ascending)
Repeat cycle	14 days, 207 orbits
Longitude offset of track #1	25.815° West
Orbit duty cycle	50%

To measure the PSF, two trihedral corner reflectors with sides of length 5 m (giving a radar cross section of 47 dBm²) were used. The two corner reflectors (Figure 5.1) were deployed on Ascension Island, which is located in the South Atlantic Ocean (7.9°S, 14.8°W). The corner reflector locations are shown in Figure 5.2 (red triangles) - one on the west side of the island, looking west, and one on the east side of the island, looking east. This configuration allowed measurements of the PSF to be made for both east and west looking PALSAR-2 passes. The corner reflectors were deployed from April 2014 – April 2015 with the first data collect occurring on 18 August 2014 close to the start of the Atlantic sector scintillation season.



Figure 5.1: Left: eastward looking corner reflector at Devil's Ashpit and right: westward looking corner reflector at Long Beach.



Figure 5.2: Map of Ascension Island showing corner reflector locations.

Ascension Island is located within the ionospheric equatorial region where electron density irregularities that cause scintillation form in the post-sunset hours, mainly between 21 – 00 LT [Aarons, 1982], but with some scintillation effects both before and after these times. PALSAR-2 images Ascension Island between 00 LT and 02 LT, which, while not ideal, still provides good opportunities for measuring scintillation effects.

Ascension Island was imaged by PALSAR-2 in a number of different ground tracks with various slant ranges and incidence angles. The radar cross section (RCS) of the corner reflectors peaks at an incidence angle of 45° , but the RCS remains high to $\sim\pm 30^\circ$. Since PALSAR-2 imagery is formed at incidence angles between 8° and 70° , the response from the corner reflectors is easily identifiable in every image.

Table 5.3: Corner reflector location details.

	EAST CORNER REFLECTOR	WEST CORNER REFLECTOR
Boresight bearing (w.r.t true North)	80°	260°
Boresight elevation	45°	45°
Latitude	-7. 9542 19°	-7. 9142 54°
Longitude	-14. 3262 05°	-14. 4020 36°
Altitude	548.32 m	42.06 m
Location accuracy	Position: ~10 cm, Angles: ~1°	
Coordinate system	WGS-84	

5.3 Island Images

A total of 76 images of the island were collected of which 61 were collected on the westward looking corner reflector and 15 were collected on the eastward corner reflector. The former is better for seeing scintillation effects as it looks at an ionosphere at an earlier local time. The data set provides a good sampling of ionospheric activity and a good sample of the scintillation season on Ascension Island (see 0) for a list of the images used here). A whole island image is shown in Figure 5.3.

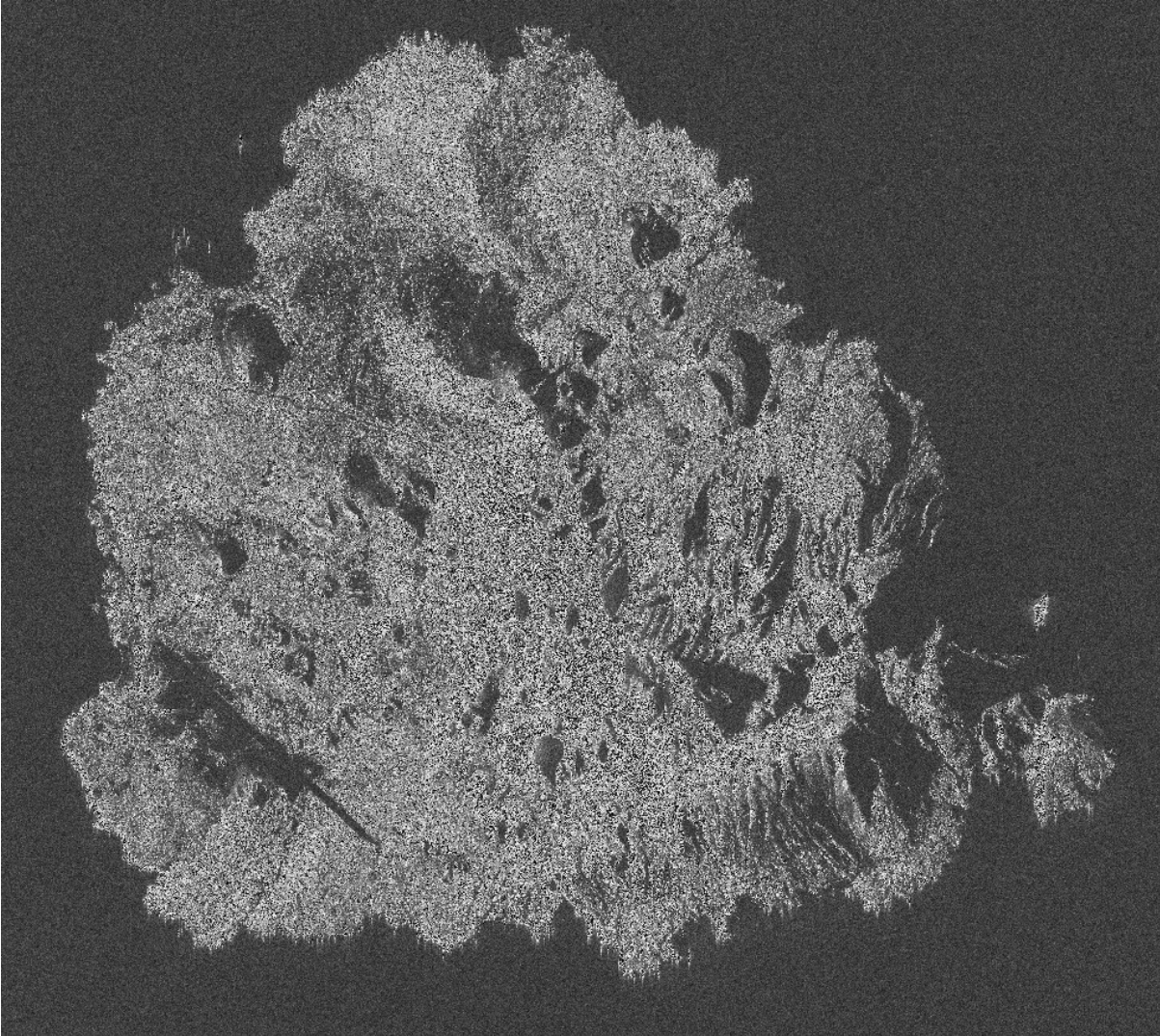


Figure 5.3: Whole island image (2014-08-18, no scintillation)

5.4 PSF Measurement Results

The PALSAR-2 images were obtained for both east and west looking passes at a range of incidence angles. The PSF was measured by identifying the corner reflector in the image, and extracting a strip of intensity values in the along-track direction, centred on the mainlobe (as determined by the pixel with the highest intensity). The sidelobes were averaged to produce a one-sided distribution.

The theoretical sidelobe function (Equation (5.12)) was fitted to the sidelobes of the measured point spread function. For curve fitting purposes the sidelobes were defined as being those

points that were no more than 35 dB below the mainlobe peak (to avoid contamination by noise), and at least 3 resolution cells away from the mainlobe peak resolution cell (to avoid contamination by the mainlobe). The constant of proportionality, T_{SLF} , and the spectral slope, p , were the free parameters of the fit, which was performed by minimising the chi-square statistic. T_{SLF} is a strength parameter, related to the intensity of the corner reflector response at resolution cell $r = 1$, i.e. the intercept of the fit, whilst p is governed by the rate at which the sidelobe level drops off away from the mainlobe. Six sample PSFs are shown here, with the rest shown in Appendix B. In contrast with the synthesized PSFs shown in Section 4, these PSF plots show a one-sided PSF (the sidelobes on each side of the mainlobe are averaged together), using a log-scale for the distance from the mainlobe in resolution cells.

The results are normalised to the peak of the mainlobe which varies from plot to plot. Theoretically, the RCS of the corner reflector for a signal incident along the boresight of the corner reflector) is 47 dBm and can be directly related to the along-track PSFs shown here since the data has a resolution of 1m. The experimental values, however, never exceed 37 dBm using the calibration supplied by the satellite operator (the Japan Aerospace Exploration Agency). Some of this discrepancy may be explained by sub-optimal incidence angles but is inconsequential in the following analysis since the sidelobe function is defined in relative terms only.

Figure 5.4 and Figure 5.5 show the measured point spread function from the corner reflector on the west side of Ascension Island unaffected by ionospheric scintillation. A clear mainlobe can be seen, with a 3dB width of one resolution cell, and a 35 dB width of eight resolution cells. The dashed lines in these and following figures describe the sidelobe function that might be expected as a consequence of the ionospheric distortion (Equation (5.12)). However, the low level of the extended sidelobe structure and the high values of p both serve to illustrate that

there has been little to no ionospheric impact and that the values of T_{SLF} and $C_k L$ should be disregarded.

In contrast, Figure 5.6 shows the effect of the ionosphere on the PSF. Compared to Figure 5.4 and Figure 5.5, more of the point spread function lies above -35 dB (that is the level of the sidelobes in comparison to the mainlobe is relatively low). The fitted sidelobe function (dashed line) provides $T_{SLF} = 2.24$ dB and $p = 2.67$ and using the relationship of T_{SLF} and p to $C_k L$ (Equation (5.14)), the value of $\log_{10} C_k L = 32.25$.

Other points to note:

- The amplitude of the mainlobe is affected by scintillation due to power being “scattered” into the sidelobes. Figure 5.7 and Figure 5.8 show PSFs recorded at the same incidence angle, but in the latter plot the intensity of the mainlobe response is reduced by ~ 7 dB, whilst the corresponding $C_k L$ value is higher.
- At incidence angles significantly different from optimum the dynamic range is reduced. As an example, in Figure 5.9 where the incidence angle is only $\sim 12^\circ$ the mainlobe intensity is only 21 dBm² and the dynamic range is low.

The majority of the phase spectral index values returned by the theoretical fit to the sidelobes lay between 1 and 3 (Figure 5.10). However, some large p values were returned (see for example Figure 5.5) when the ionospheric distortion was below the measurement capability of the experiment.

If all of the data (76 points) – even when implausible p values are returned – are included, $\log_{10} C_k L$ ranged from 25.9 to 35.3 (Figure 5.11). However, as already discussed very high p values are indicative of no or little ionospheric distortion and it is therefore fair to exclude these

points. In this analysis we have placed the threshold at a p value of five which is consistent with the GPS measurements which are reported in the next section.

Excluding p -values larger than five reduced the data set from 76 points to 60 points. That is, of the data analysed 21% of the time the technique was unable to measure any ionospheric effects. Of the 60 points where the technique was able to quantify ionospheric distortion, $\log_{10} CkL$ ranged from 30.7 to 35.0 (Figure 5.12).

This range of values is consistent with C_kL values predicted by the Wideband Model for the post-sunset period near Ascension Island – see for example [Rogers *et al.*, 2014b] - and is highly suggestive that both the theory and the associated experimental technique work.

2014-08-18 01:47 (West CR)

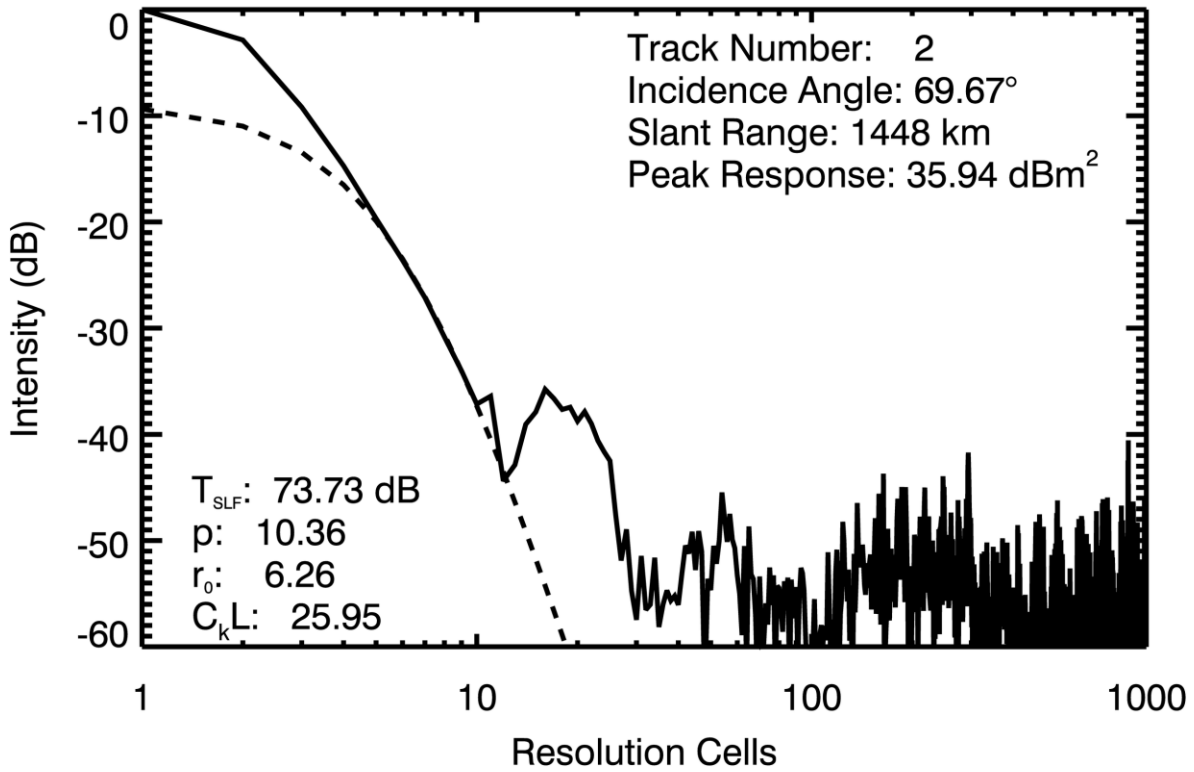


Figure 5.4: West corner reflector response, 2014-08-18 01:47.

2014-08-22 01:33 (West CR)

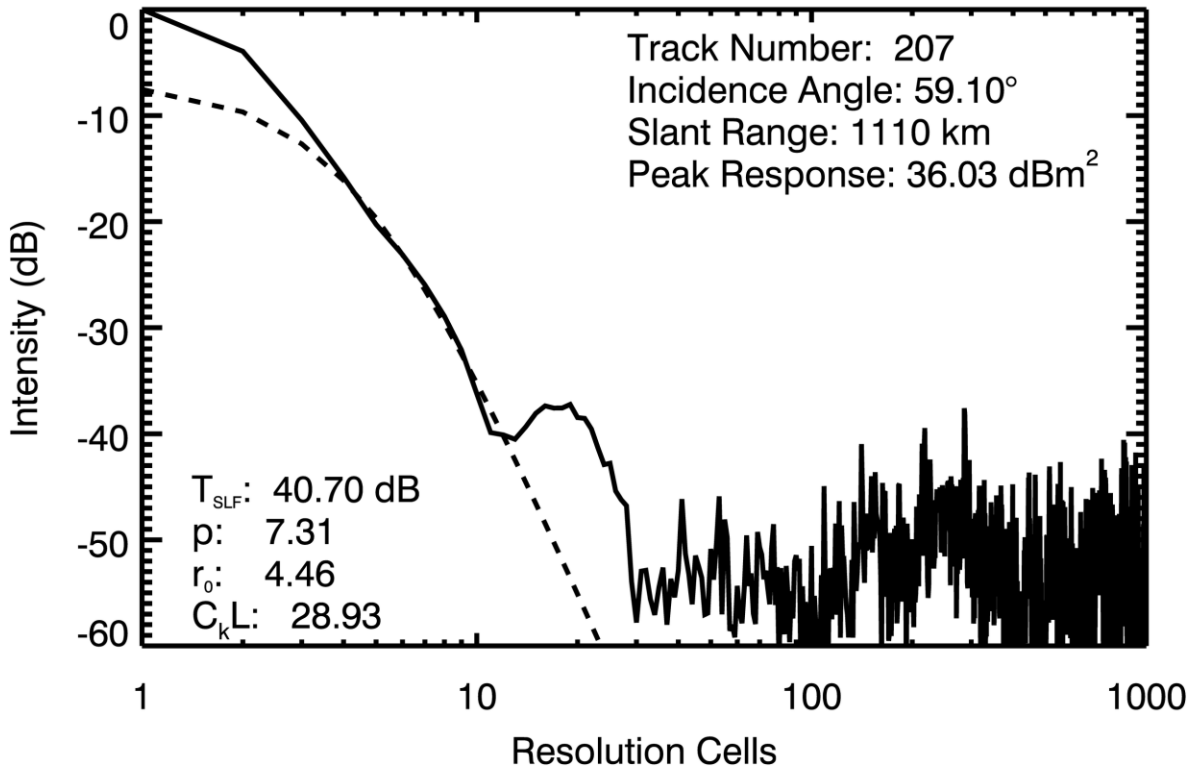


Figure 5.5: West corner reflector response, 2014-08-22, 01:33.

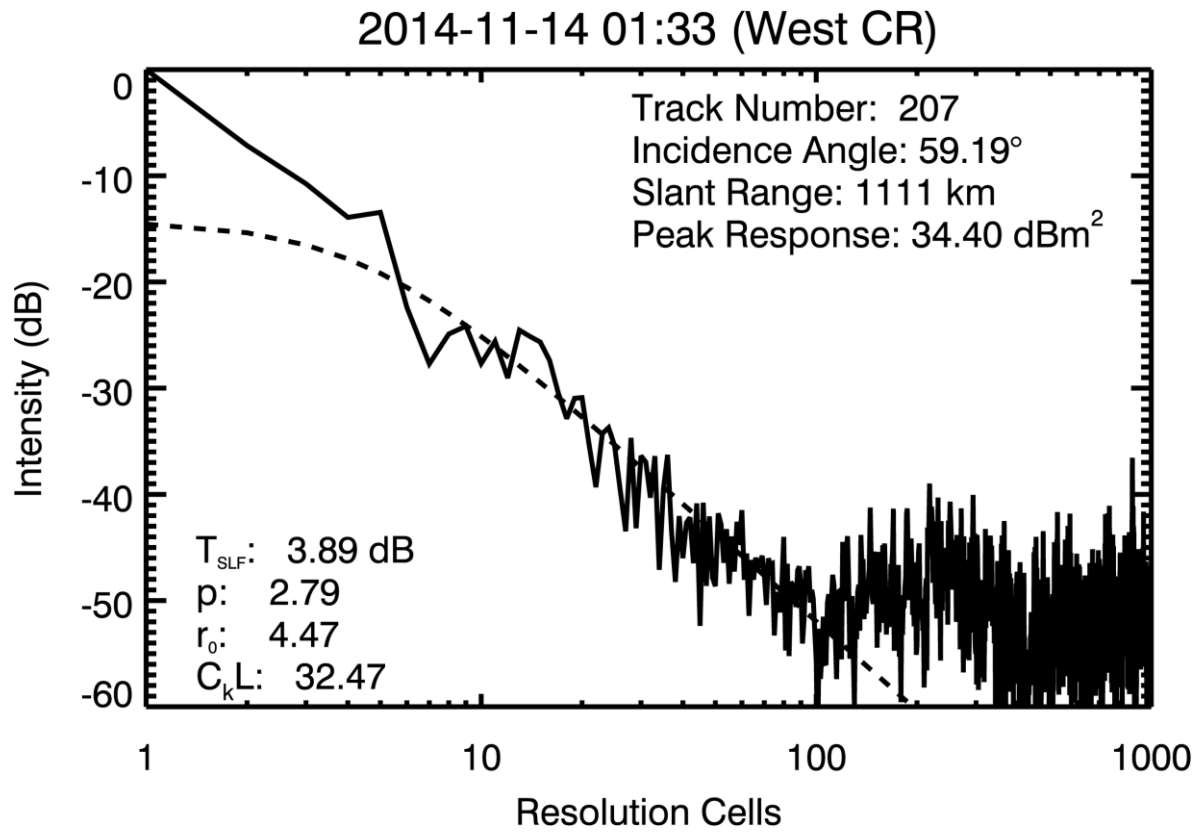


Figure 5.6: West corner reflector response, 2014-11-14 01:33

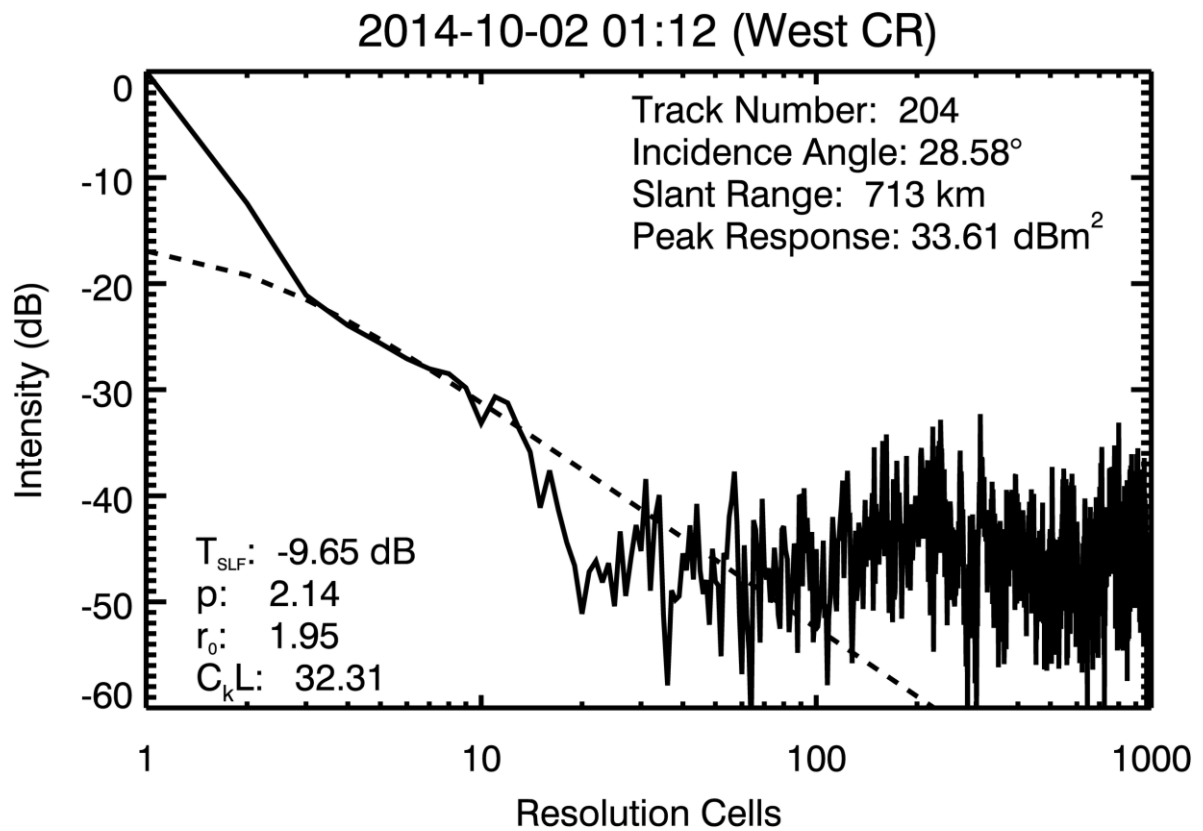


Figure 5.7: West corner reflector response 2014-10-02 01:12

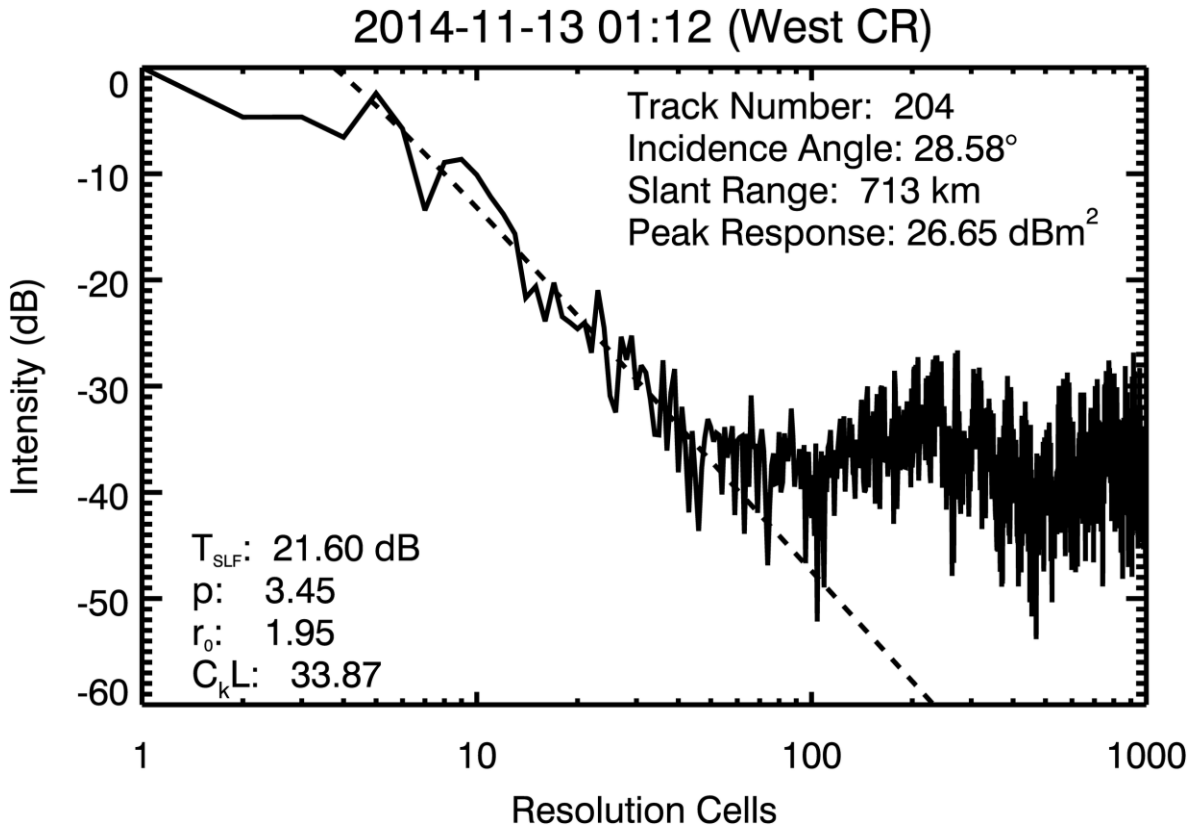


Figure 5.8: West corner reflector response, 2014-11-13 01:12

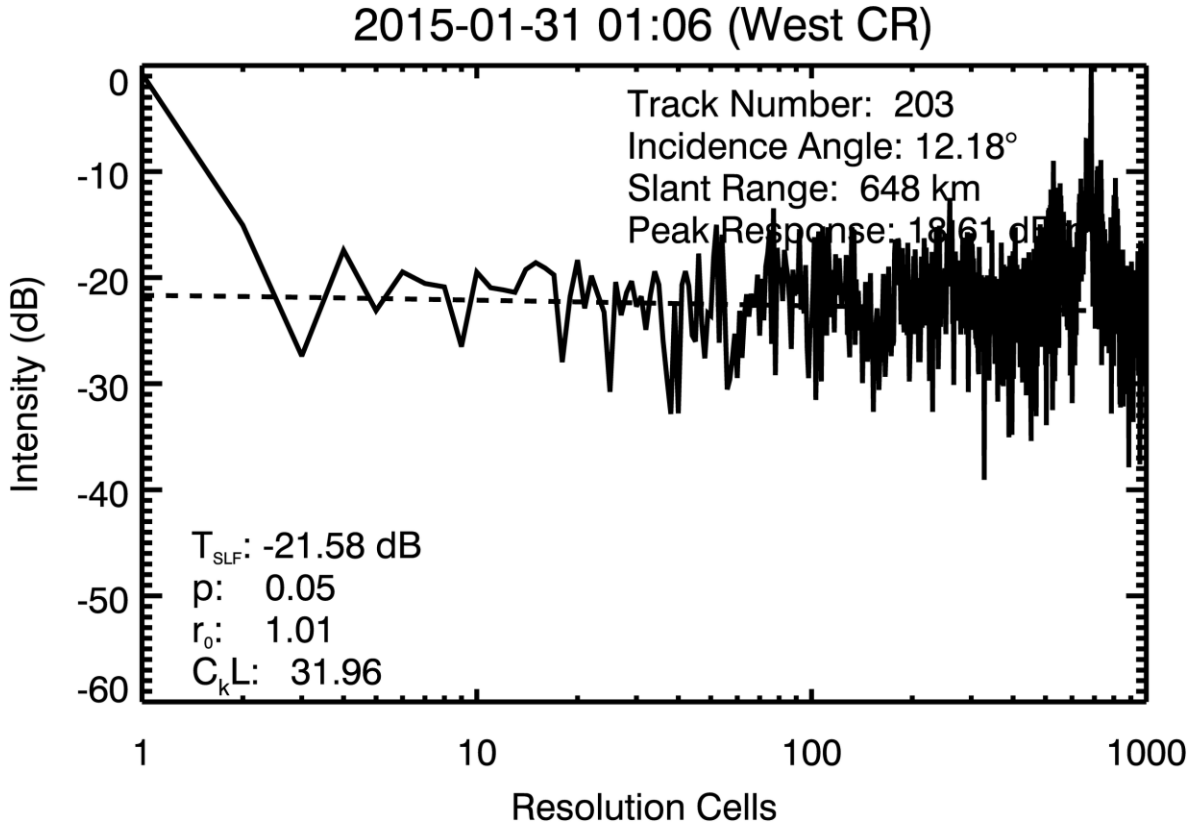


Figure 5.9: West corner reflector response, 2015-01-31 01:06

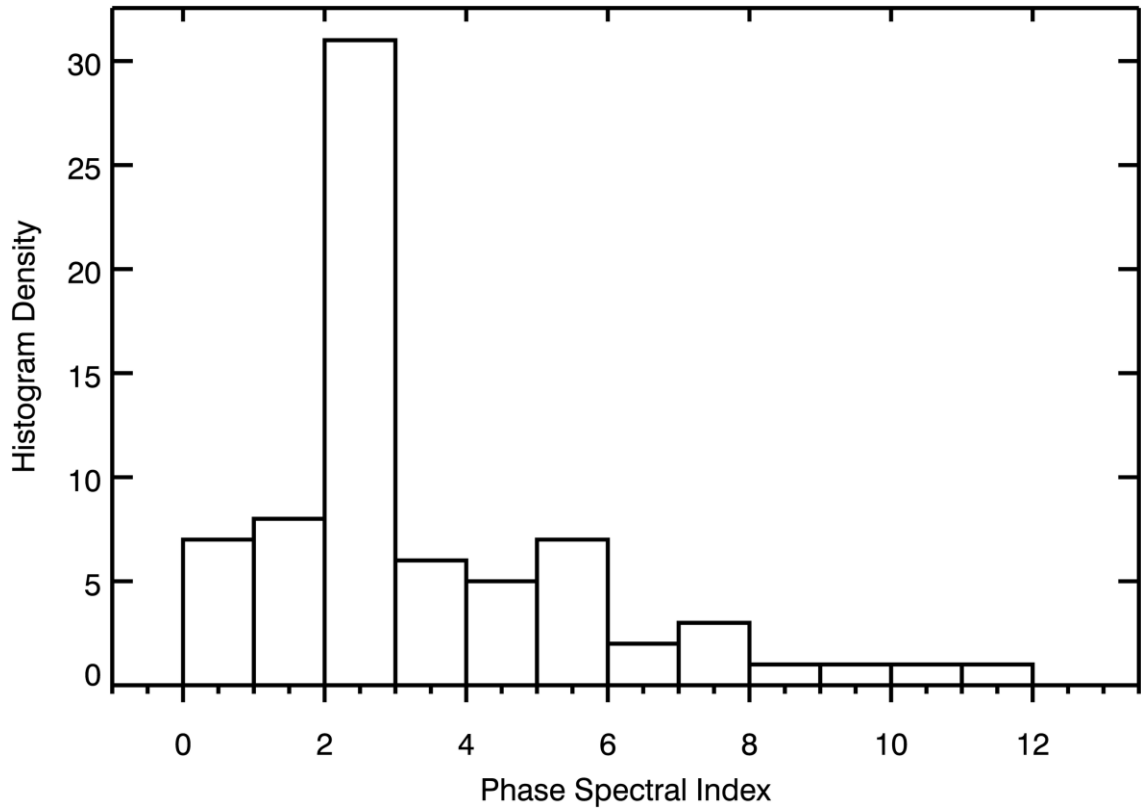


Figure 5.10: Histogram of phase spectral index (p) values from fit of theoretical sidelobe function to measured corner reflector response.

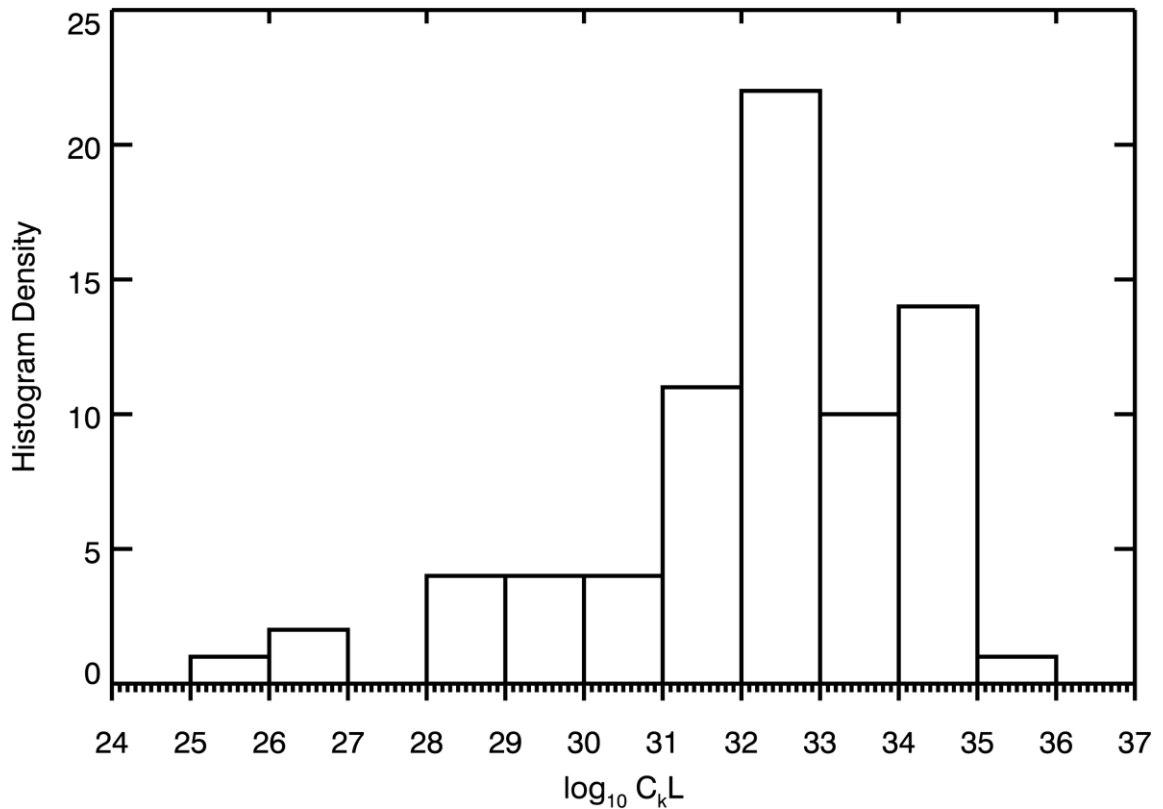


Figure 5.11: Histogram of $C_k L$ values from fit of theoretical sidelobe function to measured corner reflector response (all p values).

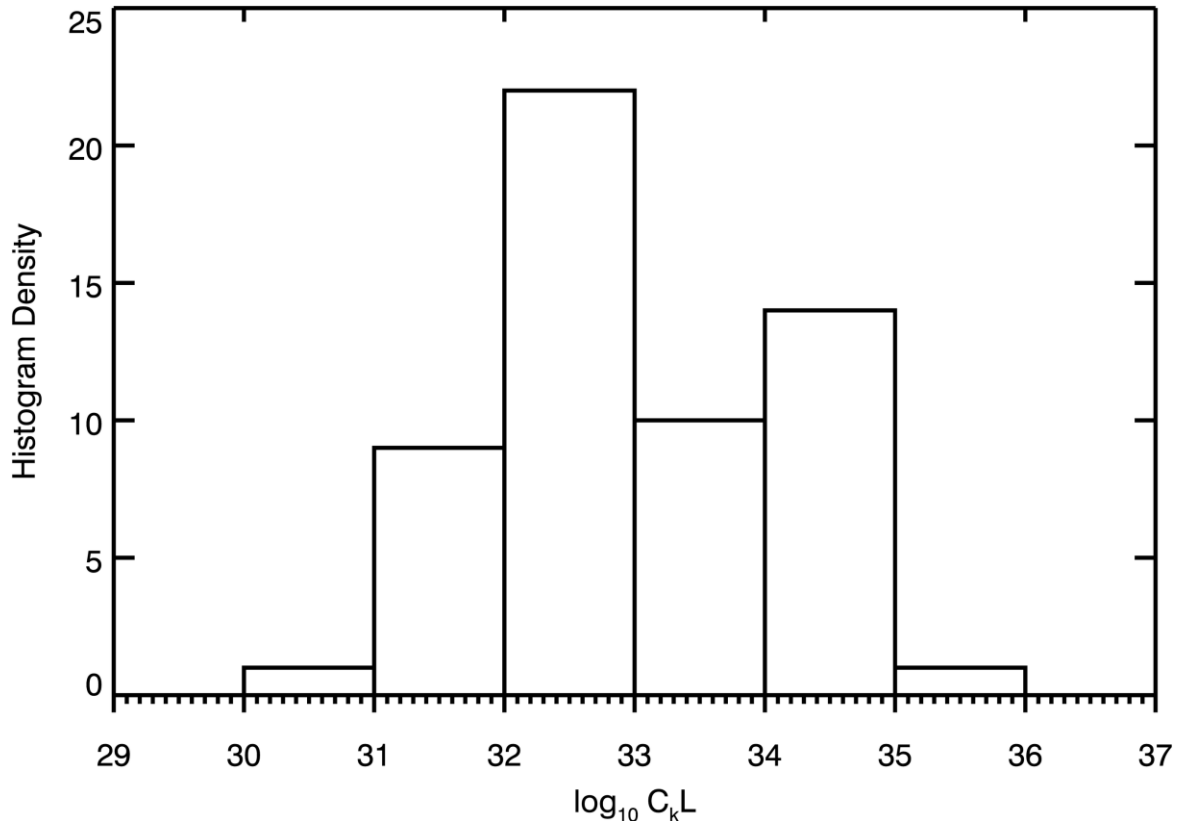


Figure 5.12: Histogram of $C_k L$ values from fit of theoretical sidelobe function to measured corner reflector response ($p \leq 5$).

5.5 Comparison with GPS $C_k L$ Results

Having demonstrated that the corner reflector renders plausible p and $C_k L$ measurements a one-to-one validation approach was sought based on measurements of GPS signals with similar, and preferably close to identical, IPPs. To do this 50 Hz GPS carrier phase data from a dual-frequency Septentrio PolaRx4 PRO GNSS receiver with an external Rubidium clock located 7.7 km from the west corner reflector and 4.2 km from the east corner reflector was used.

Rather than use the standard thirty or sixty second average for the calculation of $C_k L$, six hundred seconds of dual-frequency phase data was used. Assuming a GPS IPP velocity of ~ 100 m/s (including the effects of drift velocity and an anisotropic ionosphere), this gives a scan length across the phase screen of 60 km – similar to the scan distance of the PALSAR-2 IPP in spotlight mode (~ 50 km).

For each corner reflector measurement data from the GPS satellite with an IPP closest to the IPP of PALSAR-2 was used. In each case, the phase time series was centred at the time at which PALSAR-2 was broadside to the centre of the corresponding image.

The raw GPS data was processed in the manner described by *Mannix et al.*[2016]. Slant total electron content values were calculated through differencing of the raw GPS L1 and L2 phase, and these values were converted to the equivalent phase advance to give a phase time series. This removed the effects of the satellite motion on the phase. Further, a quadratic and linear component were removed from the 600 s phase time series, a procedure analogous to that which would be performed during the SAR imaging process.

The ionospheric variations in the GPS phase are measurements of the ionospheric phase screen as described in Section 5.1.1. As such, the phase spectrum is described in the same manner [*Rino, 1979a*]:

$$\phi(f) = T_{GPS} f^{-p_{GPS}}, \quad (5.15)$$

where p_{GPS} is the phase spectral index and T_{GPS} is given by:

$$T_{GPS} = r_e^2 \lambda^2 L \sec \theta G C_s \frac{\sqrt{\pi}}{(2\pi)^{p_{GPS}-1}} \frac{\Gamma\left(\frac{p_{GPS}}{2}\right)}{\Gamma\left(\frac{p_{GPS}+1}{2}\right)} v_{eff}^{p_{GPS}-1}, \quad (5.16)$$

where v_{eff} is the effective velocity of the GPS IPP across the phase screen, and all other symbols are as used in Section 5.1.1. This describes the power spectrum in the time domain, which is more natural for the GPS data, and it has been assumed that the frequencies involved are such that the outer scale frequency can be ignored.

A linear least-squares fit in log-log space to the power spectrum between 0.05 Hz and 1 Hz was performed to determine values for T_{GPS} (the value of the power spectrum at 1 Hz) and p_{GPS} (the

slope). In the following analysis, the quantity p referred to in Sections 5.1 and 5.2 will be denoted as p_{CR} to avoid confusion with p_{GPS} .

A series of example GPS phase power spectral density plots (PSD) are shown in Figure 5.13 - Figure 5.16. Although the absolute level of the PSD values changes between each plot, there is very little variation in the slope of the red fitted line, with the great majority of p_{GPS} values lying between 2 and 3 (Figure 5.17).

In contrast to the $C_k L$ values determined from the corner reflector (Figure 5.11), the GPS $C_k L$ values fall within a much smaller range (Figure 5.18). However, by inspection of the CR responses it was noted that higher p_{CR} values appeared to correspond with a lack of visible ionospheric effects. As such the p_{CR} values produced by the fit to the sidelobe functions were not meaningful and contaminate the analysis. An upper limit of $p_{CR} = 5$ was chosen by inspection of the CR plots to exclude any p_{CR} values that were produced from non-ionosphericly disturbed CR responses (Figure 5.12). When this limit is applied, the GPS and corner reflector $C_k L$ distributions are similar.

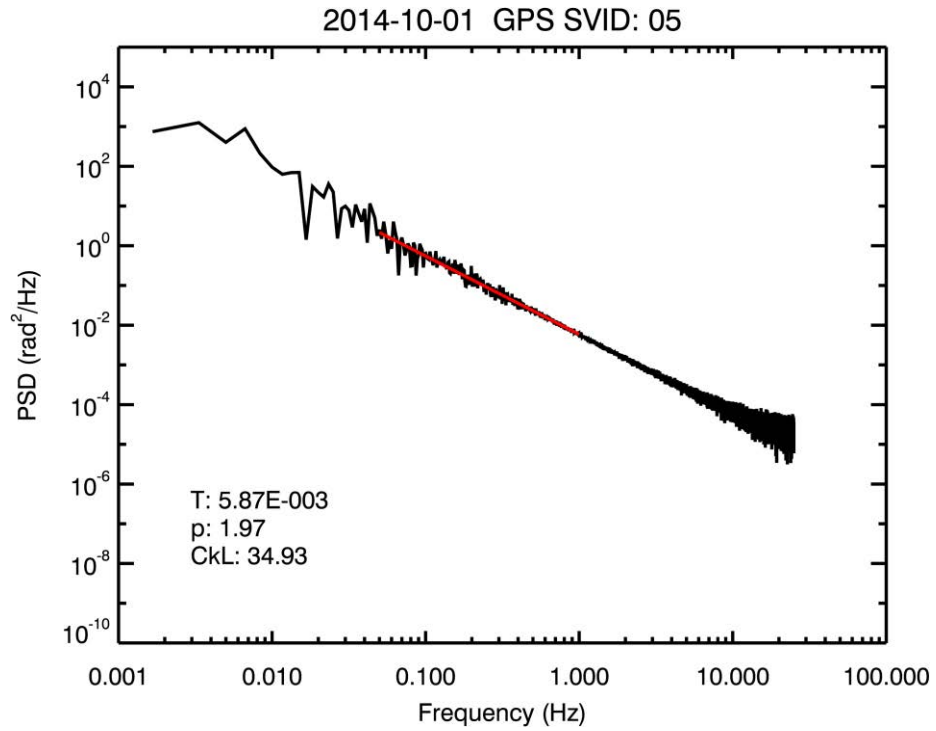


Figure 5.13: GPS phase power spectral density - GPS SVID 5 - 2014/10/01

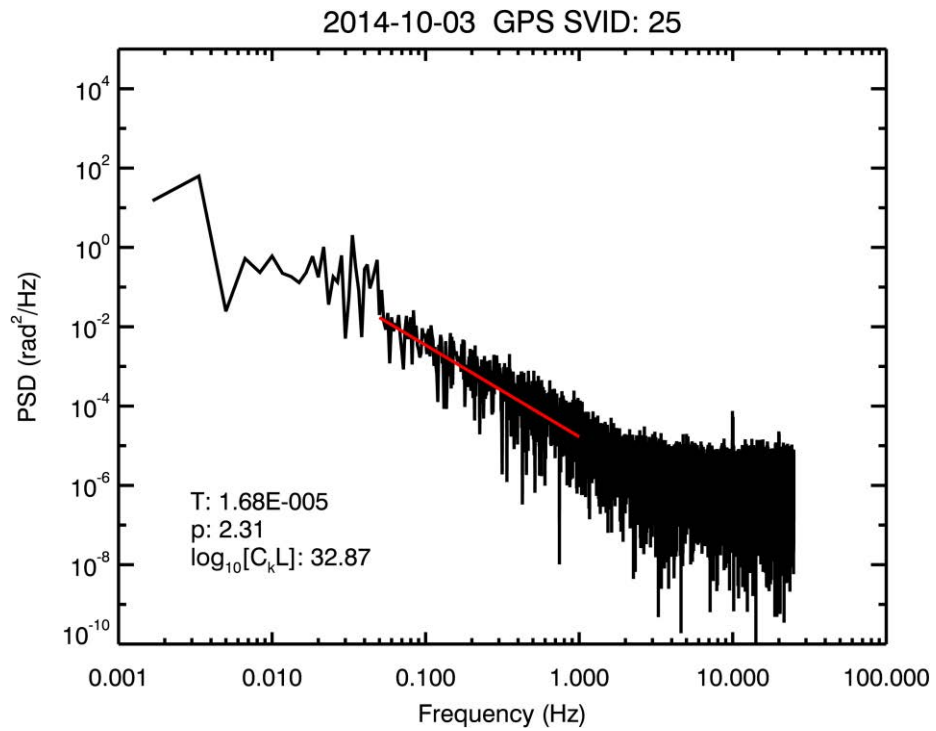


Figure 5.14: GPS phase power spectral density - GPS SVID 25 - 2014/10/03

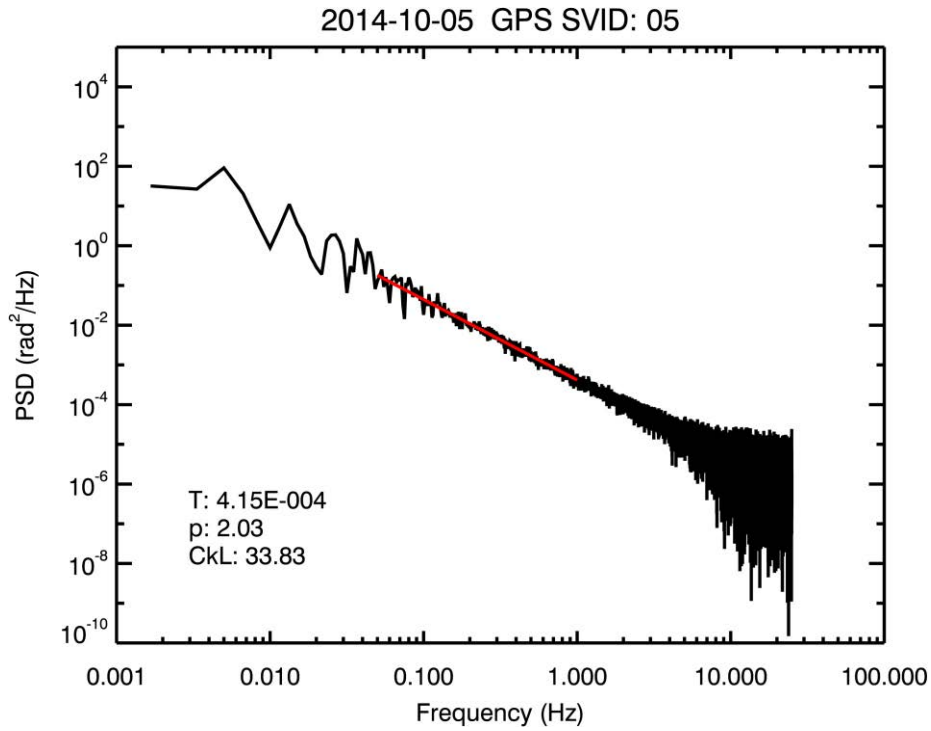


Figure 5.15: GPS phase power spectral density - GPS SVID 5 - 2014/10/05

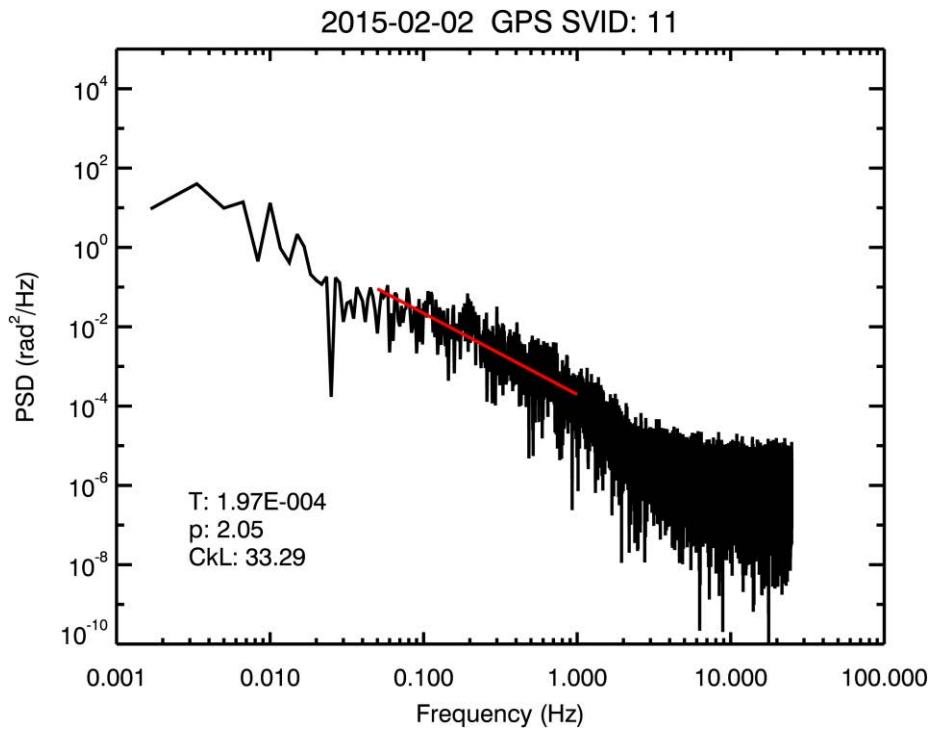


Figure 5.16: GPS phase power spectral density - GPS SVID 11 - 2015/02/02

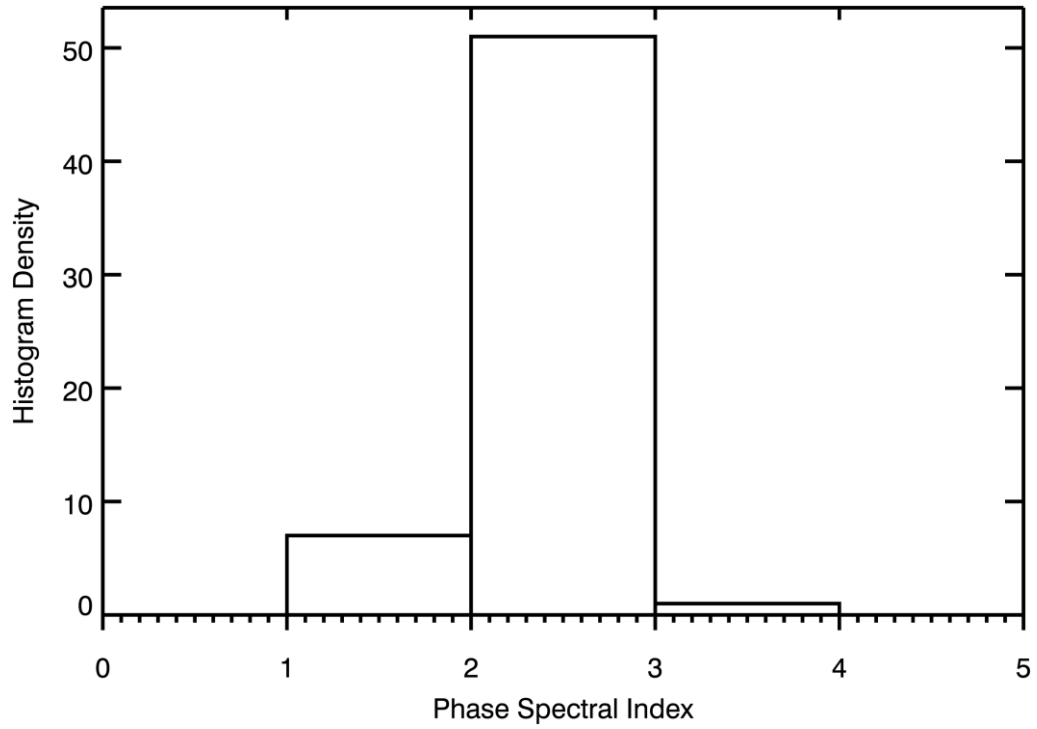


Figure 5.17: Histogram of p values from fit to measured GPS phase power spectral density.

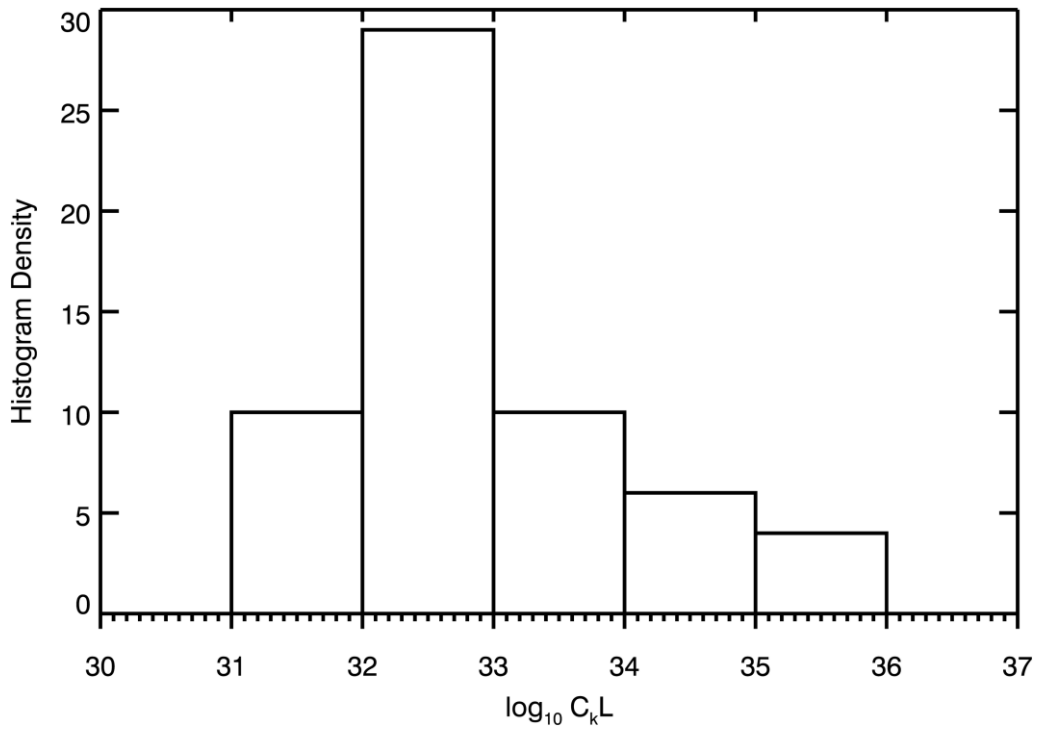


Figure 5.18: Histogram of $C_k L$ values from fit to measured GPS phase power spectral density.

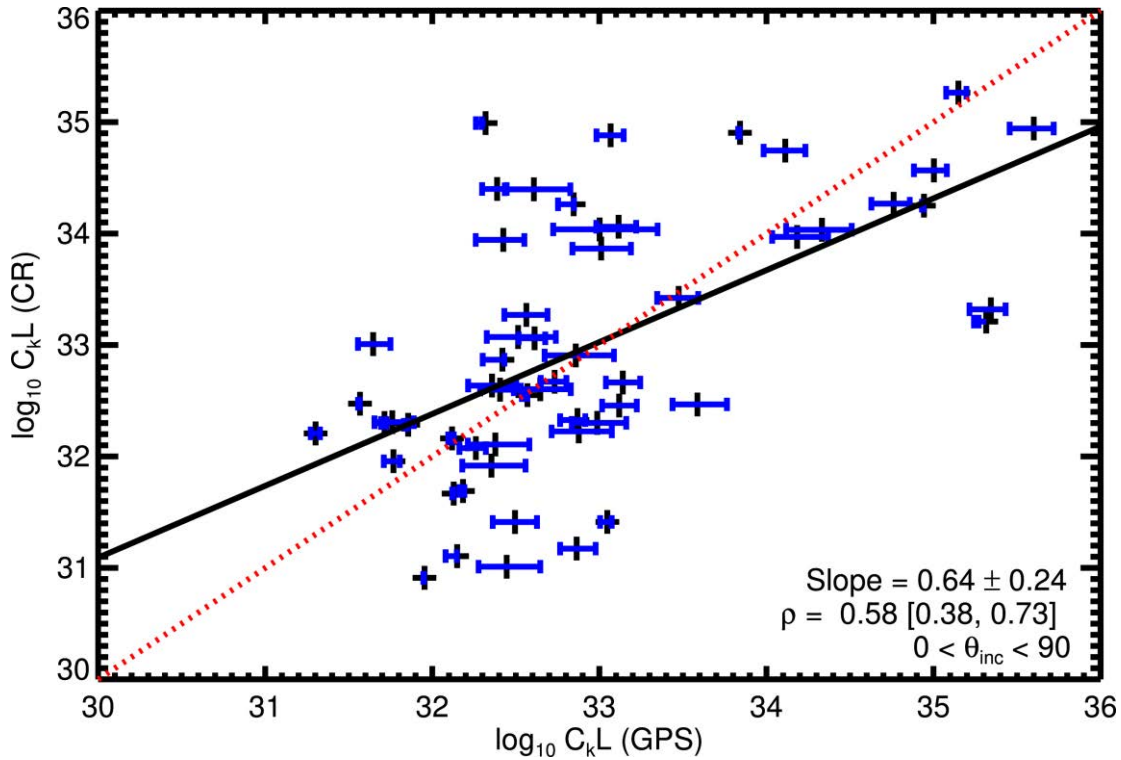


Figure 5.19: Comparison of CR and GPS values ($CR p \leq 5$).

A point-by-point comparison of the $C_k L$ values ($p_{CR} > 5$ excluded) for the two techniques is shown in Figure 5.19. Ideally the inter-comparison would follow the diagonal, but there is evidently a wide spread in the data points, with a least-squares linear fit slope of 0.62 ± 0.24 (the least absolute deviation slope is 0.73), and a Spearman's ρ correlation between the two datasets of only 0.58 (the upper and lower limits of the 95% confidence interval for this correlation are shown in brackets on the plot). The horizontal error bars describe the impact of varying the unknown ionospheric drift velocity from 50 ms^{-1} to 150 ms^{-1} .

On further inspection, it was noted that the numerous points in the top-left region (below 33 on the abscissa, and above 33 on the ordinate) were associated with measurements at incidence angles below 30° (that is close to the vertical). The low dynamic range observed in the corner reflector response at incidence angles below 30° (Section 5.4), suggests that the signal-to-clutter ratio is too low to accurately measure the sidelobe structure, and these points were excluded to give Figure 5.20.

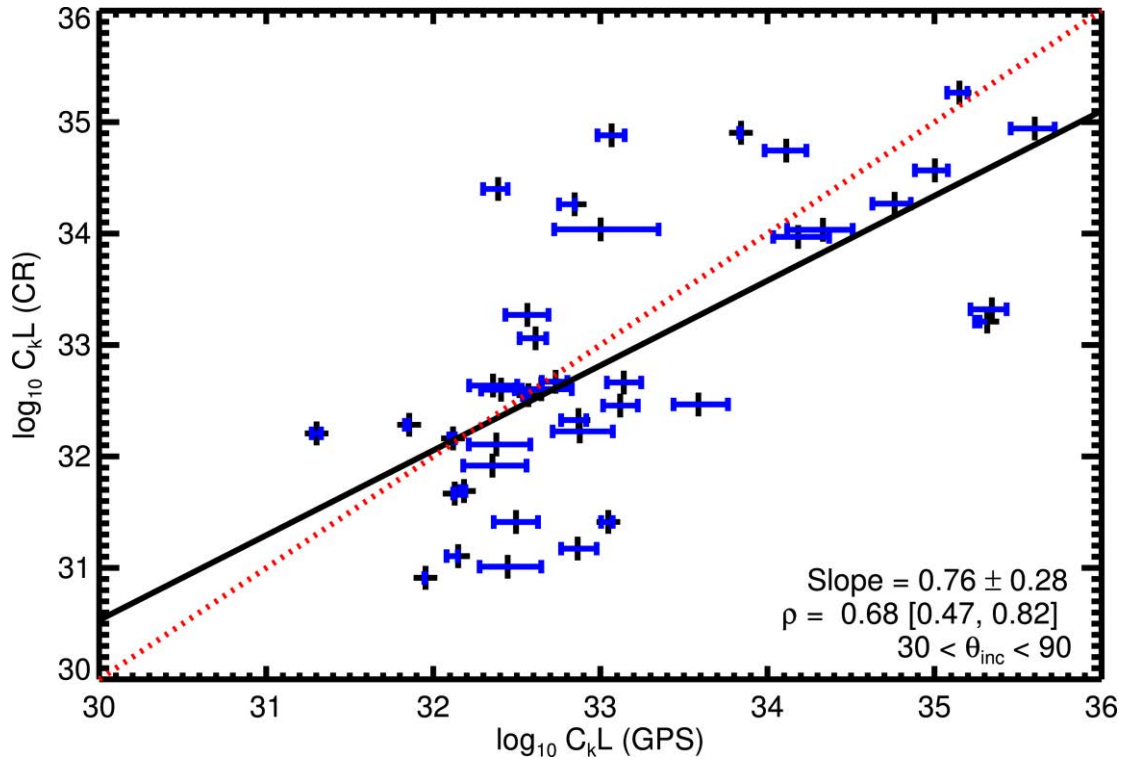


Figure 5.20: Comparison of CR and GPS $C_k L$ values (CR $p \leq 5$, incidence angles $> 30^\circ$).

The agreement between the two datasets is now much better, with a least-squares slope of 0.75 ± 0.28 (0.80 from a least absolute deviation fit), and an increased correlation coefficient of 0.66 . Some of the discrepancy is likely due to the IPP separation between the GPS and radar ray paths which varies between $100 - 500$ km. No correlation could be found between the IPP separation distance (either absolute or east-west component) and the magnitude of the difference between corresponding $C_k L$ values. However, this is probably not surprising. Section 4 has shown that spatial extrapolation of the PSF for L-band signals can only be achieved over a few kilometres. Likewise, *van de Kamp et al.* [2009] undertook measurements at 150 MHz and 400 MHz and found significant variations in signal phase over distance of 100 m to 10 km, which is indicative of temporal and spatial variations over the same distances. Much of the random error between the two data sets can thus be explained. However, the calibration error between the two data sets – which may be either a systematic offset or a problem with drawing conclusions from a

relatively small non-stationary data set - is perplexing. A number of investigations were consequently pursued.

Phase spectral index filtering

Figure 5.21 shows a comparison for the two sets of p values, subject to excising those points where $p_{CR} > 5$ and where the incidence angle is $> 30^\circ$.

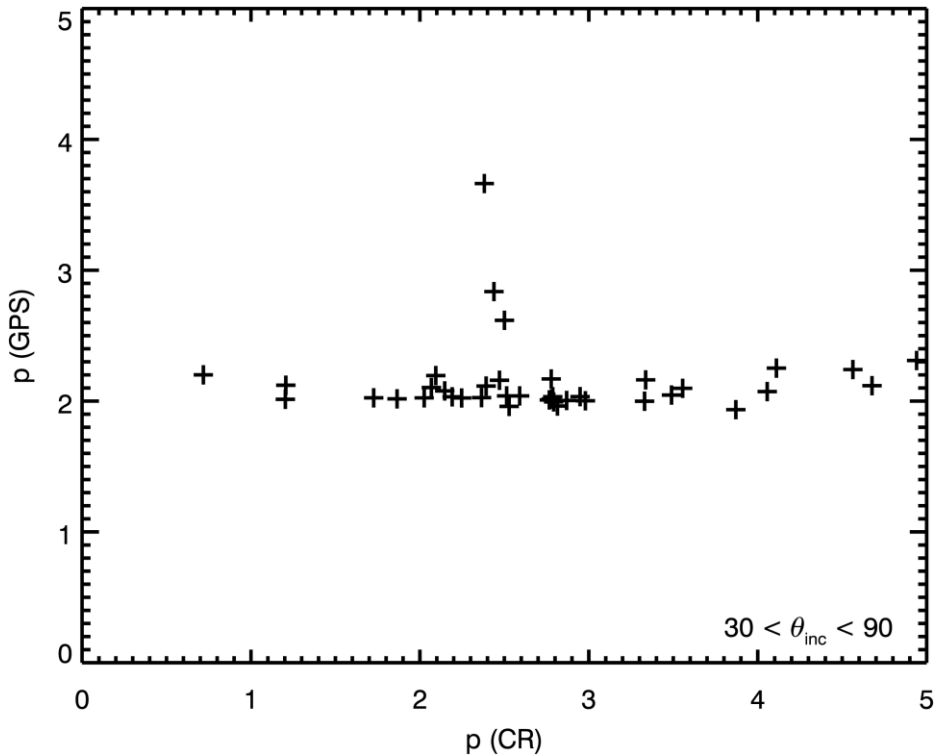


Figure 5.21: Comparison of CR and GPS phase spectral index, p -values (600 s phase power spectrum).

Surprisingly, the p_{GPS} values are almost all in the small range 1.9 - 2.3, whereas the p_{CR} values are spread across the range 0.0 - 5.0. Filtering the data further to include only C_kL values where p_{CR} lies between 1.5 and 3 was explored but is not helpful (Figure 5.22). This more aggressive filtering has mainly resulted in the removal of a cluster of points around $\log_{10}CkL_{GPS} = 33$ and $\log_{10}CkL_{CR} = 32$ and has had no significant impact on the relationship between the two datasets.

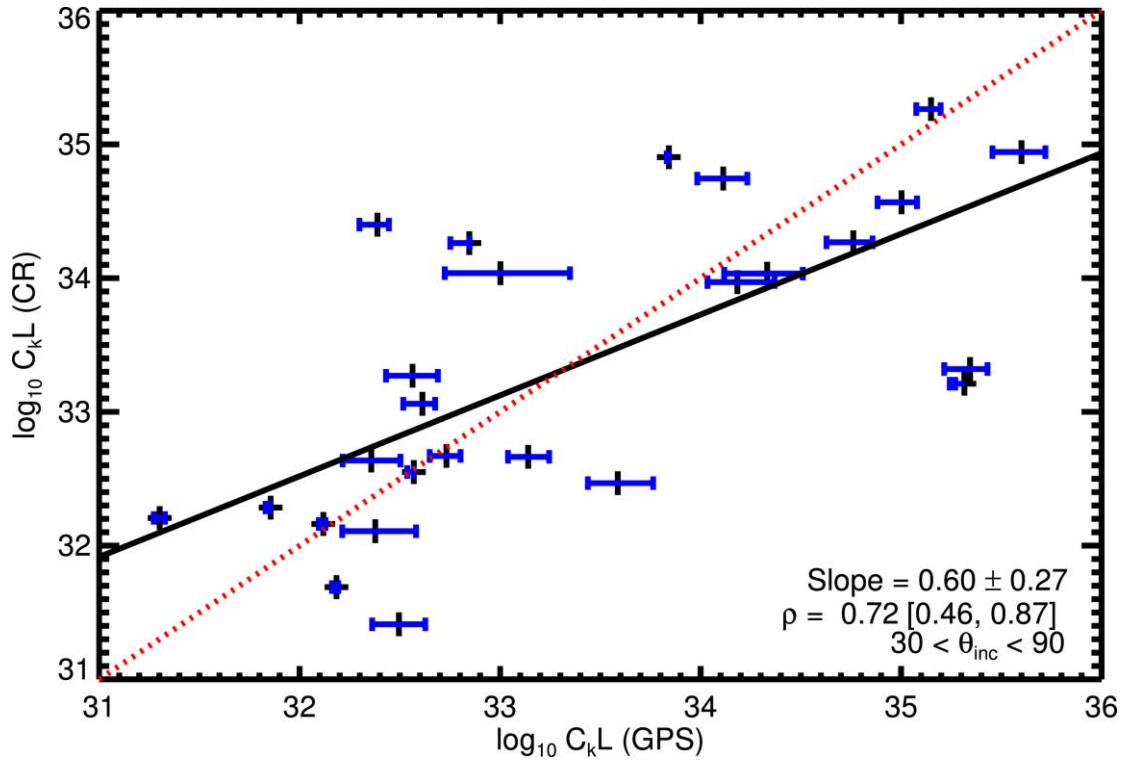


Figure 5.22: Comparison of CR and GPS $C_k L$ values ($CR p < 3$ and $CR p > 1.5$, incidence angles $> 30^\circ$).

Inspection of Outliers

There are some clear outliers in Figure 5.20, but examination of the GPS PSD for each of the outlying points showed no characteristics clearly different from the other PSDs. As noted previously, the slope of the GPS PSD (p_{GPS}), was very consistent across all of the data.

GPS Averaging Period

The effect of reducing the time over which the GPS PSD is calculated to (a more conventional) 30 s is shown in Figure 5.23. In contrast to Figure 5.21 there is now a spread of p_{GPS} values, as well as p_{CR} values.

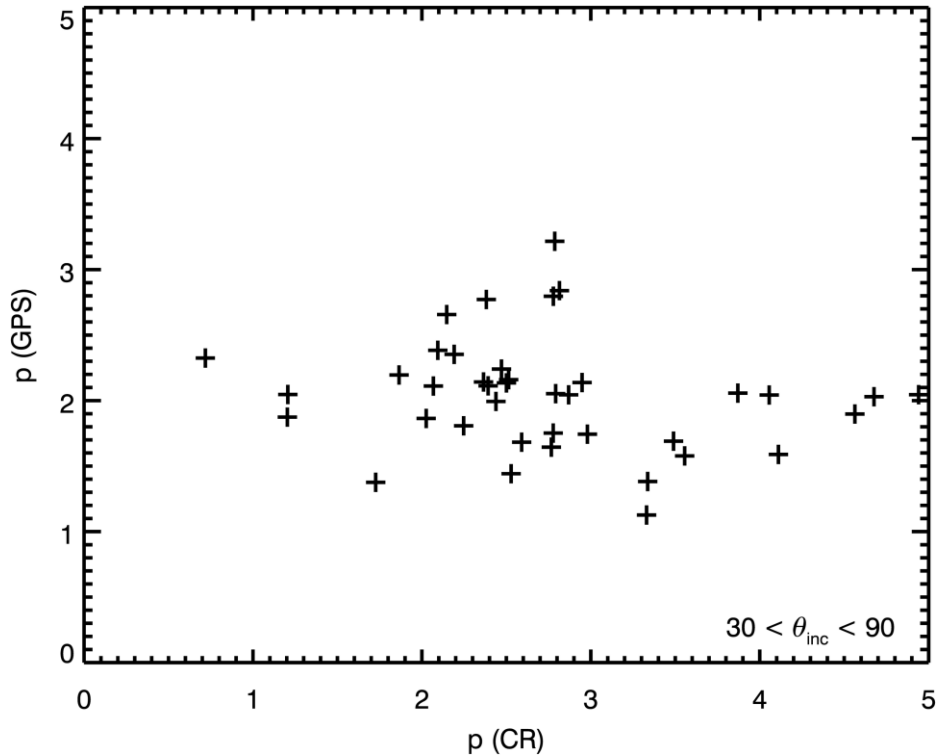


Figure 5.23: Comparison of CR and GPS phase spectral index, p , values (30 s phase power spectrum).

It is worth considering this in more detail. Regions of the ionosphere containing irregularities typically extend 100 km east-west and over 2000 km north-south direction [Aarons, 1982]. Within this region, the irregularities that cause scintillation extend over ~ 10 km or less [Basu *et al.*, 1978]. Numerous measurements have also shown that the median p value is ~ 2.5 [Basu *et al.*, 1987]. Consider first a static irregularity field where p is generally close to 2.5, but where a few irregularities exhibit a p value that is significantly higher or lower. Then the very long GPS integration time of 600 s used in this analysis (and corresponding to ~ 60 km) will wash out the extreme values to give an average close to the accepted value of ~ 2.5 . Only by reducing the integration time to 30s can these extreme p values be seen.

This, however, leaves a dichotomy. Given that the corner reflector PSDs and the 600 s GPS PSDs measure similar spatial scales they should exhibit similar ranges of p values. The solution lies in recognising that the composition of the ionosphere changes with time. The corner

reflector data is collected over ~ 10 s, and so conditions in the ionosphere are effectively frozen – there is no temporal variation. However, during the 600 s GPS data collection temporal evolution of the ionosphere is inevitable. Thus, the p_{GPS} values measured from 600 s of phase data converge towards mean values, and this accounts for the small range when compared to the p_{CR} values.

This discussion explains Figure 5.21 but it has further ramifications because it illustrates that the corner reflector GPS inter-comparison is not a wholly fair test because in the one case (the CR) the measurement is an instantaneous measurement across the 60 km aperture and in the other case (GPS) the measurement is an average over time and space.

5.6 Conclusions

An analytical description of the shape of the sidelobes of a SAR point spread function affected by ionospheric phase scintillation was successfully fitted to the measured sidelobe function.

The phase spectral index values produced by the fits are good, with most lying between 1 and 3 (Figure 5.10), with a median value of 2.61, consistent with previous measurements [*Basu et al.*, 1987]. Excluding any fits with $p > 5$ because they are anomalous, the $C_k L$ values ranged between 30.7 and 35.0, with the majority between 32-35, consistent with the values predicted by WBMOD, [*Secan et al.*, 1995; *Rogers et al.*, 2014b].

The $C_k L$ values derived from the corner reflector sidelobe fits were compared to $C_k L$ values derived from the phase spectrum of the GPS signal with a path closest to the SAR signal path. The correlation (Spearman's ρ) between the two sets of $C_k L$ values was 0.66. The reasons for the lack of strong correlation were explored, and an explanation proposed, based on both non-coincident ray paths and the temporal averaging of the GPS data as opposed to the near instantaneous snapshot of the ionosphere using the SAR. That there is a good correlation between the two techniques provides confidence in the $C_k L$ values derived from the measurement of the point spread function.

Whilst the closest GPS signal path to the SAR signal path was chosen (with the aim of maximising the correlation between the two signals), the separation of the two signal paths ranged between 100 – 500 km. Ionospheric irregularities are not correlated over these distances (the results given in Section 4.5 suggest a maximum correlation distance of ~ 3 km in the ionosphere).

The difference in temporal scales between the two techniques was considered as the cause of some of the discrepancy between the CR and GPS measurements because the irregularities that cause scintillation evolve on timescales of ~ 10 minutes [Basu *et al.*, 1978].

However, the contrasting temporal scales suggest that the CR measurements could offer a useful new perspective for ionospheric monitoring. GNSS monitoring effectively averages the signal received over a typical period of thirty to sixty seconds. In the equatorial regions ionospheric drift in the west-east direction can reach up to 100 ms^{-1} in the evening, and the irregularities extend to 100 km in the magnetic north-south direction, and 2000 km in the magnetic east-west. The GNSS IPP trajectory is typically inclined the long axis of the irregularities (along the geomagnetic field lines), and so a 30/60 second duration measurement will average down the estimates of $C_k L$.

Despite the SAR measurements taking only ten seconds to collect, the SAR IPP travels ~ 30 km across the phase screen in that time. However, as the satellite operates in a near polar orbit, and the irregularities are elongated in the north-south direction, this should cause little averaging.

The CR-derived $C_k L$ measurements appear to be sensitive down to a $\log C_k L$ of ~ 31 . The upper limit is not clear from these results, but the theory underpinning this approach assumes weak scattering, and the same applies for the GPS measurements. The data shown in Figure 19 of [Carrano *et al.*, 2012a] shows that the crossover from weak to strong scatter occurs around $C_k L = 5 \times 10^{34}$ for L-band systems. It might therefore be expected that this new L-band SAR technique will exhibit a similar limitation.

A potential limitation for the wide application of this technique is the use of large (5 m) corner reflectors. It would clearly be more convenient to use smaller corner reflectors, or indeed corner reflectors of opportunity. The RCS of the trihedral reflector scales as length to the fourth power,

and there is a linear relationship between T_{SLF} and $C_k L$ (Equation (5.14)). If the length of the corner reflector were halved to 2.5 m, the threshold sensitivity would increase by 1.2 to a $\log C_k L$ of ~ 32 - a still useful lower threshold.

This technique is in the early stages of validation, but it potentially offers several new scientific opportunities. For example, an array of small, cheap passive corner reflectors distributed over a wide (10 km or more) area might enable the measurement of the distribution of irregularities within the ionosphere. This would present a relatively inexpensive alternative to current methods of achieving this, such as incoherent scatter radar.

6 DERIVING IONOSPHERIC SCINTILLATION PARAMETERS FROM SAR SIGNALS – IMAGES

Section 5 has shown how a direct measurement of the SAR point spread function (PSF) can be used to estimate the strength of ionospheric turbulence, $C_k L$. However, this technique is dependent on the existence of a bright point target in the image such as a corner reflector (CR) – a severe practical restriction. What is needed is a SAR technique which enables the measurement of $C_k L$ without recourse to the deployment or identification of point targets.

As a consequence of its impact on the SAR PSF phase scintillation can reduce the image contrast of space-based SAR operating at L-band and below and can even defocus the entire image [Rino and Gonzalez, 1983; Belcher and Cannon, 2014]. Belcher and Cannon [2013] quantified this degradation of the PSF through an analysis of the radar clutter statistics and related those statistics to $C_k L$. In the undisturbed case these statistics are controlled by the statistics of the ground clutter only; in the disturbed case the statistics are an aggregation of the ground clutter and the impact that the ionospheric irregularities have on the SAR PSF.

This chapter will test the relationship developed by Belcher and Cannon [2013] to determine $C_k L$ from images of natural clutter in PALSAR-2 images of Ascension Island, which lies in the South Atlantic. This requires the comparison of two images, one displaying the effects of scintillation and a ‘baseline’ image unaffected by scintillation. The disturbed clutter statistics will be compared with those from an image unaffected by scintillation, and the results used to derive $C_k L$. These values will then be compared with $C_k L$ values derived from measurements of the SAR PSF derived from two trihedral corner reflectors deployed on the island and already reported in the previous chapter.

The technique requires regions where the ground clutter is homogeneous and random, for example grass, desert and natural woods and forests. These are of course widespread, and thus this technique may provide a new method for scintillation monitoring.

6.1 Statistics of natural clutter

Images of natural radar clutter are well described using a product, or compound model [Ward, 1981]. Under this approach, the imaged clutter is modelled as the product of the slowly-varying gamma distributed radar cross-section (RCS), with a zero mean complex Gaussian. The complex Gaussian represents the ‘speckle’ noise that is inherent in coherent imaging systems [Oliver, 1991]. When the gamma distribution RCS is combined with the speckle contribution under the product model, the intensity of the clutter in the image is described by a K-distribution [Oliver and Quegan, 2004a], with an order parameter ν and mean μ . The K-distribution has a probability density function (PDF) given by:

$$p(I) = \frac{2b}{\Gamma(\nu)} (\sqrt{bI})^{\nu-1} K_{\nu-1}(2\sqrt{bI}) \quad (6.1)$$

where $b = \nu/\mu$, $\Gamma(x)$ represents the gamma function, and $K_n(x)$ represents the modified Bessel function of the second kind.

The order parameter ν determines the ‘smoothness’ of the distribution. As ν tends to infinity the PDF becomes a negative exponential distribution, indicating that the PDF is completely dominated by the speckle intensity. As the order parameter reduces, more intensities occur at higher values, and so the image is ‘spikier’. This corresponds with the visibility of the underlying terrain structure in addition to the speckle contribution. Figure 6.1 illustrates the effect of the order parameter on the shape of the K-distribution.

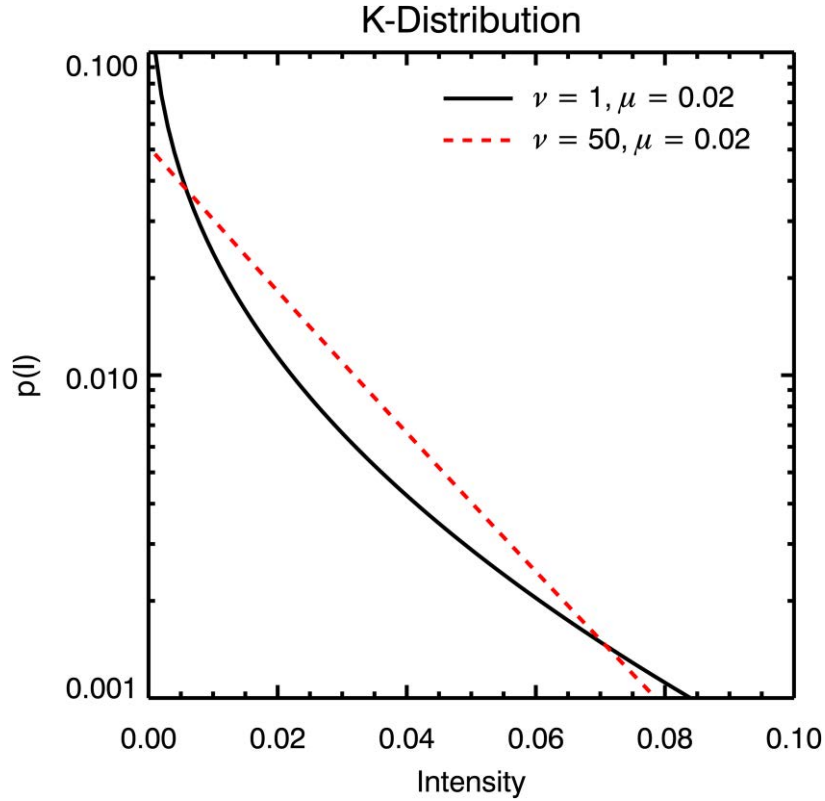


Figure 6.1: Effect of order parameter on K-distribution

6.2 Effect of the ionosphere on clutter statistics

The final image produced by a SAR is the convolution of the ionospherically degraded PSF with the underlying RCS of the scene. When the ionosphere is quiescent, and there is no phase scintillation, the PSF is a delta-like function, and thus it has no impact on the image. When the ionosphere is disturbed the phase scintillation introduces sidelobes to the PSF (see Section 5 and Appendix C for a full theoretical description). Because the scene is convolved with the ionospheric PSF, this means that each resolution cell, or pixel, in the image contains contributions from adjacent and close resolution cells. In an area of natural clutter this means that the measured cell intensity is the sum of samples from a gamma distribution.

The characteristic function (the Fourier transform of the PDF) of the gamma distribution is:

$$C_F(\omega) = (1 - i\omega\mu)^{-\nu}. \quad (6.2)$$

Adding two independent samples from the same gamma distribution results in a gamma-distributed random variable with the same mean, but a doubled order parameter when compared to the original gamma distribution. That is:

$$C_{X+Y}(\omega) = C_X(\omega)C_Y(\omega) = (1 - i\omega\mu)^{-2\nu}. \quad (6.3)$$

Assuming an ionospherically degraded PSF consisting of a delta function mainlobe and Gaussian sidelobes [Belcher and Cannon, 2014], each pixel is the sum of contributions from adjacent and close resolution cells the order parameter ν is modified by an amount dependent on the number of contributing pixels (samples), i.e. $\nu_{modified} = \nu n_{samples}$. The number of contributing samples is dependent on the correlation statistics of the underlying clutter, and the level of the sidelobes of the ionospherically degraded PSF. The correlation length, l_r , of the underlying clutter dictates at what distance a new independent sample of the gamma distribution occurs, whilst the sidelobe level governs the distance at which nearby resolution cells cease contributing to a given cell. Thus a measure of the number of samples can be obtained by integrating over the normalised sidelobe function (to give the number of resolution cells that contribute to a given cell), and dividing by the correlation length in resolution cells (to provide the number of independent samples provided by those resolution cells). The integral over the sidelobe function is called σ_{SLF}^2 ,

$$\sigma_{SLF}^2 = \int_{-\infty}^{\infty} |SLF(r)|^2 dr. \quad (6.4)$$

Thus, in the disturbed case the disturbed order parameter, ν_d is related to the undisturbed, ν_u , by:

$$\nu_d = \nu_u \left(1 + \frac{\sigma_{SLF}^2}{l_r} \right). \quad (6.5)$$

Here it has initially been assumed that every sample added to the sum is independent of the others, i.e. the correlation length l_r is set to 1.

Since power must be conserved between the disturbed and undisturbed point spread function, any increase in sidelobe levels due to the ionosphere must result in a corresponding loss of power from the mainlobe. *Belcher and Cannon* [2013] show that this theoretically results in a reduction in the mean clutter intensity, but find that this effect is counteracted by a mean increase in intensity due to the addition of ionospheric noise. Consequently, *Belcher and Cannon* [2013] find that combining the ionospherically disturbed gamma distribution with the speckle contribution under the product model, results in an a K-distribution of intensity in the image, with an unchanged mean and an identically increased order parameter, relative to the undisturbed case (see Appendix C for a more detailed theoretical description).

Consequently, by selecting an appropriate part of an image and by measuring both the order parameter when the ionosphere is undisturbed (to provide a reference value) and the order parameter when the ionosphere is disturbed, the disturbed sidelobe function can be calculated. This can, in turn, be used to determine $C_k L$ by considering the following.

Section 5, following the work of *Rino* [1979a] and *Belcher and Rodgers* [2009] described the analytical form of the sidelobe function:

$$\langle |SLF(r)|^2 \rangle = T_{SLF} \left(\sqrt{r_0^2 + r^2} \right)^{-p}. \quad (6.6)$$

Here T_{SLF} is a constant defined by:

$$T_{SLF} = 4\gamma \left[\kappa_C^{1-p} G \sec(\theta) (r_e \lambda)^2 \frac{\sqrt{\pi} \Gamma\left(\frac{p}{2}\right)}{(2\pi)^2 \Gamma\left(\frac{p+1}{2}\right)} \left(\frac{2\pi}{1000}\right)^{p+1} \right] C_k L, \quad (6.7)$$

where γ is a constant that accounts for the difference between the velocity of the radar, and the effective velocity of the signal ionospheric pierce point (IPP) as it travels across the phase screen [Belcher and Cannon, 2014], $\kappa_C = \frac{2\pi}{L_C}$, L_C is the length of the SAR IPP track on the ionospheric phase screen, G is a factor that depends on the propagation geometry, θ is the incidence angle to the ionosphere, r_e is the classical electron radius, λ is the wavelength of the signal, p is the power spectral index of the power spectrum describing the phase scintillation, and $C_k L$ is defined as the strength of the vertically-integrated spatial spectrum of the irregularities at a scale size of 1 km.

Assuming that the sidelobe function is symmetric, and using the identity:

$$\int_0^{\infty} \frac{dx}{(a^2 + x^2)^{\frac{p}{2}}} = \sqrt{\pi}(a^2)^{1-\frac{p}{2}} \Gamma\left(\frac{p-1}{2}\right), \quad (6.8)$$

it can be shown that σ_{SLF}^2 is directly proportional to $C_k L$ [Belcher and Cannon, 2013]:

$$\sigma_{SLF}^2 = 4\pi\gamma G \sec \theta (r_e \lambda_0)^2 \frac{\Gamma\left(\frac{p-1}{2}\right)}{\Gamma\left(\frac{p+1}{2}\right)} 10^{-6} \left(\frac{l_0}{1000}\right)^{p-1} C_k L. \quad (6.9)$$

Thus, measuring the change in the observed order parameter of the intensity distribution of natural clutter between an ionospherically disturbed and undisturbed SAR image allows the estimation of σ_{SLF}^2 , and hence $C_k L$.

6.3 PALSAR-2 Data

The images used in this chapter were collected using PALSAR-2, the technical characteristics of which are described in Section 5. The 14-day repeat cycle of the ALOS-2 orbit facilitates the image comparison technique described above – for a given ground track, the radar images the same area. For the purposes of measuring the clutter statistics three areas of natural clutter were

identified on Ascension Island referred to as west, east and central and marked on the map (Figure 6.2) as blue circles.

The SAR data are the same as those previously analysed in the context of the corner reflectors (Section 5) and are marked as red triangles in Figure 6.2. The clutter locations to the west and east of the island were chosen primarily for their proximity to these corner reflectors, and secondarily according to areas of appropriate (i.e. homogenous and lacking in underlying features) terrain. The clutter areas were all rocky in nature, with little vegetation.

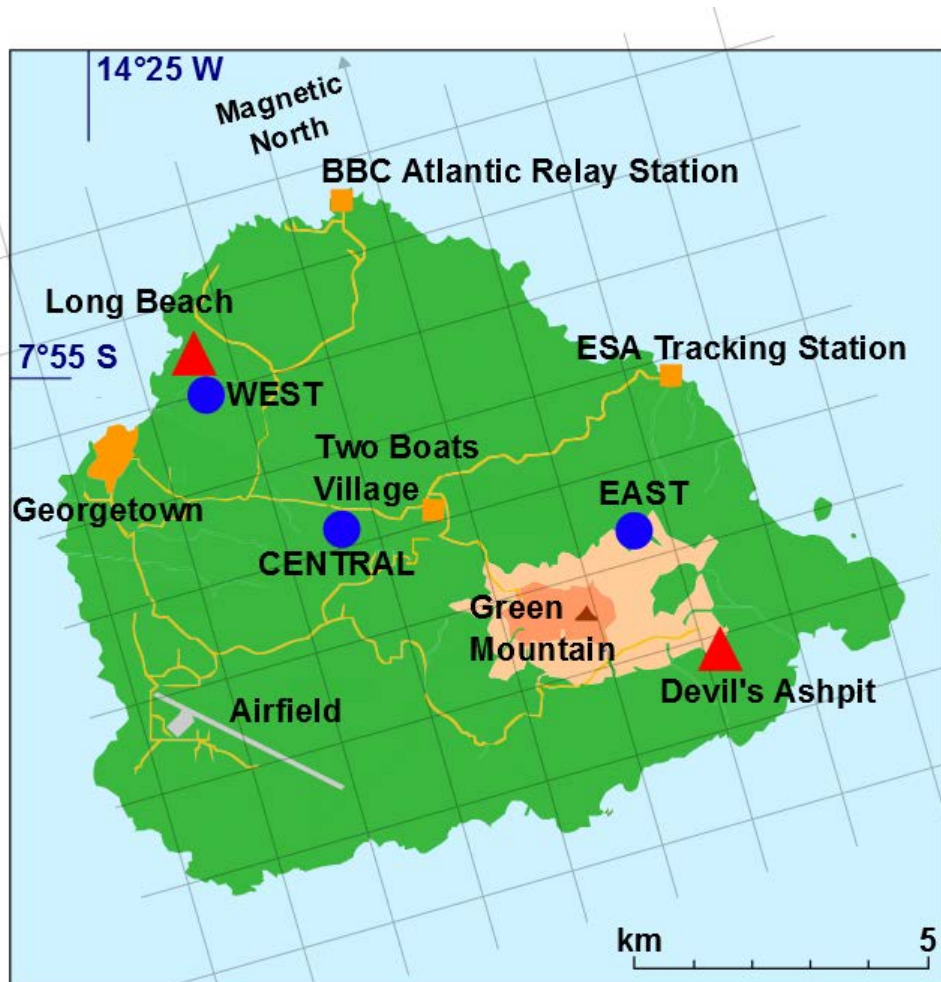


Figure 6.2: Map of Ascension Island showing clutter locations (blue circles indicate selected areas of clutter and the red triangles indicate the location of the corner reflectors).

6.4 Data Analysis

6.4.1 Clutter measurements

A total of 76 images of Ascension Island were collected. Of these, 61 were recorded with the satellite looking approximately east across the island (illuminating the west corner reflector), and 15 looking west (illuminating the east corner reflector).

The clutter areas were defined by the latitude and longitude of the bottom left corner (Table 6.1), and had a side length of 200 x 200 resolution cells. The complex pixel values were converted to intensity values, and sampling increased by a factor of two in the along-track direction to provide Nyquist-sampled intensity values to give a 200 x 400 array of intensity values.

Table 6.1: Locations of clutter areas on Ascension Island

Clutter Location	Position of bottom left corner	Distance to	
		West CR	East CR
West	-7.916414, -14.400222	312 m	9170 m
Central	-7.939600, -14.375635	4041 m	5685 m
East	-7.929528, -14.336634	7407 m	2963 m

Example images of the clutter areas are shown in Figure 6.3 and Figure 6.4 (west clutter), Figure 6.5 and Figure 6.6 (central clutter), and Figure 6.7 and Figure 6.8 (east clutter). For each area the former image is unaffected by scintillation, and the latter is shows moderate effects of scintillation. The 200 x 400 sample area is defined by the red box in each image (square as the images have been resized to account for the oversampling in the along-track direction). The pixel values in these images have undergone histogram equalization and scaling for ease of viewing so are not a true reflection of the measured intensity values.

The image pairs for each of the clutter areas clearly show the visual impact scintillation can have on the SAR image, with significant blurring occurring in the latter of each pair. The effect on the distribution of intensity values is shown in Figure 6.9 and Figure 6.10. Figure 6.9 shows the distribution of intensity values from the clutter area shown in Figure 6.3 (no scintillation), whilst Figure 6.10 shows the intensity distribution corresponding with Figure 6.4 (affected by moderate scintillation). The blue dashed line shows the best-fit (minimising the chi-squared statistic) K-distribution to the measured values (red bars), with the fitted order parameter ν and the measured mean intensity μ for each image shown on the plot.

The effect of scintillation has clearly been to increase the proportion of pixels with higher intensity values, rather than a large majority concentrated at the lowest values. This is reflected in an increase in the order parameter of the fitted K-distribution from 1.5 to 7.0.

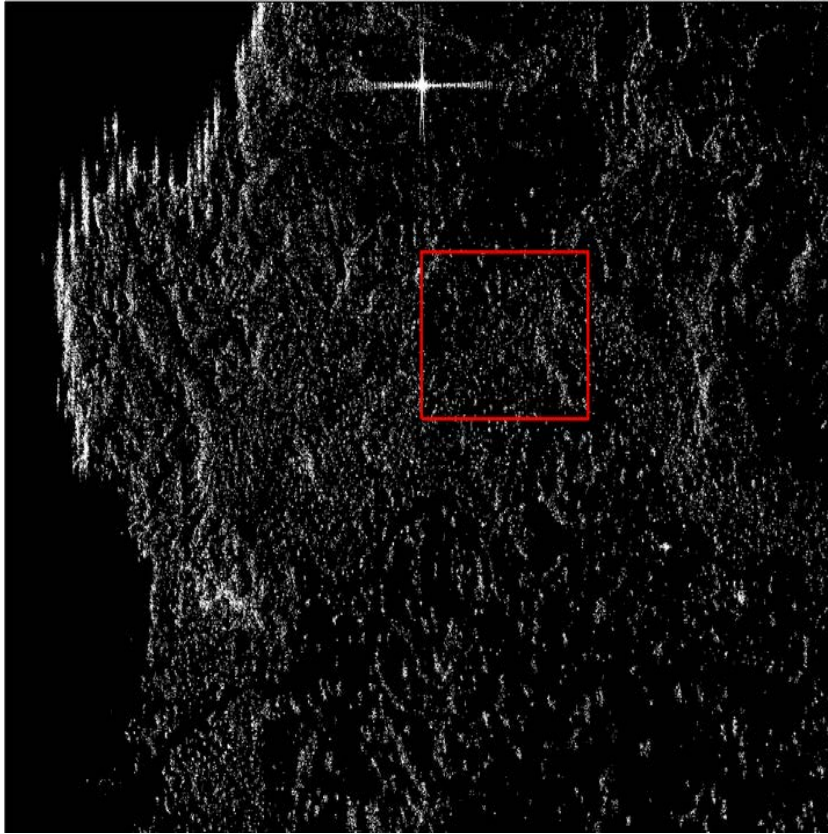


Figure 6.3: West clutter area (2014/08/18, no scintillation).

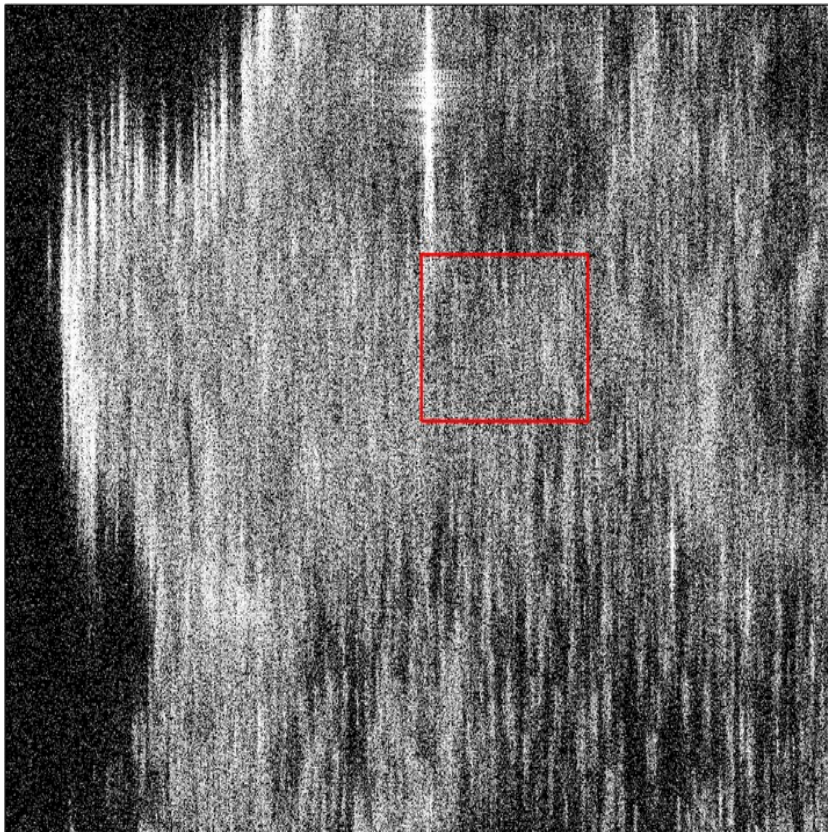


Figure 6.4: West clutter area (2014/10/27, moderate scintillation).

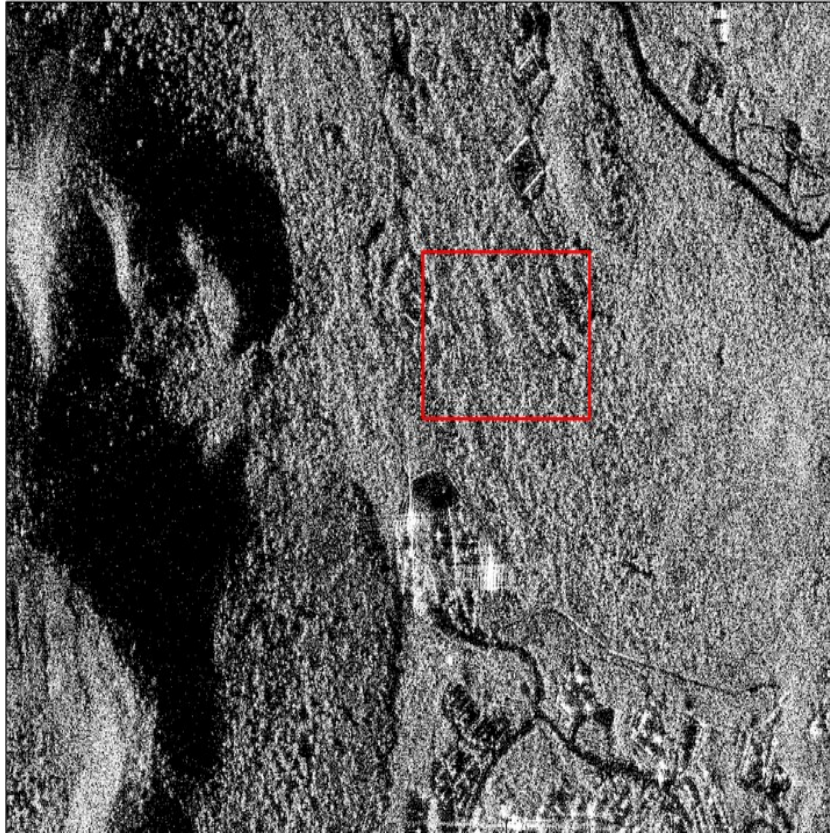


Figure 6.5: Central clutter area (2014/08/18, no scintillation).

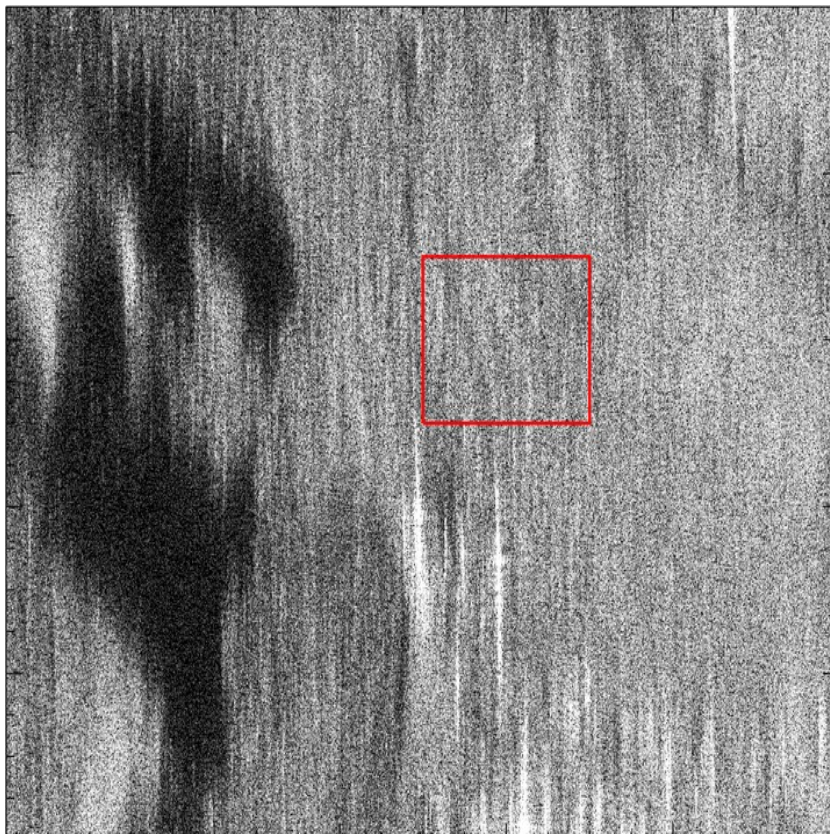


Figure 6.6: Central clutter area (2014/10/27, moderate scintillation).

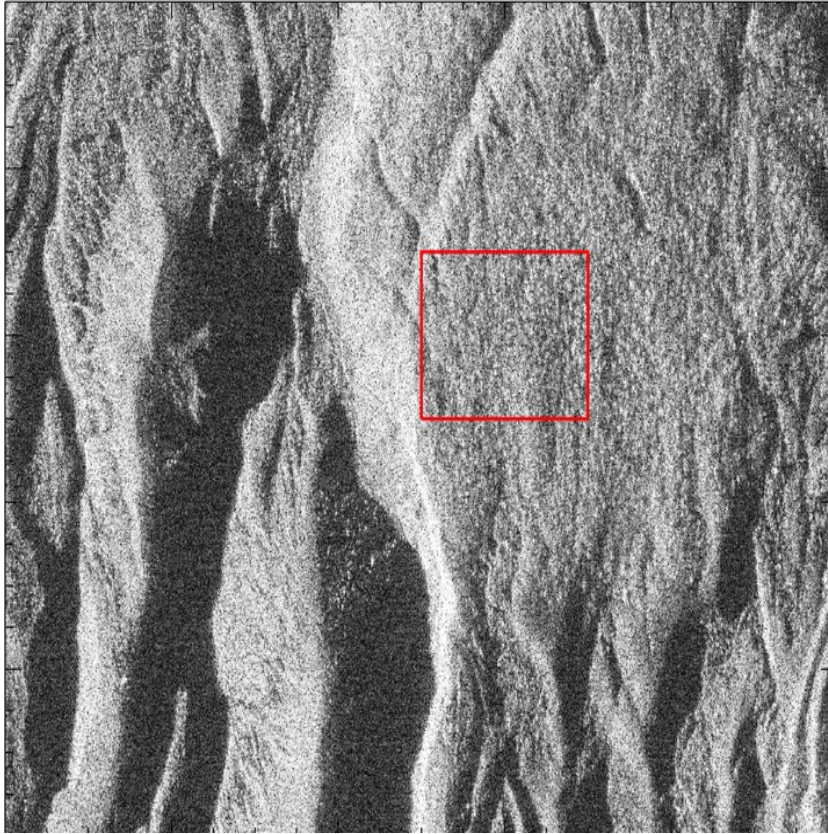


Figure 6.7: East clutter area (2014/08/18, no scintillation).

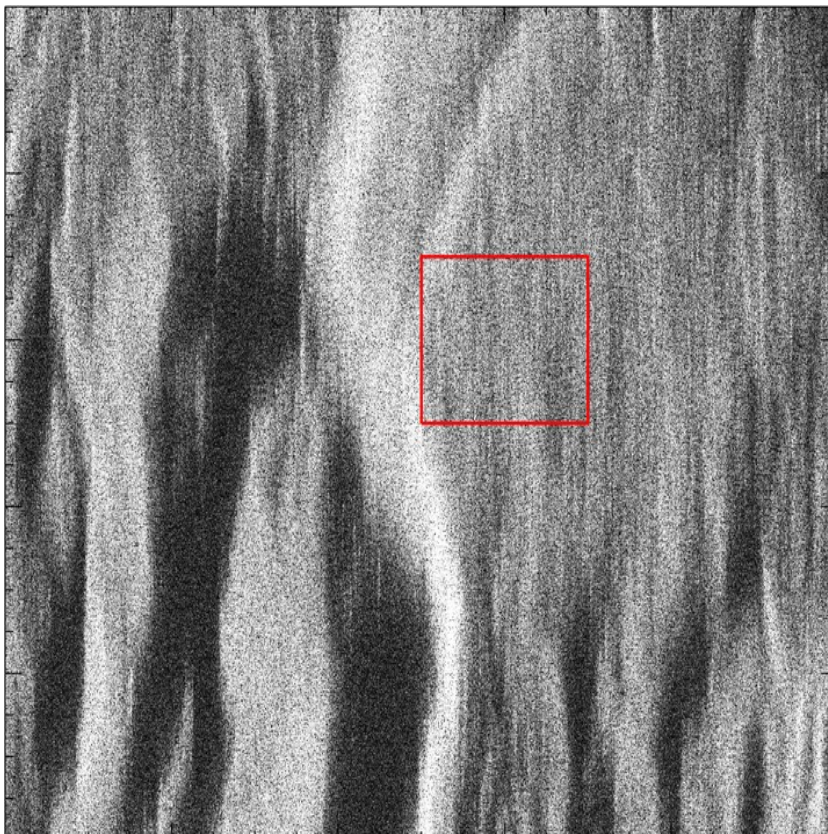


Figure 6.8: East clutter area (2014/10/27, moderate scintillation).

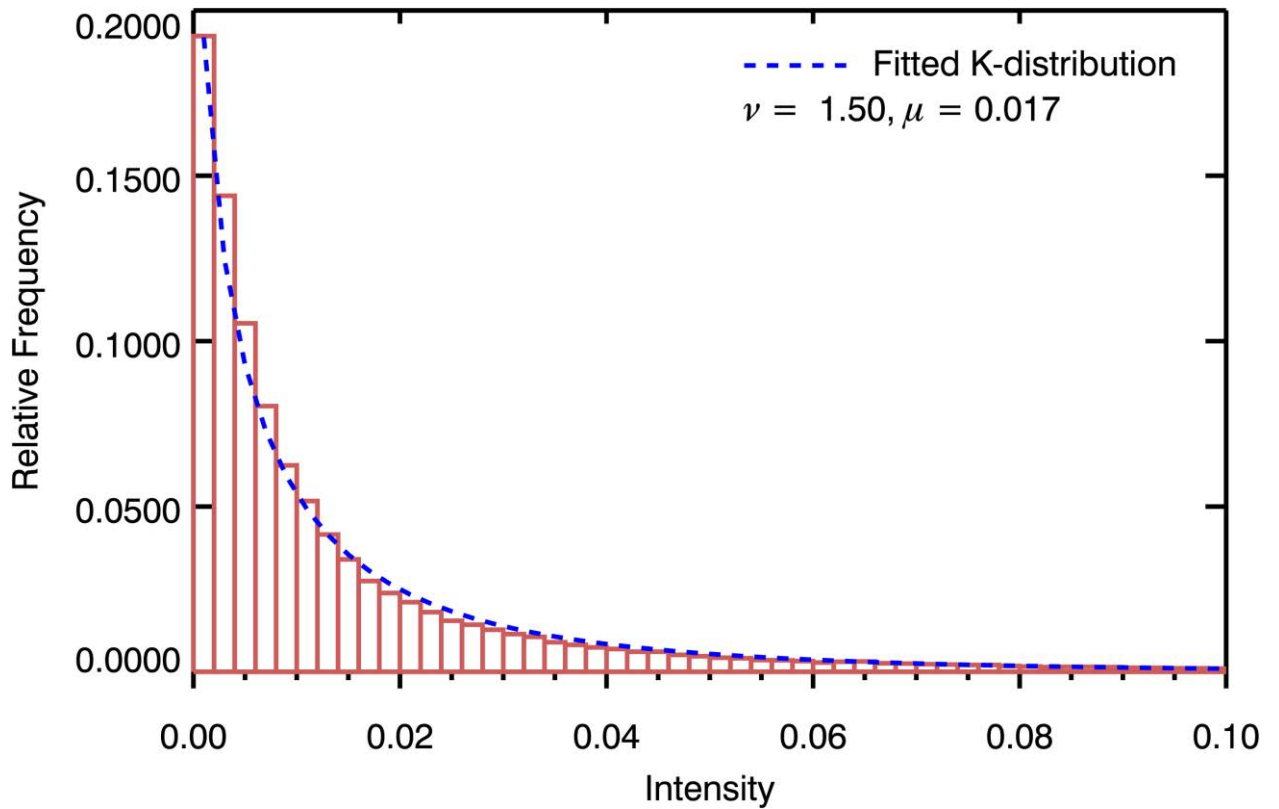


Figure 6.9: Histogram of west clutter intensity values (Figure 6.3, 2014/08/18, no scintillation)

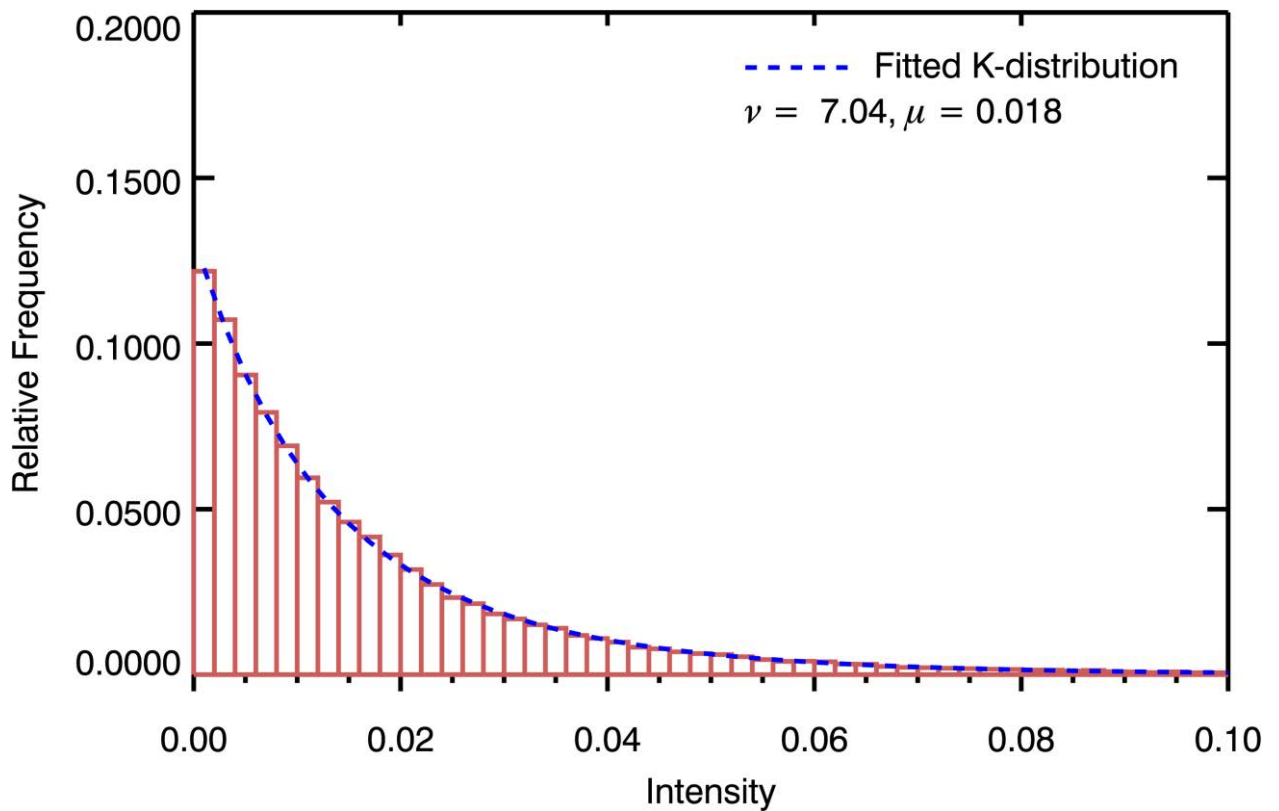


Figure 6.10: Histogram of west clutter intensity values (Figure 6.4, 2014/10/27, moderate scintillation)

The order parameter of the observed clutter intensity in each image was estimated using the natural-log method of *Blacknell and Tough* [2001] for ease of computation:

$$v = \left[\frac{\langle I \log I \rangle}{\langle I \rangle} - \langle \log I \rangle - 1 \right]^{-1}. \quad (6.10)$$

From Equation (6.5), calculating the ratio between the order parameter of an image affected by scintillation v_d , and the order parameter of an image unaffected by scintillation v_u , allows the calculation of σ_{SLF}^2 , and hence $C_k L$ (Equation (6.9)):

$$\frac{v_d}{v_u} - 1 = \sigma_{SLF}^2. \quad (6.11)$$

To do this for several images requires the identification of a reference image unaffected by scintillation that can act as a baseline measure of the order parameter (v_u).

The images (with fixed pixel sizes) were recorded at a range of incidence angles (Table 6.2) and consequently the corresponding areas have slightly different sizes. As such, only data from the same incidence angles can be used to calculate the order parameter ratio. Since the order parameter of an undisturbed image should be lower than any disturbed image, the baseline order parameters for each clutter area, at each incidence angle, were chosen from the image that provided the lowest average order parameter from the three clutter patches at that incidence angle.

The $C_k L$ resulting from the measured σ_{SLF}^2 for each incidence angle was calculated from Equation (6.9), using a p value of 2.5, as suggested by previous measurements of the ionosphere [*Basu et al.*, 1987], and an outer scale size l_0 of 10 km. The G factor was calculated according to the appendix of *Rino* [1982], and the γ factor from the approach described in *Belcher and Cannon* [2014].

Table 6.2: Incidence angle distribution for PALSAR-2 dataset.

SAR look direction	Incidence angle (°)	Image count
East (West CR)	12	9
	29	9
	42	9
	52	9
	29	10
	65	7
	70	8
West (East CR)	24	3
	29	4
	57	3
	64	2
	69	3

Histograms describing the C_kL distribution for each of the clutter areas are shown in Figure 6.11 (west clutter), Figure 6.12 (central clutter) and Figure 6.13 (east clutter). The estimated $\log_{10} C_kL$ values from each of the areas range from 29.3 to 34.0.

Each of the C_kL distributions shows a similar spread, with the majority of the values falling between 31.0 and 32.5. However, in comparison with the west clutter, the central and the east clutter show more values in the upper range of 31.5 to 32.5.

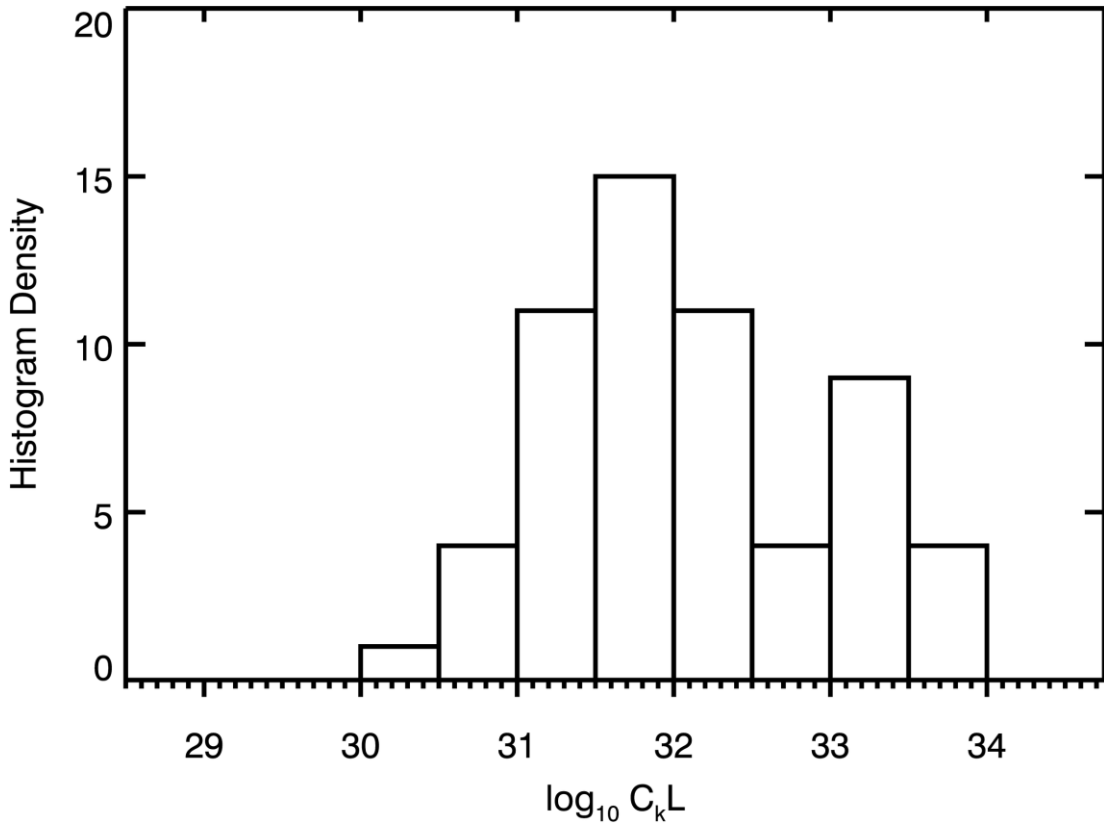


Figure 6.11: $C_k L$ distribution from west clutter.

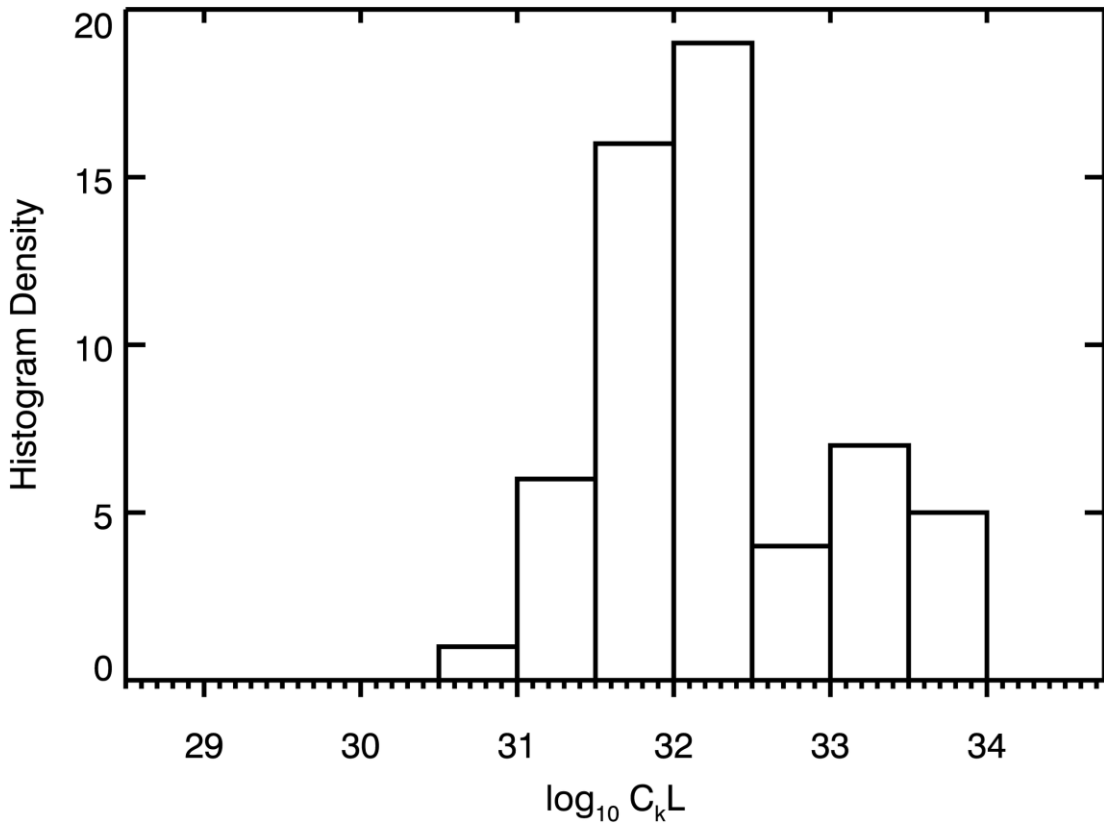


Figure 6.12: $C_k L$ distribution from central clutter.

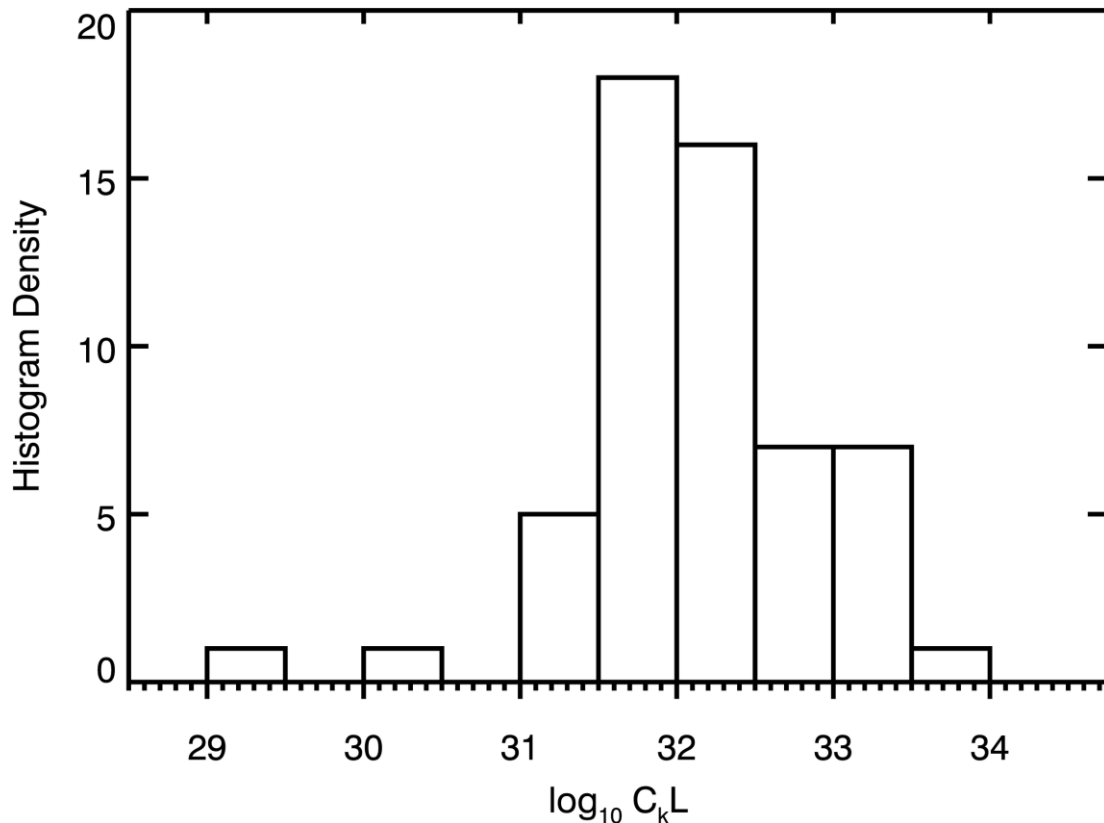


Figure 6.13: $C_k L$ distribution from east clutter.

6.5 Comparison with corner reflector derived $C_k L$

Section 5 described a method of estimating $C_k L$ using measurements of the SAR point spread function made using two trihedral corner reflectors. The corner reflector measurements utilised the same dataset as that used for these clutter measurements, and thus a comparison between the two techniques can be made. The $C_k L$ comparison for each of the clutter areas is shown in Figure 6.14, Figure 6.15 and Figure 6.16, with a $y=x$ relationship shown as a red dashed line.

Data for which p_{CR} (the p value produced from the corner reflectors) is greater than 5 has been excluded, as such values indicate ionospheric distortion below the measurement capability of the corner reflector technique (Section 5). This provided between 47 and 49 points for each plot (the number of points differs between clutter areas as the undisturbed order parameter is not necessarily the lowest order parameter measured for that area).

The distribution of the points for each plot is similar. The C_kL derived from the west clutter shows good correlation (Spearman's $\rho = 0.84$, with the 95% confidence interval values shown in brackets on the plot), with the corner reflector C_kL , but the east and central data sets are not as well correlated (ρ of 0.71 and 0.64 respectively). In all three cases the average C_kL is lower than the corresponding corner reflector C_kL .

Inspection of the data showed that the points clustered in the bottom right of each plot generally corresponded with data collected at incidence angles less than 30° . Section 5 also noted that corner reflector measurements at incidence angles less than 30° had a low signal-to-noise ratio, and did not compare well with independent GPS measurements of the ionosphere. Excluding these points from the analysis leaves ~ 32 points in each plot.

The effect of excluding data with incidence angles less than 30° is shown in Figure 6.17, Figure 6.18 and Figure 6.19. The removal of the points noted above has reduced the spread of the points significantly for all of the datasets. As such, the correlation between the corner reflector values and the clutter values is much improved, with ρ values of 0.91, 0.90 and 0.75 for the west, central and east clutter measurements respectively. However, the points are still below the $y=x$ line.

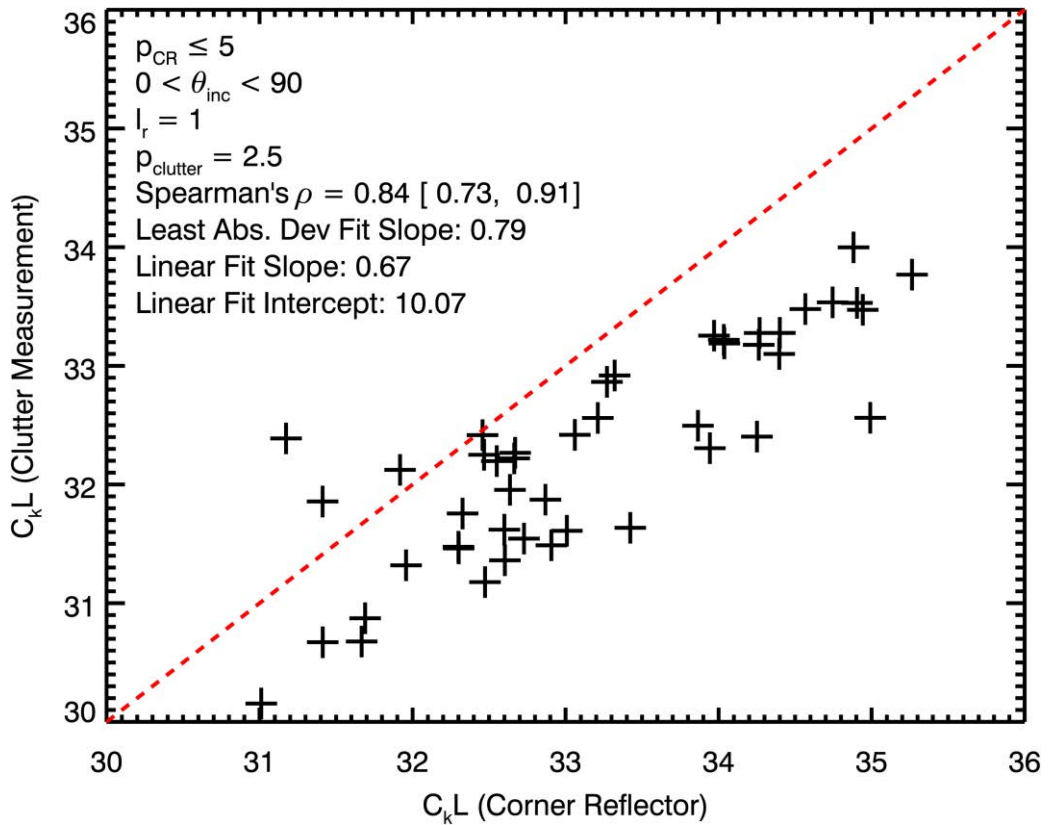


Figure 6.14: Corner reflector, clutter C_kL comparison - west clutter - $p_{CR} < 5$.

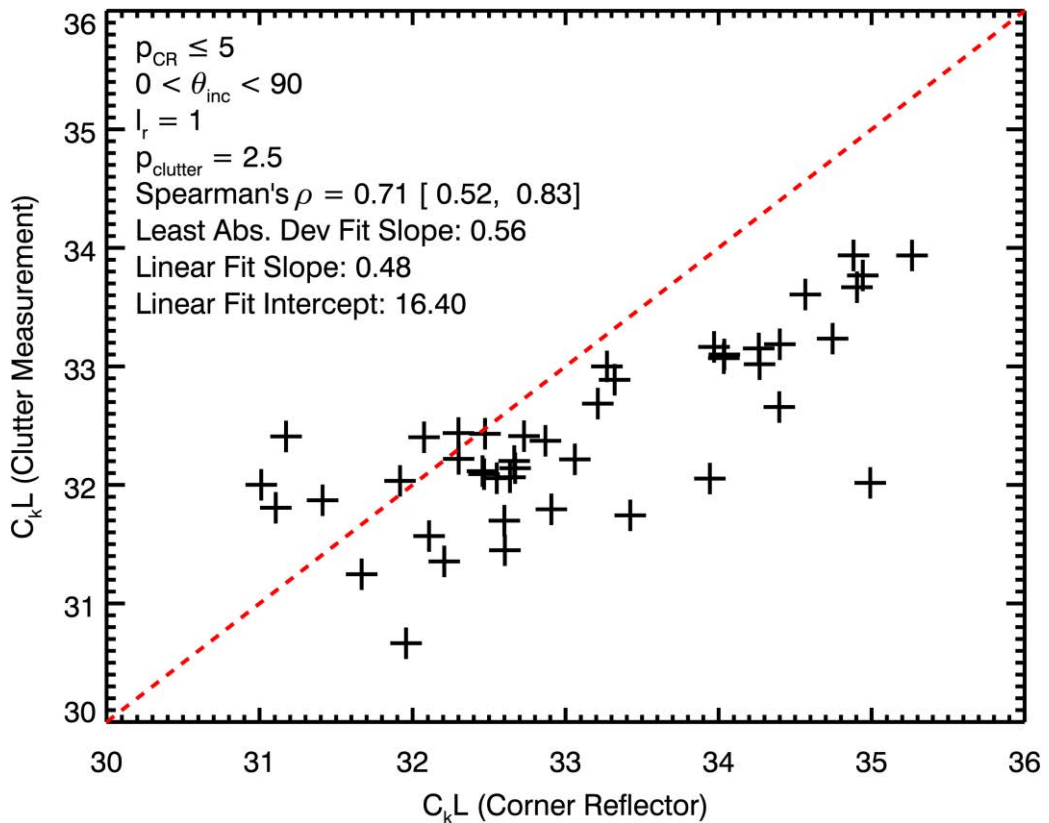


Figure 6.15: Corner reflector, clutter C_kL comparison - central clutter - $p_{CR} < 5$.

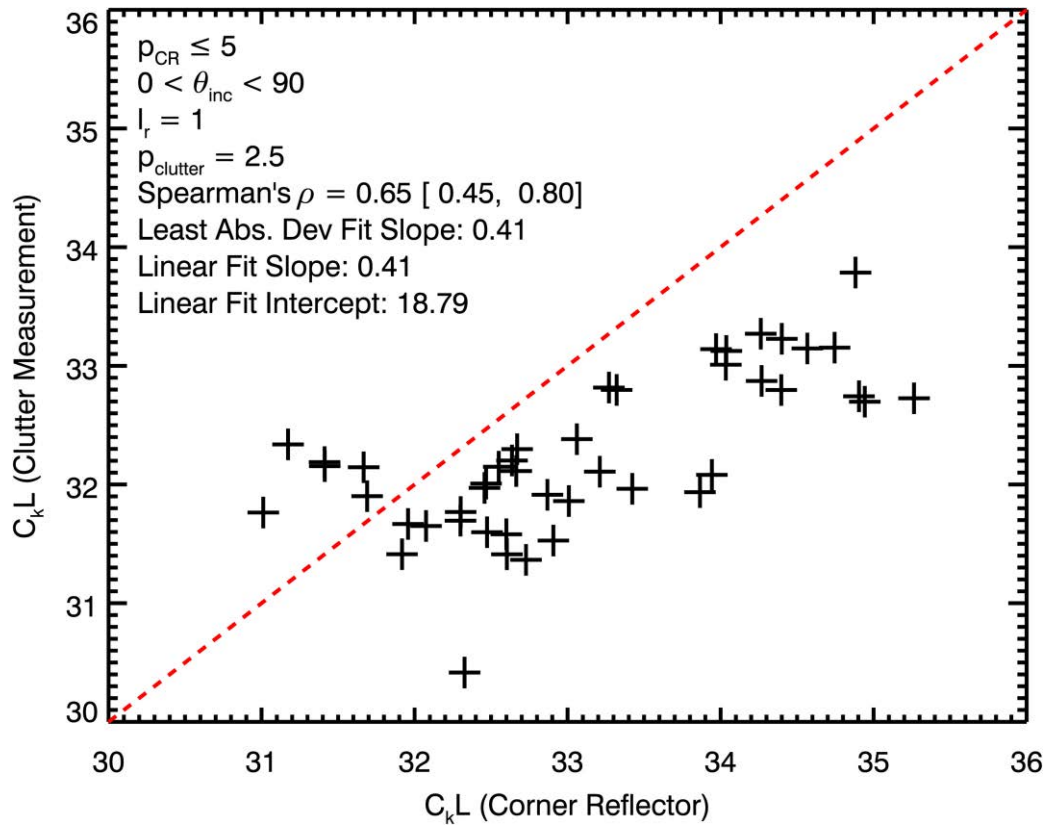


Figure 6.16: Corner reflector, clutter C_kL comparison - east clutter - $p_{CR} < 5$.

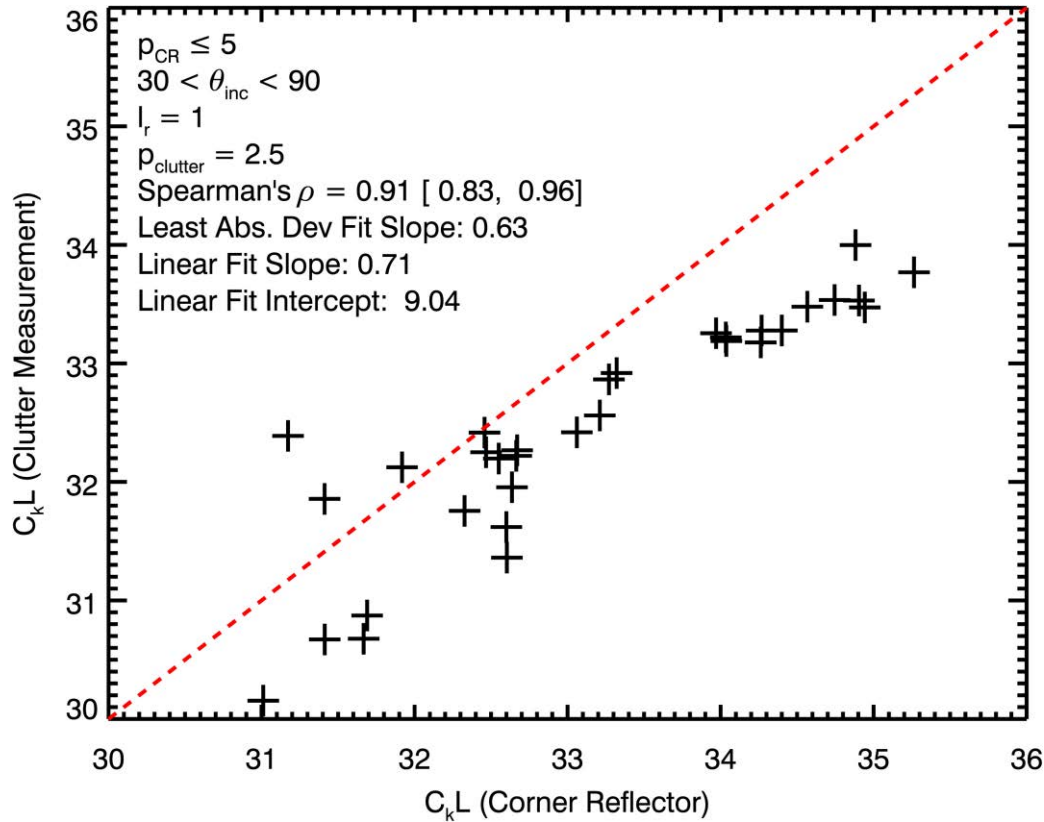


Figure 6.17: Corner reflector, clutter C_kL comparison - west clutter - $p_{CR} < 5$, $\theta_{inc} > 30^\circ$.

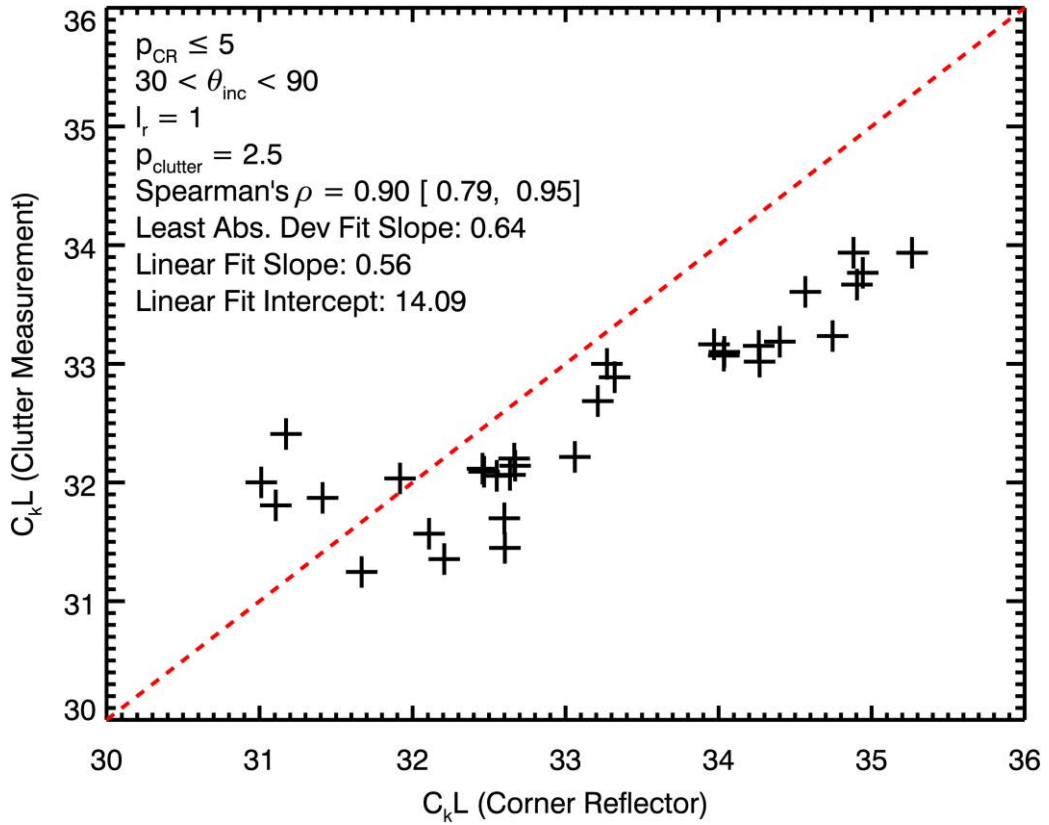


Figure 6.18: Corner reflector, clutter C_kL comparison - central clutter - $p_{CR} < 5$, $\theta_{inc} > 30^\circ$.

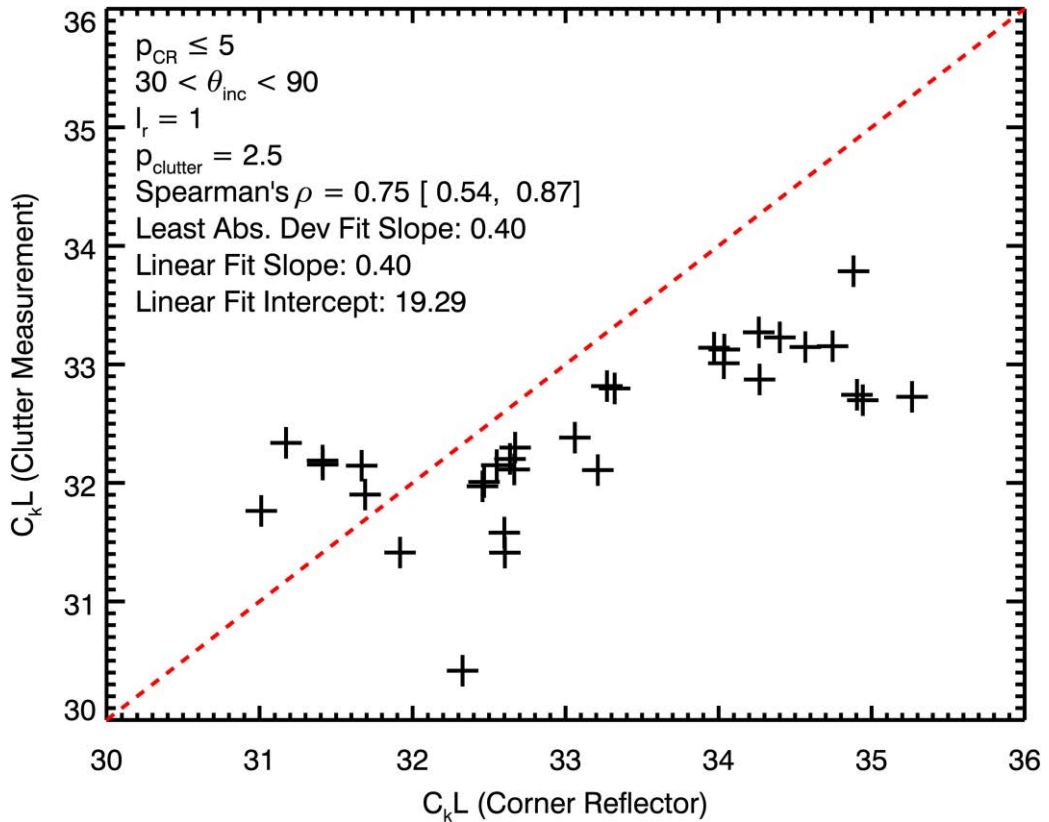


Figure 6.19: Corner reflector, clutter C_kL comparison - east clutter - $p_{CR} < 5$, $\theta_{inc} > 30^\circ$.

6.5.1 Effect of correlation length

In the analysis above, the correlation length, l_r , of Equation (6.5) is assumed to be unity. (The correlation length is the distance at which an independent sample of the underlying gamma-distributed RCS of the terrain is assumed to occur.) If this assumption is untrue, it would result in a negative bias of the clutter $C_k L$ values relative to the corner reflector $C_k L$ values.

The correlation length was determined by measuring the along-track autocorrelation function (ACF) for each clutter area and is calculated by squaring the FFT of each intensity image and then performing the inverse FFT. The resulting ACF was then averaged in the range direction to provide a single along-track ACF for each clutter area.

The correlation length was determined by fitting the theoretical form of the along track ACF, as described by *Belcher and Cannon* [2013], leaving the correlation length as a free parameter. The order parameter used for the fit was estimated using the peak value of the ACF to ensure an estimate consistent with the ACF theory. The function was fitted to the ACF between resolution cells 2.5 and 10 to avoid contamination by the mainlobe at low r values, and the noise floor at higher r values. The theoretical form of the intensity ACF, from *Belcher and Cannon* [2014] and *Oliver and Quegan* [2004a], transformed to be a function of 3 dB resolution cells r , is given by:

$$ACF(r) = 1 + 2^{-4r^2} + \frac{1}{v} \left[\exp\left(-\frac{2r}{l_r}\right) + 2^{-8r^2} \right]. \quad (6.12)$$

Examples of the intensity ACF are shown in Figure 6.20, Figure 6.21 and Figure 6.22. The west and central clutter areas have very similar ACFs, resulting in similar correlation lengths, while the slope of the fit to the eastern area (Figure 6.21) is shallower, resulting in a longer correlation length.

Correlation lengths were calculated for each clutter area, at each incidence angle, from the image that provided the lowest average order parameter measurement at each incidence angle. The effect of using these correlation lengths on the comparison between the corner reflector and the clutter $C_k L$ values is shown in Figure 6.23, Figure 6.24 and Figure 6.25. For the west and central clutter areas especially, almost all the values now lie very close to the $y=x$ line. The east clutter plot also has most of its points close to the $y=x$ line, albeit with slightly more spread in comparison to the west and central clutter plots. The slope of the linear and least absolute deviation fits has also increased.

Notwithstanding this improvement, the clutter $C_k L$ values (ordinate) very rarely go below 32, unlike the corner reflector $C_k L$ values, which have a minimum less than 31. Similarly, the clutter $C_k L$ values almost never exceed 34.5, unlike the corner reflector $C_k L$ values, which reach a maximum above 35. In fact, at lower corner reflector $C_k L$ values (< 32.5), the points tend to be above the $y=x$ line, while at high corner reflector $C_k L$ values (> 33.5) the points tend to be below the $y=x$ line, i.e. the range of clutter $C_k L$ values is less than that of the CR $C_k L$ values. It is possible that the assumption of a typical p value of 2.5 is limiting the variability of the clutter $C_k L$ values.

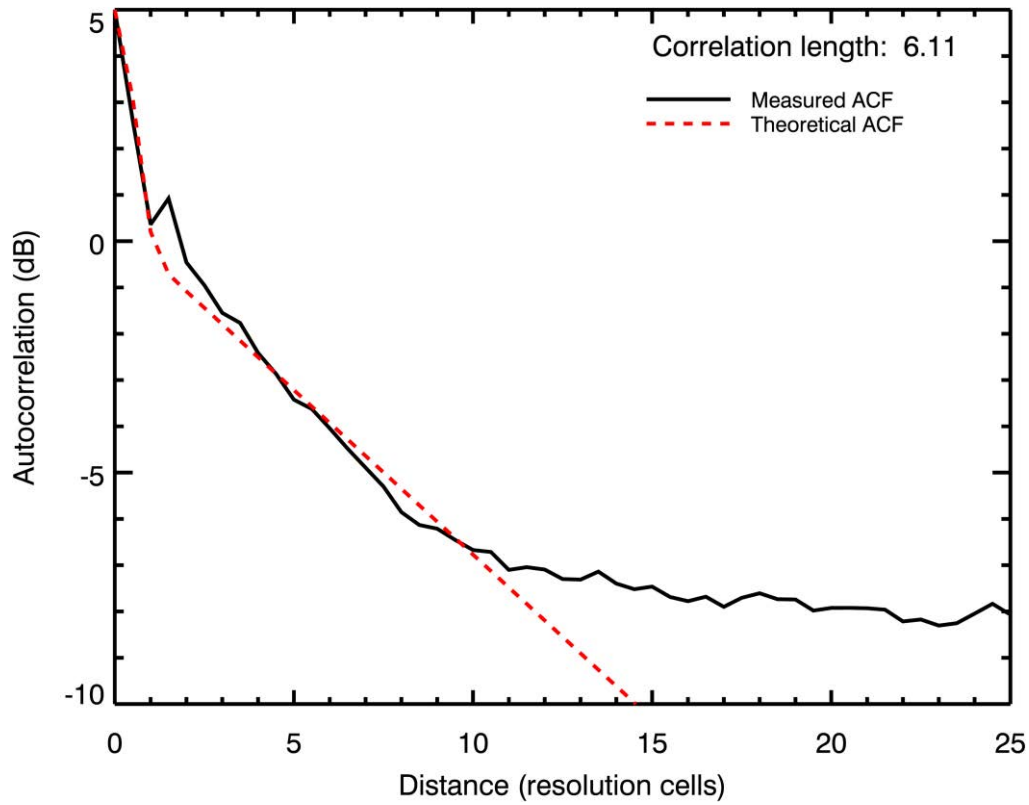


Figure 6.20: Along-track intensity autocorrelation function - west clutter (Figure 6.3, 2014/08/18, no scintillation)

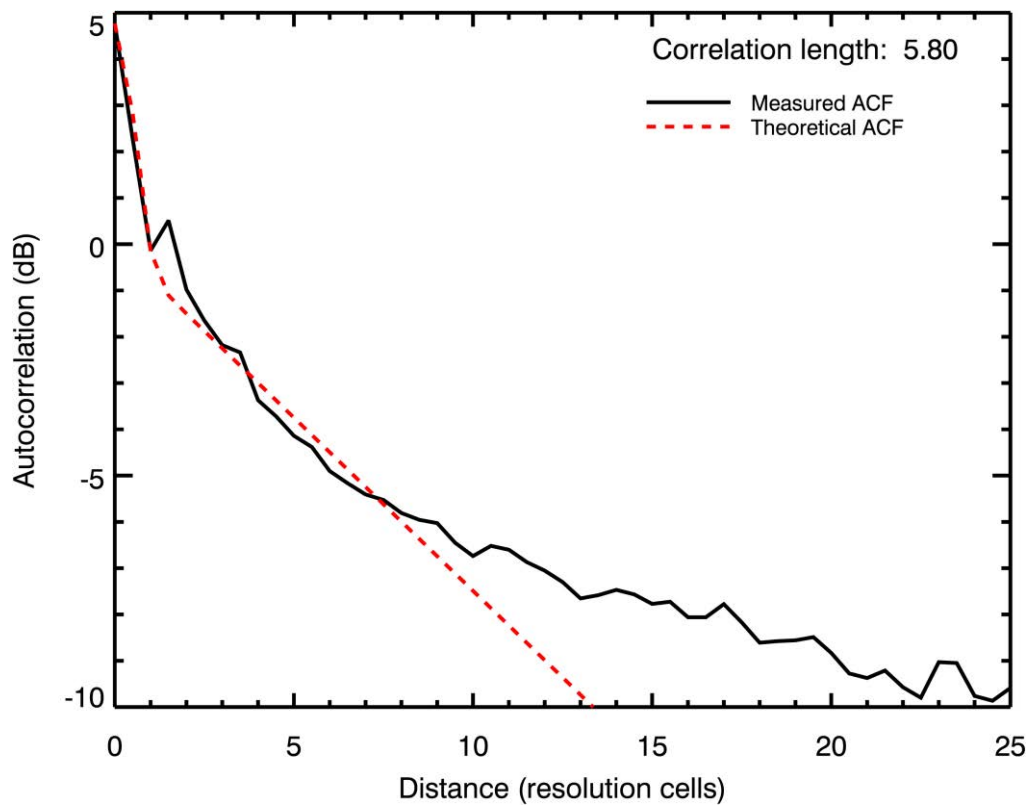


Figure 6.21: Along-track intensity autocorrelation function - central clutter (Figure 6.5, 2014/08/18, no scintillation)

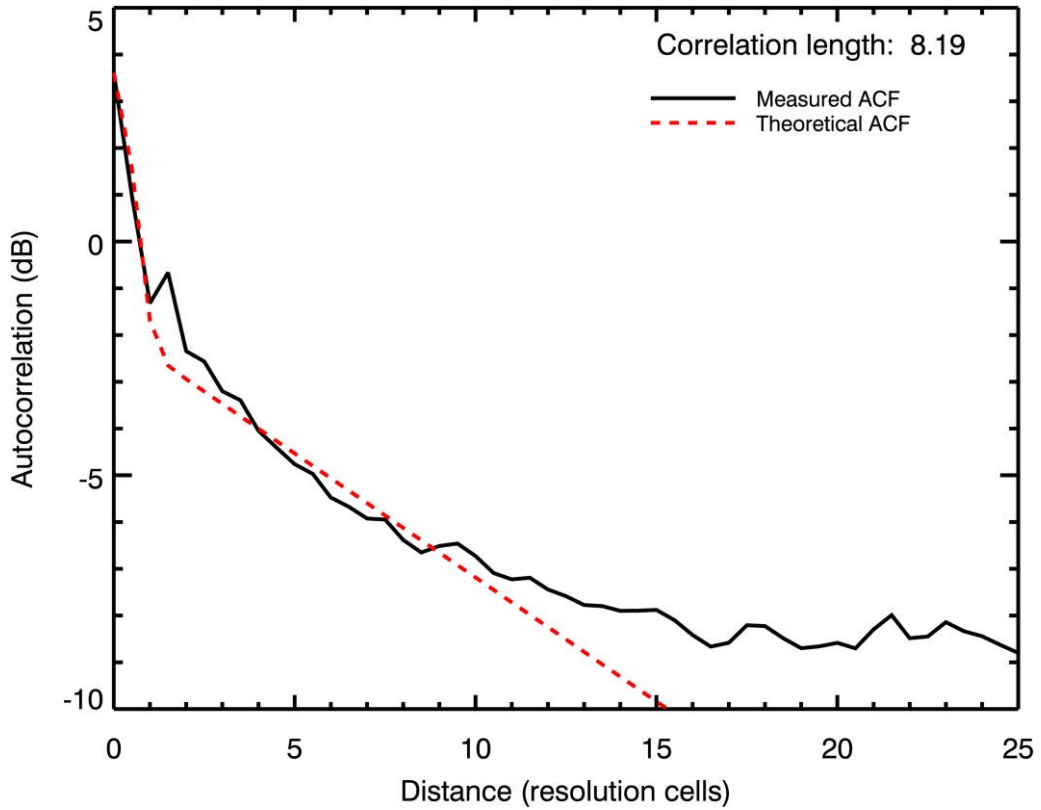


Figure 6.22: Along-track intensity autocorrelation function - east clutter (Figure 4, 2014/08/18, no scintillation)

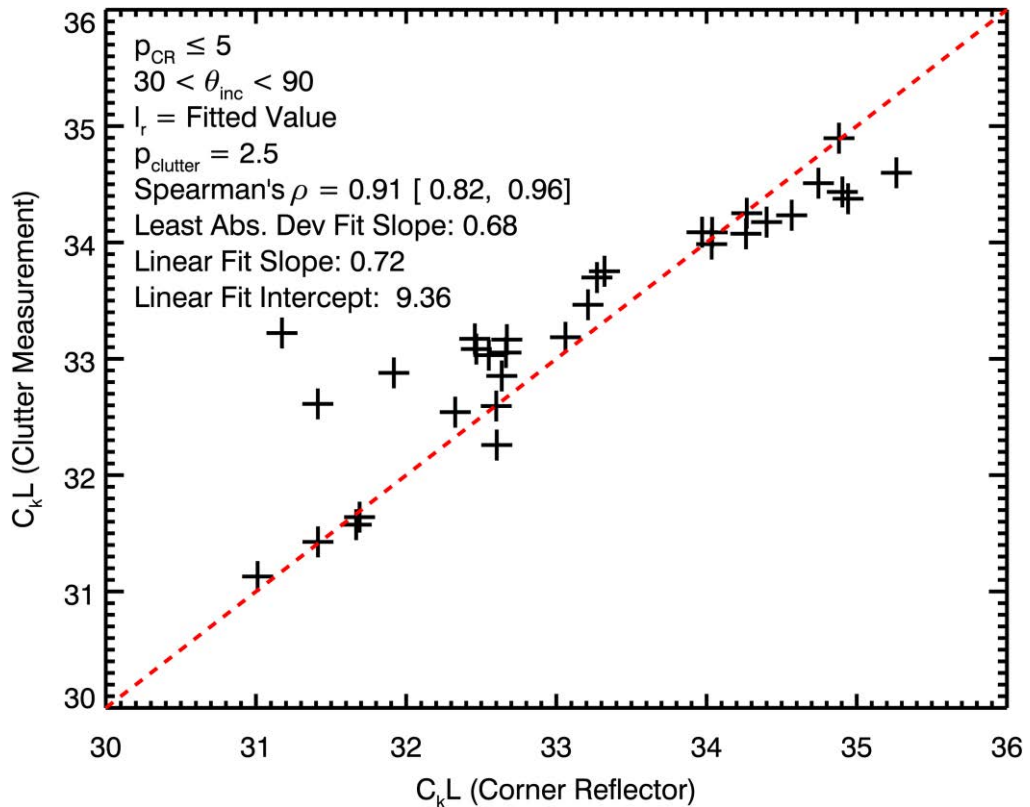


Figure 6.23: Corner reflector, clutter C_kL comparison - west clutter - $p_{CR} < 5$, $\theta_{inc} > 30^\circ$, $l_r = ACF$ Fit.

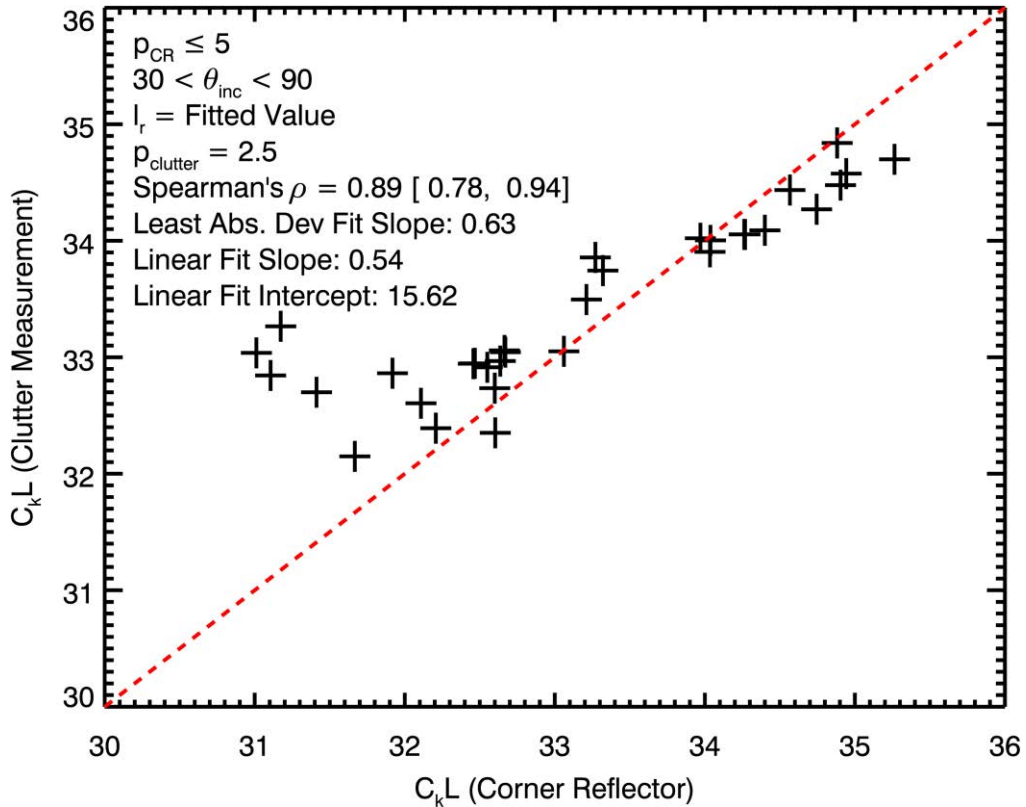


Figure 6.24: Corner reflector, clutter C_kL comparison - central clutter - $p_{CR} < 5$, $\theta_{inc} > 30^\circ$, $l_r = \text{ACF Fit}$.

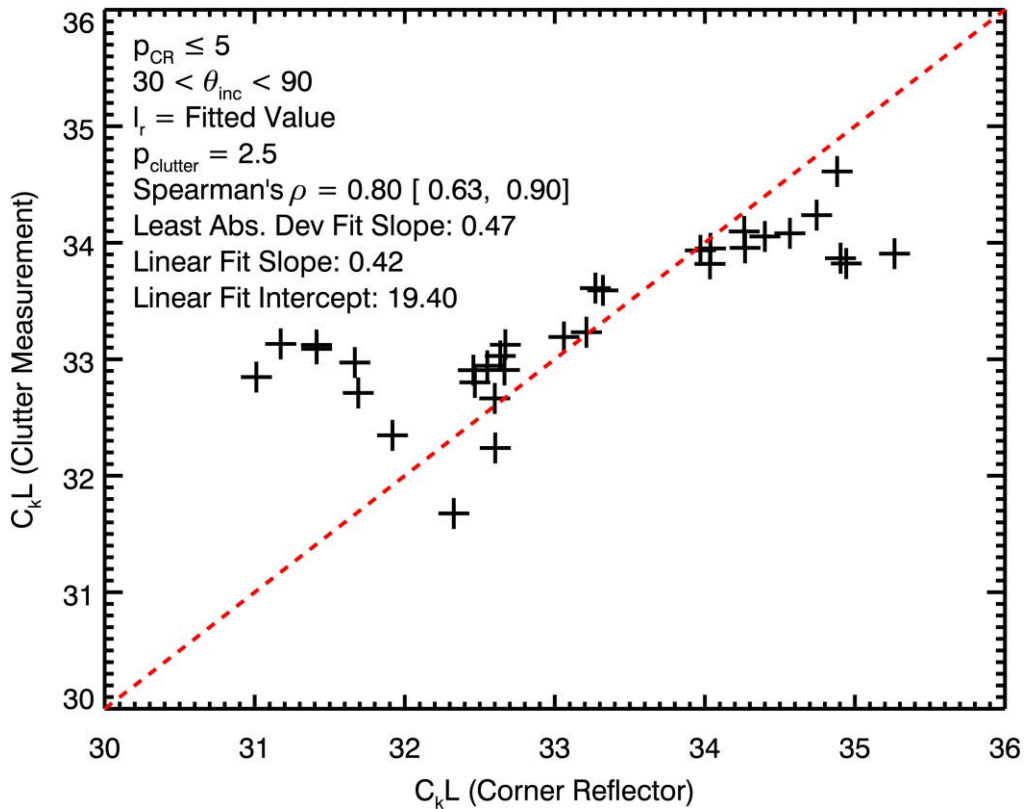


Figure 6.25: Corner reflector, clutter C_kL comparison - east clutter - $p_{CR} < 5$, $\theta_{inc} > 30^\circ$, $l_r = \text{ACF Fit}$.

6.5.2 Effect of p value

In the calculation of the clutter C_kL values, a value of $p_{clutter} = 2.5$ has been assumed. However, it would be instructive to take advantage of the independent measure of p provided by the corner reflector measurements. This will allow the limitations of the assumption of $p = 2.5$ to be studied.

Figure 6.26, Figure 6.27 and Figure 6.28 show the C_kL comparison when $p_{clutter} = p_{CR}$. In comparison with Figure 6.23, Figure 6.24 and Figure 6.25, the points are more evenly spread around the $y=x$ line at all corner reflector C_kL values. This is reflected both in the increased values of the correlation coefficient (0.96, 0.97 and 0.91 for the west, central and east clutter respectively), and also the slope of the linear fit to the data (1.01, 0.83 and 0.72, same order).

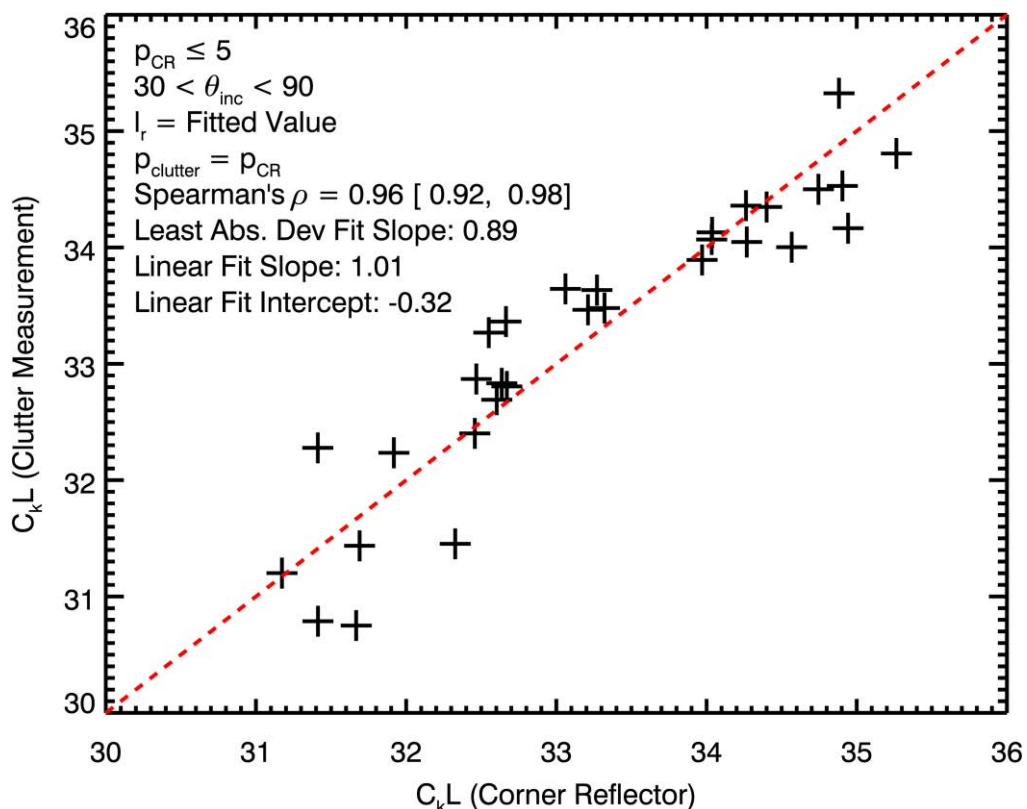


Figure 6.26: Corner reflector, clutter C_kL comparison - west clutter - $p_{CR} < 5$, $\theta_{inc} > 30^\circ$, $l_r = \text{ACF Fit}$, $p_{clutter} = p_{CR}$.

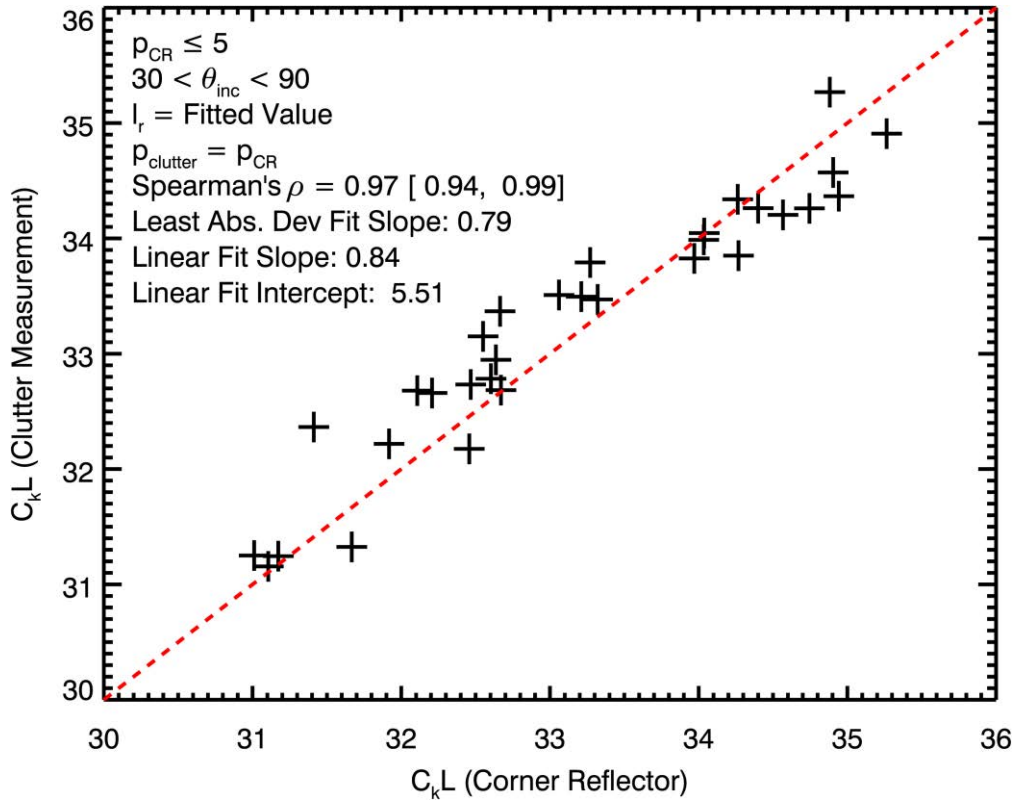


Figure 6.27: Corner reflector, clutter C_kL comparison - central clutter - $p_{CR} < 5$, $\theta_{inc} > 30^\circ$, $l_r = \text{ACF Fit}$, $p_{clutter} = p_{CR}$.

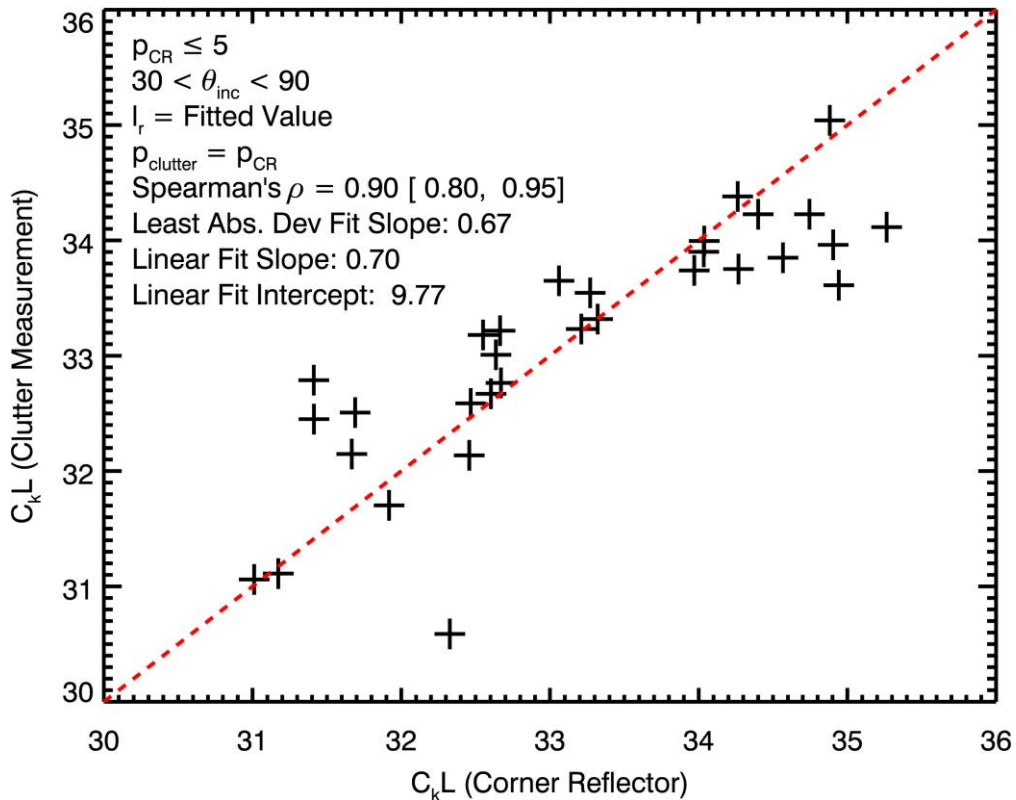


Figure 6.28: Corner reflector, clutter C_kL comparison - east clutter - $p_{CR} < 5$, $\theta_{inc} > 30^\circ$, $l_r = \text{ACF Fit}$, $p_{clutter} = p_{CR}$.

6.5.3 Effect of distance

The above comparisons have included corner reflector C_kL derived from both the corner reflectors on Ascension Island. The majority (~80%) of the data points are from the corner reflector on the west side of the island. Excluding the data from the corner reflector on the east side of the island will allow any change in the relationship between the clutter and corner reflector C_kL values with distance to be examined. The west clutter area is closest to the west corner reflector, followed by the central clutter, and then the east clutter area (Table 6.1).

Figure 6.29, Figure 6.30 and Figure 6.31 show the C_kL comparison using just data from the west corner reflector. The correlation coefficient is very high for each clutter area. However, the slope of a linear fit to the data from each clutter area decreases with distance, with values of 1.08, 0.86 and 0.76 respectively.

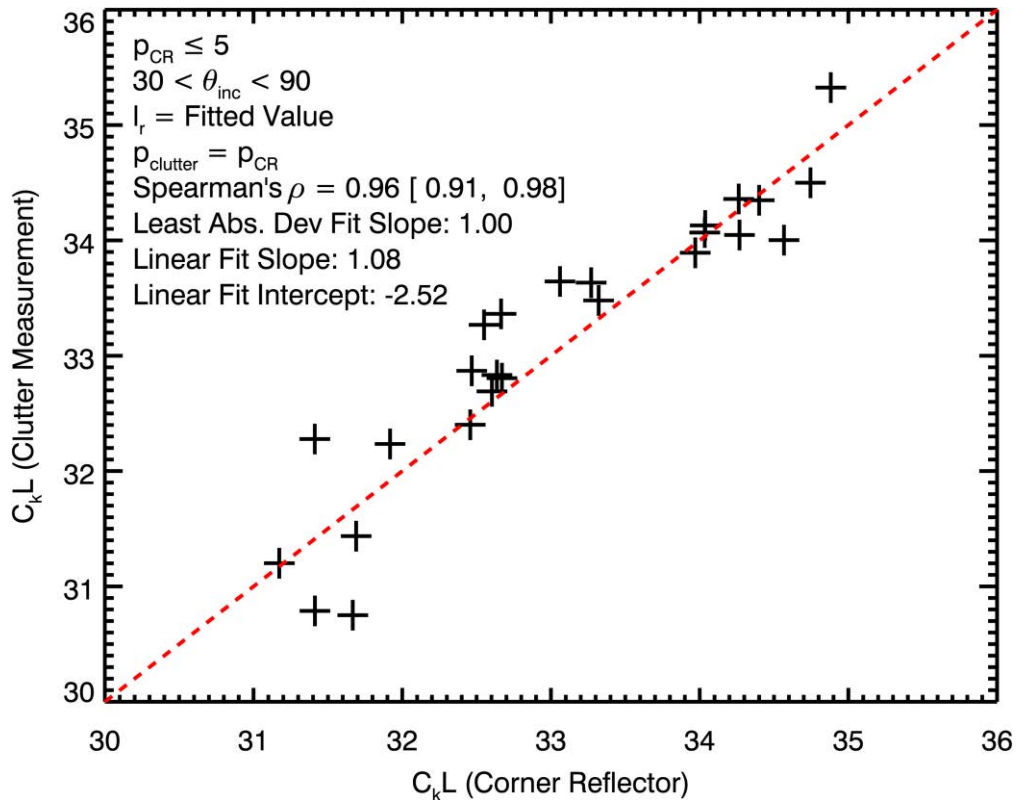


Figure 6.29: Corner reflector, clutter C_kL comparison - west clutter - $p_{CR} < 5$, $\theta_{inc} > 30^\circ$, $l_r = \text{ACF Fit}$, $p_{clutter} = p_{CR}$, west corner reflector only.

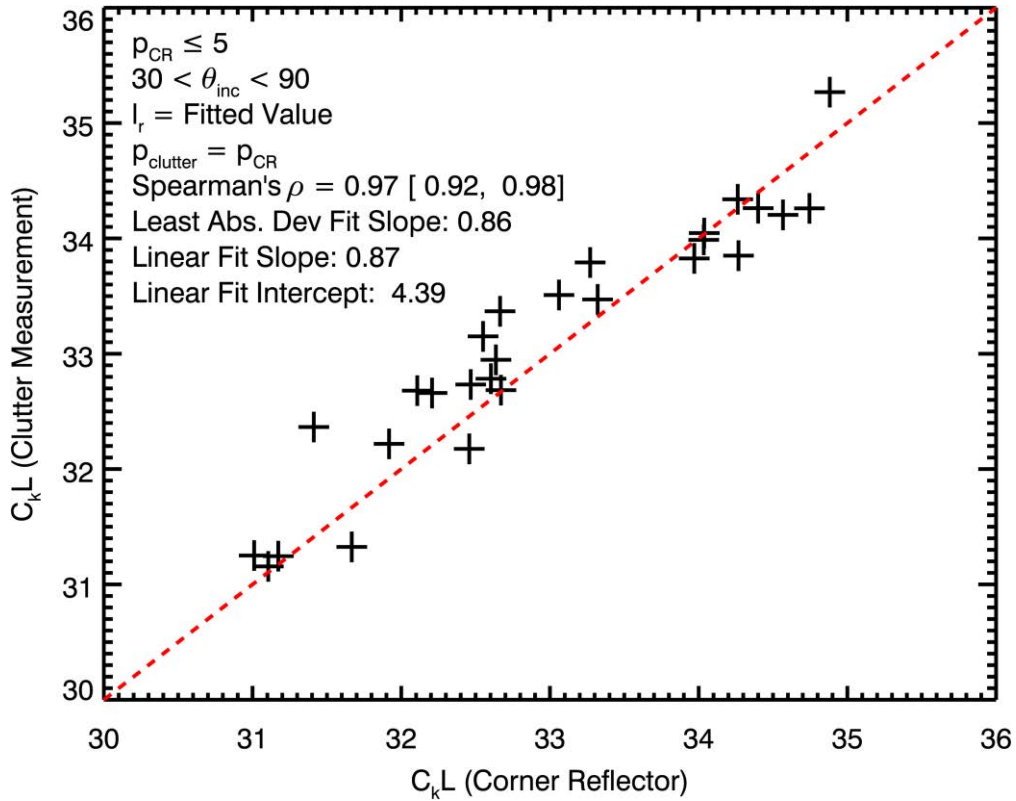


Figure 6.30: Corner reflector, clutter C_kL comparison - central clutter - $p_{CR} < 5$, $\theta_{inc} > 30^\circ$, $l_r = \text{ACF Fit}$, $p_{clutter} = p_{CR}$, west corner reflector only.

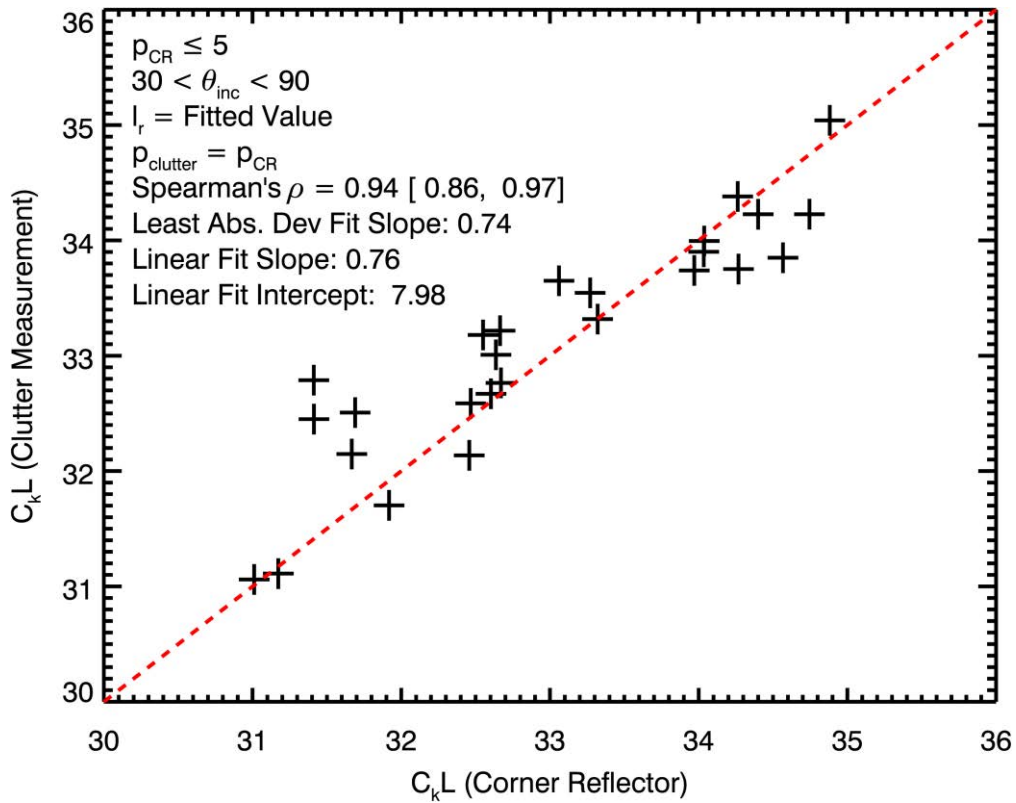


Figure 6.31: Corner reflector, clutter C_kL comparison - east clutter - $p_{CR} < 5$, $\theta_{inc} > 30^\circ$, $l_r = \text{ACF Fit}$, $p_{clutter} = p_{CR}$, west corner reflector only.

6.6 Discussion and conclusions

Measurements of natural clutter at three locations on Ascension Island were made using PALSAR-2 and the order parameter of the K-distributed clutter intensity, were estimated for 76 images. The difference in order parameter between a single image and a designated undisturbed image was used to estimate a value for the integrated strength of ionospheric turbulence, $C_k L$.

The $\log_{10} C_k L$ values calculated using this technique ranged from 29.3 to 34.0. These values are broadly consistent with predictions of the Wideband Model for the post-sunset period near Ascension Island [Belcher and Rogers, 2009] as well as estimates of $C_k L$ made in Section 5 using corner reflectors on Ascension Island.

Using this comparison, the effect of various assumptions used in calculating the clutter $C_k L$ values was investigated. It was found that the correlation length of the clutter measured was an important factor in correctly determining the $C_k L$ – ignoring the correlation length led to underestimation of $C_k L$ when compared to the corner reflector derived $C_k L$. Similarly it was found that the assumption that the phase spectral index p , of the ionospheric phase screen power spectrum, was equal to 2.5, was a limiting factor in accurately estimating $C_k L$. If the same p value is used for the clutter and corner reflector derived $C_k L$ values, excellent agreement between the two data sets was achieved, with correlation coefficients of 0.96, 0.97 and 0.91 for the west, central and east clutter respectively. This excellent agreement gives confidence in the use of the clutter measurement technique in calculating $C_k L$.

If p is assumed to be 2.5 there is still good agreement between the two datasets, although they do deviate at low (< 32.5) and high (> 33.5) $\log_{10} C_k L$ values. This is an important result, as

most SAR images will lack an independent measure of p , and so will require this assumption to be made.

The corner reflector $C_k L$ values were primarily (~80%) derived from the west corner reflector. The data from the east corner reflector was excluded to allow the effect of the distance of the clutter area from the corner reflector to be studied. The clutter results all showed very good agreement with the west corner reflector results, with all the areas having correlation coefficients of 0.94 or better. However, the slope of a linear fit to the data at each area was reduced as the distance between clutter area and corner reflector was increased. The reduction in the slope at the central clutter area relative to the west clutter area may suggest that the clutter measurements could be used to measure differences in ionospheric conditions over ranges of ~4 km. However, a more detailed study of this technique is required to rule out contamination of the results by underlying terrain effects.

7 DERIVING IONOSPHERIC SCINTILLATION PARAMETERS FROM SAR SIGNALS – AMPLITUDE SCINTILLATION

Section 5 and Section 6 have described two techniques to estimate the ionospheric strength of turbulence $C_k L$ using synthetic aperture radar (SAR) images. These techniques measure the effects of phase scintillation on the image. However, the images are also affected by scintillation of the intensity of the signal, the effects of which can sometimes be seen as azimuthal streaking in the image [Shimada *et al.*, 2008; Pi *et al.*, 2012b].

Previous work has attempted to mitigate and understand this striping effect [Roth *et al.*, 2012], but Belcher and Cannon [2014] have suggested that it may be possible to use this effect to retrieve scintillation parameters, and even irregularity characteristics from SAR images.

Unlike the clutter phase measurement technique described in Section 6, which requires pairs of images, this intensity technique only requires a single image if a homogeneous underlying terrain can be identified. If this is possible it is feasible to differentiate the ionospheric effects from the underlying terrain effects. However, in practice such terrain is uncommon and consequently a technique based on image pairs has been developed to overcome this requirement.

7.1 Effect of intensity scintillation on SAR images

The effects of intensity scintillation are sometimes visible as ‘striping’ in the along-track dimension of the SAR image. This striping occurs mainly in images recorded near the magnetic equator [Shimada *et al.*, 2008]. Belcher and Cannon [2014] studied the theoretical impact of intensity scintillation on SAR images, and determined that the structure of the striping was dependent on the imaging geometry such that it occurs when the along track direction approximately coincides with the direction of the geomagnetic field. This can be seen in Figure

7.1, which has been adapted from [Belcher and Cannon, 2014]. An error was noted in the calculation of the original figure, which has been corrected in the figure displayed here. The figure shows, for a satellite in a sun-synchronous, near-polar orbit, how the ratio of satellite velocity to the effective velocity of the ionospheric pierce point changes with latitude and longitude (this ratio, called γ is explained further below). Near the magnetic equator, the irregularities that cause scintillation are extended along the geomagnetic field lines in the magnetic north-south direction. As such, the effective velocity of the IPP is reduced, leading to an increase in the velocity ratio. This conclusion was supported by a recent empirical study performed using PALSAR data [Meyer et al., 2015].

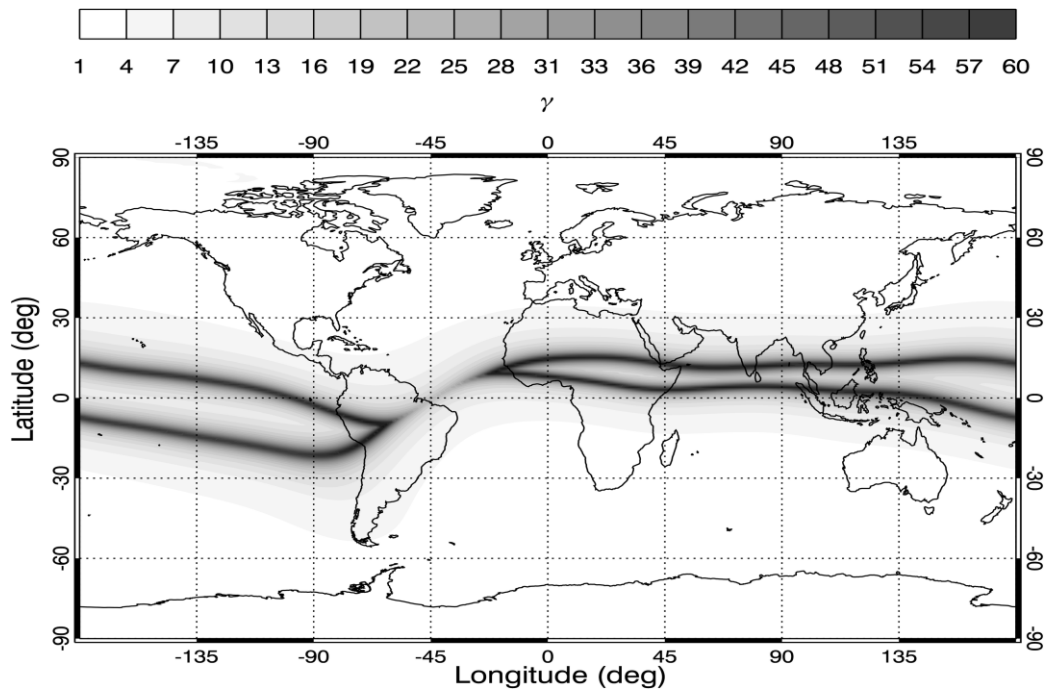


Figure 7.1: Ascending node velocity ratio γ for a 2200 LT sun-synchronous satellite at an altitude of 698 km. Adapted from [Belcher and Cannon, 2014].

Intensity scintillation is typically characterised by the S_4 index, defined as the standard deviation of the intensity divided by the mean intensity [Briggs and Parkin, 1963]:

$$S_4^2 = \frac{\langle I^2 \rangle}{\langle I \rangle^2} - 1. \quad (7.1)$$

Using the Nakagami-m distribution to describe the statistical properties of intensity scintillation, *Belcher and Cannon* [2014] show that the contrast (standard deviation of the divided by the mean) of the intensity modulation (striping) induced in a SAR image by the ionosphere can be used to derive the one way S_4 index:

$$S_4^2 = \frac{N}{12} \left(c_d^2 - 4 + 4 \sqrt{1 + c_d^2 + \frac{c_d^4}{16}} \right), \quad (7.2)$$

where N is the number of independent Fresnel zones encountered by the SAR signal in the ionosphere. *Belcher and Cannon* [2014] postulate that the value of N is given by:

$$N = \frac{L_{SA}}{\gamma Z_F}, \quad (7.3)$$

where L_{SA} is the synthetic aperture length, Z_F is the Fresnel zone size and γ is the previously discussed ratio between the velocity along the synthetic aperture, and the effective scan velocity of the signal across the ionosphere. The γ term accounts for the fact the Fresnel zone is at the phase screen height, and for any anisotropy in the ionosphere. $\frac{L_{SA}}{\gamma} = L_C$, the length of the SAR signal path in the ionosphere, and so N is this length divided by the Fresnel zone size.

For an image with no underlying terrain variation that has been processed to remove the effect of speckle, c_d is equivalent to the contrast of the image. In practice, it is difficult to measure the contrast of the stripes because they are often contaminated by variations in the underlying terrain. This is discussed further in Section 7.3.1.

7.2 PALSAR Data

The above theory has been tested using a very small set of data. The images used in this section were collected by the first Phased Array L-Band SAR (PALSAR), a sun-synchronous SAR in low Earth orbit (698 km altitude), again operating frequency at 1270 MHz [*Rosenqvist et al.*,

2007]. The orbit of PALSAR followed repeat ground tracks, and typically produced imagery at an incidence angle of 34.3°. This allows comparisons to be made between repeated imagery of the same area under different levels of ionospheric scintillation. The details of the images used are listed in Table 7.1.

Table 7.1. PALSAR images disturbed by scintillation (D) and undisturbed (U).

Pair	Scene Centre (latitude, longitude)	Scene Dimensions	Date	
Figure 7.2	8.1905 S, 53.7662 W	70 x 60 km	D	2010/11/23
			U	2010/10/08
Figure 7.3	6.6357 S, 64.8670 W	30 x 65 km	D	2010/11/19
			U	2011/04/06
Figure 7.4	9.6770 S, 52.8943 W	70 x 60 km	D	2010/11/19
			U	2011/04/06

All of the disturbed images show the characteristic azimuthal striping due to intensity scintillation (Figure 7.2a, Figure 7.3a, Figure 7.4a). In Figure 7.2, the striping is the only visible difference between the two images. In contrast, Figure 7.3 shows both the striping, and a significant loss of detail between the two images. As a consequence, the undisturbed image (Figure 7.3a) clearly contains detail that is not present in the disturbed image (Figure 7.3b). This also appears to be the case for Figure 7.4, although it is not as immediately evident. We will show that the loss of detail is likely due to the effects of phase scintillation.

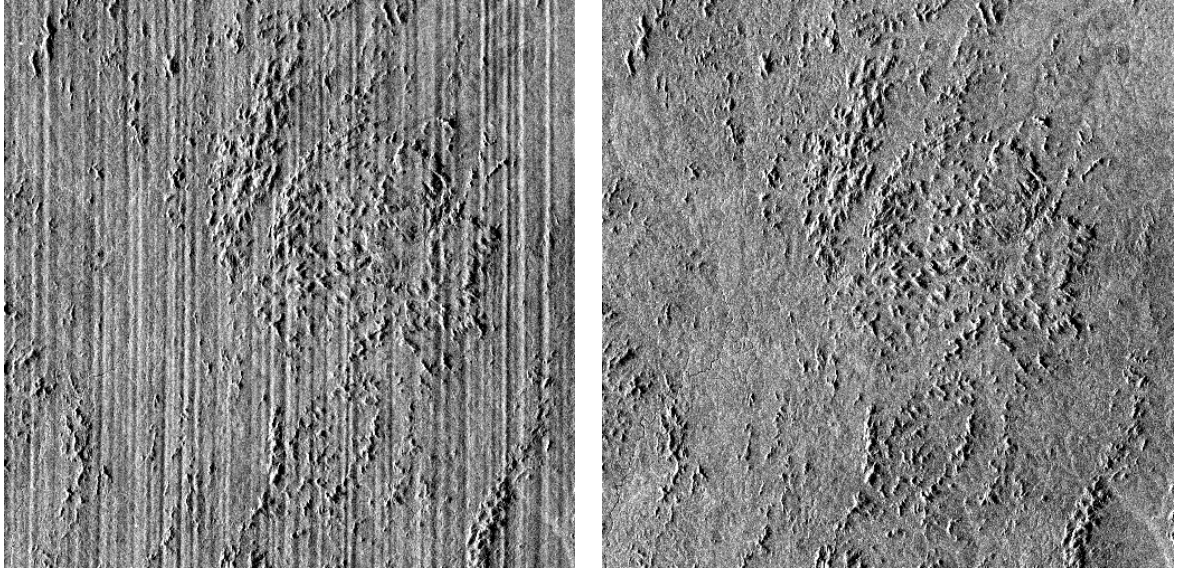


Figure 7.2. a) Disturbed image (left) and b) Undisturbed image (right)

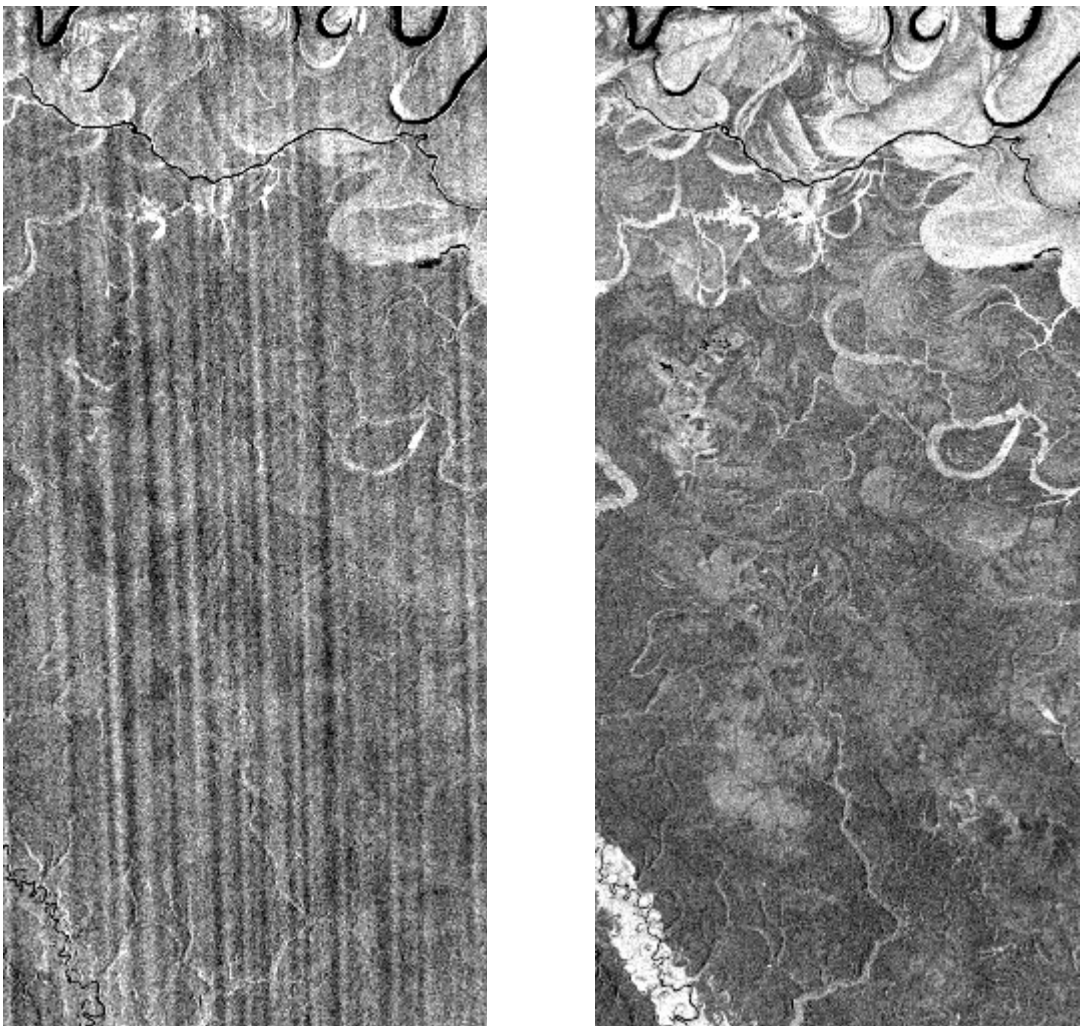


Figure 7.3. a) Disturbed image (left) and b) Undisturbed image (right)

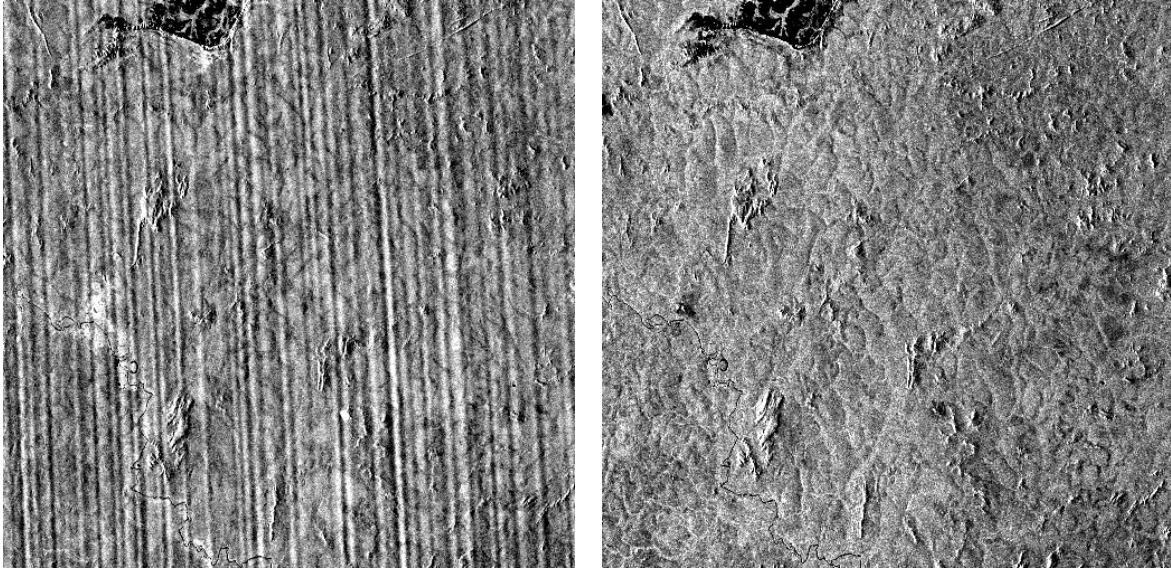


Figure 7.4. a) Disturbed image (left) and b) Undisturbed image (right)

7.3 Results

7.3.1 Estimating S_4

A method of estimating the S_4 scintillation using the contrast of the along-track striping was described in Section 7.1 but the change in intensity can only be ascribed solely to the ionospheric element if the underlying RCS is constant. The approach adopted here uses a pair of images, one disturbed by the ionosphere, and one undisturbed, and through a process of division the effects of the underlying scene was removed to isolate the ionospheric striping.

However, before this can be done the effects of speckle in the image must be removed. Fortunately, the intensity scintillation is correlated over the Fresnel zone (and often further due to elongation of the irregularities along the magnetic field lines), so the image may be averaged down to remove speckle and still provide an accurate representation of the underlying RCS multiplied by the effect of the striping.

To achieve this the complex pixel images were converted to intensity values. Each pair of images was co-registered via cross-correlation to remove any relative shift in terrain features between the pair. The images were then split into multiple vertical sub-image stripes with dimensions of 25 pixels in the range direction, and 250 pixels in the along-track direction. The individual pixel intensity values within each stripe were averaged to give a mean intensity for each stripe. These along-track dimension of the stripes is sufficiently small that any deviation in the direction of the stripes from the along-track direction has little effect on the measurement of the striping.

To remove the underlying terrain the stripe intensity values of the disturbed image were then divided by the corresponding values from the undisturbed image. The resulting intensity values were then combined into groups of 16 in the range direction, and the contrast (standard deviation, divided by the mean) of each group was calculated. Using Equation (7.2), the contrast value for each group was used to calculate S_4 , with N calculated for each image pair according to (7.3), producing a grid of S_4 values across the image.

A representation of the residual images produced by the division process described in Section 7.3.1 are shown for each image pair in Figure 7.5, Figure 7.6 and Figure 7.7. The sizes of a strip, and a group of 16 strips are shown on each image in white. Although they are not exactly equivalent to the actual residual images (which are too small to display), they allow visual evaluation of the effect of the division process.

The image produced by the image pair in Figure 7.2 shows that the terrain has been successfully removed, leaving only the intensity change due to the striping (Figure 7.5). The image was processed as described in Section 7.3.1, and the S_4 calculated for each group of 16 strips. The mean S_4 over the entire image was 0.076. Figure 7.6 shows the residual image from the images

in Figure 7.3. In this case the division process has been unsuccessful in removing the terrain, and so the contrast of the striping cannot be measured. The residual image from Figure 7.4 is shown in Figure 7.7. Although there are still some areas where the terrain is still visible in the image, for the majority of the image the division process has been successful. The mean S_4 across the image was 0.074.

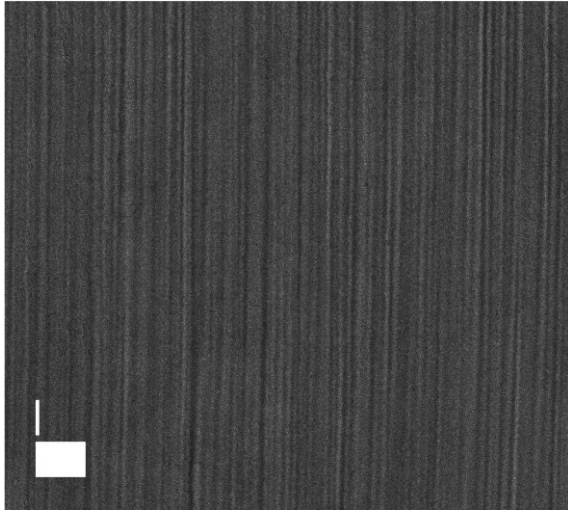


*Figure 7.5. Residual intensity image from images in Figure 7.2.
Each resolution cell is 10×25m.*



*Figure 7.6. Residual intensity image from Figure 7.3.
Each resolution cell is 10×25m*

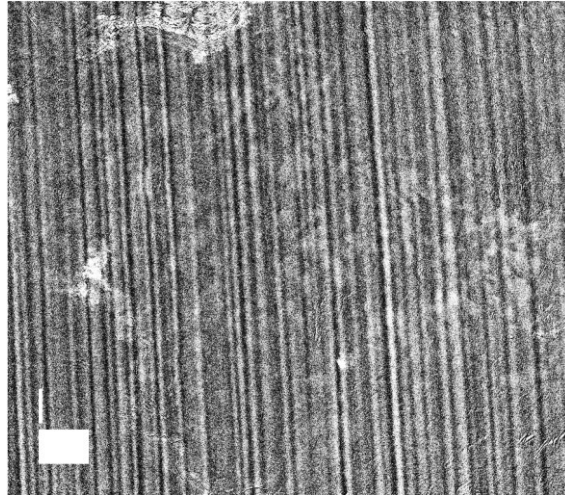


*Figure 7.7. Residual intensity image from Figure 7.4.
Each resolution cell is 10×25m.*

7.3.2 Effect of phase scintillation

As noted above, the residual intensity image produced from the image pair in Figure 7.3 is difficult to extract striping information from, as it has retained significant features due to the underlying terrain. This could be caused by phase scintillation washing out the terrain detail in the disturbed image. To test this theory, the clutter statistics measurement technique described in Section 6 was used to measure the impacts of phase scintillation on each of the image pairs. All of the image pairs contain large areas of forest canopy, ideal for the clutter measurements described in Section 6. Twenty such areas, with side length 50 x 1024 pixels (chosen so that they fit inside a stripe), were found in each image, and used to measure the change in the order parameter of the clutter intensity distribution between the undisturbed and disturbed image in each pair as described in Section 6.

For the image pairs in Figure 7.2 and Figure 7.4, the mean order parameter ratio was 0.995 and 0.991 respectively. In contrast, the image pair shown Figure 7.3 has a mean order parameter ratio of 1.714, showing a clear increase in the order parameter of the clutter intensity distribution.

7.4 Discussion

Three PALSAR images affected by azimuthal striping – a characteristic effect of ionospheric amplitude scintillation – were analysed in an attempt to estimate the S_4 scintillation index using a method described by *Belcher and Cannon* [2014]. The technique used requires underlying terrain with no variation in order to isolate the effect of the striping. The three images were each combined with an image of the same scene unaffected by the ionosphere in an attempt to remove the underlying terrain variation.

For the image pairs in Figure 7.2 and Figure 7.4, the underlying terrain was removed successfully (Figure 7.5, Figure 7.7). The mean S_4 values measured were 0.074 (Figure 7.5) and 0.076 (Figure 7.7). Data from the Low-latitude Ionospheric Sensor Network provided an independent S_4 value of 0.16 for the images in Figure 7.2, much higher than the calculated value. No such data existed for the pair in Figure 7.4.

The S_4 values calculated were much lower than typical values of S_4 indicating the presence of scintillation [*Carrano et al.*, 2012b], and given the obvious visual impact on the image, higher S_4 values might be expected. The S_4 calculation depends heavily on γ , a term that accounts for both the phase screen height and anisotropy in the ionosphere, and is dependent on the geomagnetic field. The gamma values in this study were calculated according to *Belcher and Cannon* [2013], and are dependent on the International Geomagnetic Reference Field. All of the images used in this study are located in Brazil, relatively close to the South Atlantic geomagnetic anomaly, and as such the gamma values are subject to a high gradient – any small error in calculation would lead to a large effect on the final result. More data is therefore needed to properly test the validity of this approach to measuring S_4 .

For the image pair in Figure 7.3, the terrain removal approach was unsuccessful. The terrain clearly remained in the residual image, making it impossible to measure the striping. This was due to the lack of detail in the disturbed image, compared to the undisturbed image. The loss of detail could be due to degradation of the SAR point spread function driven by ionospheric phase scintillation (Section 5). This interpretation is supported by the fact that another symptom of phase scintillation – an increase in the estimated order parameter of the clutter intensity distribution between the undisturbed and disturbed image – was also observed. Therefore, when phase scintillation and amplitude scintillation occur together, measurement of amplitude scintillation as described here may be hindered.

The analysis reported here has failed to substantiate the theory of *Belcher and Cannon* [2014] and evidently more work is required to further investigate this. A larger-scale study, combined with a local independent measure of ionospheric conditions for each image pair, would allow the relationship between the striping and ionospheric conditions to be examined in detail.

8 CONCLUSIONS AND FUTURE WORK

The ionosphere can adversely affect synthetic aperture radar (SAR) images in many ways. Space-based SAR systems have become a vital tool in many remote-sensing applications, and thus understanding and mitigating the effects of the ionosphere on these systems is extremely important.

An obvious starting point for research in this area is to identify SAR images for which there are corresponding measurements of the ionosphere the SAR signals travelled through. However, datasets such as this are relatively sparse. In view of this, Section 4 presents a method of using GPS signal phase and amplitude data to synthesize the effect of the ionosphere on an L-Band SAR point spread function (PSF). The SAR PSF describes the characteristics of the SAR image, and thus can be used to provide insight into the effect of the ionosphere on the image. GPS signals are already widely used as an ionospheric monitoring tool, and so perform a dual-role, allowing both a measurement of conditions in the ionosphere, and of the ionospheres presumed impact on the SAR image. The technique was tested using a large dataset of GPS signals recorded on Ascension Island (in the equatorial regions) under a variety of ionospheric conditions. The results were consistent with existing weak scatter theory, giving confidence that this technique provides an accurate assessment of ionospheric scintillation effects on SAR.

One possible method of correcting the effects of ionospheric phase scintillation on SAR images is via a correction applied to the SAR signal phase, derived from measurements of a point target at a reference location in the image. Theoretically, this point target could be used to estimate the phase shift due to the ionosphere on each radar pulse, which could then be applied to other points across the image. Using the above synthetization technique, the practical effectiveness

of such a phase correction method was investigated. It was estimated that this technique could improve image quality at up to 6000 m from the reference point.

Whilst correction of ionospheric impacts on SAR data is important, the possibilities of using SAR as a tool to measure the ionosphere itself were also studied. In light of the previously mentioned lack of coincident SAR and ionospheric data, an experiment was undertaken on Ascension Island, in which simultaneous GNSS and SAR measurements were recorded. Two trihedral corner reflectors (CR) were deployed on the island, to provide bright point targets in the SAR images, enabling direct measurement of the SAR point spread function (PSF). Around 75 images, together with corresponding GNSS data were analysed.

Using this dataset, two investigations into the potential for using SAR to measure the ionosphere were undertaken. The first was a large-scale study of a previously presented theory [Belcher and Rogers, 2009] relating the shape of the SAR PSF to the irregularity distribution in the ionosphere (in terms of the ionospheric strength of turbulence, $C_k L$). The results were very promising, with the results derived from the CR measurements showing reasonably good agreement with $C_k L$ values estimated from the GNSS data, after accounting for differences in the spatial and temporal scales. The CR measurement technique was sensitive to $\log_{10} C_k L$ values ranging from 31 to 36.

The requirement for a bright point target (such as a CR) in the image is a severe limitation for the practical application of this technique as a worldwide ionospheric mapping tool. However, the change in the SAR PSF induced by the ionosphere should also be observable as measurable changes in the properties of the image. One such property is the statistics of areas of natural clutter in the image (as proposed by [Belcher and Cannon, 2013]), and the second investigation attempted to measure $C_k L$ from the statistics of three areas of natural clutter in each of the

images of Ascension Island. These were in turn compared with the CR-derived C_kL measurements. Using an independent measure of p (the slope of the irregularity spectrum), the clutter measurement results showed excellent agreement with the C_kL values derived from the CRs. Using an average p value of 2.5, the agreement was still good. Furthermore, differences in the C_kL values measured at the three clutter locations suggested the possibility of using this technique to measure changes in C_kL over distances of 4 km.

Finally, whilst the previous two investigations focussed on measuring the impact of phase scintillation on SAR images, a third, small-scale study was undertaken to extend a previously reported technique to measure the amplitude scintillation index S_4 from SAR images. This technique uses the ‘striping’ that is sometimes visible in the along-track direction of SAR images taken near the magnetic equator – a characteristic effect of amplitude scintillation. The previous work identified a homogenous area in a striping affected image and measured the stripe intensity from that. Such a technique is difficult to automate, and will not always be possible due to the underlying terrain. Thus this study attempted to use pairs of images of a single location, one affected by the ionosphere and one unaffected, to remove the intensity variations in the image driven by the underlying terrain, and thus extract the intensity modulation due to the striping. Three scenes were used in this study, all located in the Amazon rainforest. For two of the three scenes, the terrain removal process worked reasonably well (from a visual analysis). However, the S_4 values measured did not show good agreement with simultaneous GNSS measurements of S_4 . The final image pair identified an important practical issue with the terrain removal process. The image affected by the ionosphere appeared to show the impacts of both phase and amplitude scintillation. The effect of the phase scintillation is to wash out the terrain detail, which cannot then be removed from the affected image.

8.1 Future Work

In the continued absence of widely-available coincident SAR and ionosphere data, the GNSS synthesization technique described here could be take advantage of the prevalence of GNSS signals to perform a large-scale and long-term study of the possible ionospheric impacts on SAR world-wide. In addition, whilst the results were consistent with existing weak scatter theory, a direct comparison with real SAR data would be an excellent and useful test of this technique.

The results from the corner reflector C_kL measurement technique showed reasonable agreement with simultaneous GNSS measurements, with the variations between the two datasets being ascribed to practical differences between the two measurement techniques.

These differences are key - the CR data offers the potential for a measurement of the ionosphere made over long spatial scales (~30 km) but short (~10 s) temporal scales – a feat not possible with GNSS measurements. One possibility this suggests is to use an array of relatively small CRs to measure the distribution of ionospheric irregularities. This would potentially provide a cheap alternative to current methods of achieving the same result.

The clutter C_kL measurements were extremely promising. Further work to develop the technique to investigate over what separations differences in C_kL could be measured would be useful. The development of a robust, automated technique to process SAR images of a given scene, which finds and analyses clutter areas to give C_kL values seems feasible. One significant limitation of the clutter technique is that some types of natural clutter – specifically ocean waves – are not suitable for use, as they do not remain static between images. A potential solution to this would be to find a relationship between wave clutter and another environmental observable, such as wind conditions.

Finally, the study of the amplitude scintillation measurement technique should be extended. A useful next step would be a larger scale study, using many more image pairs, allowing insight into the relationship between phase and amplitude scintillation effects in SAR images.

APPENDIX A. LIST OF PALSAR-2 IMAGES

Table A.1: Details of the PALSAR-2 images used in this work

Date	Time	Track Number	Corner reflector illuminated	Incidence Angle (corner reflector)
2014/08/18	01:47:15	2	West	69.67
2014/08/19	00:31:48	198	East	57.22
2014/08/22	01:33:33	207	West	59.1
2014/10/01	00:52:24	201	East	23.69
2014/10/02	01:12:59	204	West	28.58
2014/10/03	01:33:33	207	West	59.18
2014/10/05	00:38:40	199	East	48.89
2014/10/11	01:06:07	203	West	12.15
2014/10/12	01:26:41	206	West	51.63
2014/10/21	01:19:50	205	West	41.7
2014/10/25	01:06:07	203	West	12.16
2014/10/26	01:26:42	206	West	51.64
2014/10/27	01:47:15	2	West	69.73
2014/10/28	00:31:48	198	East	57.15
2014/10/29	00:52:24	201	East	23.68
2014/10/30	01:12:59	204	West	28.57
2014/10/31	01:33:33	207	West	59.19
2014/11/01	00:18:03	196	East	68.53
2014/11/02	00:38:40	199	East	48.89
2014/11/04	01:19:50	205	West	41.7
2014/11/05	01:40:24	1	West	65.04
2014/11/06	00:24:55	197	East	63.51
2014/11/08	01:06:07	203	West	12.14
2014/11/09	01:26:42	206	West	51.64
2014/11/10	01:47:15	2	West	69.72
2014/11/11	00:31:48	198	East	57.15
2014/11/12	00:52:24	201	East	23.68
2014/11/13	01:12:59	204	West	28.58
2014/11/14	01:33:33	207	West	59.19
2014/11/15	00:18:04	196	East	68.53
2014/11/16	00:38:40	199	East	48.89
2014/11/18	01:19:51	205	West	41.71
2014/11/19	01:40:24	1	West	65.04
2014/11/20	00:24:56	197	East	63.5
2014/11/22	01:06:08	203	West	12.16
2014/11/23	01:26:42	206	West	51.65
2014/11/27	01:12:59	204	West	28.65
2014/11/28	01:33:34	207	West	59.21

2014/11/29	00:18:04	196	East	68.52
2014/11/30	00:38:40	199	East	48.88
2014/12/02	01:19:50	205	West	41.72
2014/12/03	01:40:24	1	West	65.05
2014/12/06	01:06:08	203	West	12.18
2014/12/07	01:26:42	206	West	51.66
2014/12/08	01:47:16	2	West	69.73
2014/12/11	01:13:00	204	West	28.65
2014/12/12	01:33:33	207	West	59.2
2014/12/16	01:19:51	205	West	41.74
2014/12/17	01:40:24	1	West	65.05
2014/12/20	01:06:07	203	West	12.17
2014/12/21	01:26:42	206	West	51.66
2014/12/22	01:47:15	2	West	69.73
2014/12/25	01:12:59	204	West	28.63
2014/12/26	01:33:33	207	West	59.2
2014/12/30	01:19:51	205	West	41.74
2014/12/31	01:40:24	1	West	65.05
2015/01/03	01:06:08	203	West	12.2
2015/01/04	01:26:42	206	West	51.66
2015/01/05	01:47:15	2	West	69.73
2015/01/08	01:12:59	204	West	28.63
2015/01/09	01:33:33	207	West	59.2
2015/01/13	01:19:50	205	West	41.74
2015/01/14	01:40:24	1	West	65.05
2015/01/17	01:06:07	203	West	12.19
2015/01/18	01:26:41	206	West	51.66
2015/01/19	01:47:15	2	West	69.73
2015/01/22	01:12:59	204	West	28.65
2015/01/23	01:33:32	207	West	59.2
2015/01/27	01:19:50	205	West	41.73
2015/01/28	01:40:23	1	West	65.05
2015/01/31	01:06:07	203	West	12.18
2015/02/01	01:26:41	206	West	51.66
2015/02/02	01:47:14	2	West	69.73
2015/02/05	01:12:59	204	West	28.64
2015/02/06	01:33:33	207	West	59.2
2015/02/10	01:19:50	205	West	41.73

APPENDIX B. PLOTS OF PALSAR-2 POINT SPREAD FUNCTIONS MEASURED FROM IMAGES

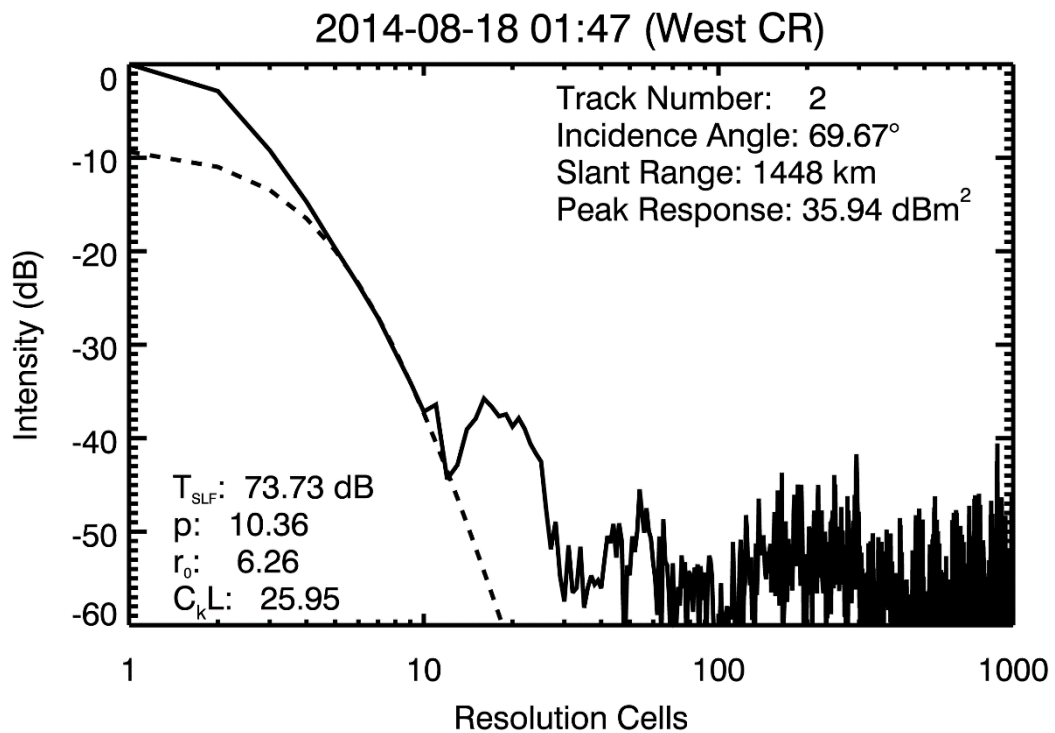


Figure B.1: PALSAR-2 PSF – 2014-08-18

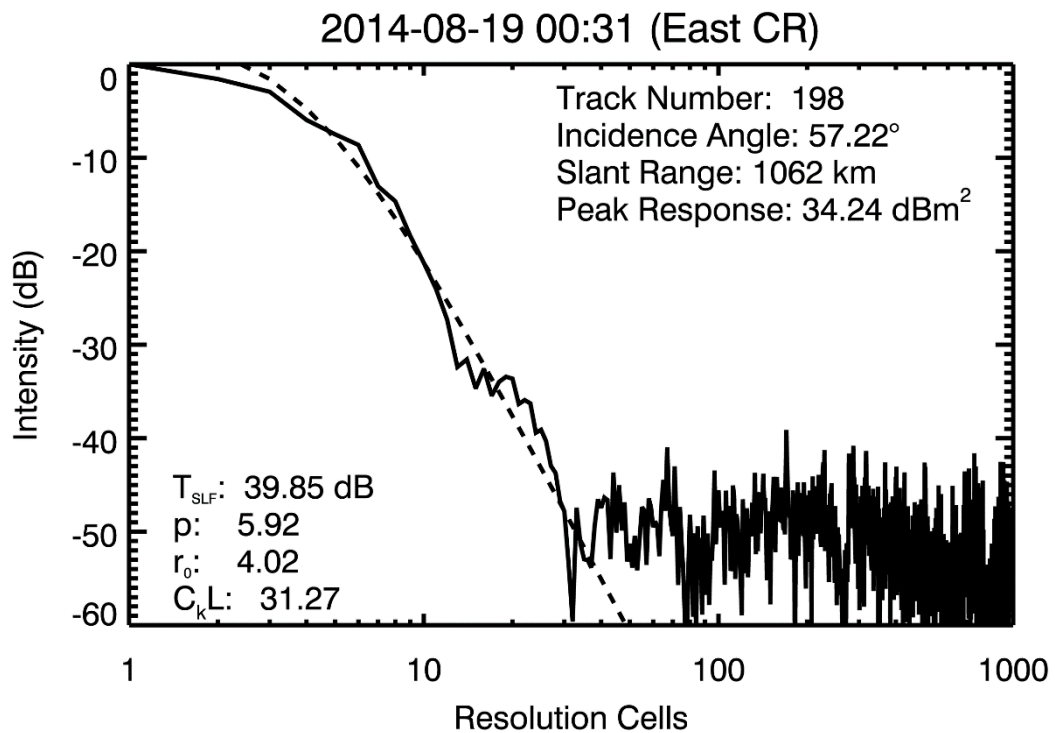


Figure B.2: PALSAR-2 PSF - 2014-08-19

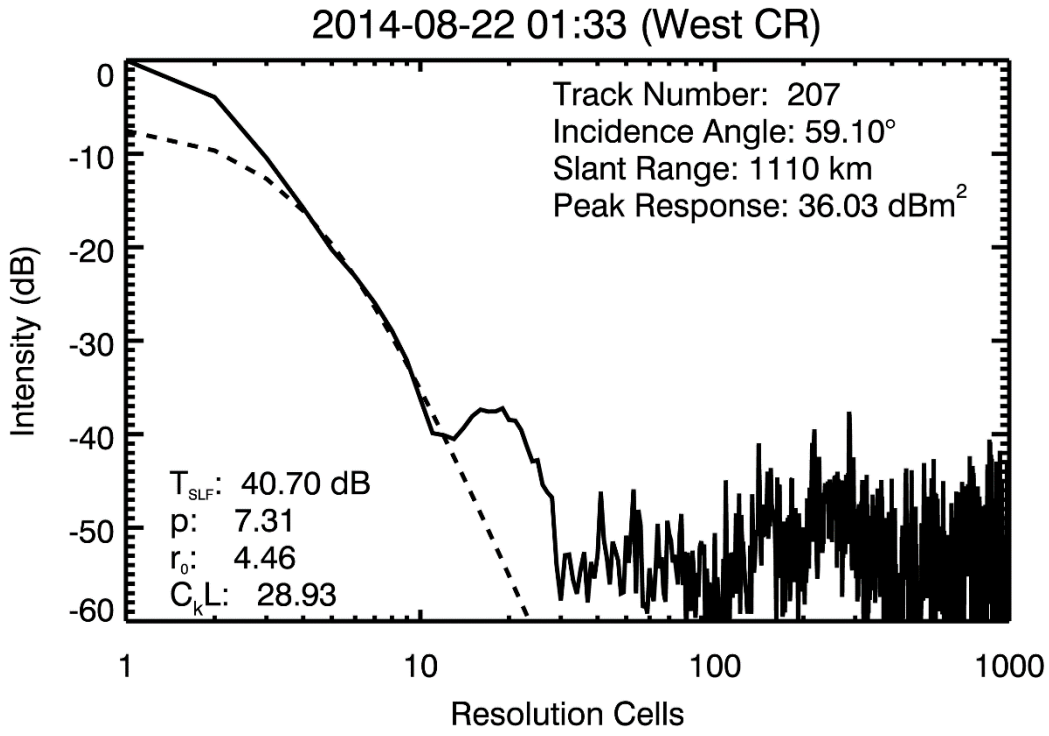


Figure B.3: PALSAR-2 PSF - 2014-08-22

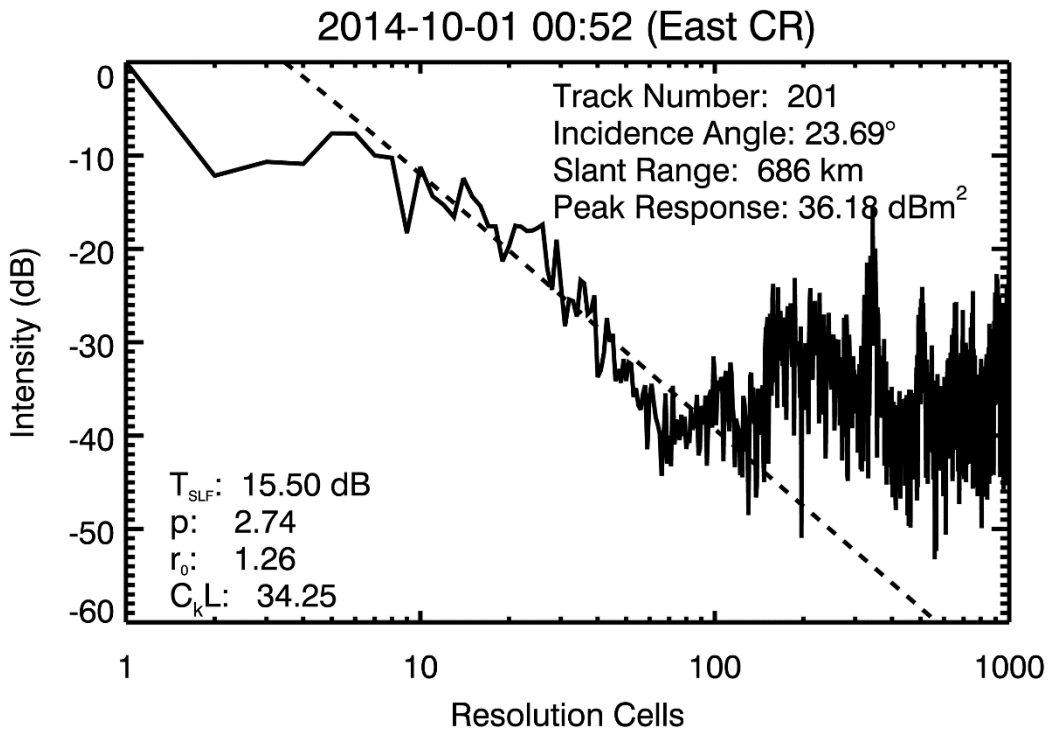


Figure B.4: PALSAR-2 PSF - 2014-10-01

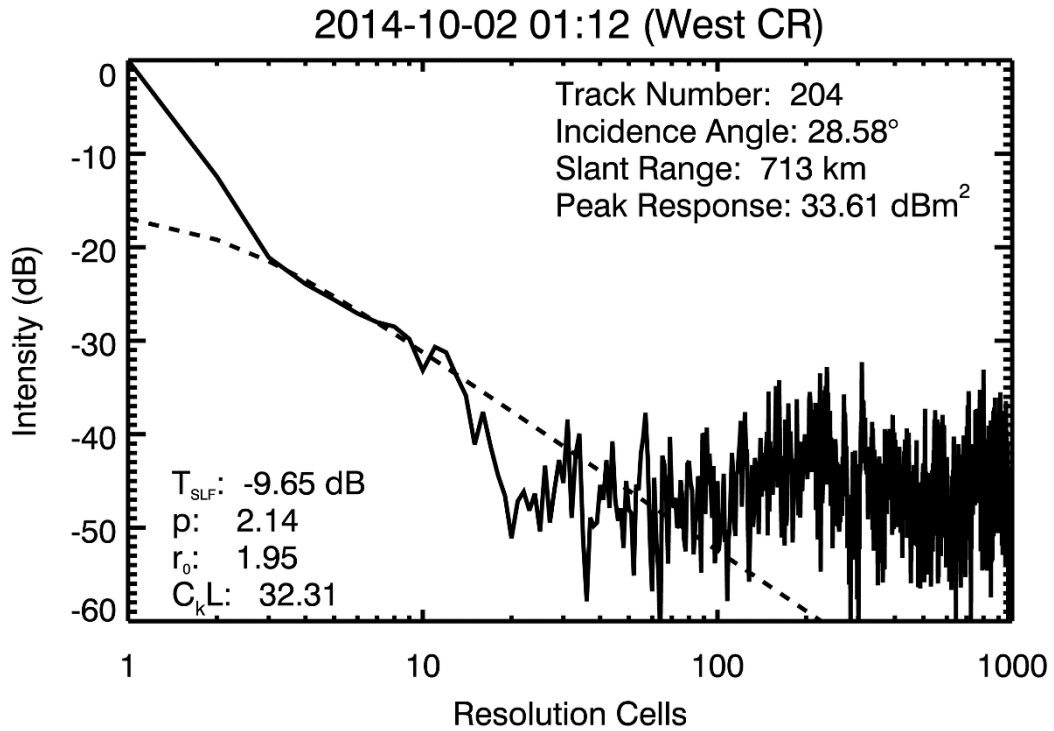


Figure B.5: PALSAR-2 PSF - 2014-10-02

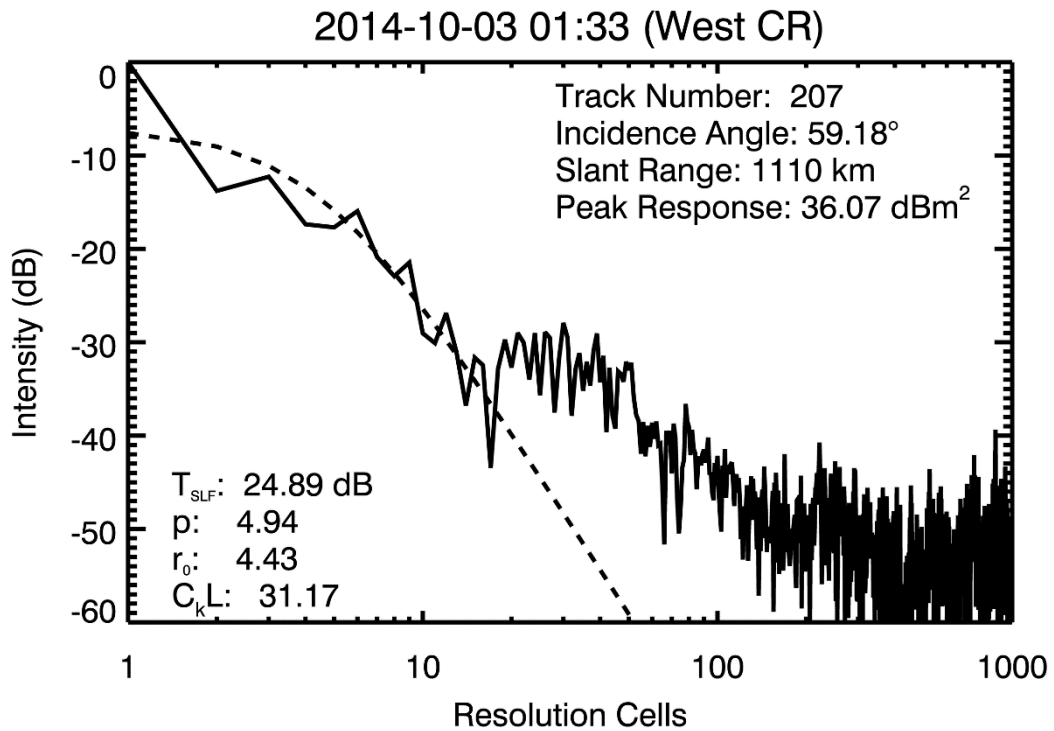


Figure B.6: PALSAR-2 PSF - 2014-10-03

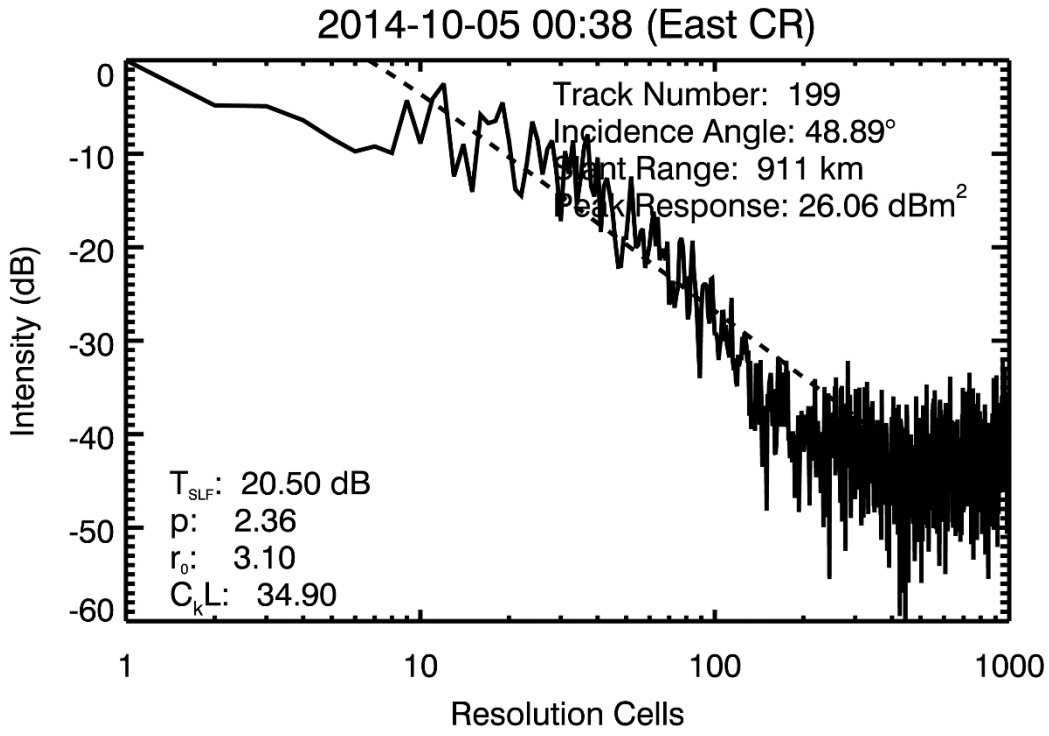


Figure B.7: PALSAR-2 PSF - 2014-10-05

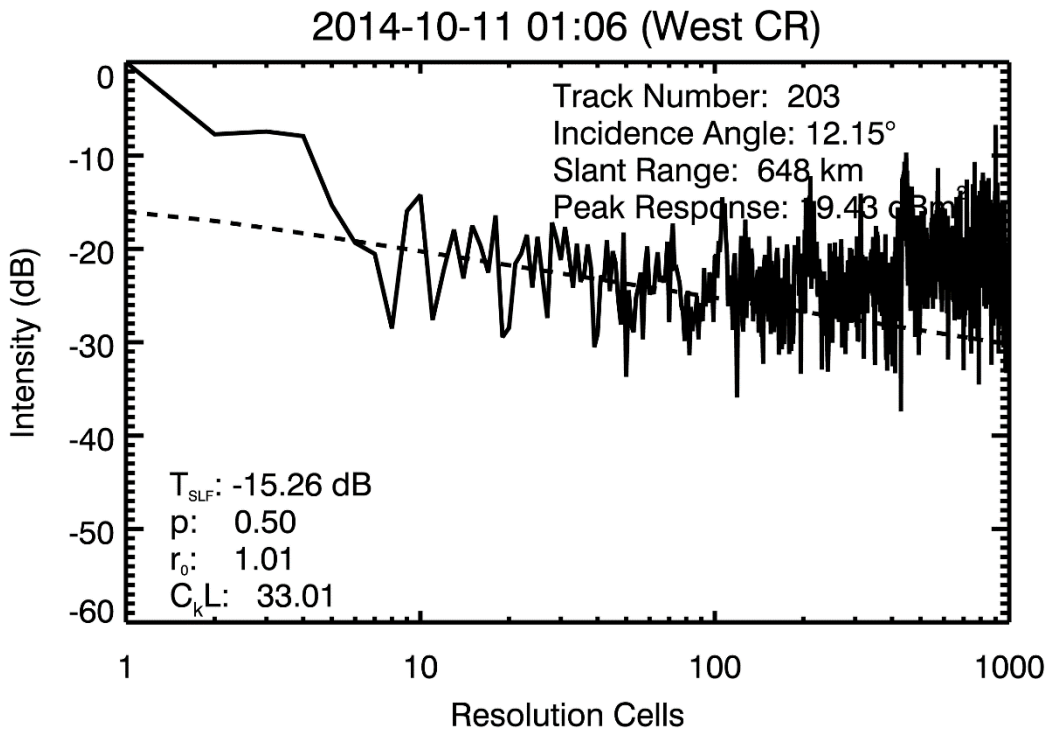


Figure B.8: PALSAR-2 PSF - 2014-10-11

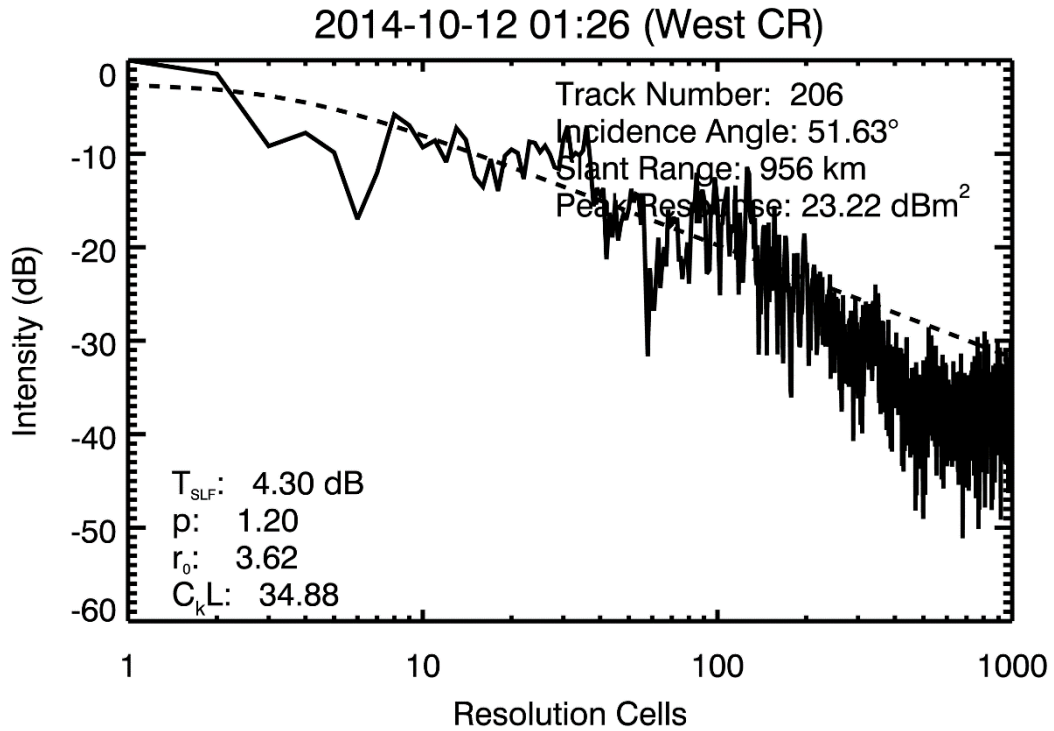


Figure B.9: PALSAR-2 PSF - 2014-10-12

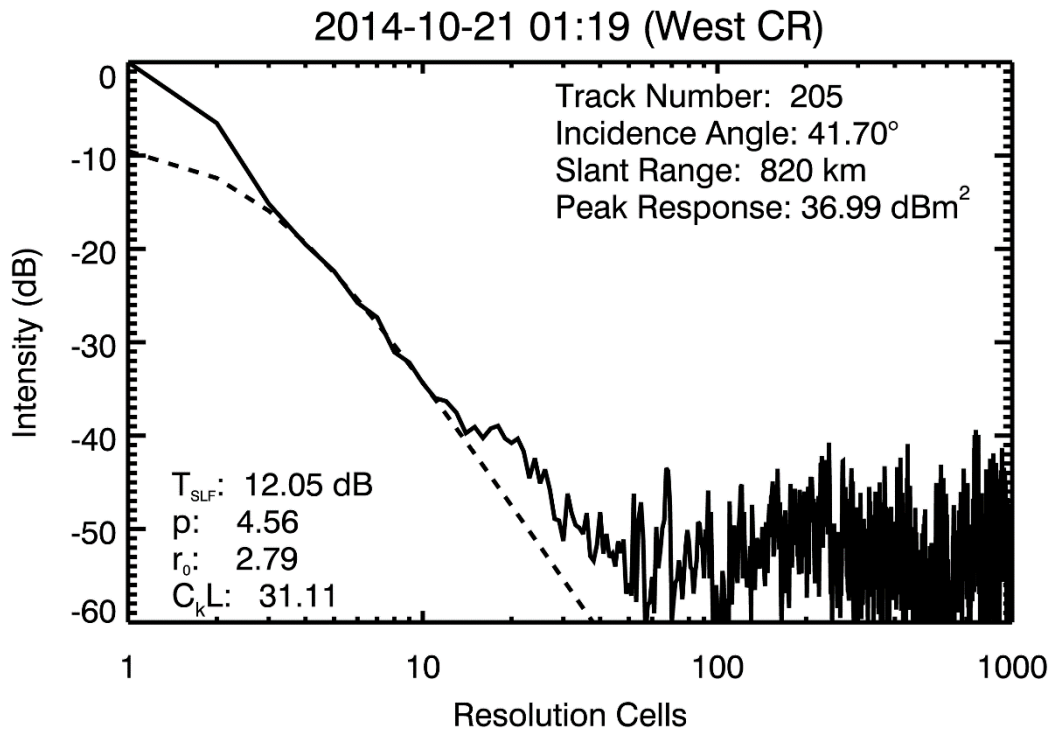


Figure B.10: PALSAR-2 PSF - 2014-10-21

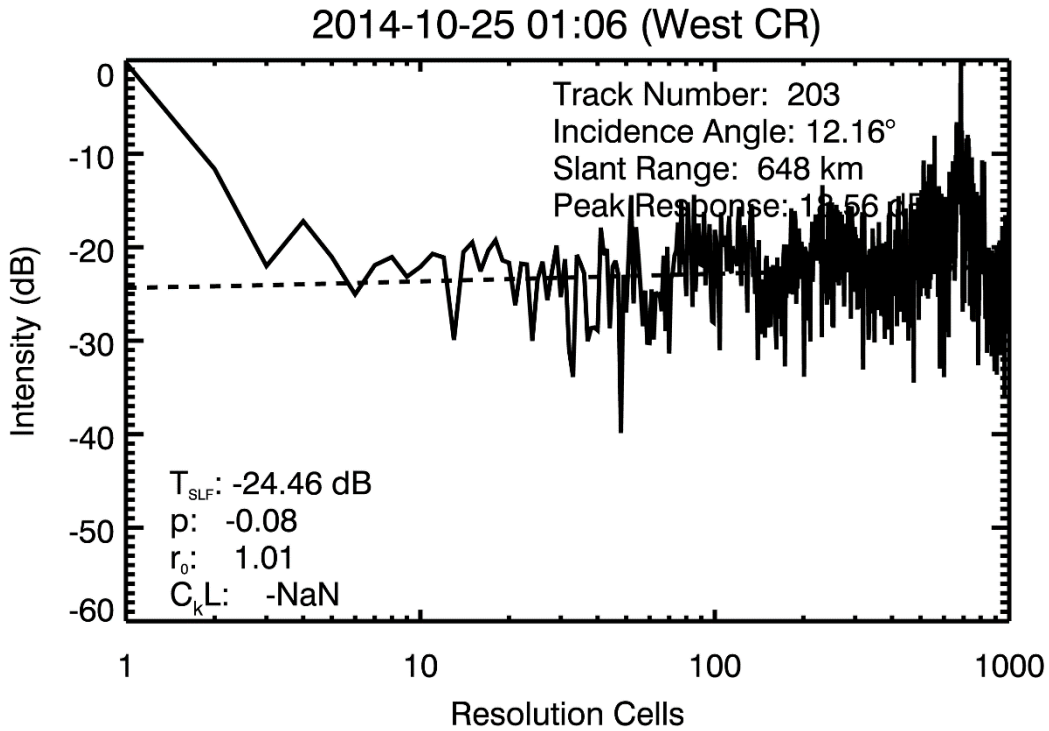


Figure B.11: PALSAR-2 PSF - 2014-10-25

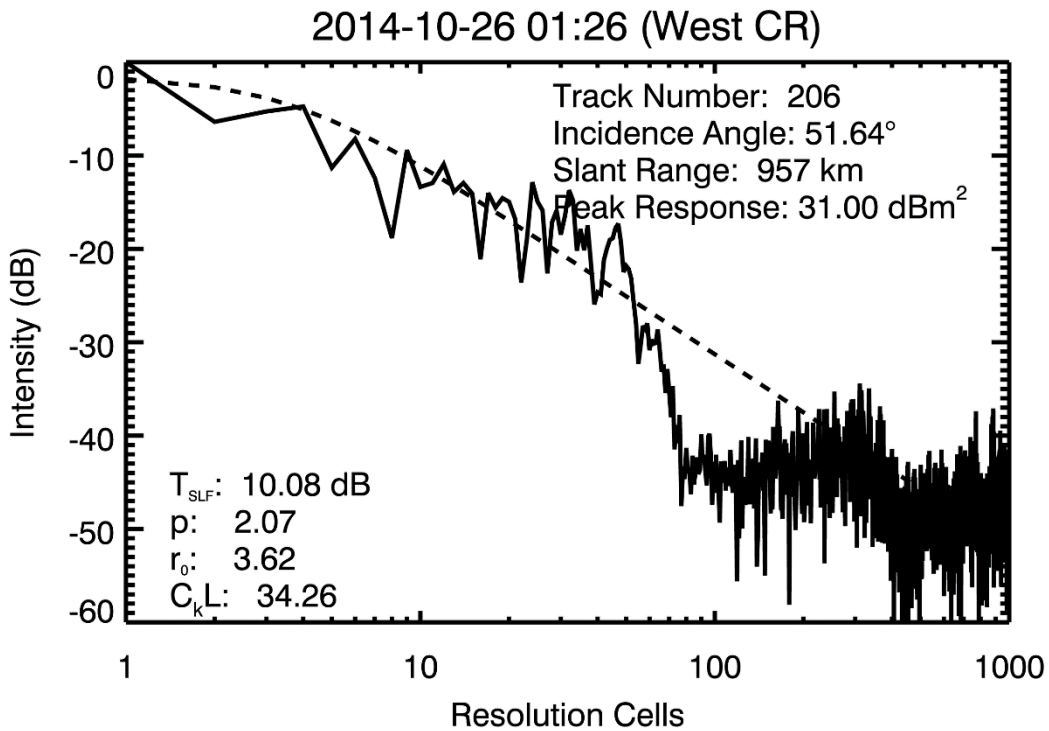


Figure B.12: PALSAR-2 PSF - 2014-10-26

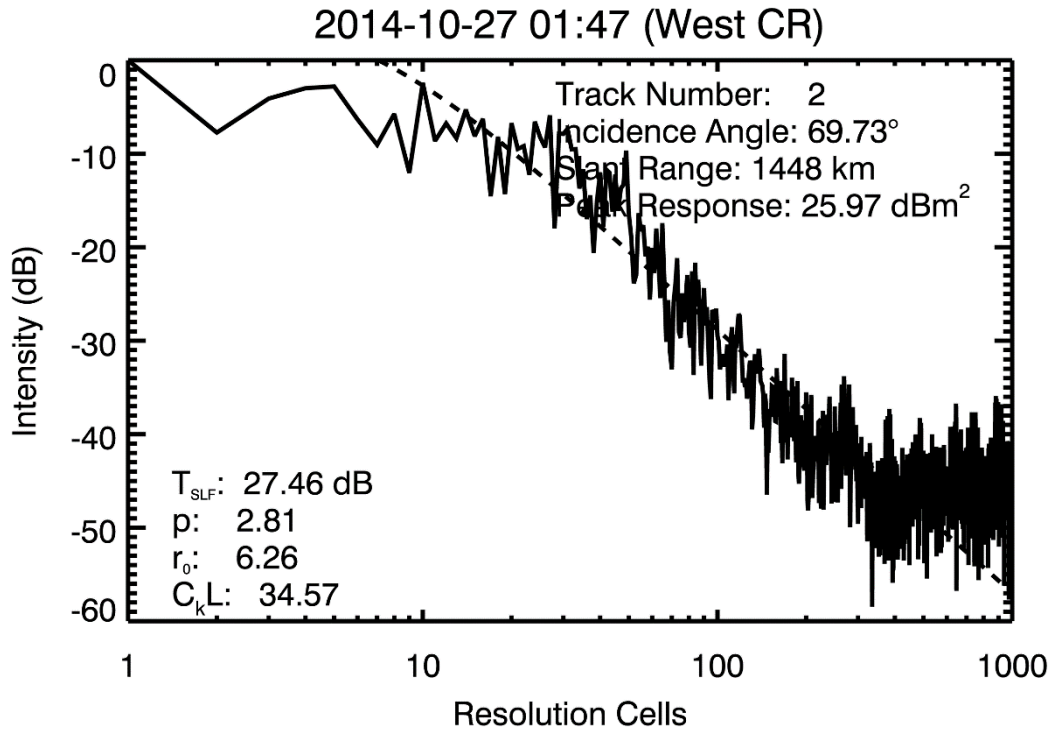


Figure B.13: PALSAR-2 PSF - 2014-10-27

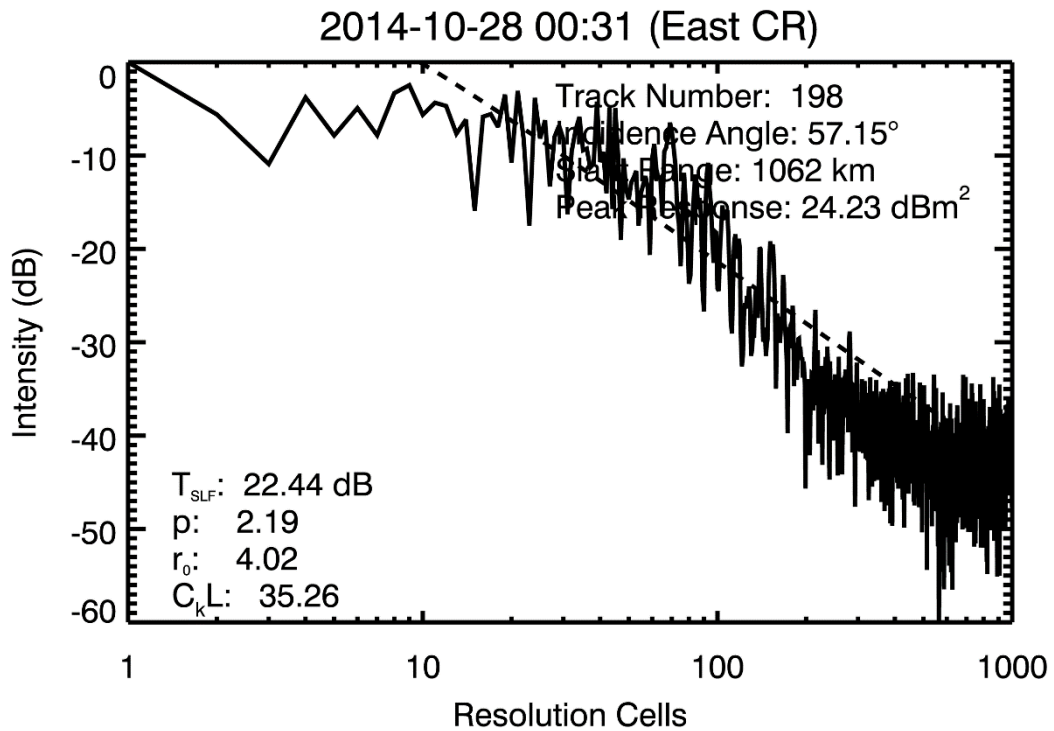


Figure B.14: PALSAR-2 PSF - 2014-10-28

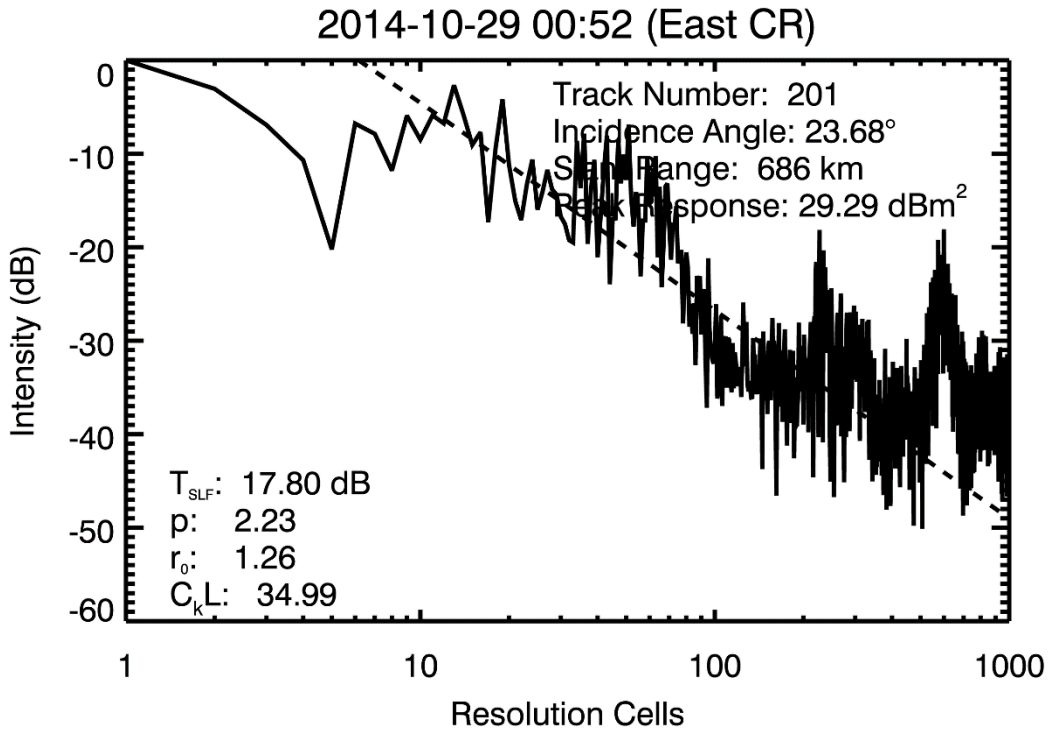


Figure B.15: PALSAR-2 PSF - 2014-10-29

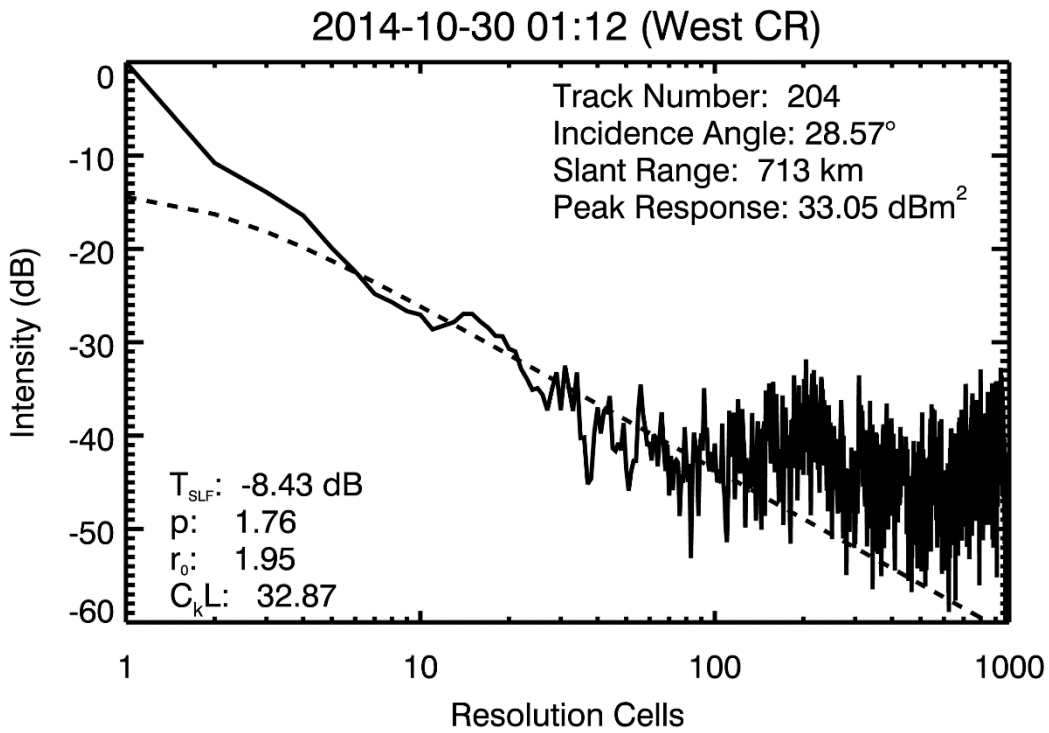


Figure B.16: PALSAR-2 PSF - 2014-10-30

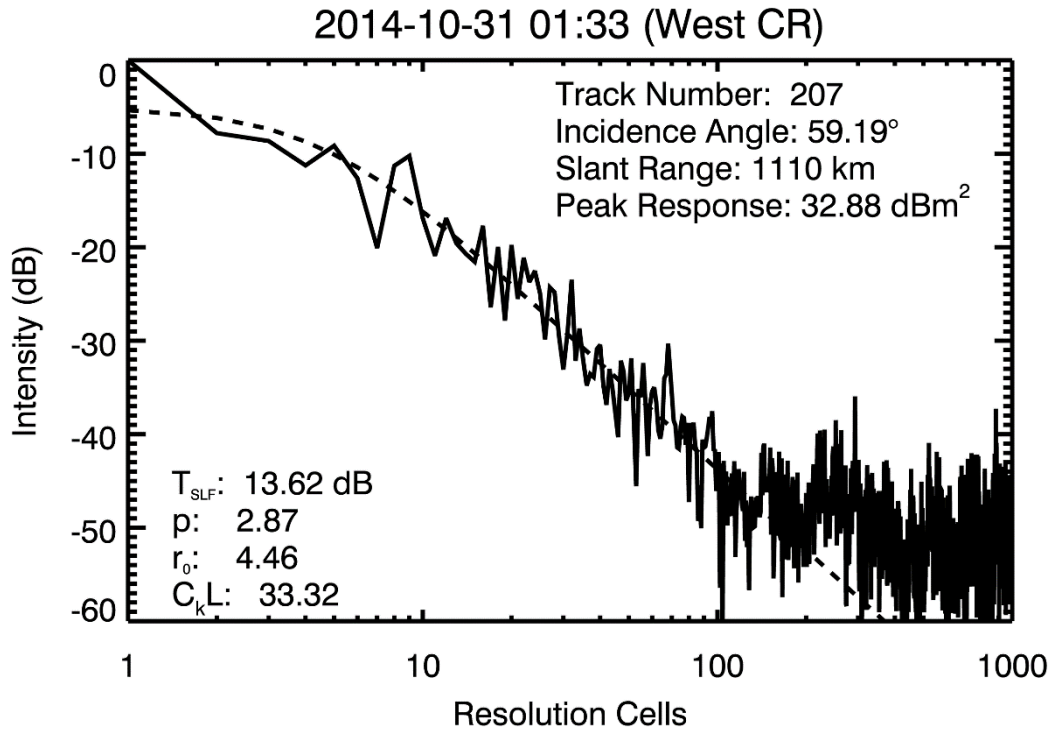


Figure B.17: PALSAR-2 PSF - 2014-10-31

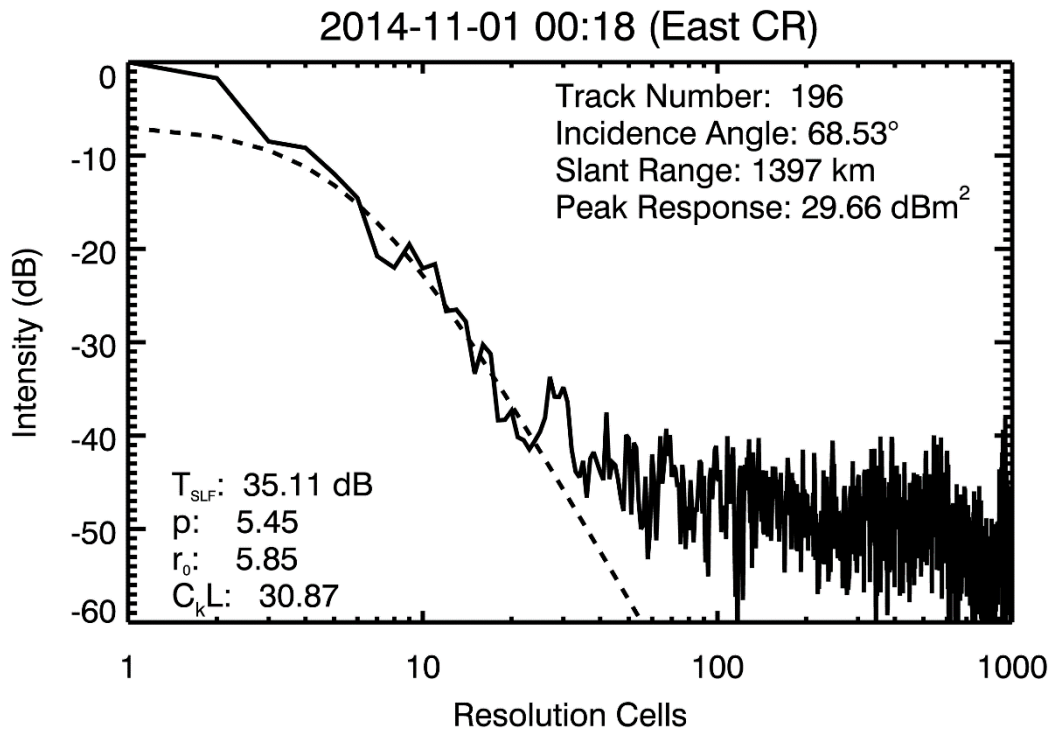


Figure B.18: PALSAR-2 PSF - 2014-11-01

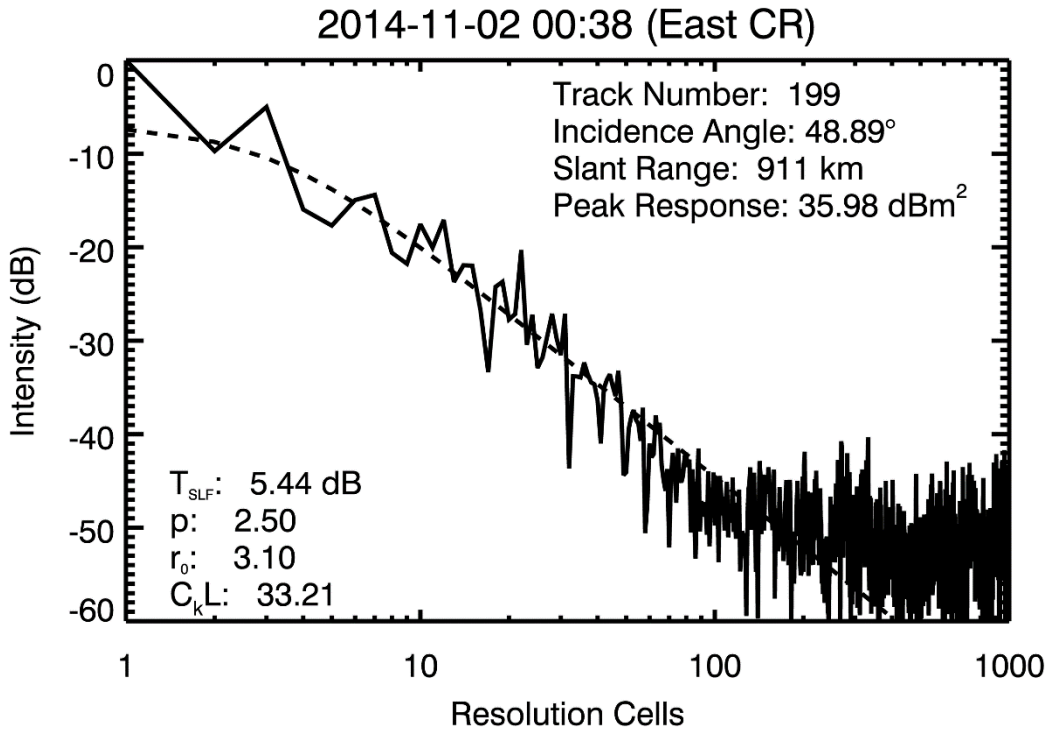


Figure B.19: PALSAR-2 PSF - 2014-11-02

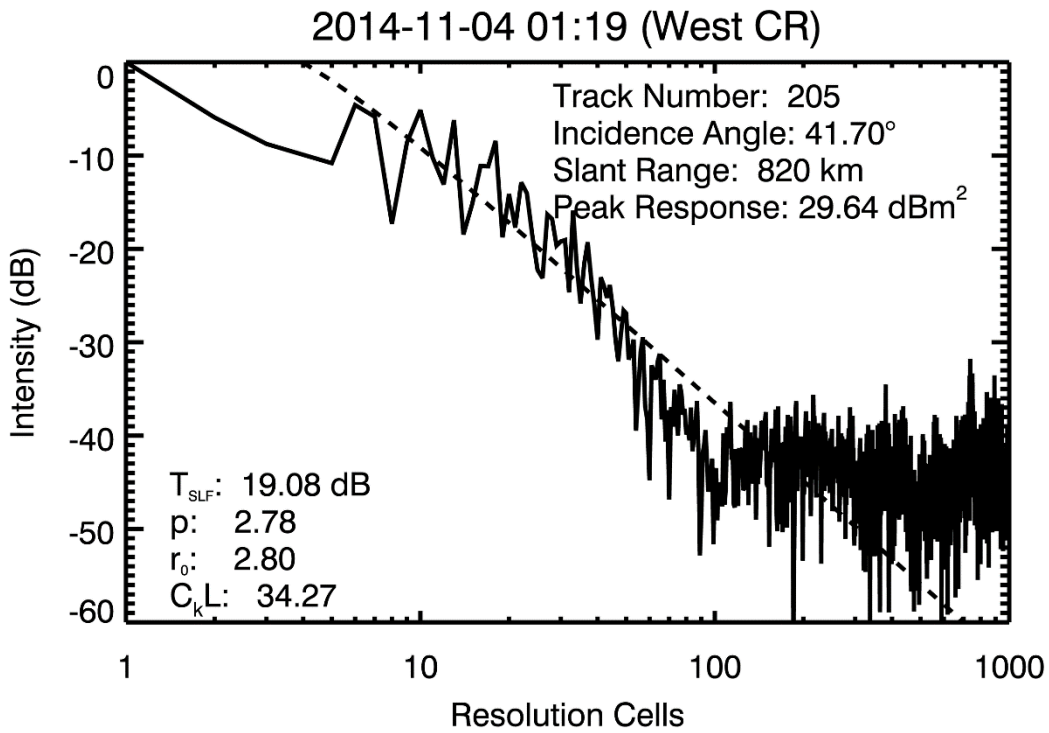


Figure B.20: PALSAR-2 PSF - 2014-11-04

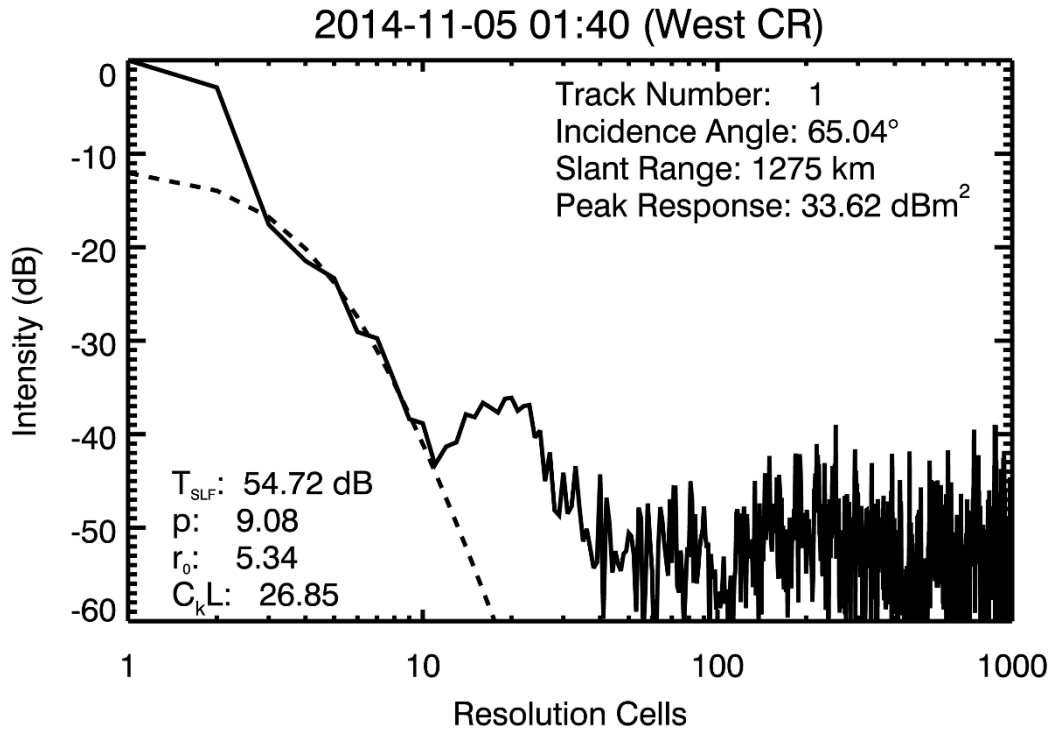


Figure B.21: PALSAR-2 PSF - 2014-11-05

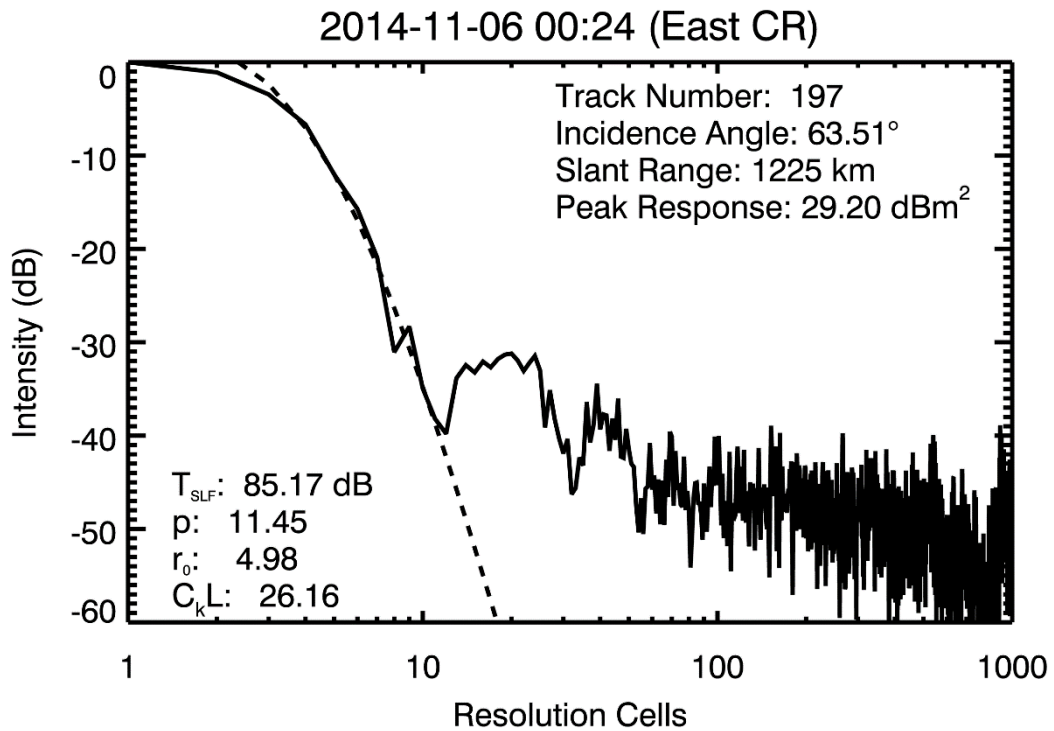


Figure B.22: PALSAR-2 PSF - 2014-11-06

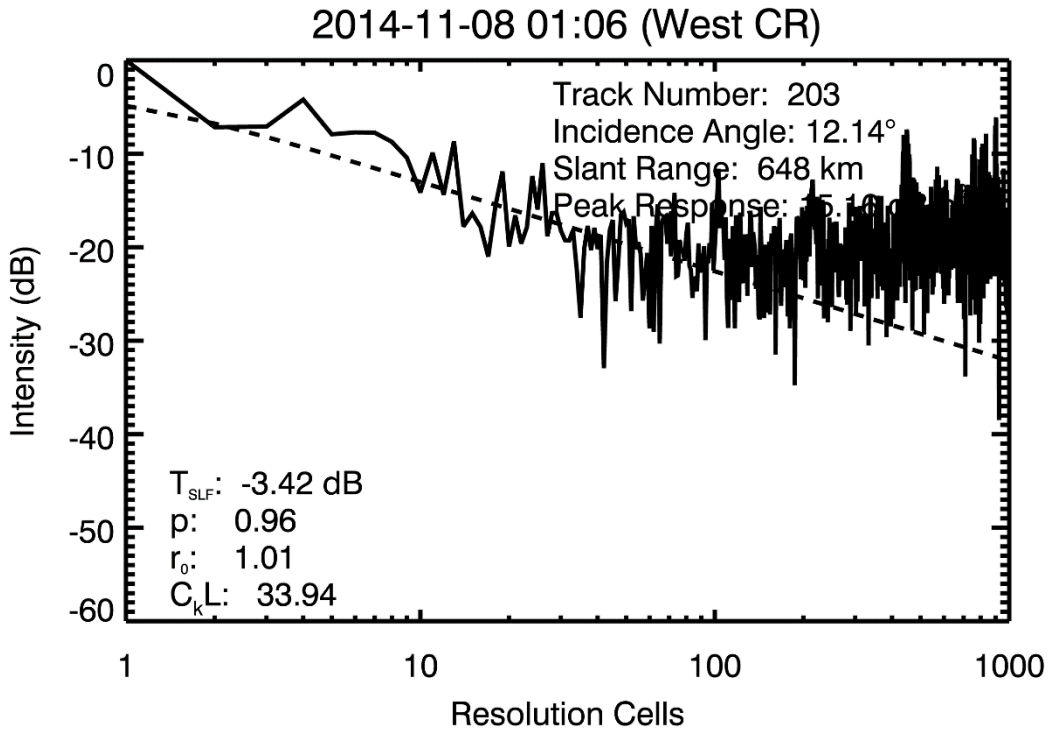


Figure B.23: PALSAR-2 PSF - 2014-11-08

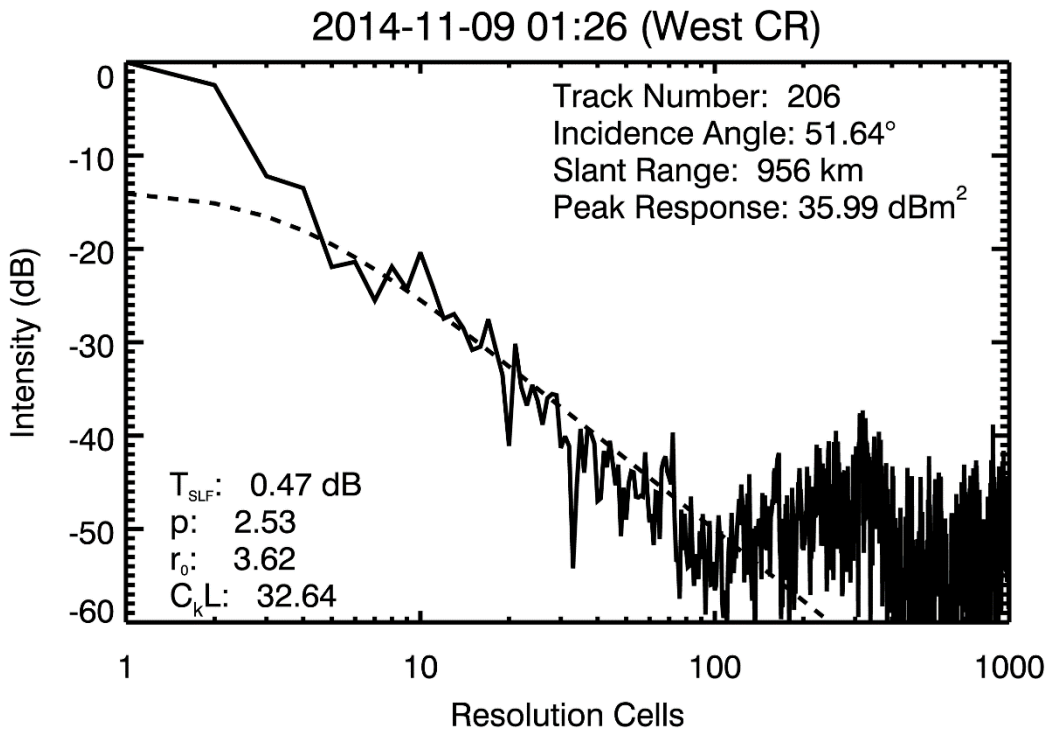


Figure B.24: PALSAR-2 PSF - 2014-11-09

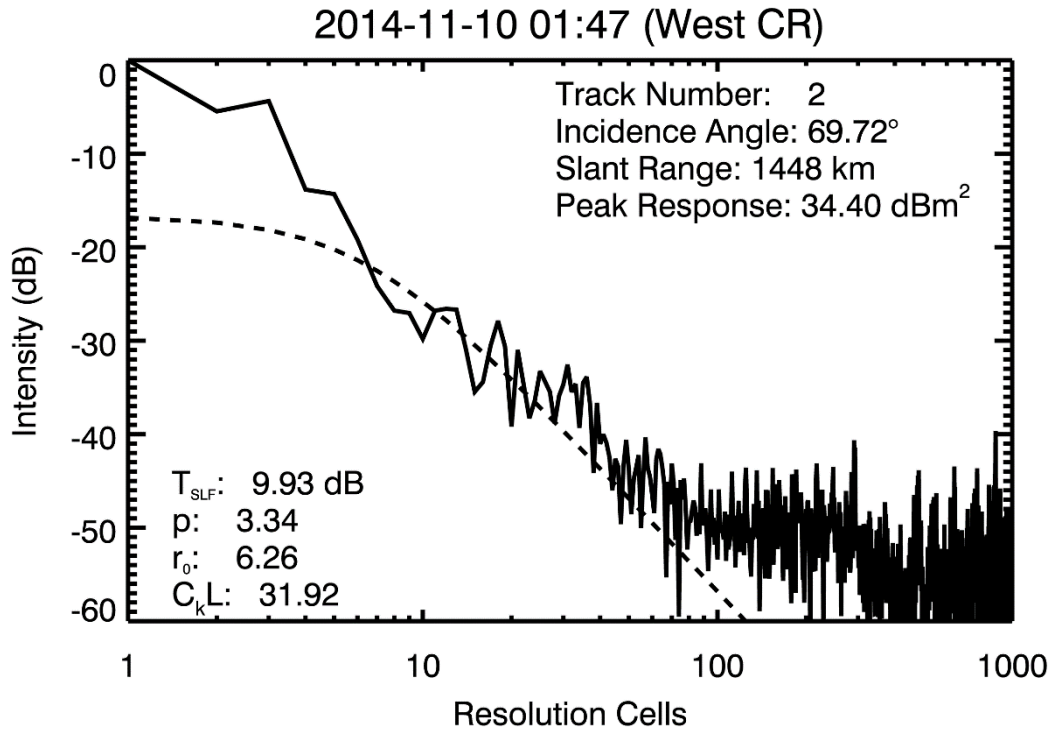


Figure B.25: PALSAR-2 PSF - 2014-11-10

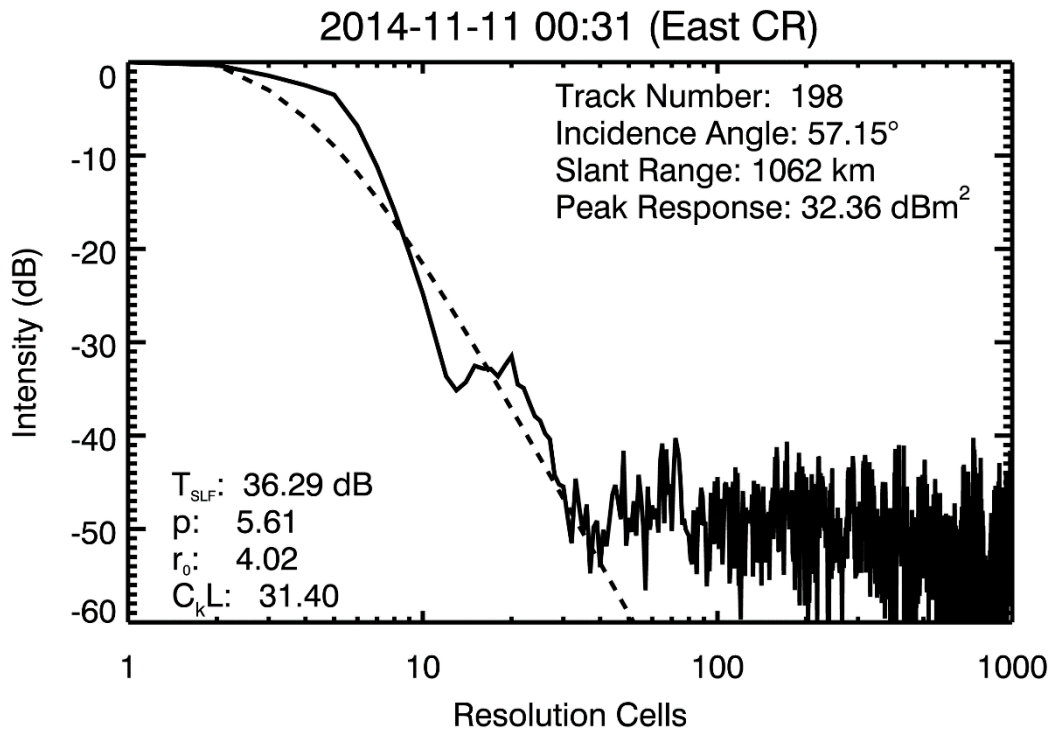


Figure B.26: PALSAR-2 PSF - 2014-11-11

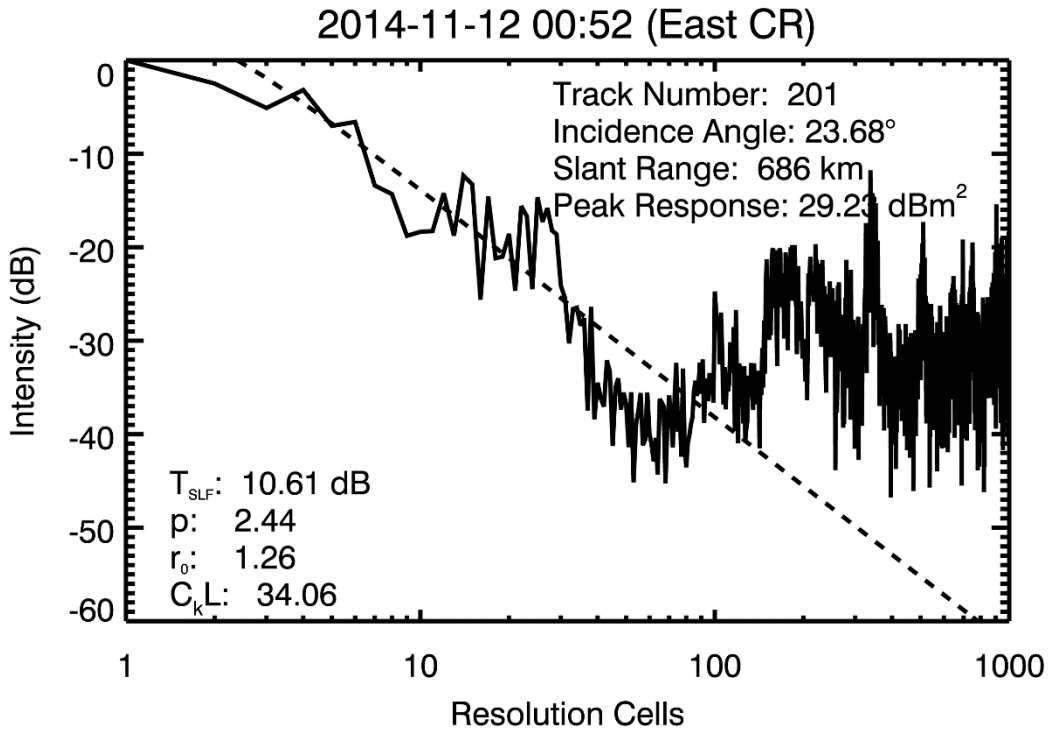


Figure B.27: PALSAR-2 PSF - 2014-11-12

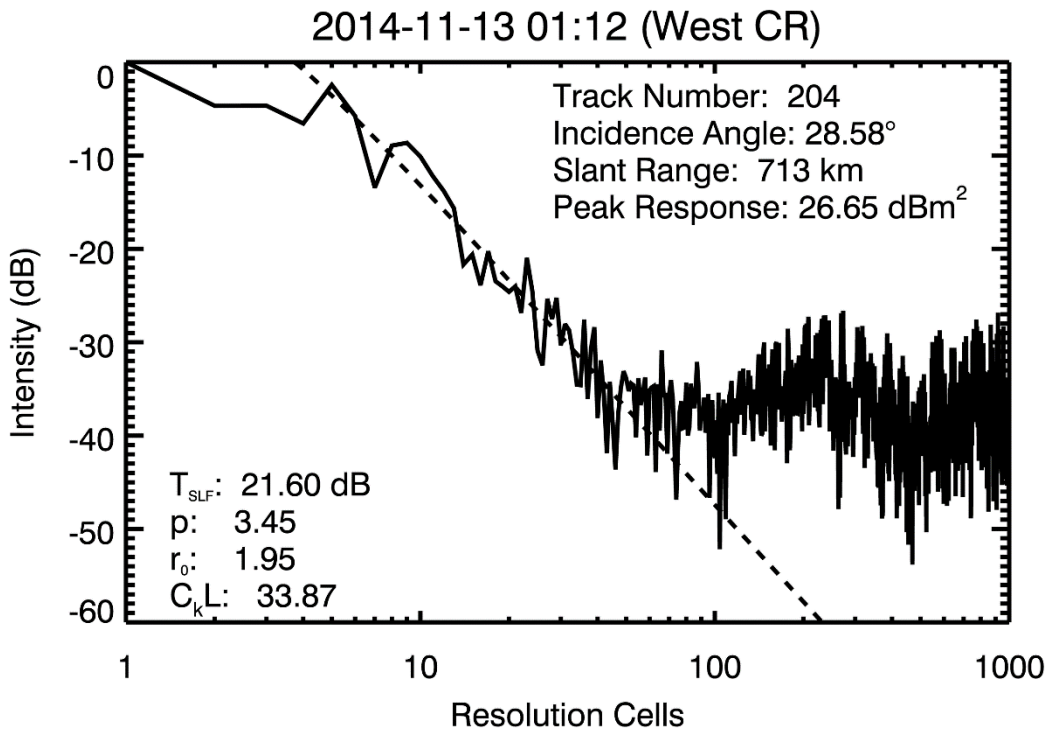


Figure B.28: PALSAR-2 PSF - 2014-11-13

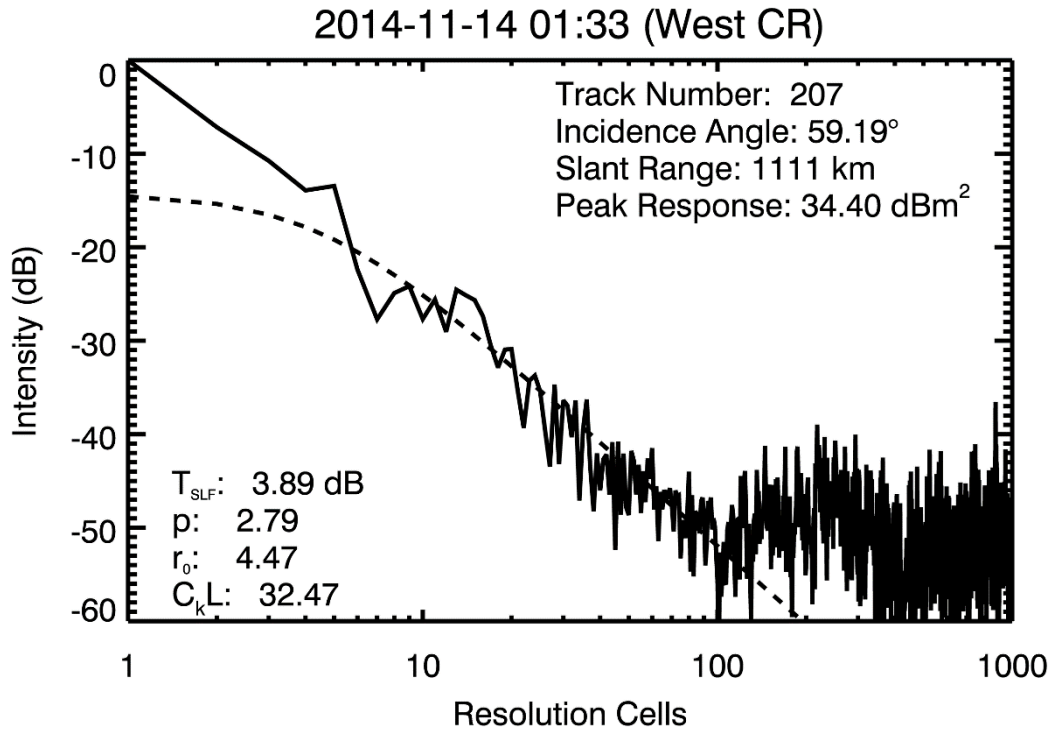


Figure B.29: PALSAR-2 PSF - 2014-11-14

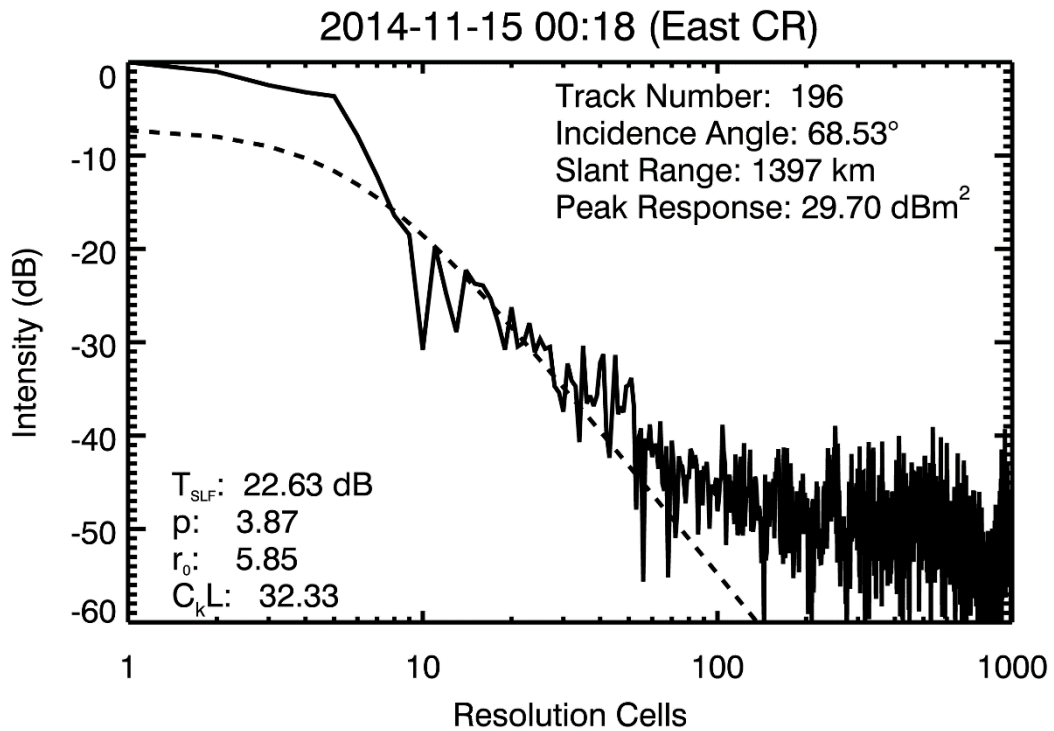


Figure B.30: PALSAR-2 PSF - 2014-11-15

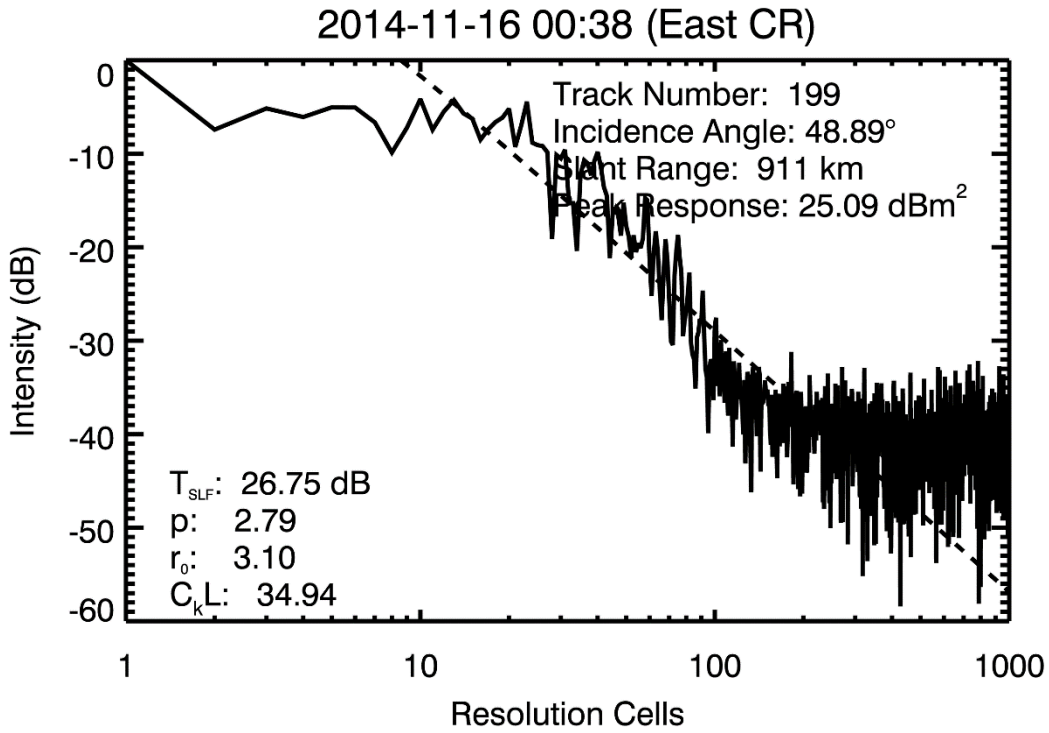


Figure B.31: PALSAR-2 PSF - 2014-11-16

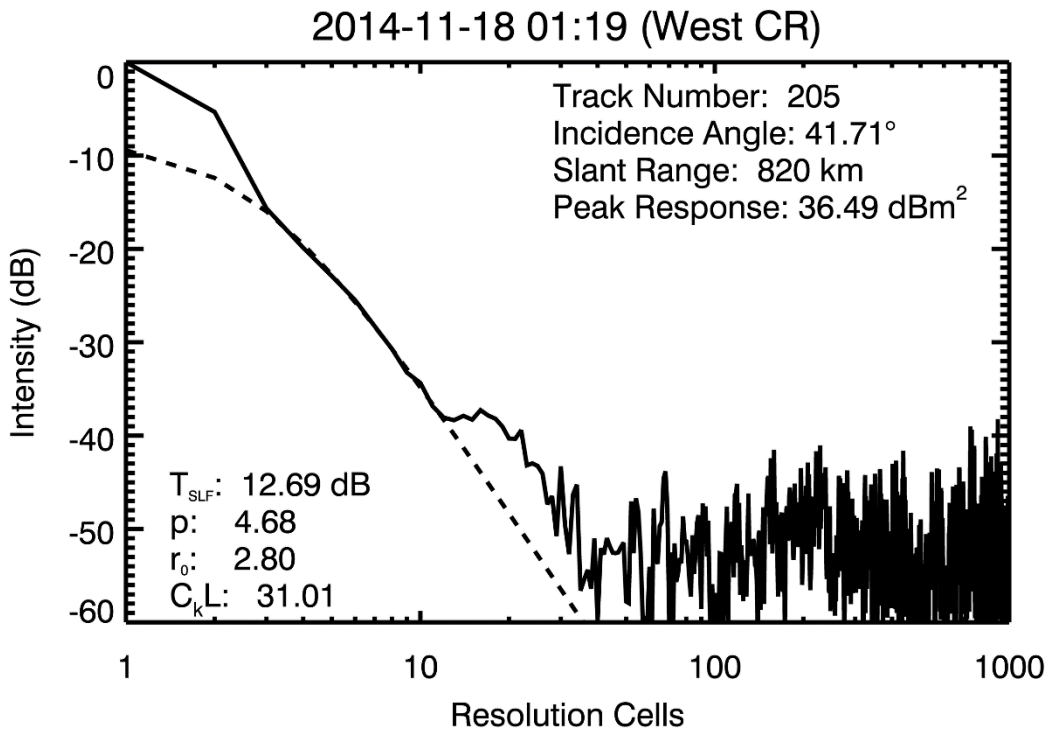


Figure B.32: PALSAR-2 PSF - 2014-11-18

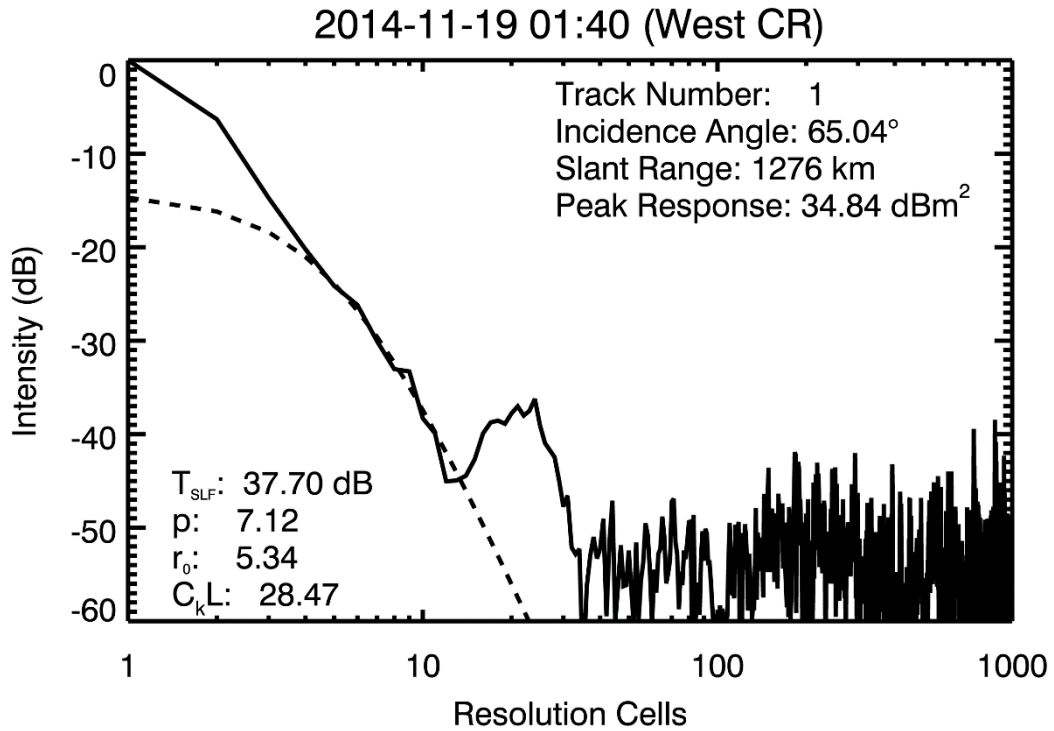


Figure B.33: PALSAR-2 PSF - 2014-11-19

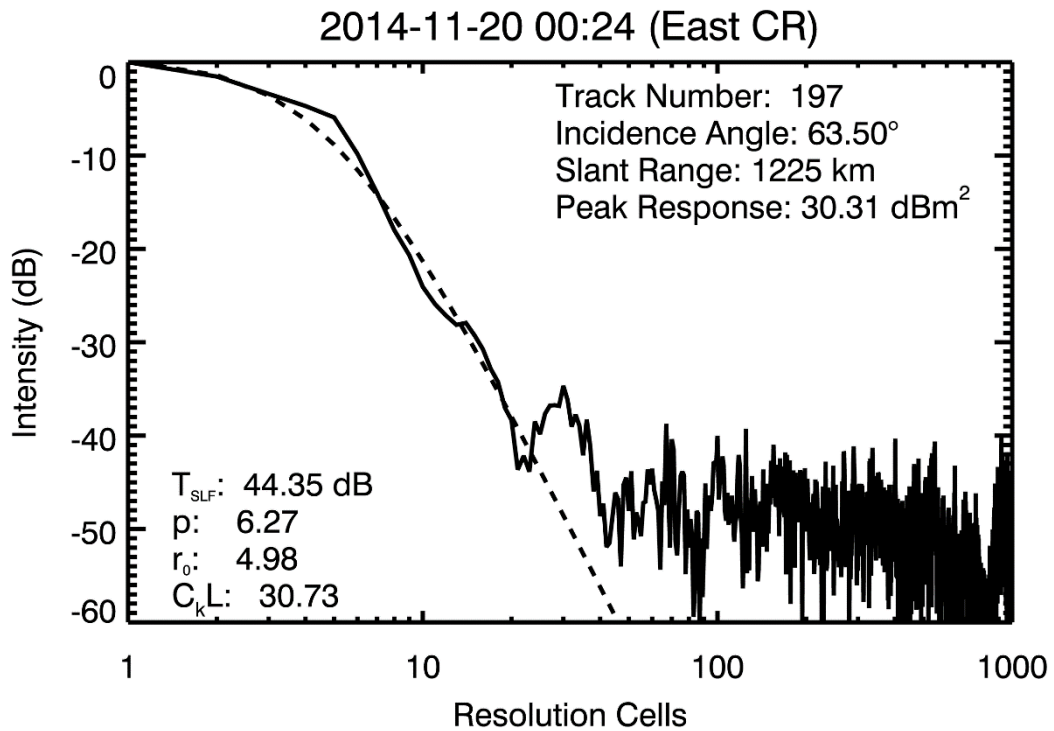


Figure B.34: PALSAR-2 PSF - 2014-11-20

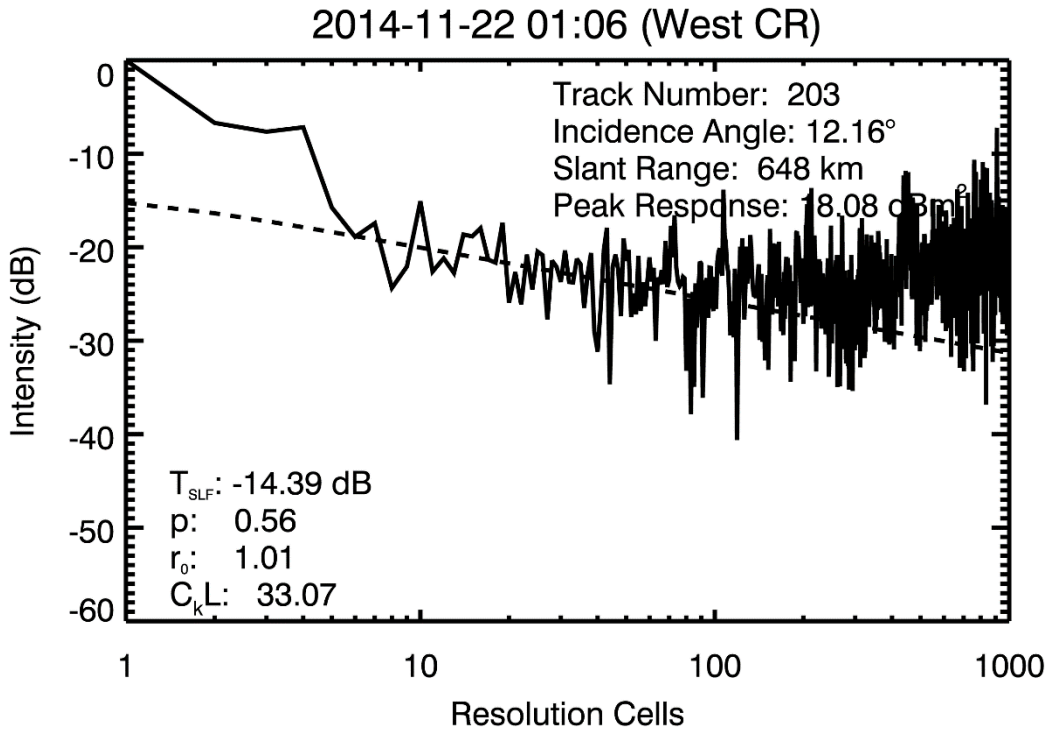


Figure B.35: PALSAR-2 PSF - 2014-11-22

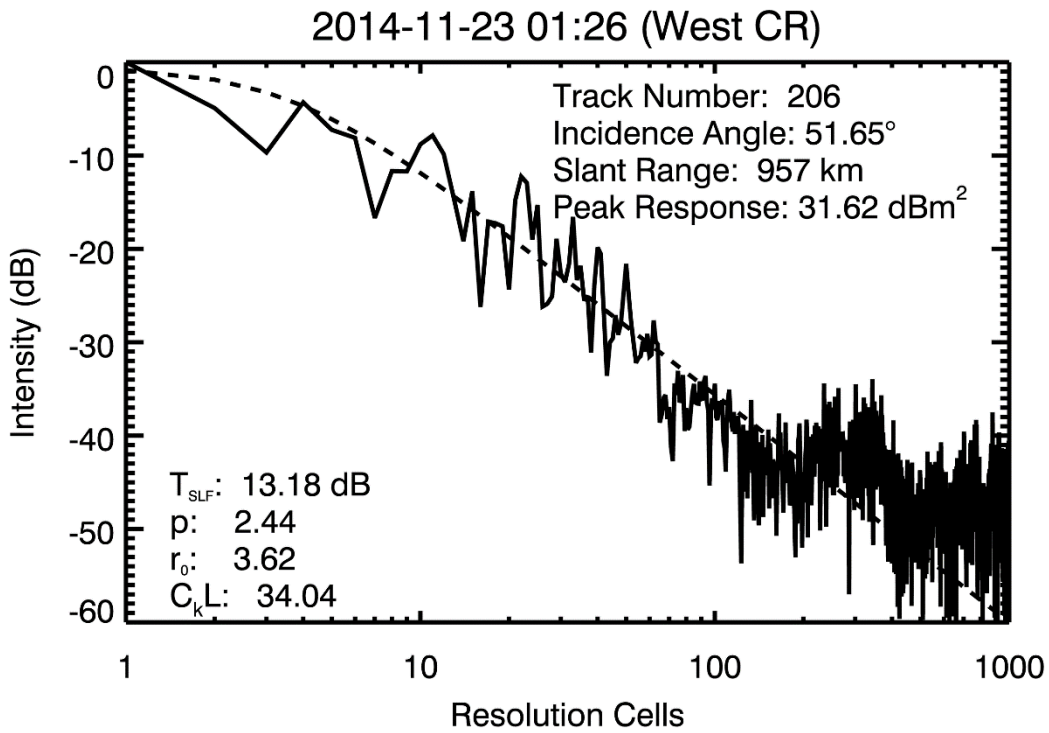


Figure B.36: PALSAR-2 PSF - 2014-11-23

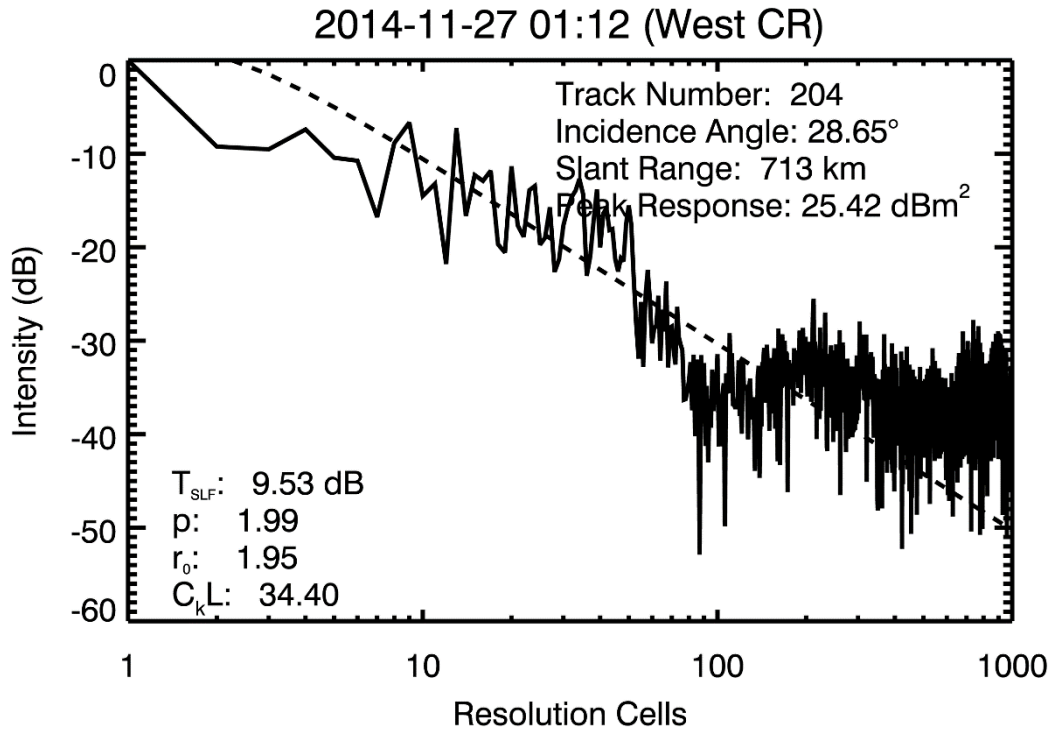


Figure B.37: PALSAR-2 PSF - 2014-11-27

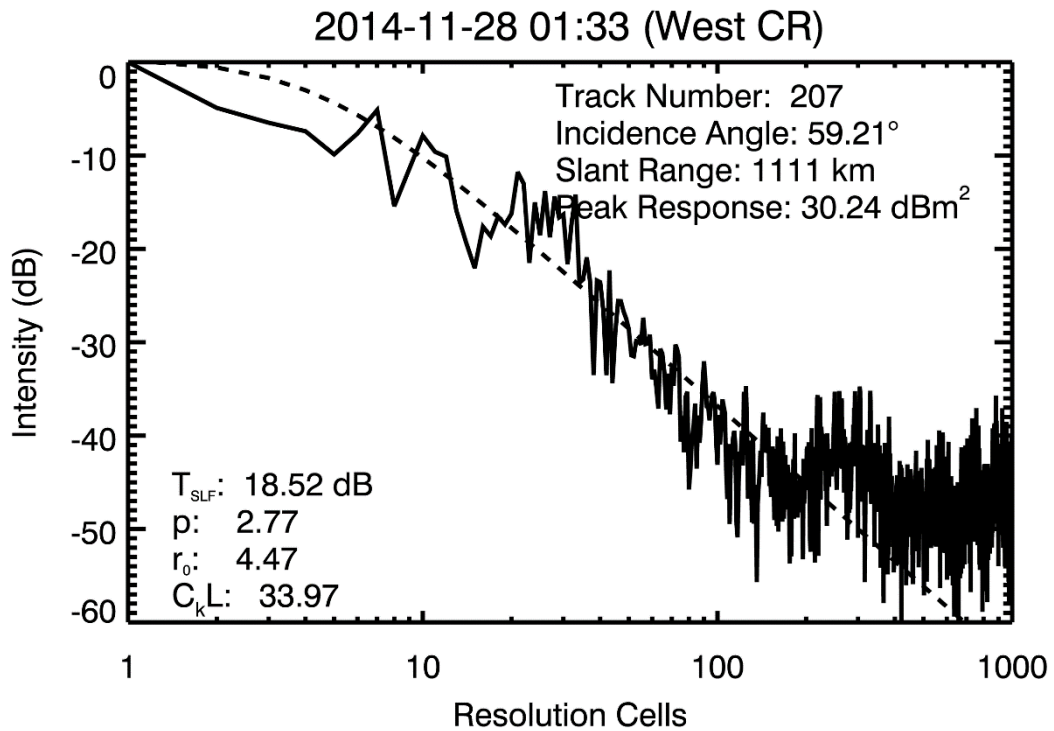


Figure B.38: PALSAR-2 PSF - 2014-11-28

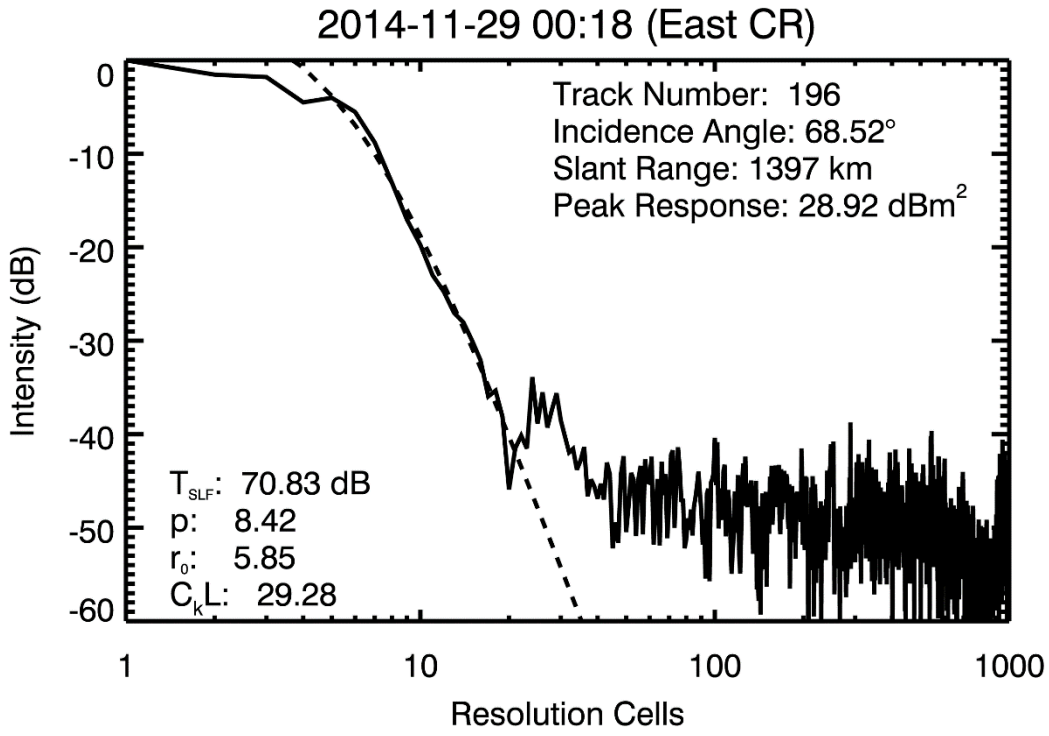


Figure B.39: PALSAR-2 PSF - 2014-11-29

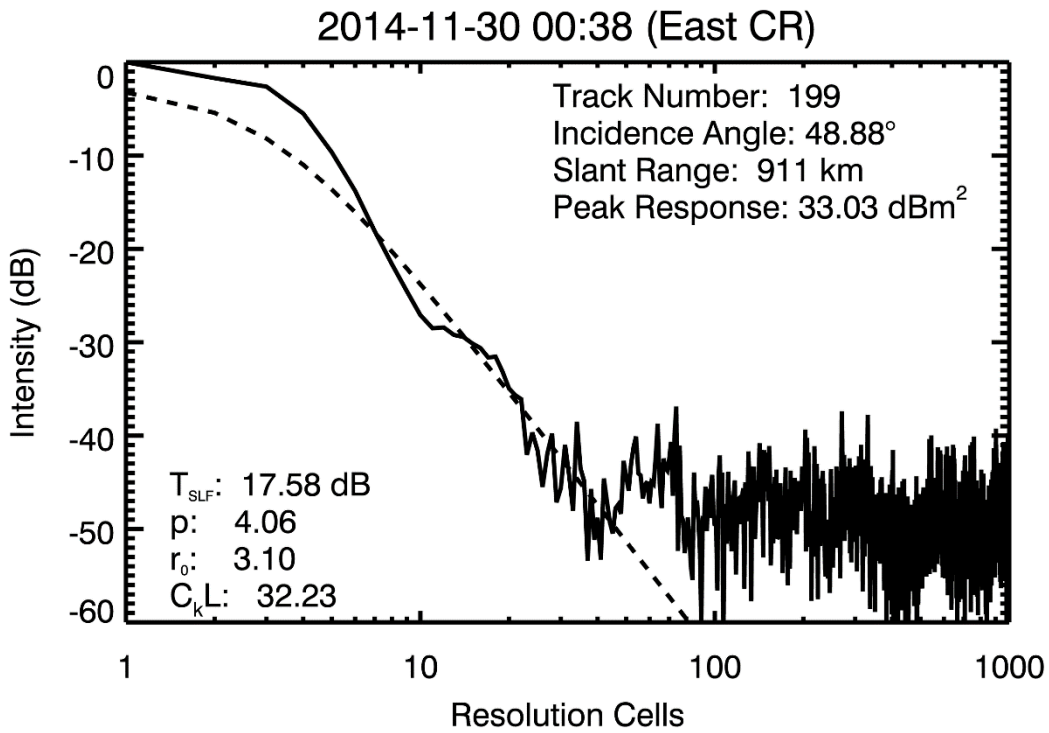


Figure B.40: PALSAR-2 PSF - 2014-11-30

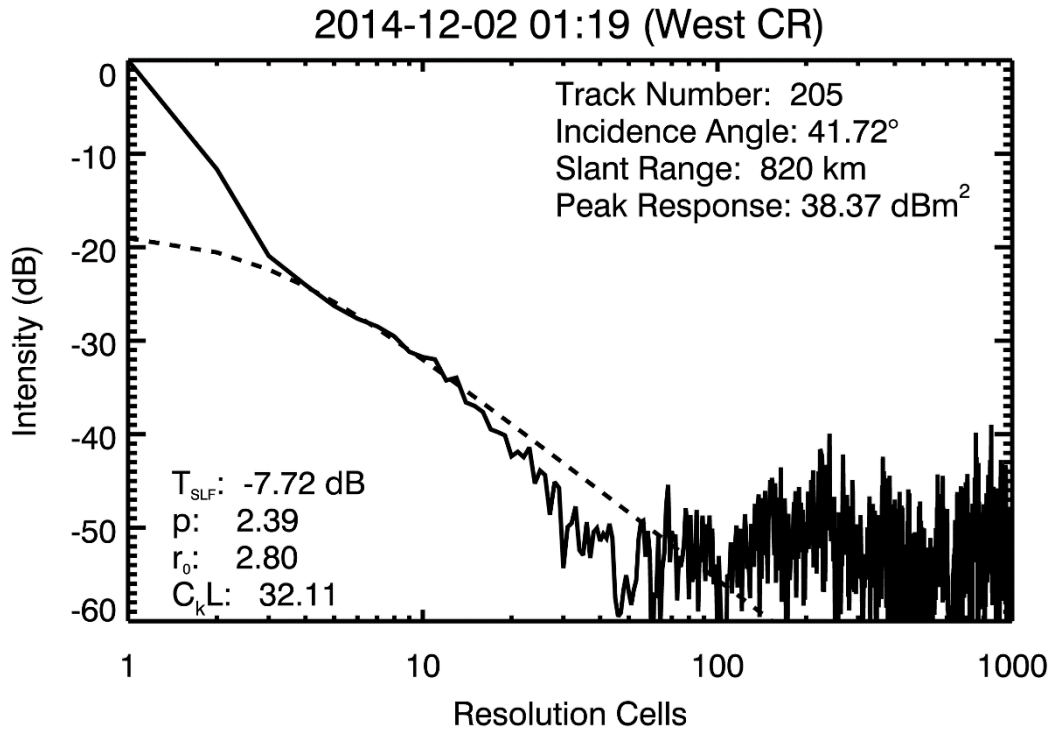


Figure B.41: PALSAR-2 PSF - 2014-12-02

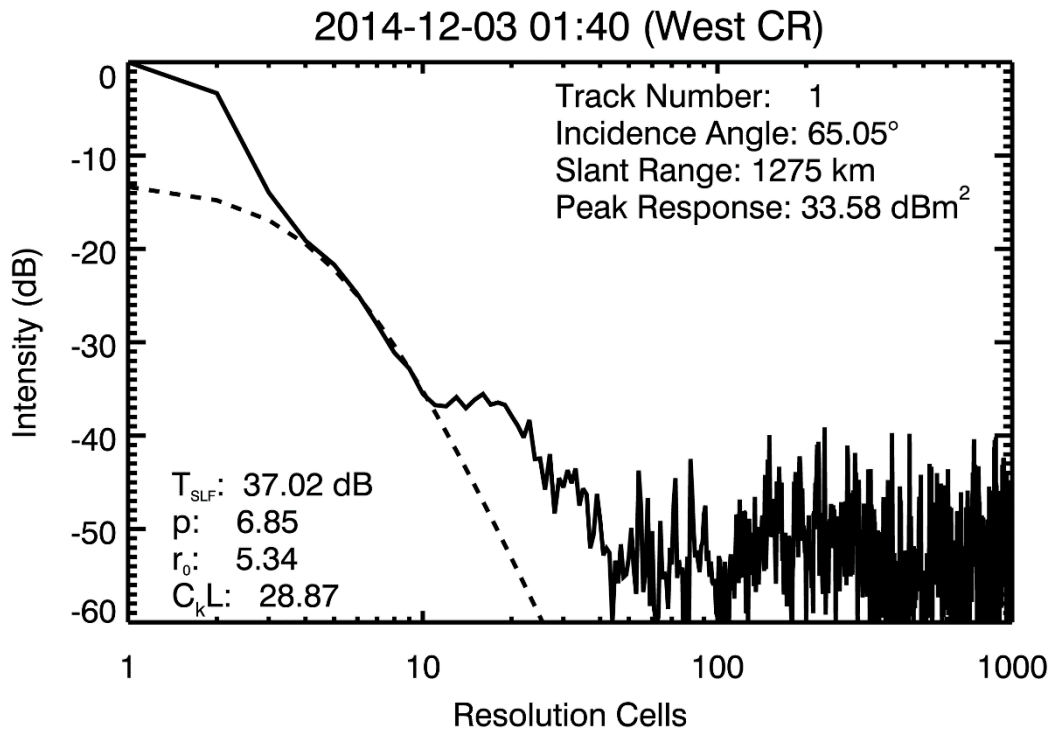


Figure B.42: PALSAR-2 PSF - 2014-12-03

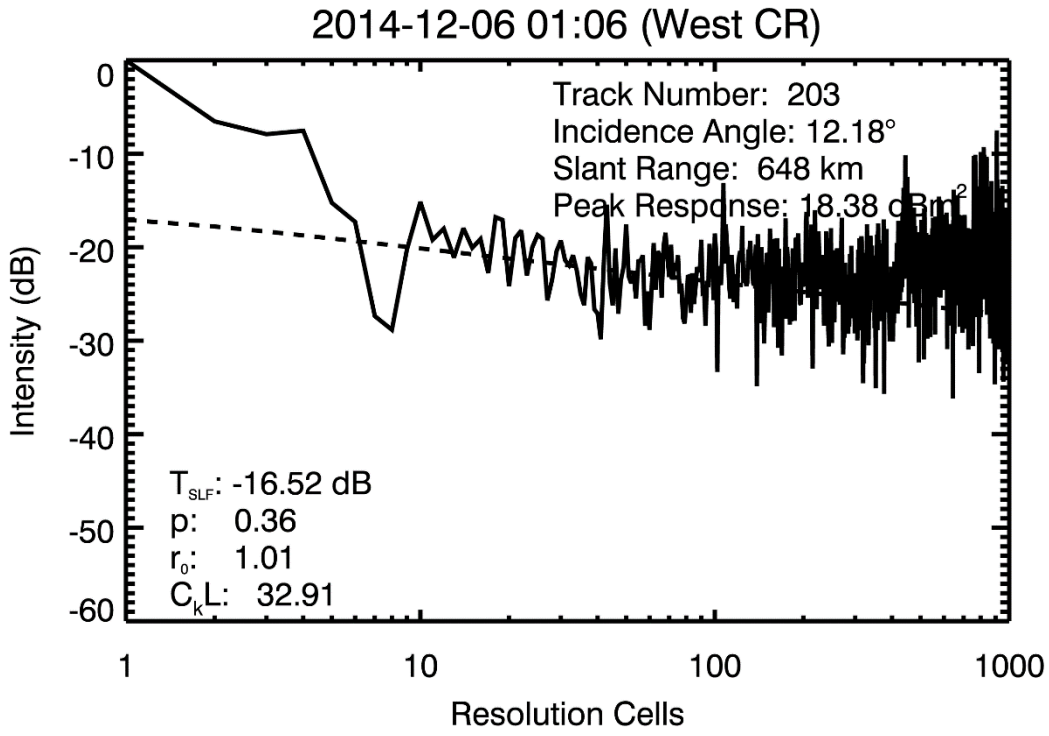


Figure B.43: PALSAR-2 PSF - 2014-12-06

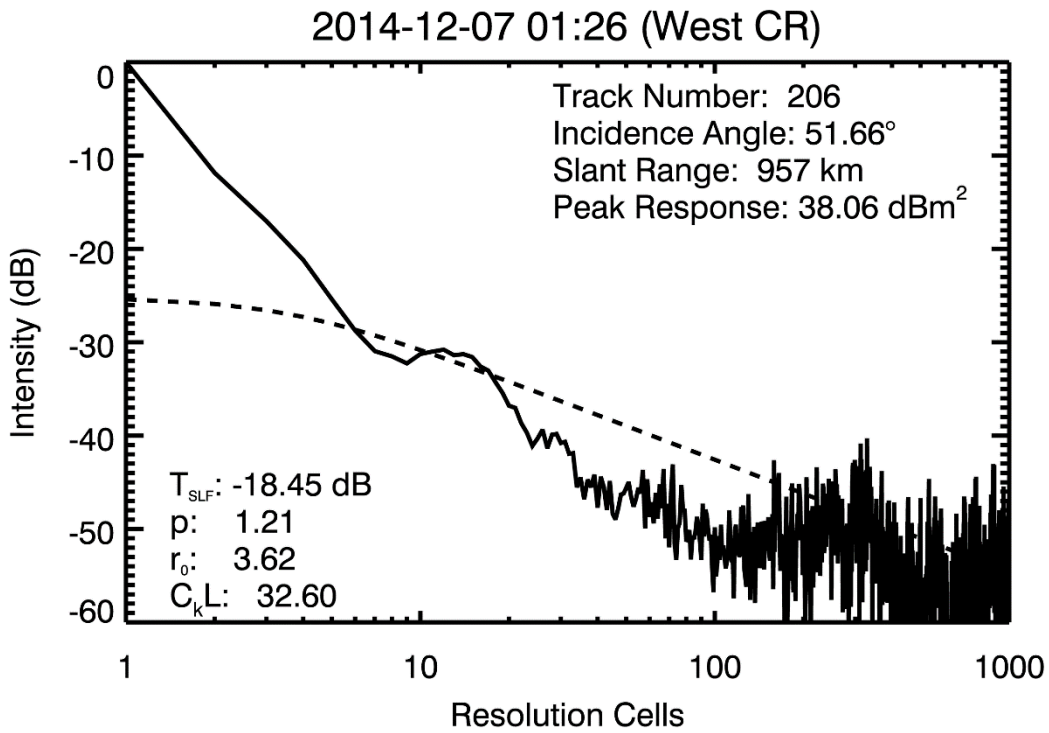


Figure B.44: PALSAR-2 PSF - 2014-12-07

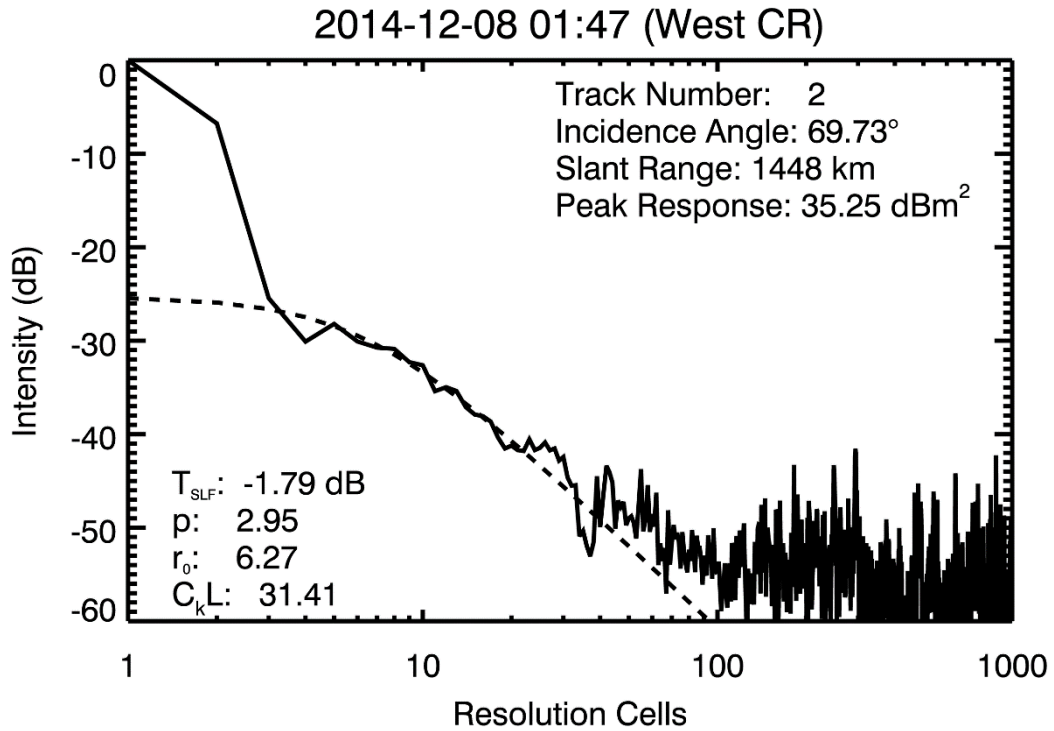


Figure B.45: PALSAR-2 PSF - 2014-12-08

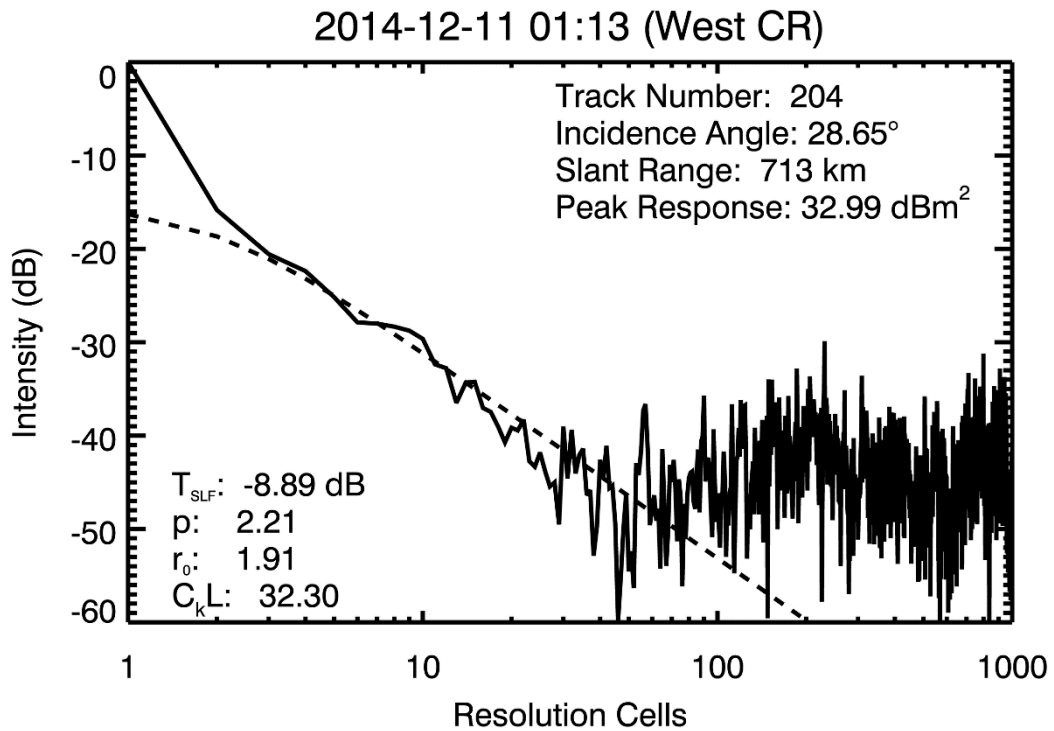


Figure B.46: PALSAR-2 PSF - 2014-12-11

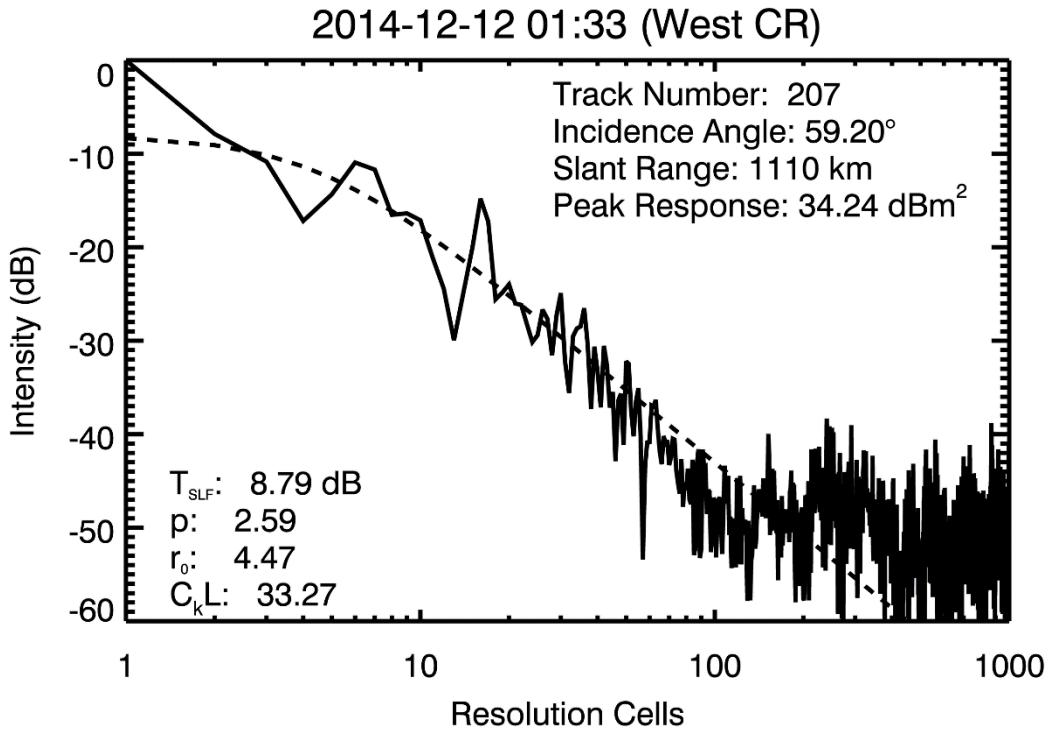


Figure B.47: PALSAR-2 PSF - 2014-12-12

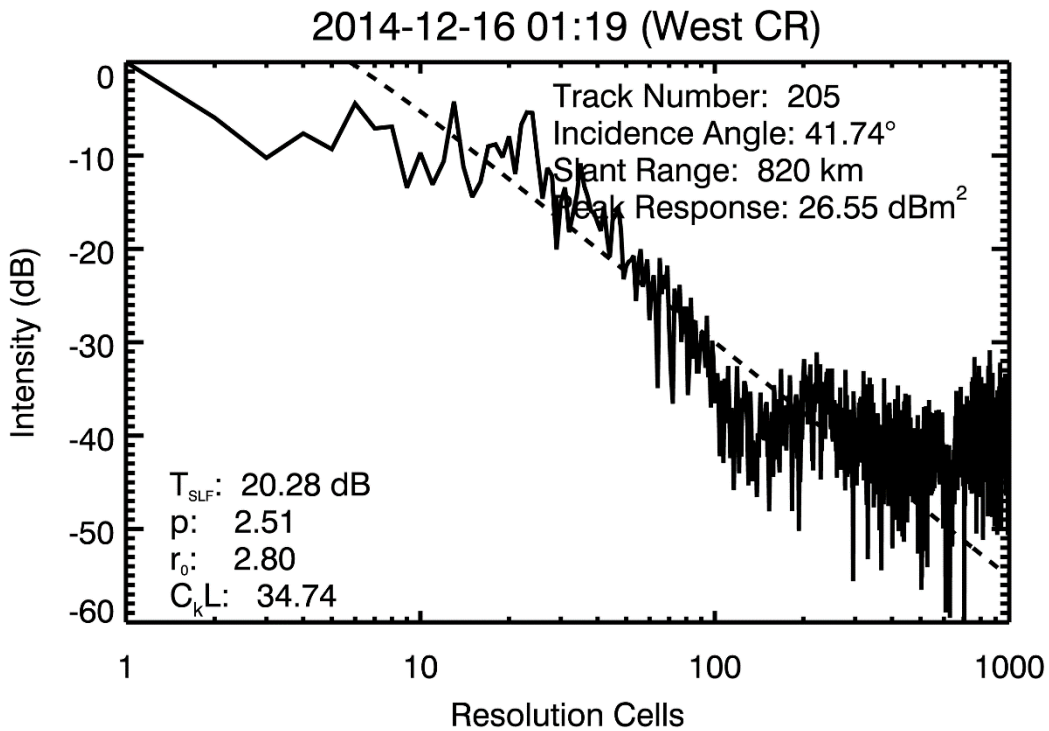


Figure B.48: PALSAR-2 PSF - 2014-12-16

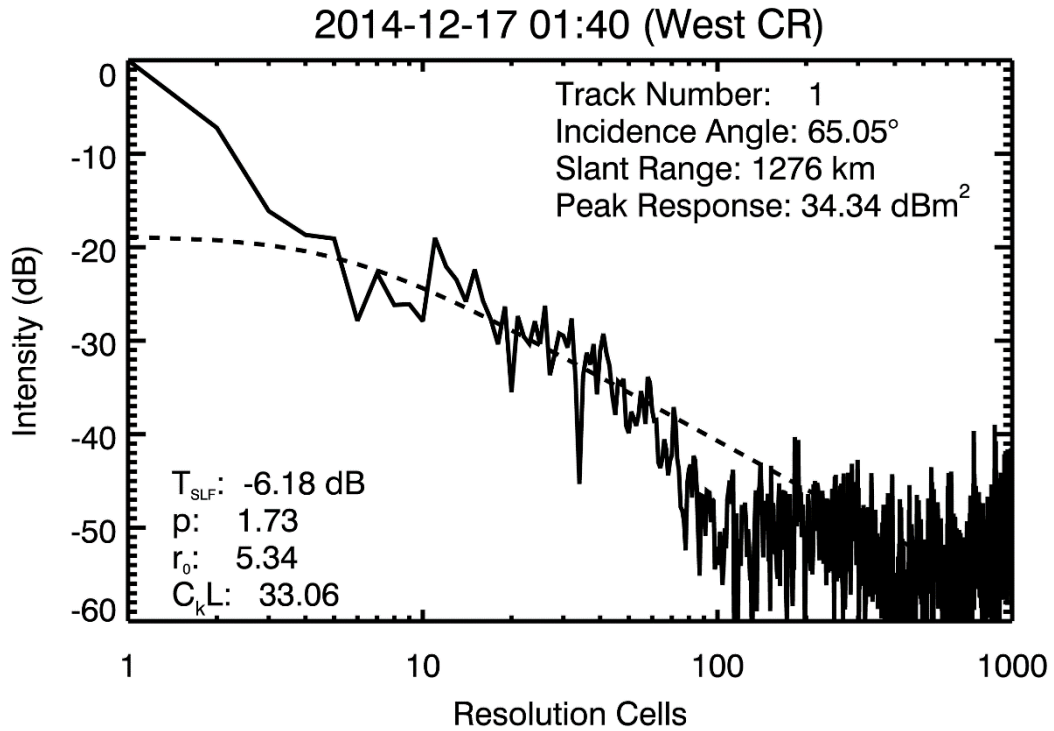


Figure B.49: PALSAR-2 PSF - 2014-12-17

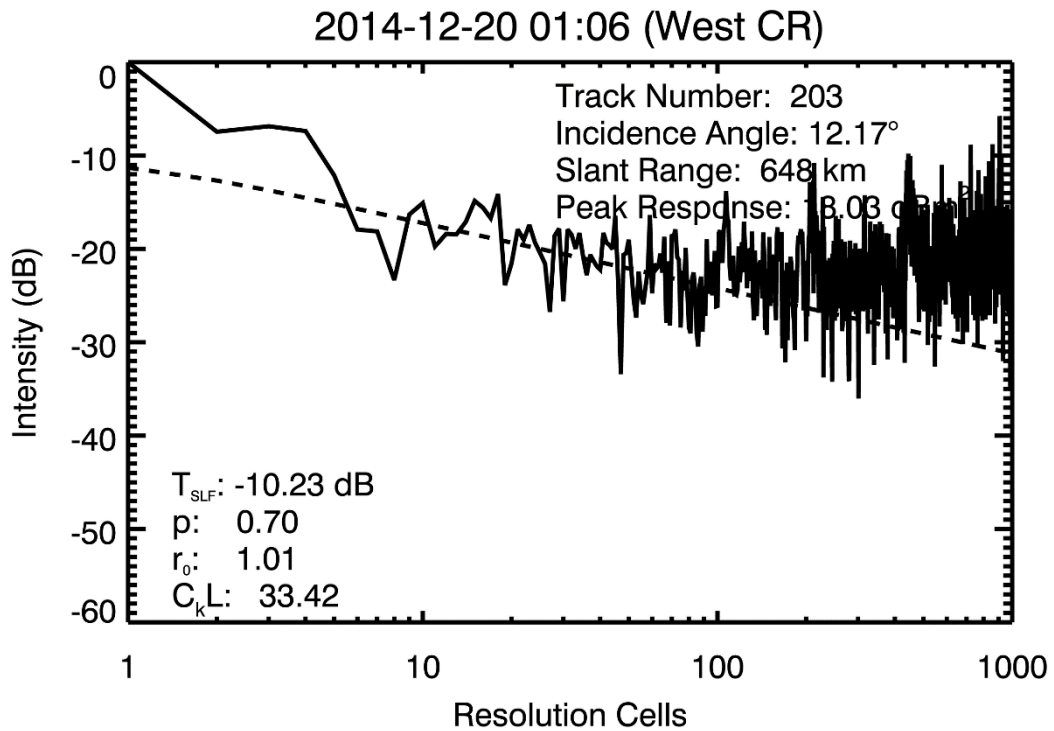


Figure B.50: PALSAR-2 PSF - 2014-12-20

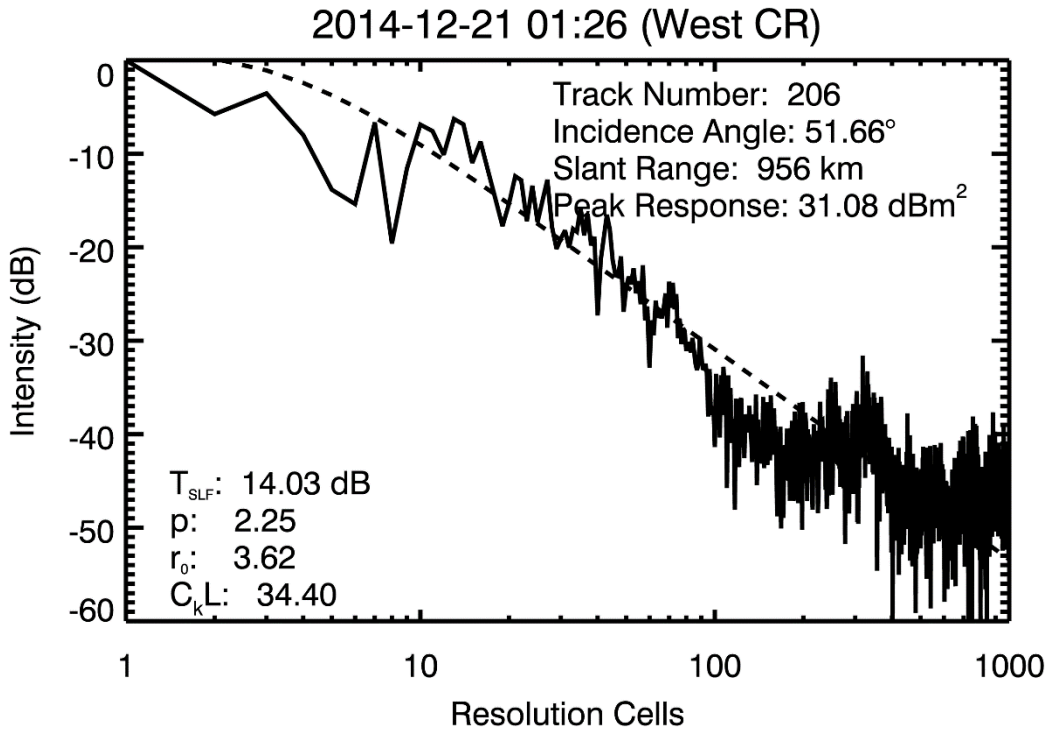


Figure B.51: PALSAR-2 PSF - 2014-12-21

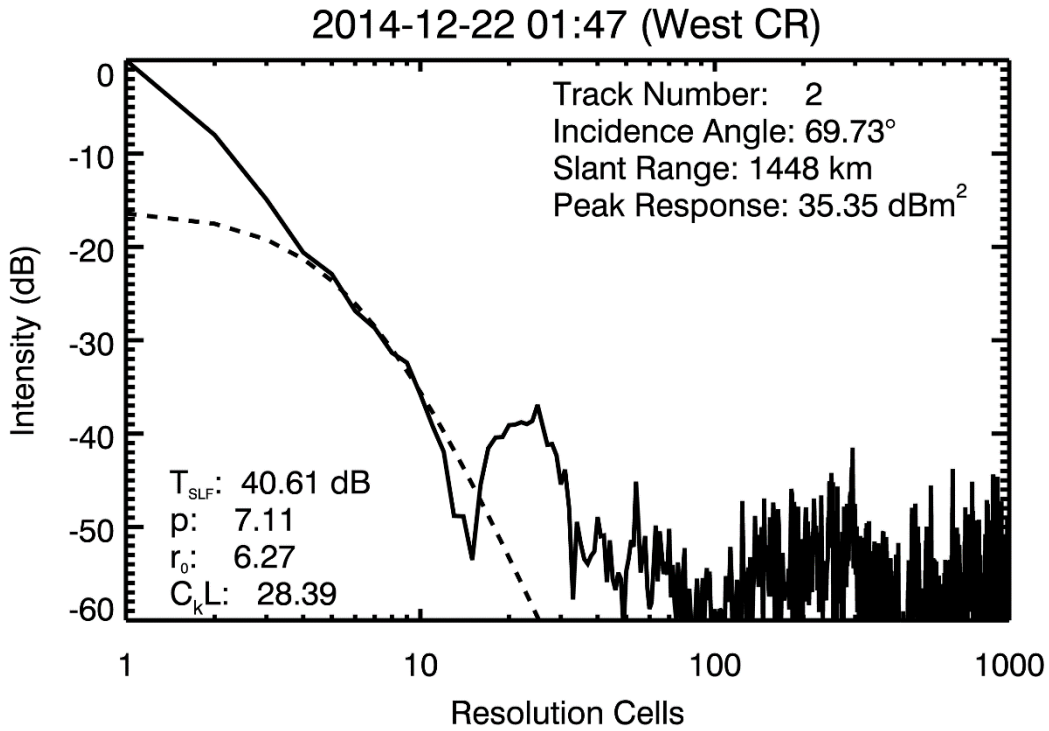


Figure B.52: PALSAR-2 PSF - 2014-12-22

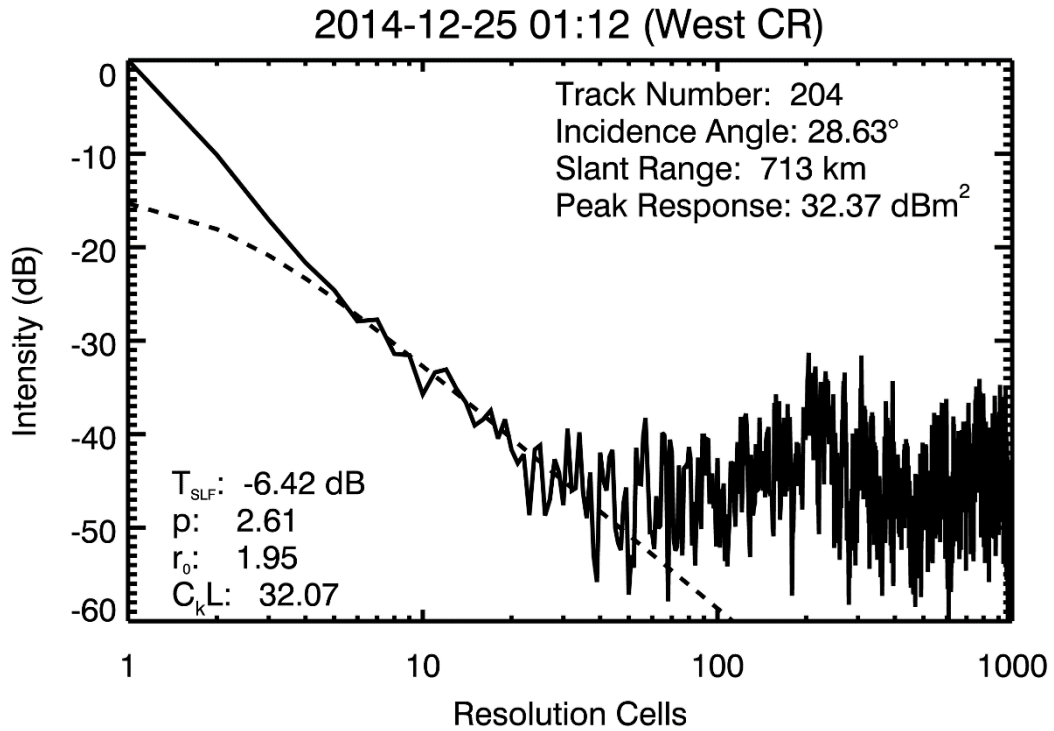


Figure B.53: PALSAR-2 PSF - 2014-12-25

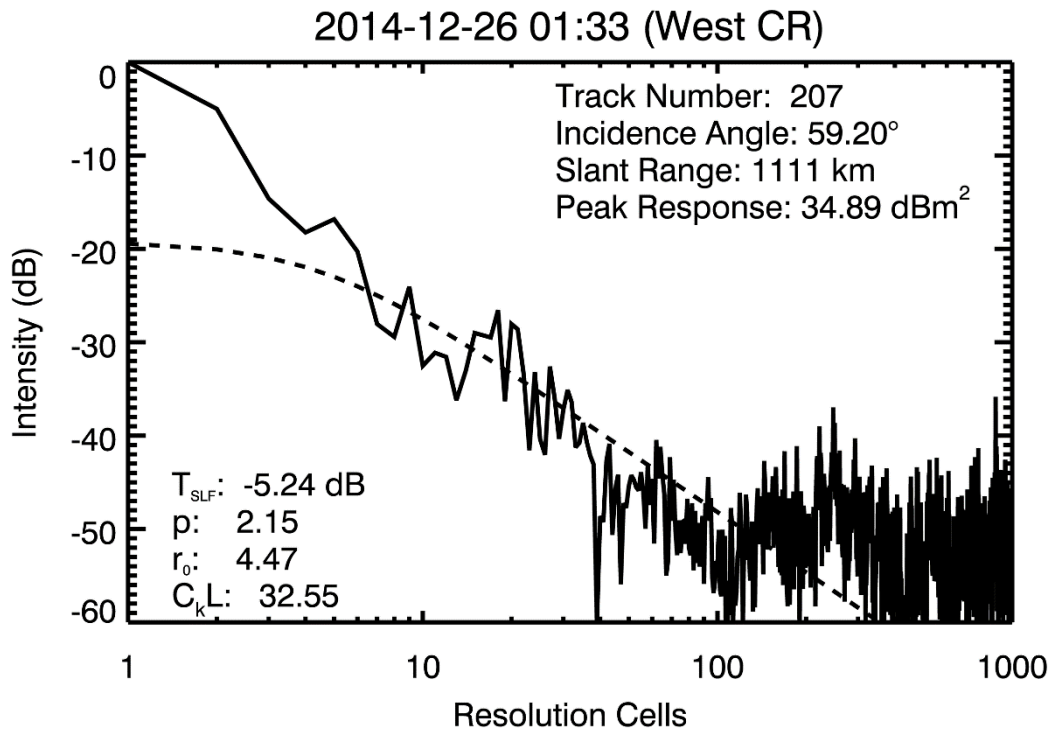


Figure B.54: PALSAR-2 PSF - 2014-12-26

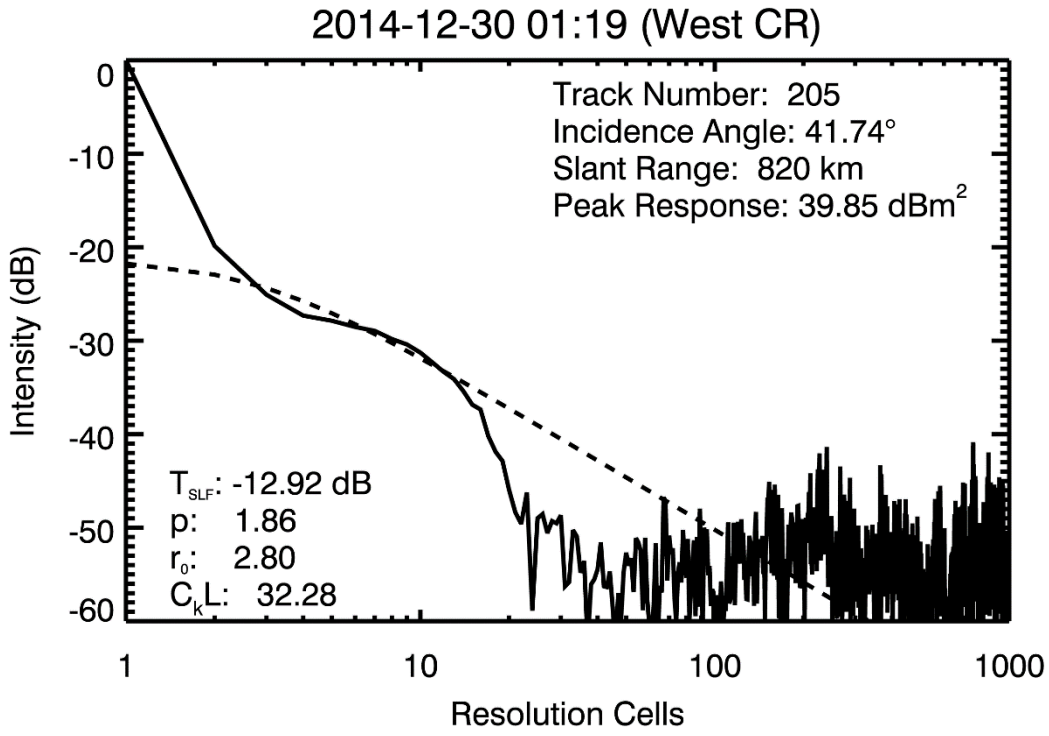


Figure B.55: PALSAR-2 PSF - 2014-12-30

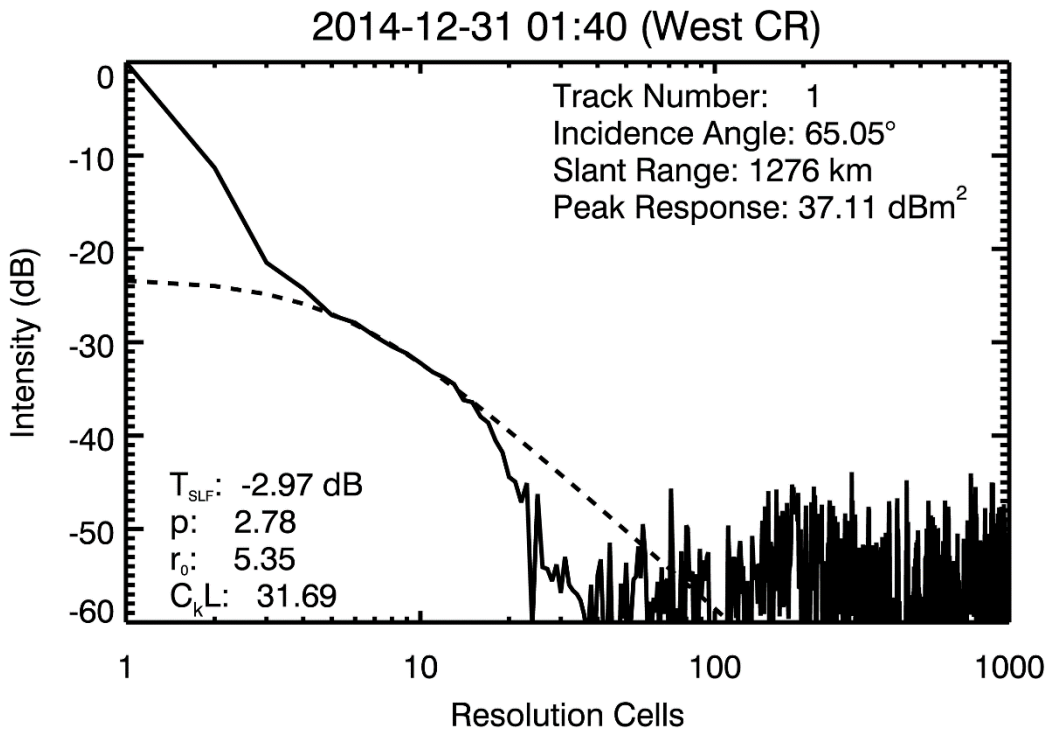


Figure B.56: PALSAR-2 PSF - 2014-12-31

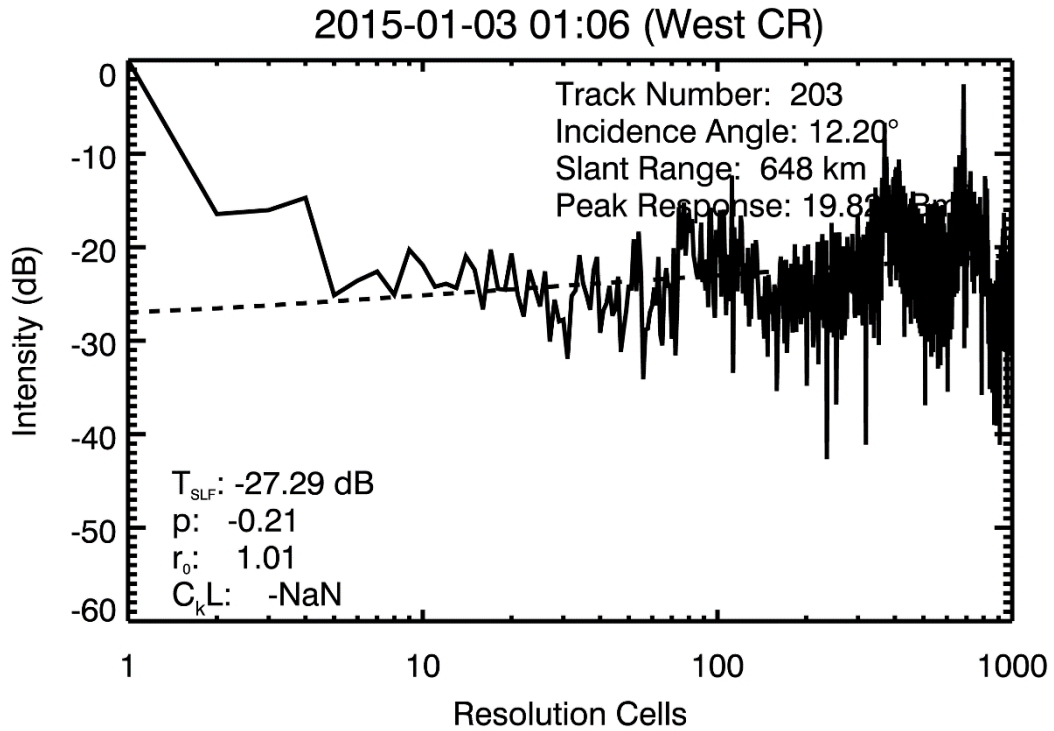


Figure B.57: PALSAR-2 PSF - 2015-01-03

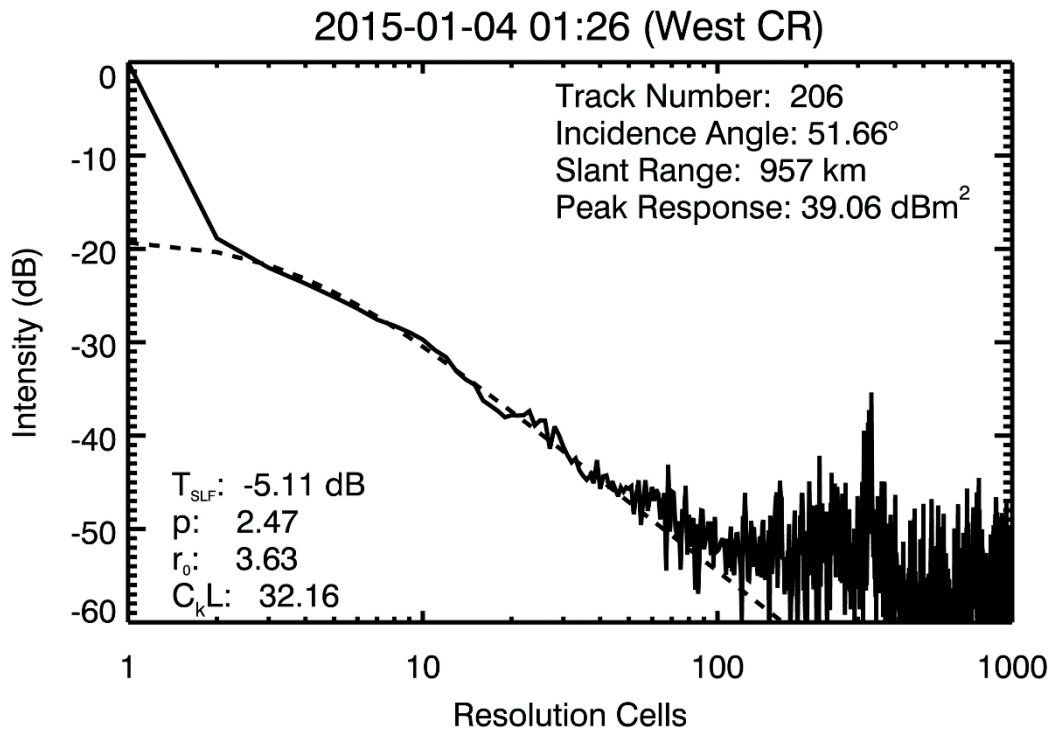


Figure B.58: PALSAR-2 PSF - 2015-01-04

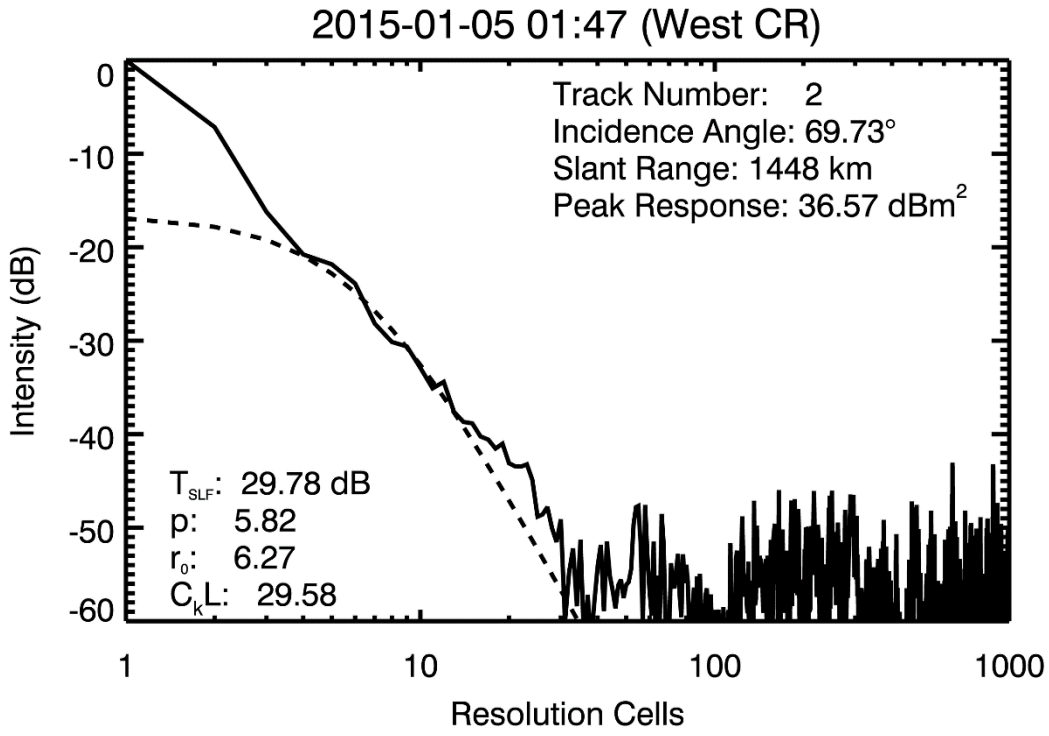


Figure B.59: PALSAR-2 PSF - 2015-01-05

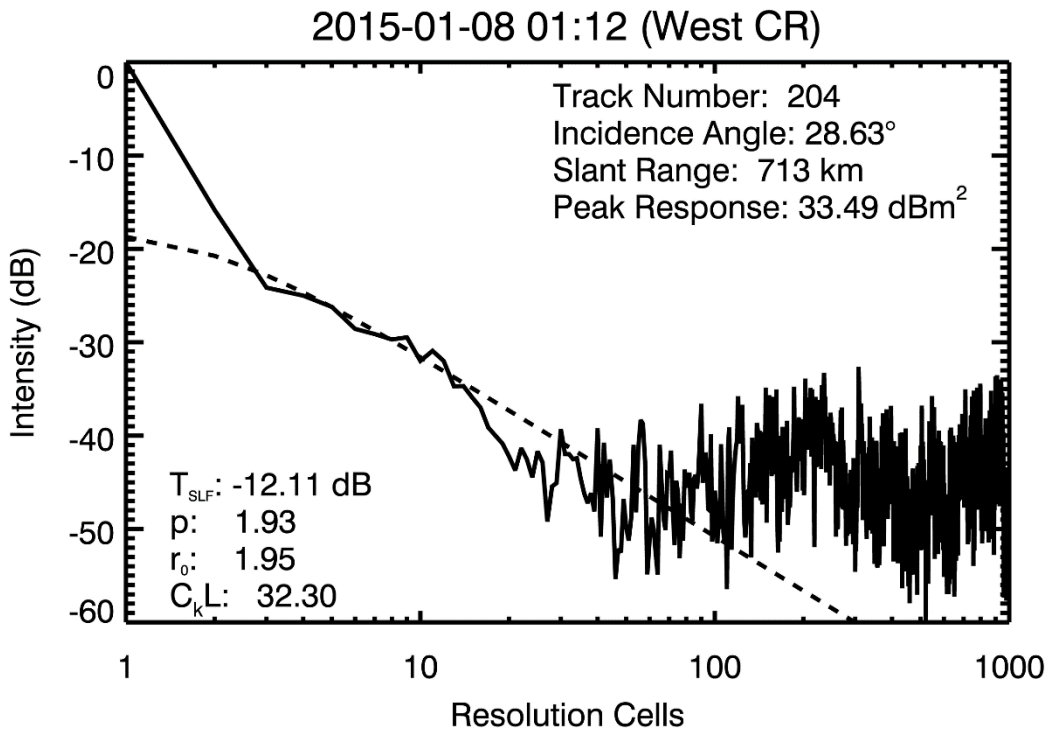


Figure B.60: PALSAR-2 PSF - 2015-01-08

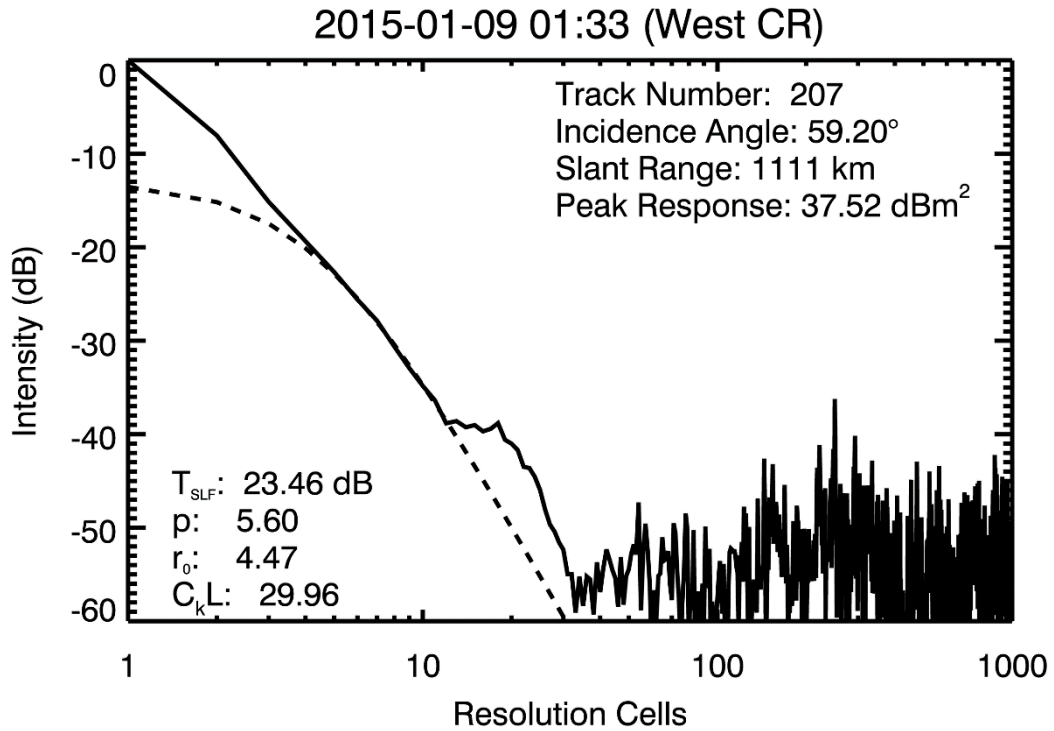


Figure B.61: PALSAR-2 PSF - 2015-01-09

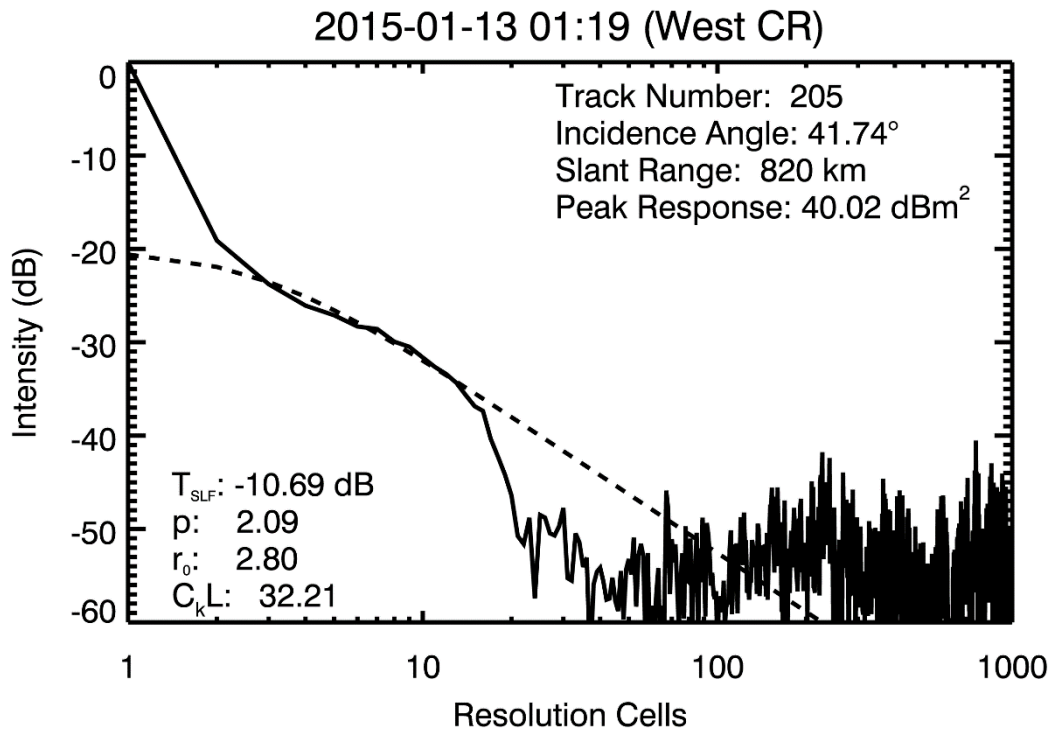


Figure B.62: PALSAR-2 PSF - 2015-01-13

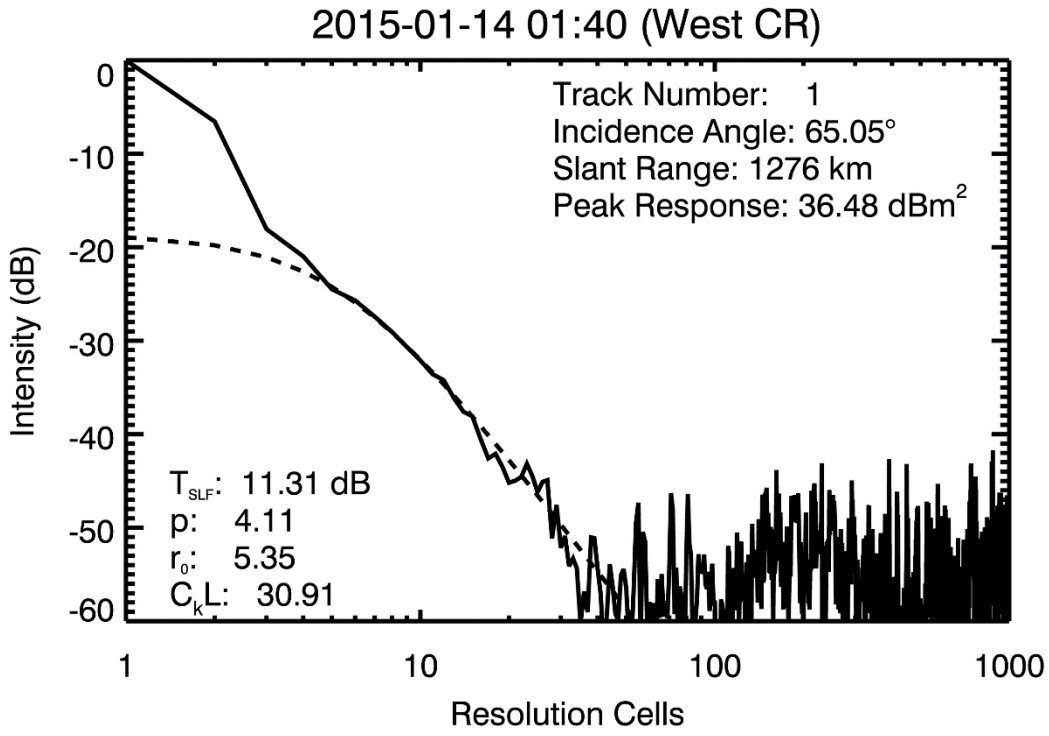


Figure B.63: PALSAR-2 PSF - 2015-01-14

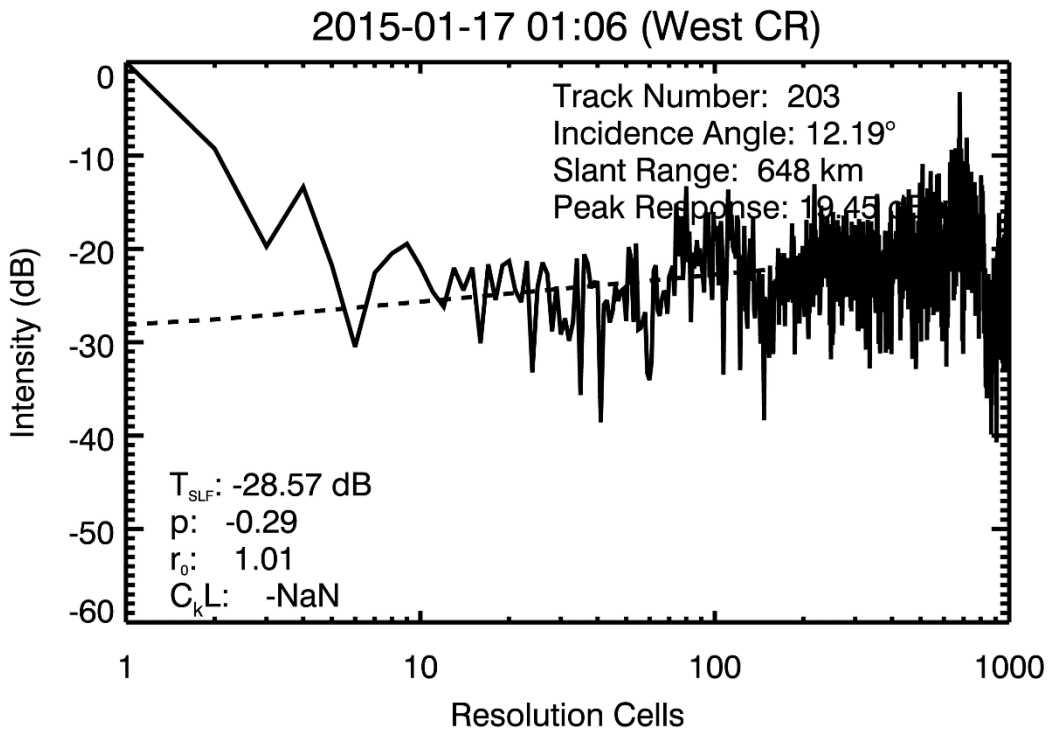


Figure B.64: PALSAR-2 PSF - 2015-01-17

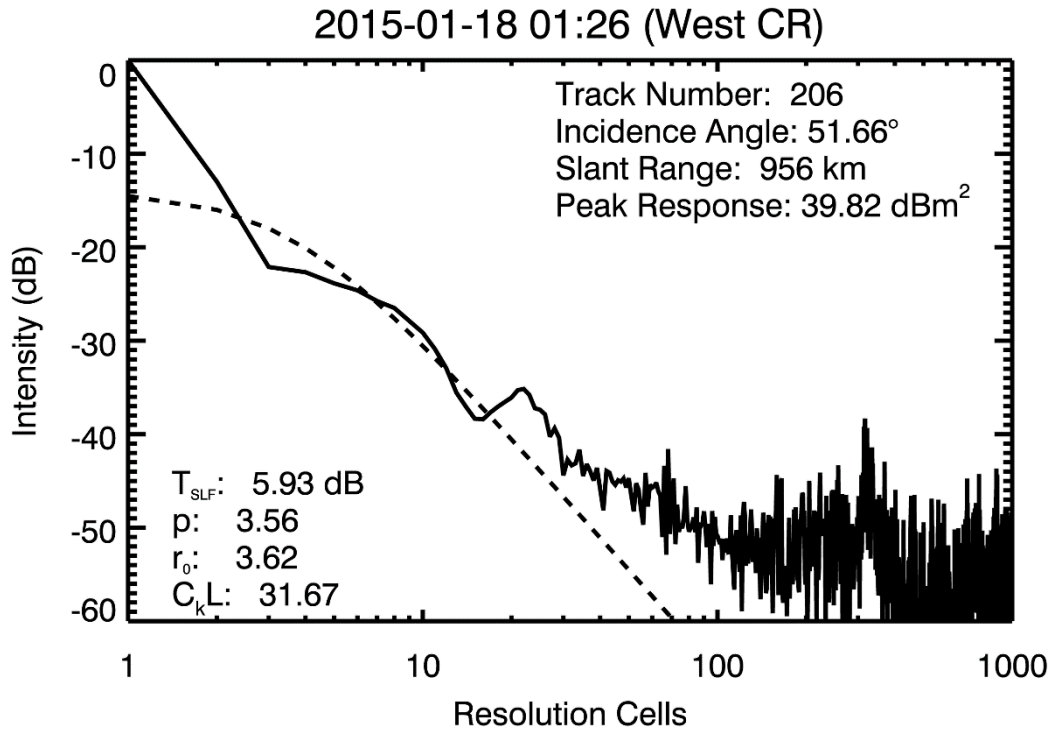


Figure B.65: PALSAR-2 PSF - 2015-01-18

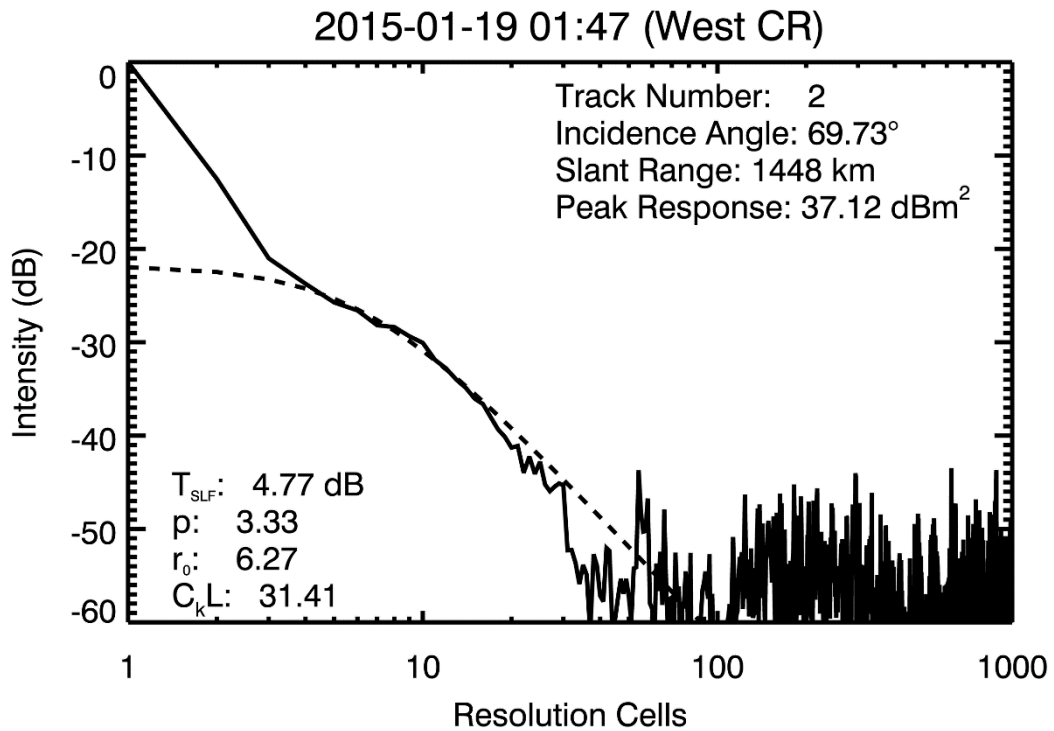


Figure B.66: PALSAR-2 PSF - 2015-01-19

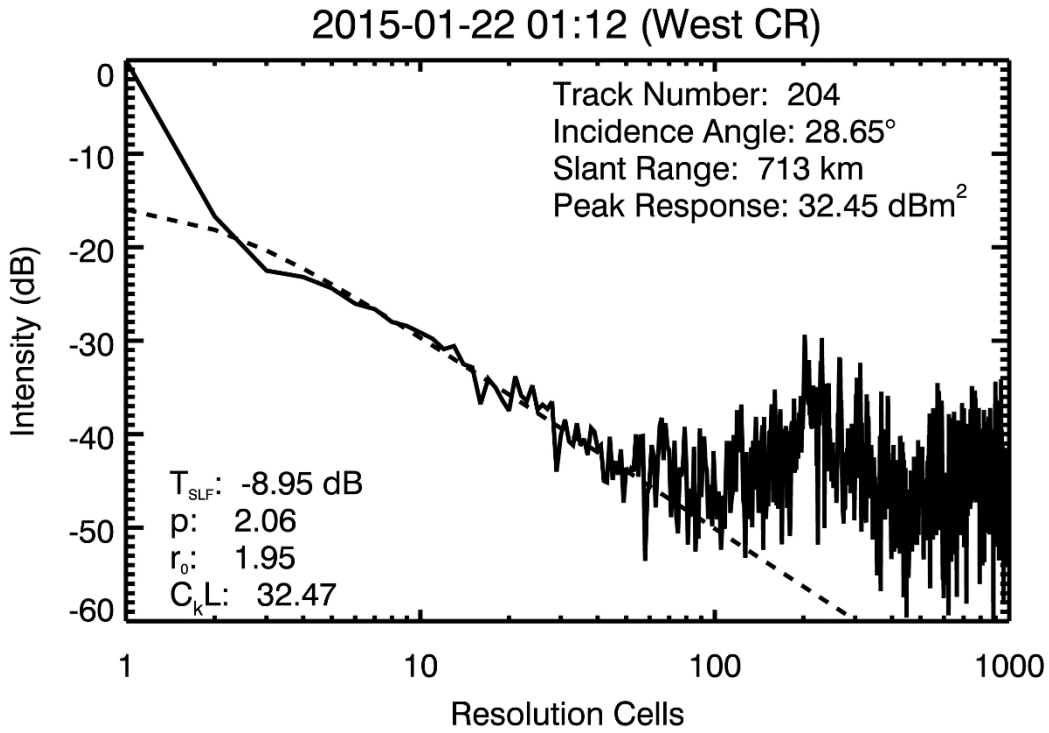


Figure B.67: PALSAR-2 PSF - 2015-01-22

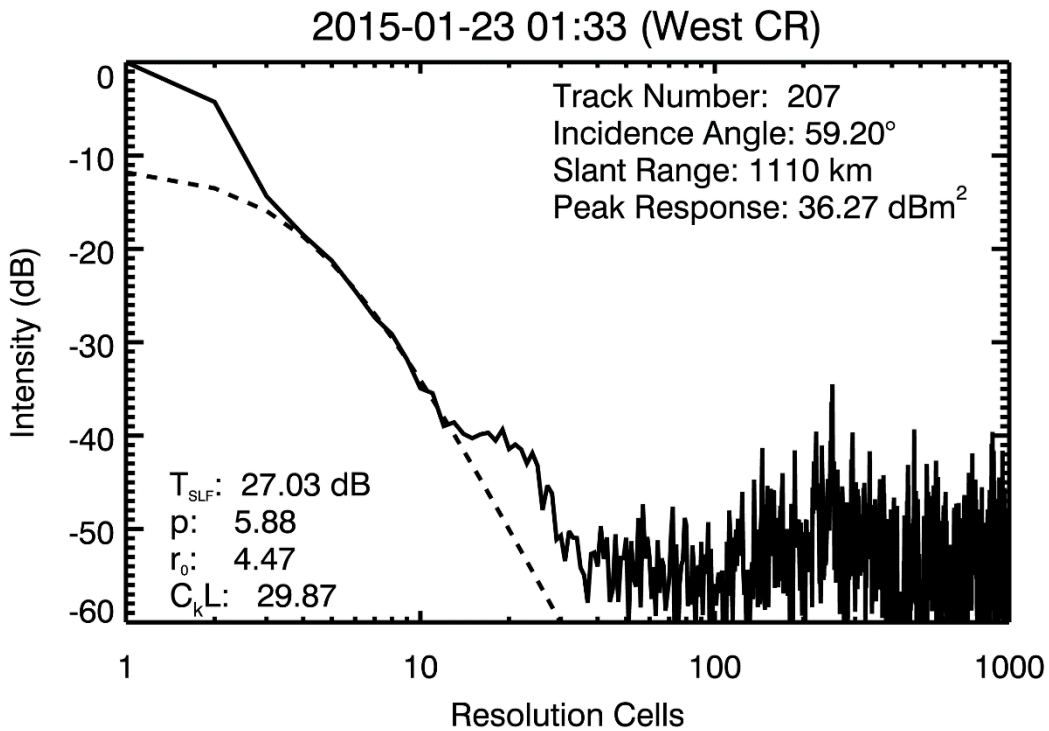


Figure B.68: PALSAR-2 PSF - 2015-01-23

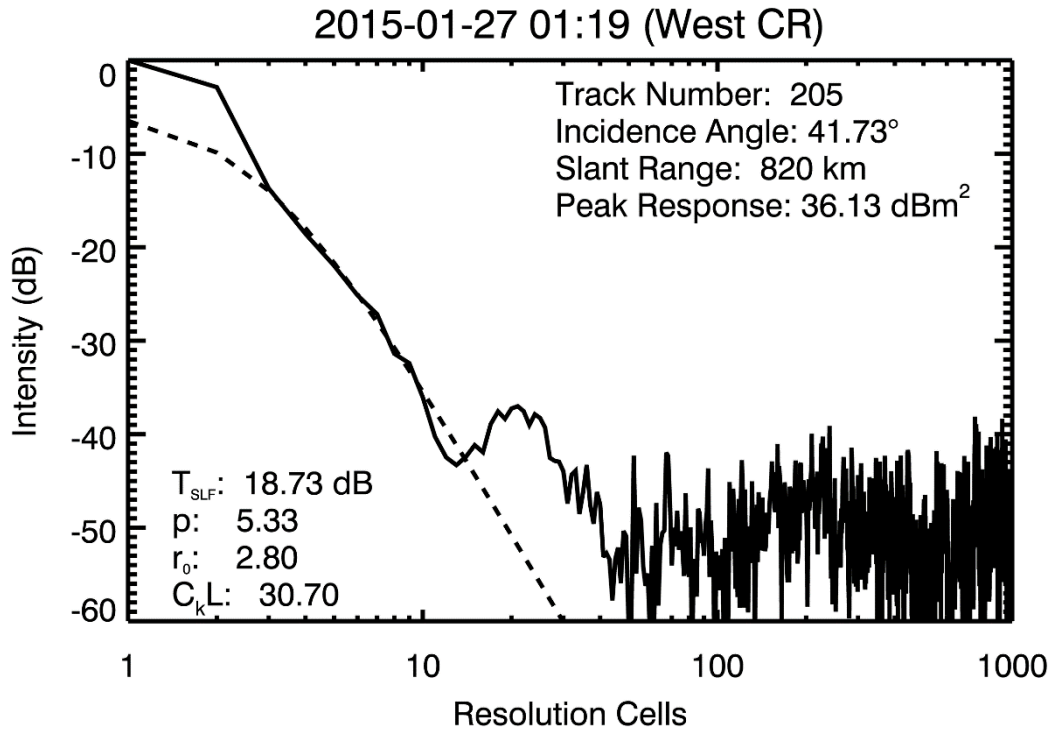


Figure B.69: PALSAR-2 PSF - 2015-01-27

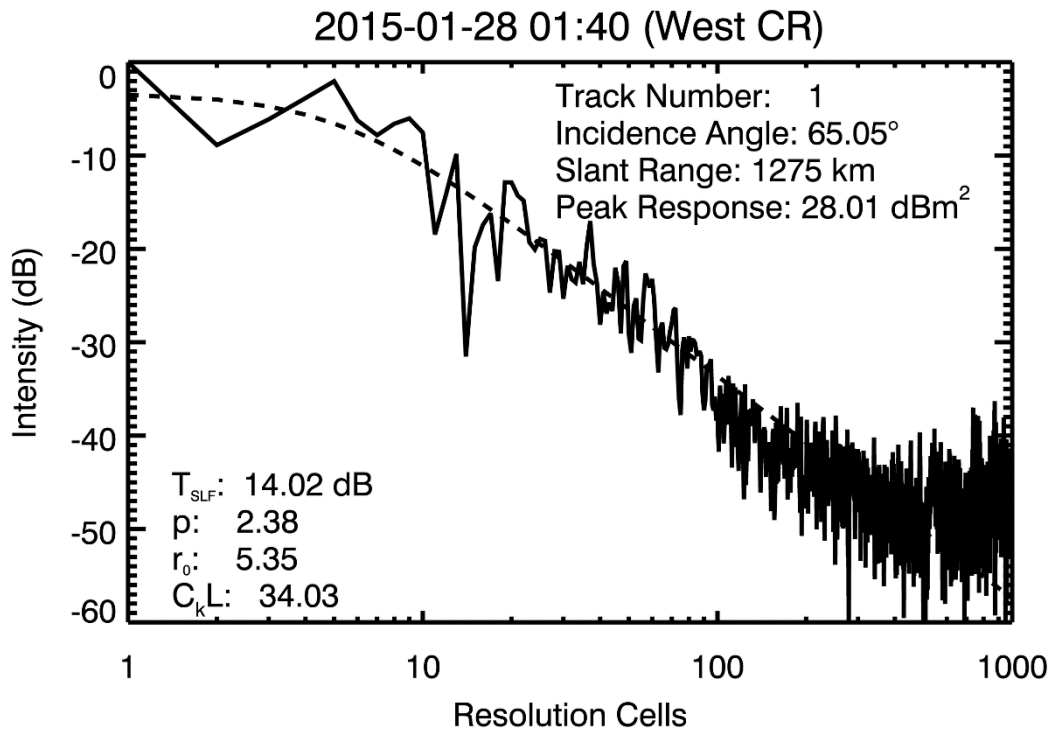


Figure B.70: PALSAR-2 PSF - 2015-01-28

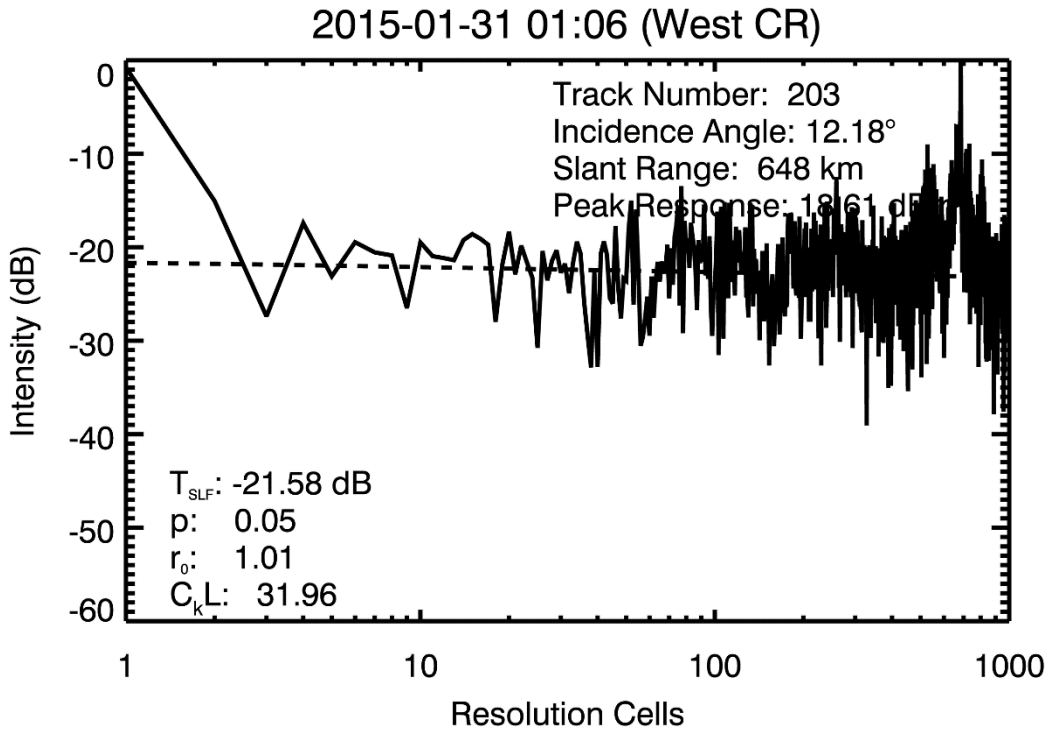


Figure B.71: PALSAR-2 PSF - 2015-01-31

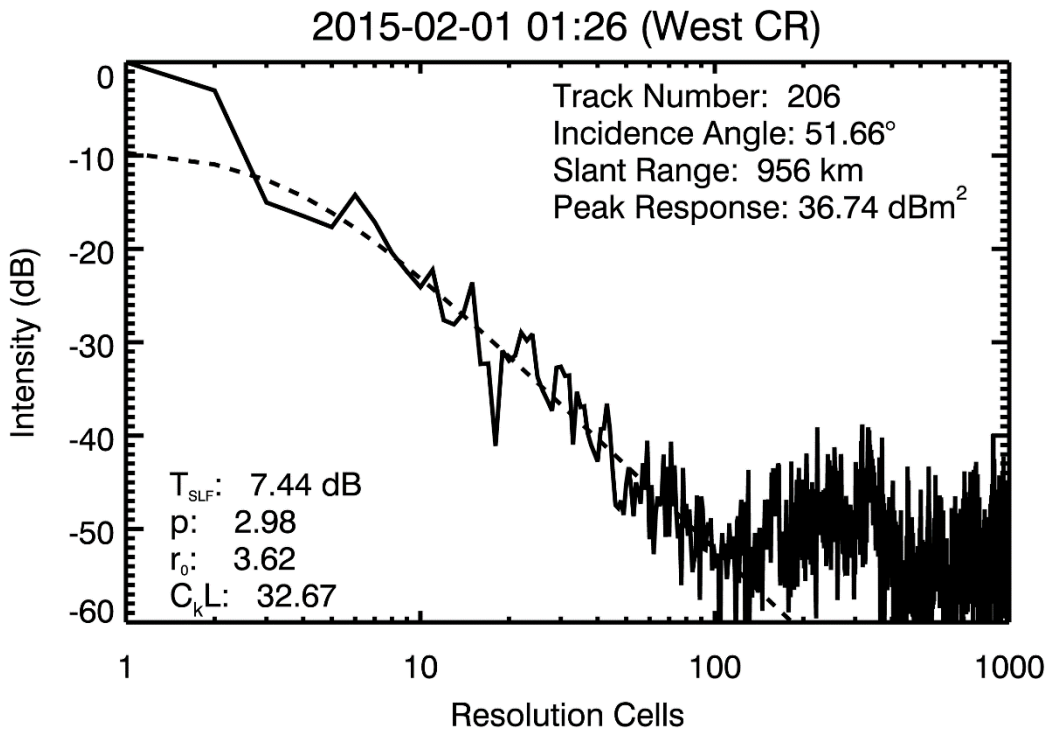


Figure B.72: PALSAR-2 PSF - 2015-02-01

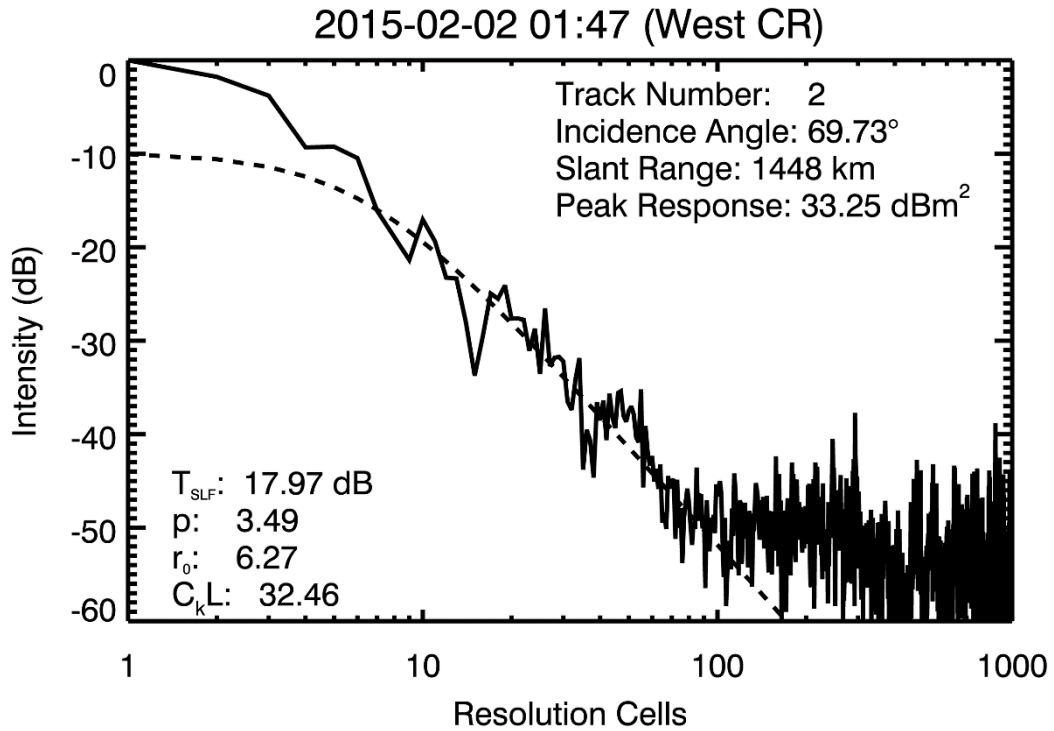


Figure B.73: PALSAR-2 PSF - 2015-02-02

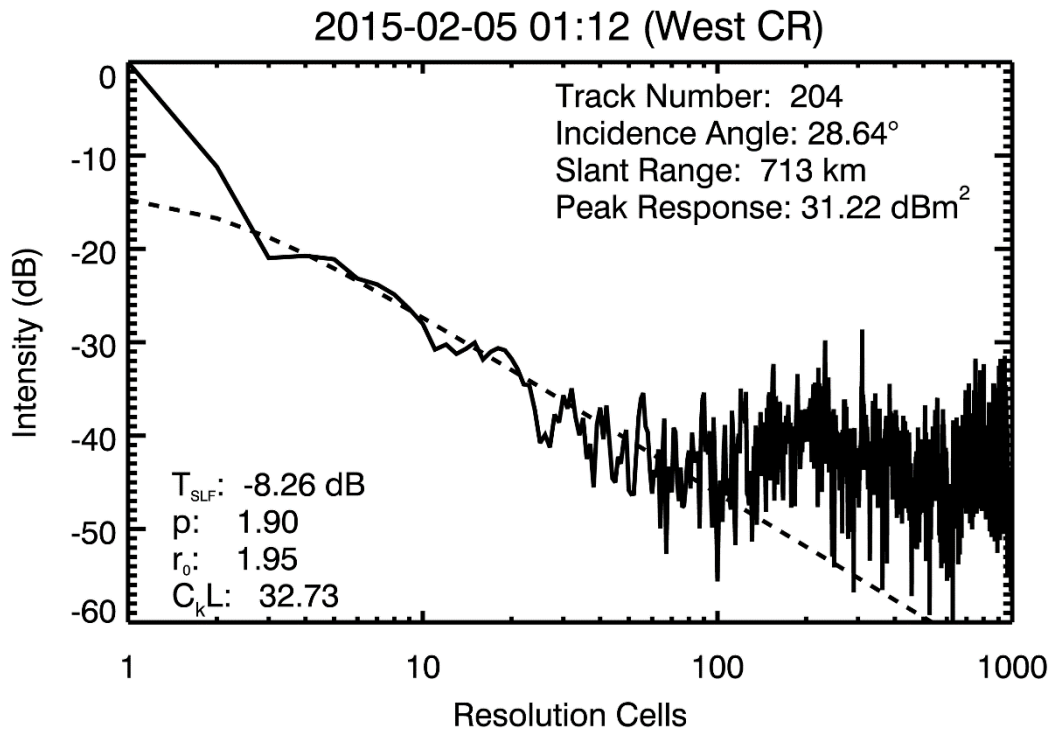


Figure B.74: PALSAR-2 PSF - 2015-02-05

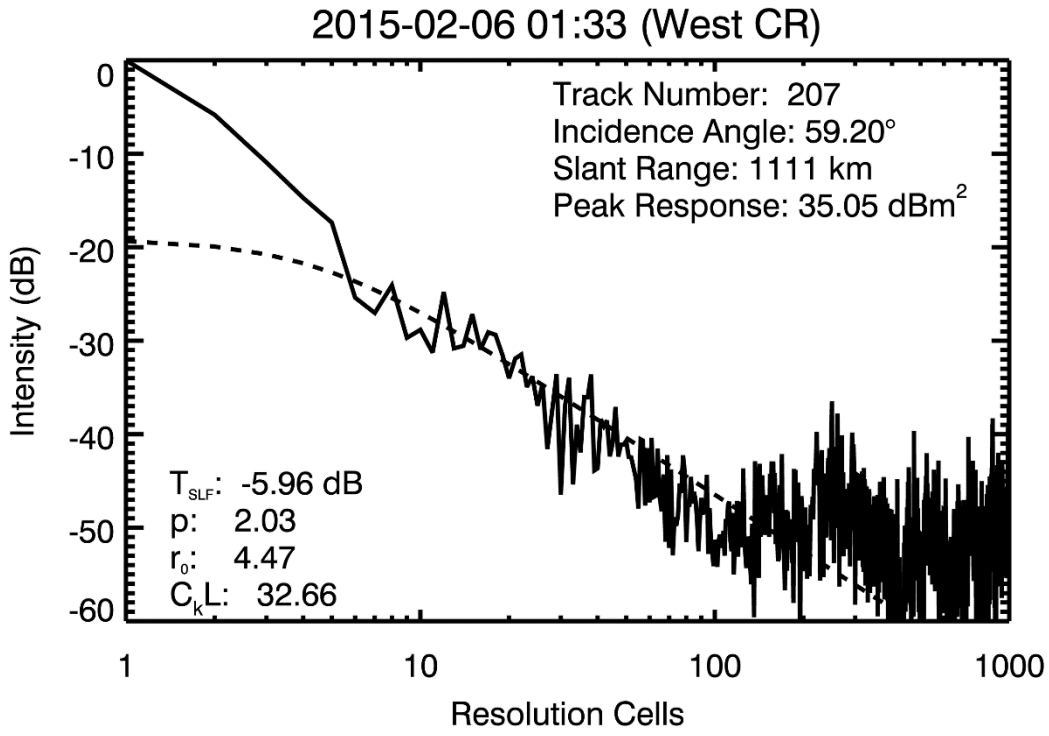


Figure B.75: PALSAR-2 PSF - 2015-02-06

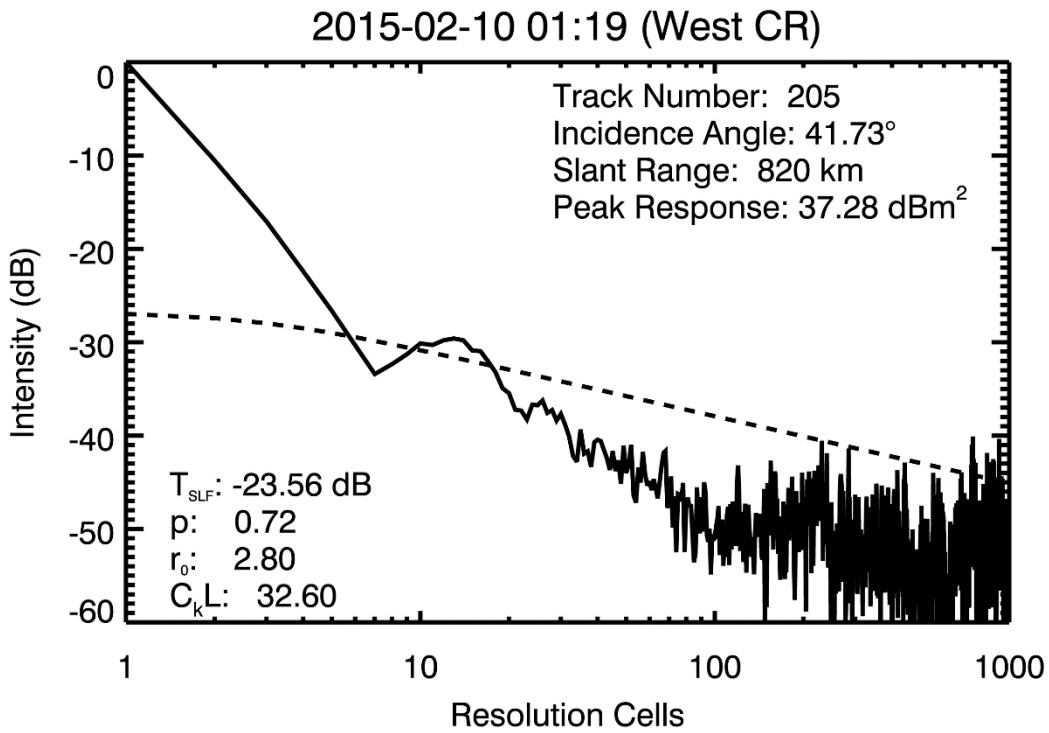


Figure B.76: PALSAR-2 PSF - 2015-02-10

APPENDIX C. SAR/IONOSPHERE THEORY

This appendix aims to bring together and summarise the previous work relating ionospheric conditions with synthetic aperture radar (SAR) data that much of this thesis builds upon. No new work is presented here, rather it is hoped that bringing the mathematics and reasoning that already exist in separate sources, a useful and informative reference for the rest of the thesis can be provided. The work here is mainly drawn from the following references: [Belcher and Rogers, 2009; Belcher and Cannon, 2013].

Formation and Structure of the SAR PSF

The SAR image is generated by the Fourier transform over the synthetic aperture of the received signal reflected from ground targets. If the ground targets include a point-like target (i.e. a corner-reflector), then the point spread function (PSF) can be measured. This signal, as discussed in Section 5 and by *Oliver and Quegan* [2004b], is:

$$h(x) = F\{A(x) \exp[i\psi(x)]\} \quad (C.1)$$

where $h(x)$ represents the SAR point spread function, $F\{\dots\}$ denotes the Fourier transform, $A(x)$ is the amplitude weighting over the synthetic aperture, $\psi(x)$ is the residual phase modulation over the synthetic aperture due to the ionosphere and x is the distance along the synthetic aperture. Thus if the amplitude weighting is constant across the synthetic aperture ($A(x) = 1/L_{SA}$) the PSF will be given by $\text{sinc}(\pi x L_{SA})$ where L_{SA} is the length of the synthetic aperture.

Typically, $A(x)$ is chosen such that the PSF will be a delta-function in the absence of any ionospheric effects (i.e. when $\psi(x) = 0$). If the phase effects remain within the weak scattering regime, so the phase variations are small ($\sigma_\psi(\text{rads}) < \pi/2$), the following exponential can be simplified:

$$\exp[i\psi(x)] \simeq 1 + i\psi(x) \quad (C.2)$$

Under the above assumptions, the PSF can then be approximated as the sum of a mainlobe (a delta-like function, driven by the amplitude weighting $A(x)$), plus sidelobes (induced by the ionospheric phase variation $\psi(x)$):

$$h(x) = F\{A(x)\} + iF\{\psi(x)\} \quad (C.3)$$

Effect of the ionosphere on the SAR image

The complex ionospherically disturbed image $d(r)$ is given by the convolution:

$$d(r) = \frac{1}{\sqrt{\alpha_{TP}}} \int_{-\infty}^{\infty} u(r)h(r - \xi)d\xi \quad (C.4)$$

where $u(r)$ describes the complex undisturbed image, $h(r - \xi)$ is the ionospheric point spread function and $\alpha_{TP} = \int_{-\infty}^{\infty} |h(r)|^2 dr$ is a scaling factor to ensure that the total power in the PSF is conserved [Belcher and Cannon, 2013].

$u(r)$ is the image in the case of an undisturbed ionosphere. As such the PSF is assumed to be a delta-like function [Belcher and Cannon, 2013]. The image is formed from the convolution of the ground targets with the PSF. If the PSF is a delta function, this convolution will have no effect, and so $u(r)$ is equivalent to the ‘ground truth’ of the terrain being imaged.

Using Equation (C.3):

$$d(r) = \frac{1}{\sqrt{\alpha_{TP}}} \left[u(r) + \int_{-\infty}^{\infty} u(r)SLF(r - \xi)d\xi \right] \quad (C.5)$$

We see that the mainlobe, corresponding to the undisturbed image $u(r)$, has been attenuated by a factor $\sqrt{\alpha_{TP}}$, and the power has been redistributed into the sidelobes. [Belcher and Cannon, 2013].

Thus it can be seen that the effect of the ionosphere is to add random noise to each resolution cell of the undisturbed image, with the amount of noise determined by the value of $u(r)$. For convenience, this random noise will be called ionospheric noise.

If the image is of a homogenous area with stationary ergodic statistics, the convolution in (C.4) can be simplified to an integration over the product of $u(r)$ and $SLF(r)$. This is true because, under the assumption of homogeneity, stationarity and ergodicity, each $u(r)$ is representative of the entire distribution. Therefore, convolving with the SLF at each r , is equivalent to an integration over all r for the product $u(r)$ and $SLF(r)$.

Then the amount of ionospheric noise added to each resolution cell is given by:

$$n_{\sigma} = \int_{-\infty}^{\infty} u(r)SLF(r)dr \quad (C.6)$$

Effect of the ionosphere on clutter statistics

SAR image statistics are usually described by a compound model [Ward, 1981]. Natural clutter, such as forests and wave swell, is well described by a slowly varying underlying cross-section σ_0 , described by a gamma distribution [Belcher and Cannon, 2013]. This is combined with a zero mean complex Gaussian [Carretero-Moya et al., 2010] describing the ‘speckle’ noise, which is a characteristic of coherent imaging systems.

Combining a gamma distribution with a complex Gaussian in a compound model results in a K-distribution of observed amplitude and intensity with phases uniformly distributed over 2π [Belcher and Cannon, 2013].

The complex image can, therefore, be represented by:

$$u(r) = \sqrt{\sigma_0(r)}\epsilon(r) \quad (\text{C.7})$$

where $\sigma_0(r)$ is the RCS of the underlying terrain (assumed to be gamma distributed, have a mean μ and be correlated over l_r resolution cells), and $\epsilon(r)$ the complex Gaussian that describes the speckle (uncorrelated from one resolution cell to the next). Each component of $\epsilon(r)$ (ϵ_R (real, in-phase) and ϵ_Q (imaginary, quadrature)), is a zero mean Gaussian of variance 0.5, so that $\langle |\epsilon(r)|^2 \rangle = 1$. The mean image intensity is, therefore, $\langle I \rangle = \langle |u(r)|^2 \rangle = \langle \sigma_0 \rangle = \mu$ [Belcher and Cannon, 2013].

Effect of ionospheric noise on the observed underlying RCS

The ionospheric noise is described by the sidelobe function, where each point (as a function of r) may be represented as a complex number $\eta(r)$ composed of two independent, zero-mean, Gaussian random variables, η_R and η_Q , where the variances of η_R and η_Q are determined by an envelope or shape function ($\langle |SLF(r)|^2 \rangle$), previously discussed in Section 5.

$$SLF(r) = \eta(r) \quad (\text{C.8})$$

Therefore the ‘ionospheric noise’ added by the sidelobe function, can be rewritten, using equations (C.6), (C.7) and (C.8), as:

$$n_\sigma(r) = \int_{-\infty}^{\infty} \sqrt{\sigma_0(\xi)}\epsilon(\xi)\eta(\xi)d\xi \quad (\text{C.9})$$

Since both ϵ and η are Gaussian distributed, they may be replaced by a single equivalent Gaussian with a variance equal to the sum of both their variances.

Since the underlying cross-section σ_0 varies slowly about its mean, and is highly correlated from one resolution cell to the next, the product model ([Ward, 1981]) suggests that the intensity probability density function can be obtained by determining the probability of intensity for a given σ_0 , and calculating the probability of that σ_0 occurring:

$$p(I) = \int_0^{\infty} p(\sigma_0)p(I|\sigma_0)d\sigma_0 \quad (C.10)$$

Then, assuming the statistics of the underlying cross-section σ_0 are stationary, the effect of the sidelobe function (the complex Gaussian $\eta(r)$) on the image can be determined separately to the effect of σ_0 [Belcher and Cannon, 2013].

The total variance of $\eta(r)$ is a summation over many Gaussian components, and so the result can be written as a single equivalent Gaussian representing the sidelobes. Integrating $|\eta(r)|^2$ provides the power in the sidelobes, and since $\eta(r)$ is zero mean, the power is equal to the variance of the equivalent Gaussian.

$$\int_{-\infty}^{\infty} |\eta(r)|^2 dr = \sigma_{SLF}^2 \quad (C.11)$$

And so, using Equation (C.9), if the underlying RCS σ_0 is constant and ignoring the speckle contribution (which will be addressed below), the total ionospheric noise power, as given by its variance is:

$$\sigma_n^2 = \sigma_0 \sigma_{SLF}^2 \quad (C.12)$$

The above demonstrates that in the presence of ionospheric disturbance, zero mean complex Gaussian noise is added to each image pixel. The variance of the noise is proportional to the underlying RCS [Belcher and Cannon, 2013].

Effect of ionospheric noise on speckle

The noise in each pixel can be considered to be multiplied by the *gamma-distributed* cross-section that results from the combination of the speckle contribution $\epsilon(r)$ with the underlying clutter RCS. The ionospheric noise contribution (Equation (C.12)) must be combined with the Gaussian that causes the speckle noise [Belcher and Cannon, 2013]. The variance of the resulting complex Gaussian is the sum of the variances of the two component Gaussians:

$$\sigma_{\epsilon,SLF} = 1 + \sigma_{SLF}^2 \quad (C.13)$$

The probability density function of the intensity of a complex Gaussian distribution is a negative exponential distribution.

So, for a given σ_0 , the intensity pdf of the ionospherically disturbed image is given by:

$$p(I|\sigma_0) = \frac{1}{\sigma_0(1 + \sigma_{SLF}^2)} \exp\left\{-\frac{I}{\sigma_0(1 + \sigma_{SLF}^2)}\right\} \quad (C.14)$$

The effect of the ionospheric noise, as characterised by σ_{SLF}^2 , has resulted in an increase in speckle intensity for a given background cross-section σ_0 [Belcher and Cannon, 2013].

Smoothing effect on the cross-section $\sigma_0(r)$

The sections above discuss the impact of the ionosphere in terms of adding random (Gaussian) noise to the image. However, any PSF induced by the ionosphere that is not a delta function will also act to smooth the underlying cross-section. This smoothing is described by the convolution of the underlying cross-section with the PSF [Belcher and Cannon, 2013].

In the absence of any ionospheric effects, the underlying cross-section σ_0 of natural clutter is considered to be gamma-distributed. The gamma pdf is given by:

$$p(\sigma_0) = \frac{1}{\Gamma(\nu)} b^\nu \sigma_0^{\nu-1} \exp\{-b\sigma_0\} \quad (C.15)$$

Where ν is the order parameter and $b = \nu/\mu$. When the underlying terrain is constant and perfectly smooth (ordered), $\nu \rightarrow \infty$ and the pdf tends to a delta function centred on the mean μ . For $\nu = 1$ the pdf is a negative exponential [Belcher and Cannon, 2013].

Effect on the mean of the distribution

In the case of the disturbed ionosphere, the existence of sidelobes in the induced ionospheric PSF mean that power has been redistributed from the mainlobe, and so the mean intensity of the observed RCS is reduced. The ionospherically disturbed mean is given by:

$$\mu_d = \frac{\mu}{\alpha_{TP}} = \frac{\mu}{1 + \sigma_{SLF}^2} \quad (C.16)$$

α_{TP} is the constant used to conserve the total power in equation (C.4). We have seen that the ionospherically disturbed speckle power is given by $\sigma_0(1 + \sigma_{SLF}^2)$, and consequently the mean is reduced by a factor $(1 + \sigma_{SLF}^2)$.

Effect on the shape/order parameter of the distribution

As seen above, the formation of the ionospherically disturbed image is described by the convolution of the underlying cross-section with the ionospheric PSF. In a discrete sense, this means that the intensity value in each pixel is the result of a sum over the product of the underlying RCS with the PSF. Summing values from a gamma distribution results in a gamma distributed variable with the same mean but a different order parameter to the original distribution.

The characteristic function of the Gamma distribution is:

$$C_F(\omega) = (1 - i\omega\mu)^{-\nu} \quad (C.17)$$

The characteristic function of the sum of two independent variables from the same random distribution is given by the product of the characteristic function of the distribution: $C_{X+Y}(\omega) = C_X(\omega)C_Y(\omega)$. It follows that when summing two independent variables from the same gamma distribution, the characteristic function of the result is given by:

$$C_{X+Y}(\omega) = (1 - i\omega\mu)^{-2\nu} \quad (C.18)$$

i.e. the mean remains the same but the order parameter is increased. So adding n independent samples from a gamma distribution, to a sample from that gamma distribution, results in a variable from a gamma distribution with the same mean, and an order parameter a factor of $(1 + n)$ greater than that of the original distribution.

Determining the number of independent samples that are summed as a result of the convolution is therefore important in determining the effect on the order parameter.

The number of samples summed overall is given by the number of independent resolution cells in the image. However, given the nature of the sidelobe function, which typically falls off with distance from the mainlobe, clearly those cells closer to the mainlobe will be more significant than those further away.

One approach to take this into account is to integrate over the (normalised) sidelobe function, to effectively provide a ‘count’ of the number of cells that contribute to the observed intensity at a given cell.

$$\int_{-\infty}^{\infty} |\eta(r)|^2 dr = \sigma_{SLF}^2 \quad (C.19)$$

Note that summing over the sidelobes is an approximation because they are not all of the same power, as would be required for addition of two gamma distributed variables of the same mean and order.

The correlation of the underlying terrain should be taken into account as well. If the underlying RCS is highly correlated from one resolution cell to the next, then samples from adjacent resolution cells will not be independent. A simple approach to describing this correlation is to use a correlation length l_r (in resolution cells) beyond which a new independent sample of σ_0 is considered to occur [Belcher and Cannon, 2013].

Dividing the number of resolution cells that contribute by this correlation length thus allows the estimation of the disturbed order parameter:

$$v_d = v \left(1 + \frac{\sigma_{SLF}^2}{l_r} \right) \quad (C.20)$$

Thus the probability of observing cross-section σ_0 in disturbed ionospheric conditions is approximated by combining Equation (C.15) and Equation (C.20) :

$$p(\sigma_0) = \frac{1}{\Gamma(v_d)} \left(\frac{v_d}{\mu_d} \right)^{v_d} \sigma_0^{v_d-1} \exp\left\{-\frac{v_d}{\mu_d} \sigma_0\right\} \quad (C.21)$$

The inherent assumptions made here include [*Belcher and Cannon, 2013*]:

- The PSF is equal to the ensemble average PSF. (The PSF is a random function, but ensemble average is representative)
- The PSF is spatially invariant. (In reality PSF varies randomly over image)
- The PSF can be computed by adding intensities.(Integration over PSF is actually performed in amplitude, but adding intensities still conserves power).
- The PSF fully represents the effect on individual scatterers. (Filtering the underlying cross section with PSF does not represent effect on individual scatterers, as they are not necessarily coherent over the synthetic aperture. The approximation is reasonable providing the clutter coherence length does not change over the synthetic aperture. This will be the case provided the PSF is not defocused)

The errors in these approximation typically only manifest in the higher order moments [*Oliver, 1991*].

Ionospherically disturbed pdf

Using the product model described above (Equation (C.10)), the probability of observing an intensity I is the product of the probability of observing I for a given RCS σ_0 , with the probability of that σ_0 occurring.

$$p(I) = \int_0^{\infty} p(\sigma_0)p(I|\sigma_0)d\sigma_0 \quad (C.22)$$

Without ionospheric effects, the product model combines Equation (C.15) and Equation (C.16), with $\sigma_{SLF}^2 = 0$ (as the induced PSF is a delta function):

$$p(I) = \int_0^{\infty} \frac{b\sigma^{\nu-1}}{\Gamma(\nu)} \exp(-b\sigma) \frac{1}{\sigma} \exp\left(-\frac{I}{\sigma}\right) d\sigma \quad (C.23)$$

where $b = \nu/\mu$.

We use the identity [Gradshteyn and Ryzhik, 2014]:

$$\int_0^{\infty} x^{\nu-1} e^{-\frac{\beta}{x}-\gamma x} dx = 2 \left(\frac{\beta}{\gamma}\right)^{\frac{\nu}{2}} K_{\nu}(2\sqrt{\beta\gamma}) \quad (C.24)$$

$[Re(\beta) > 0, Re(\gamma) > 0]$

This results in a K distribution of order ν and mean μ :

$$p(I) = \frac{2}{\Gamma(\nu)} b^{\frac{\nu+1}{2}} I^{\frac{\nu-1}{2}} K_{\nu-1}[2\sqrt{bI}] \quad (C.25)$$

Where $K_{\nu-1}$ is the modified Bessel function of the second kind.

For the ionospherically disturbed case, using Equation (C.14) and Equation (C.21), the intensity pdf is similarly given by:

$$p(I) = \frac{2b_d}{\Gamma(\nu_d)} (\sqrt{b_d I})^{\nu_d-1} K_{\nu_d-1}(2\sqrt{b_d I}) \quad (C.26)$$

where $b_d = \nu_d/\mu$, $\nu_d = \nu(1 + \sigma_{SLF}^2)$ and $\mu = \mu_d(1 + \sigma_{SLF}^2)$.

So the increase in speckle intensity because of added ionospheric noise has been cancelled out by the decrease in the observed underlying cross-section. The result is a K-distribution with same mean but an increased order parameter when compared to the undisturbed case. The important result here is that, under ionospheric effects, the clutter remains K-distributed, but with a higher order parameter [*Belcher and Cannon, 2013*].

LIST OF REFERENCES

- Aarons, J. (1982), Global morphology of ionospheric scintillations, *Proc. IEEE*, 70(4), 360–378, doi:10.1109/proc.1982.12314.
- Aarons, J., M. Mendillo, R. Yantosca, and E. Kudeki (1996), GPS phase fluctuations in the equatorial region during the MISETA 1994 campaign, *J. Geophys. Res. Sp. Phys.*, 101(A12), 26851–26862, doi:10.1029/96JA00981.
- Anderson, D. N., and R. G. Roble (1981), Neutral wind effects on the equatorial F-region ionosphere, *J. Atmos. Terr. Phys.*, 43(8), 835–843, doi:10.1016/0021-9169(81)90061-1.
- Angling, M. J., P. S. Cannon, and P. Bradley (2007), Ionospheric Propagation, in *Propagation of Radiowaves*, edited by L. W. Barclay, The Institution of Engineering and Technology, IET Radiowave propagation course.
- Basu, S., and K. M. Groves (2001), Specification and Forecasting of Outages on Satellite Communication and Navigation Systems, in *Space Weather*, pp. 423–430, American Geophysical Union, doi:10.1029/GM125p0423.
- Basu, S., S. Basu, J. Aarons, J. P. McClure, and M. D. Cousins (1978), On the coexistence of kilometer- and meter-scale irregularities in the nighttime equatorial F region, *J. Geophys. Res. Sp. Phys.*, 83(A9), 4219–4226, doi:10.1029/JA083iA09p04219.
- Basu, S., J. P. McClure, S. Basu, W. B. Hanson, and J. Aarons (1980), Coordinated study of equatorial scintillation and in situ and radar observations of nighttime F region irregularities, *J. Geophys. Res. Sp. Phys.*, 85(A10), 5119–5130, doi:10.1029/JA085iA10p05119.
- Basu, S., E. MacKenzie, E. Costa, P. Fougere, H. Carlson, and H. Whitney (1987), 250 MHz/GHz Scintillation Parameters in the Equatorial, Polar, and Auroral Environments, *IEEE J. Sel. Areas Commun.*, 5(2), 102–115, doi:10.1109/JSAC.1987.1146533.
- Basu, S. et al. (1996), Scintillations, plasma drifts, and neutral winds in the equatorial ionosphere after sunset, *J. Geophys. Res. Sp. Phys.*, 101(A12), 26795–26809, doi:10.1029/96JA00760.
- Belcher, D. P. (2008a), Sidelobe prediction in transionospheric SAR imaging radar from the ionospheric turbulence strength CkL, in *International Conference on Radar*, pp. 54–59, IEEE, Adelaide, SA, doi:10.1109/radar.2008.4653891.
- Belcher, D. P. (2008b), Theoretical limits on SAR imposed by the ionosphere, *Radar, Sonar Navig. IET*, 2(6), 435–448, doi:10.1049/iet-rsn:20070188.
- Belcher, D. P., and C. J. Baker (1996), High resolution processing of hybrid strip-map/spotlight mode SAR, *IEE Proc. - Radar, Sonar Navig.*, 143(6), 366, doi:10.1049/ip-rsn:19960790.
- Belcher, D. P., and P. S. Cannon (2013), Ionospheric effects on synthetic aperture radar (SAR) clutter statistics, *IET Radar, Sonar Navig.*, 7(9), 1004–1011, doi:10.1049/iet-rsn.2012.0227.

- Belcher, D. P., and P. S. Cannon (2014), Amplitude scintillation effects on SAR, *IET Radar, Sonar Navig.*, 8, doi:10.1049/iet-rsn.2013.0168.
- Belcher, D. P., and N. C. Rogers (2009), Theory and simulation of ionospheric effects on synthetic aperture radar, *IET Radar, Sonar Navig.*, 3(5), 541, doi:10.1049/iet-rsn.2008.0205.
- Belcher, D. P., P. S. Cannon, A. Gustavsson, and M. J. Angling (2015), The Ascension Island experiment: Measurement of ionospheric scintillation effects on PALSAR2, in *International Geoscience and Remote Sensing Symposium 2015 (IGARSS 2015)*, IEEE, Milan, Italy, 26-31 July.
- Bhattacharyya, A., and T. Beach (2000), Nighttime equatorial ionosphere: GPS scintillations and differential carrier phase fluctuations, *Radio Sci.*, 35(1), 209–224.
- Blacknell, D., and R. J. A. Tough (2001), Parameter estimation for the K-distribution based on $[z \log(z)]$, *IEE Proceedings-Radar, Sonar Navig.*, 148(6), 309–312, doi:10.1049/ip-rsn.
- Briggs, B., and I. Parkin (1963), On the variation of radio star and satellite scintillations with zenith angle, *J. Atmos. Terr. Phys.*, 25(v).
- Cannon, P. S. (2009), Mitigation and exploitation of the ionosphere: A military perspective, *Radio Sci.*, 44(RS0A20), 1–8, doi:10.1029/2008RS004021.
- Carrano, C., and K. Groves (2010), Temporal decorrelation of GPS satellite signals due to multiple scattering from ionospheric irregularities, *Proc. 2010 Inst. Navig. ...*, 361–374.
- Carrano, C. S., K. M. Groves, W. J. McNeil, and P. H. Doherty (2012a), Scintillation characteristics across the GPS frequency band, in *Proceedings of ION-GNSS-2012*, pp. 1972–1989, Institute of Navigation, Nashville.
- Carrano, C. S., K. M. Groves, W. J. McNeil, and P. H. Doherty (2012b), Scintillation characteristics across the GPS frequency band, in *Proceedings of ION-GNSS*, pp. 1972–1989, Institute of Navigation, Nashville.
- Carrano, C. S., K. M. Groves, and R. G. Caton (2012c), Simulating the impacts of ionospheric scintillation on L band SAR image formation, *Radio Sci.*, 47(3), 1–14, doi:10.1029/2011RS004956.
- Carretero-Moya, J., J. Gismero-Menoyo, A. Blanco-del-Campo, and A. Asensio-Lopez (2010), Statistical analysis of a high-resolution sea-clutter database, *Geosci. Remote Sensing, IEEE Trans.*, 48(4), 2024–2037.
- Caton, R., and K. Groves (2006), Longitudinal correlation of equatorial ionospheric scintillation, *Radio Sci.*, 41(5), 1–8, doi:10.1029/2005RS003357.
- Cervera, M. A., and R. M. Thomas (2006), Latitudinal and temporal variation of equatorial ionospheric irregularities determined from GPS scintillation observations, *Ann. Geophys.*, 24(12), 3329–3341, doi:10.5194/angeo-24-3329-2006.
- Chen, K., and Y. Gao (2005), Real-time precise point positioning using single frequency data, *ION GNSS*.

- Davies, K. (1990), *Ionospheric Radio*, edited by I. of E. Engineers, Peregrinus.
- Van Dierendonck, A. J., J. Klobuchar, and Q. Hua (1993), Ionospheric scintillation monitoring using commercial single frequency C/A code receivers, in *Proceedings of ION GPS*, vol. 93, pp. 1333–1342.
- Elvidge, S. (2014), On the use of multi-model ensemble techniques for ionospheric and thermospheric characterisation, University of Birmingham.
- Entekhabi, D., E. G. Njoku, P. E. O. Neill, K. H. Kellogg, W. T. Crow, W. N. Edelstein, J. K. Entin, S. D. Goodman, T. J. Jackson, and J. Johnson (2010), The soil moisture active passive (SMAP) mission, *Proc. IEEE*, 98(5), 704–716.
- Forte, B., and S. M. Radicella (2002), Problems in data treatment for ionospheric scintillation measurements, *Radio Sci.*, 37(6), 5–8, doi:10.1029/2001rs002508.
- Freeman, A. (1992), SAR calibration: an overview, *Geosci. Remote Sensing, IEEE Trans.*, 30(6), 1107–1121, doi:10.1109/36.193786.
- Ghafoori, F., and S. Skone (2015), Impact of equatorial ionospheric irregularities on GNSS receivers using real and synthetic scintillation signals, , 294–317, doi:10.1002/2014RS005513.Received.
- Gradshteyn, I. S., and I. M. Ryzhik (2014), Definite Integrals of Elementary Functions, in *Table of Integrals, Series, and Products*, p. 340, Elsevier Science.
- Hanson, W. B., and R. J. Moffett (1966), Ionization transport effects in the equatorial F region, *J. Geophys. Res.*, 71(23), 5559–5572, doi:10.1029/JZ071i023p05559.
- Hargreaves, J. K. (1992), Ionospheric Phenomena at Middle and Low Latitudes, in *The Solar-Terrestrial Environment*, pp. 249–311, Cambridge Atmospheric and Space Science, doi:10.1017/CBO9780511628924.
- Harris, F. J. (1978), On the use of windows for harmonic analysis with the discrete Fourier transform, *Proc. IEEE*, 66, 51–83, doi:10.1109/PROC.1978.10837.
- Hélière, F., F. Fois, C.-C. Lin, K. Scipal, M. Arcioni, P. Bensi, M. Davidson, P. Silvestrin, M. R. Drinkwater, and R. Meynart (2013), Biomass: new mission selected as the 7th ESA Earth Explorer Mission, in *Towards Horizon 2020*, pp. 89–98.
- Hernández-Pajares, M., J. M. Juan, J. Sanz, À. Aragón-Àngel, A. García-Rigo, D. Salazar, and M. Escudero (2011), The ionosphere: effects, GPS modeling and the benefits for space geodetic techniques, *J. Geod.*, 85(12), 887–907.
- Hobbs, S., C. Mitchell, B. Forte, R. Holley, B. Snapir, and P. Whittaker (2014), System design for geosynchronous synthetic aperture radar missions, *Geosci. Remote Sensing, IEEE Trans.*, 52(12), 7750–7763.
- Hofmann-Wellenhof, B., H. Lichtenegger, and J. Collins (1997), *Global Positioning System: theory and practice*, Fourth Ed., Springer-Verlag.
- Ishimaru, A., Y. Kuga, J. Liu, Y. Kim, and T. Freeman (1999), Ionospheric effects on synthetic

- aperture radar at 100 MHz to 2 GHz, *Radio Sci.*, 34(1), 257–268, doi:10.1029/1998RS900021.
- van de Kamp, M. M. J. L., P. S. Cannon, and R. J. Watson (2010), V/UHF space radars: Spatial phase decorrelation of transionospheric signals in the equatorial region, *Radio Sci.*, 45(4), n/a–n/a, doi:10.1029/2009RS004226.
- van de Kamp, M., P. S. Cannon, and M. Terkildsen (2009), Effect of the ionosphere on defocusing of space-based radars, *Radio Sci.*, 44(RS1003), doi:10.1029/2007rs003808.
- Kankaku, Y., S. Suzuki, and Y. Osawa (2013), ALOS-2 mission and development status, *Int. Geosci. Remote Sens. Symp.*, 2396–2399, doi:10.1109/IGARSS.2013.6723302.
- Kerr, Y. H. (2007), Soil moisture from space: Where are we?, *Hydrogeol. J.*, 15(1), 117–120.
- Kintner, P., H. Kil, T. Beach, and E. Paula (2001), Fading timescales associated with GPS signals and potential consequences, *Radio Sci.*, 36(4), 731–743.
- Kivelson, M. G., and C. T. Russell (1995), *Introduction to Space Physics*, Cambridge University Press.
- Knepp, D. L. (1983), Multiple phase-screen calculation of the temporal behavior of stochastic waves, *Proc. IEEE*, 71(6), 722–737, doi:10.1109/PROC.1983.12660.
- Knepp, D. L., and K. M. Groves (2011), The effect of ionospheric scintillation on phase gradient autofocus processing of synthetic aperture radar, *Gen. Assem. Sci. Symp. 2011 XXXth URSI*, 1–4, doi:10.1109/URSIGASS.2011.6050878.
- Kouba, J. (2009), A guide to using International GNSS Service (IGS) products, *Int. GNSS*.
- de La Beaujardière, O. (2004), C/NOFS: A mission to forecast scintillations, *J. Atmos. Solar-Terrestrial Phys.*, 66(17), 1573–1591.
- Mannix, C. R., D. P. Belcher, P. S. Cannon, and M. J. Angling (2016), Using GNSS Signals as a Proxy for SAR Signals: Correcting Ionospheric Defocussing, *Radio Sci.*, 51, n/a–n/a, doi:10.1002/2015RS005822.
- Massonnet, D., and J. C. Souyris (2008), 3.12.2 Azimuth Impulse Response (AIR), in *Imaging with Synthetic Aperture Radar*, pp. 160–161, EFPL Press.
- Meyer, F., and R. Bamler (2006), Methods for small scale ionospheric TEC mapping from broadband L-band SAR data, in *IEEE Conference on Geoscience and Remote Sensing Symposium, 2006. IGARSS 2006*, pp. 3718–3721.
- Meyer, F., R. Bamler, N. Jakowski, and T. Fritz (2006), The potential of low-frequency SAR systems for mapping ionospheric TEC distributions, *Geosci. Remote Sens. Lett. IEEE*, 3(4), 560–564.
- Meyer, F. J., and J. B. Nicoll (2008a), Prediction, detection, and correction of Faraday rotation in full-polarimetric L-band SAR data, *Geosci. Remote Sensing, IEEE Trans.*, 46(10), 3076–3086.
- Meyer, F. J., and J. B. Nicoll (2008b), Prediction, detection, and correction of Faraday rotation

- in full-polarimetric L-band SAR data, *Geosci. Remote Sensing, IEEE Trans.*, 46(10), 3076–3086, doi:10.1109/TGRS.2008.2003002.
- Meyer, F. J., K. Chotoo, S. D. Chotoo, B. D. Huxtable, and C. S. Carrano (2015), The Influence of Equatorial Scintillation on L-Band SAR Image Quality and Phase, *Geosci. Remote Sensing, IEEE Trans.*, PP(99), 1–12, doi:10.1109/TGRS.2015.2468573.
- Nickisch, L. J. (2004), A power law power spectral density model of total electron content structure in the polar region, *Radio Sci.*, 39(1), 8–15, doi:10.1029/2002RS002818.
- Oliver, C. (1991), Information from SAR images, *J. Phys. D. Appl. Phys.*, 1493.
- Oliver, C., and S. Quegan (2004a), Data Models, in *Understanding Synthetic Aperture Radar Images*, pp. 123–156, SciTech Publ., Raleigh, N.C.
- Oliver, C., and S. Quegan (2004b), Principals of SAR Image Formation, in *Understanding Synthetic Aperture Radar Images*, pp. 11–42, SciTech Publ., Raleigh, N.C.
- Ott, E. (1978), Theory of Rayleigh-Taylor bubbles in the equatorial ionosphere, *J. Geophys. Res.*, 83(A5), 2066, doi:10.1029/JA083iA05p02066.
- Øvstedal, O. (2002), Absolute positioning with single-frequency GPS receivers, *GPS Solut.*, 5(4), 33–44.
- Pi, X. (2015), Ionospheric Effects on Spaceborne Synthetic Aperture Radar and A New Capability of Imaging the Ionosphere from Space, *Sp. Weather*, 13(11), n/a–n/a, doi:10.1002/2015SW001281.
- Pi, X., a. J. Mannucci, U. J. Lindqwister, and C. M. Ho (1997), Monitoring of global ionospheric irregularities using the Worldwide GPS Network, *Geophys. Res. Lett.*, 24(18), 2283–2286, doi:10.1029/97GL02273.
- Pi, X., A. Freeman, B. Chapman, P. Rosen, and Z. Li (2011), Imaging ionospheric inhomogeneities using spaceborne synthetic aperture radar, *J. Geophys. Res.*, 116(A4), A04303, doi:10.1029/2010JA016267.
- Pi, X., F. J. Meyer, K. Chotoo, A. Freeman, R. G. Caton, and C. T. Bridgwood (2012a), Impact of ionospheric scintillation on spaceborne SAR observations studied using GNSS,
- Pi, X., K. Chotoo, A. Freeman, and R. Caton (2012b), Impact of ionospheric scintillation on spaceborne SAR observations studied using GNSS, in *Proceedings of the 25th International Technical Meeting of The Satellite Division of the Institute of Navigation (ION GNSS 2012)*, pp. 1998–2006, Nashville, TN.
- Quegan, S., and J. Lamont (1986), Ionospheric and tropospheric effects on synthetic aperture radar performance, *Int. J. Remote Sens.*, 7(4), 525–539, doi:10.1080/01431168608954707.
- Rignot, E. J., R. Zimmermann, and J. J. van Zyl (1995), Spaceborne applications of P band imaging radars for measuring forest biomass, *Geosci. Remote Sensing, IEEE Trans.*, 33(5), 1162–1169.
- Rino, C. L. (1979a), A power law phase screen model for ionospheric scintillation: 1. Weak

- scatter, *Radio Sci.*, 14(6), 1135–1145, doi:10.1029/RS014i006p01135.
- Rino, C. L. (1979b), A power law phase screen model for ionospheric scintillation: 2. Strong scatter, *Radio Sci.*, 14(6), 1147–1155.
- Rino, C. L. (1982), On the application of phase screen models to the interpretation of ionospheric scintillation data, *Radio Sci.*, 17(4), 855–867, doi:10.1029/RS017i004p00855.
- Rino, C. L., and V. H. Gonzalez (1983), Propagation effects in satellite-borne synthetic aperture radars, in *AGARD Propagation Factors Affecting Remote Sensing by Radio Waves (SEE N84-15646 06-43)*.
- Rogers, N. C., and S. Quegan (2014), Satellite Synthetic Aperture Radar Images, , 52(8), 4799–4807.
- Rogers, N. C., P. S. Cannon, and K. M. Groves (2009), Measurements and simulation of ionospheric scattering on VHF and UHF radar signals: Channel scattering function, *Radio Sci.*, 44(June), 1–10, doi:10.1029/2008RS004033.
- Rogers, N. C., S. Quegan, J. S. Kim, and K. P. Papathanassiou (2014a), Impacts of Ionospheric Scintillation on the BIOMASS P-Band Satellite SAR, *Geosci. Remote Sensing, IEEE Trans.*, 52(3), 1856–1868, doi:10.1109/TGRS.2013.2255880.
- Rogers, N. C., S. Quegan, J. S. Kim, and K. P. Papathanassiou (2014b), Impacts of Ionospheric Scintillation on the BIOMASS P-Band Satellite SAR, *Geosci. Remote Sensing, IEEE Trans.*, 52(3), 1856–1868, doi:10.1109/TGRS.2013.2255880.
- Rosenqvist, A., M. Shimada, N. Ito, and M. Watanabe (2007), ALOS PALSAR: A pathfinder mission for global-scale monitoring of the environment, *IEEE Trans. Geosci. Remote Sens.*, 45, 3307–3316, doi:10.1109/TGRS.2007.901027.
- Roth, A. P., B. D. Huxtable, K. Chotoo, S. D. Chotoo, and R. G. Caton (2012), Detection and mitigation of ionospheric stripes in PALSAR data, in *International Geoscience and Remote Sensing Symposium (IGARSS)*, pp. 1621–1624, doi:10.1109/IGARSS.2012.6351218.
- Rufenach, C. L. (1972), Power-law wavenumber spectrum deduced from ionospheric scintillation observations, *J. Geophys. Res.*, 77(25), 4761–4772, doi:10.1029/JA077i025p04761.
- Schunk, R., and A. Nagy (2009), *Ionospheres: physics, plasma physics, and chemistry*, Cambridge university press.
- Secan, J. A., E. J. Fremouw, and R. E. Robins (1987), A review of recent improvements to the WBMOD ionospheric scintillation model, *Eff. Ionos. Commun. Navig. Surveill. Syst. Ed. by J Goodman (US Govt Print. Off. Springfield, Va., USA)*, 607–618.
- Secan, J. A., R. M. Bussey, E. J. Fremouw, and S. Basu (1995), An improved model of equatorial scintillation, *Radio Sci.*, 30(3), 607–617, doi:10.1029/94RS03172.
- Seeber, G. (1993), *Satellite geodesy: foundations, methods, and applications*, W. de Gruyter.

- Shimada, M., Y. Muraki, and Y. Otsuka (2008), Discovery of Anomalous Stripes Over the Amazon by the PALSAR onboard ALOS satellite, in *Geoscience and Remote Sensing Symposium, 2008. IGARSS 2008. IEEE International*, vol. 2, pp. II-387-II-390, doi:10.1109/igarss.2008.4779009.
- Shimada, M., O. Isoguchi, T. Tadono, and K. Isono (2009), PALSAR radiometric and geometric calibration, *IEEE Trans. Geosci. Remote Sens.*, 47(12), 3915–3932, doi:10.1109/TGRS.2009.2023909.
- Stimson, G. W. (1998), *Introduction to airborne radar*, SciTech Pub.
- Sultan, P. J. (1996), Linear theory and modeling of the Rayleigh-Taylor instability leading to the occurrence of equatorial spread F, *J. Geophys. Res.*, 101(A12), 26875, doi:10.1029/96JA00682.
- Tralli, D. M., R. G. Blom, V. Zlotnicki, A. Donnellan, and D. L. Evans (2005), Satellite remote sensing of earthquake, volcano, flood, landslide and coastal inundation hazards, *ISPRS J. Photogramm. Remote Sens.*, 59(4), 185–198.
- Umeki, R., C. H. Lui, and K. C. Yeh (1977), Multifrequency spectra of ionospheric amplitude scintillation, *J. Geophys. Res.*, 82(19), 2752–2760.
- Vexcel Corporation (2003), *PALSAR Algorithm Description - VX-PALSAR-010 v1.0*, Boulder, CO.
- Ward, K. (1981), Compound representation of high resolution sea clutter, *Electron. Lett.*, 17(16), 561–563.
- Woodman, R. F., and C. La Hoz (1976), Radar observations of F region equatorial irregularities, *J. Geophys. Res.*, 81(31), 5447–5466, doi:10.1029/JA081i031p05447.
- Xu, Z.-W., J. Wu, and Z.-S. Wu (2004), A survey of ionospheric effects on space-based radar, *Waves in Random Media*, 14(2), S189–S273, doi:10.1088/0959-7174/14/2/008.
- Yeh, K. C., C. H. Liu, and M. Y. Youakim (1975), A theoretical study of the ionospheric scintillation behavior caused by multiple scattering, *Radio Sci.*, 10(1), 97–106, doi:10.1029/RS010i001p00097.